ADVANCES IN SCANNING FORCE MICROSCOPY OF BIOLOGICAL STRUCTURES

Thesis by

Steven Manning Clark

In Partial Fulfillment of the Requirements

for the Degree of

Doctor of Philosophy

California Institute of Technology

Pasadena, California

1993

(Defended November 23, 1992)

Acknowledgments

There are many people who have played a role in both my scientific and personal development during the course of this work. I would like to take this opportunity to thank several individuals for the outstandingly positive contributions which they have made, even some of which they may not be aware. First, I would like to thank Professors J. D. Baldeschwieler and J.-P. Revel for their constant support of my work both financially and scientifically. Their enthusiasm and positive outlook were crucial on many occasions. I would like to thank Professors P. J. Bjorkman and D. C. Rees for teaching me what I know about molecular structure and methods for its study. I would also like to thank Professor L. E. Hood for his support in the form of an infrastructure at Caltech and a general appreciation of biotechnology. I should also thank Professor S. E. Fraser, who always seemed to have an encouraging word for my efforts, and Professor B. Wold for withstanding some buffeting on my account.

There are several other people who deserve thanks as well. I would like to thank Charles Spence without whose help the project would have either never been completed or been finished in half the time. I would also like to thank the other members of the Baldeschwieler laboratory who introduced me to scanned probe microscopes and provided a valuable foil for many ideas.

Finally, I would like to thank my wife, Lynne, for providing a constant source of motivation. I should also thank my children, Julia and Andrew for sometimes being patient and almost always understanding.

Abstract

A multifacted approach to the imaging of biological structures by scanning force microscopy is described. The major problems addressed are the distortion of biological samples by excessive forces applied by the cantilever stylus and sample motion relative to the imaging substrate.

The first two chapters discuss the design of digital signal processor based scanning force microscope control electronics and a novel microscope head that eliminates the application of excessive forces to the sample caused by electronic or vibrational noise.

The third chapter presents a novel use of chemical vapor deposition for application of heterofunctional alkoxysilanes to scanning force microscopy imaging subsrates. This technique provides imaging substrates which have chemical groups that can be used for sample immobilization without compromising substrate smoothness. The use of the chemically derivatized substrates for scanning force microscopy is also explored.

The final chapter presents high resolution images of bovine liver catalase micro-crystals. The images of the protein micro-crystals show resolution on the order of 2 to 3 nanometers allowing the visualization of individual catalase tetramers. To our knowledge this is the first report of images of protein micro-crystals taken by scanning force microscopy which have resolution comparable to that of electron microscopy.

Table of Contents

Acknowledgements		iii
Abstract		iv
List of Figures		vi
List of Tables		xi
Introduction		1
Chapter I.	Hardware for Digitally Controlled Scanned Probe Microscopes (In Press *Review of Scientific Instruments*)	21
Appendix A.	Digital Signal Processor Based Design of Low Noise Drive Electronics for Scanned Probe Microscopy	71
Appendix B.	Digital Signal Processor Control of Scanned Probe Microscopes	146
Chapter II.	A High Performance Scanning Force Microscope Head Design (Submitted to *Review of Scientific Instruments*)	191
Appendix C.	Design Details of the Scanning Force Microscope Head	210
Chapter III.	A Covalent Sample Immobilization Chemistry for Scanned Probe Microscopy (To Be Submitted to *Journal of Structural Biology*)	247
Appendix D.	Detailed Protocols for the Preparation of Chemically Derivatized Substrates for Scanned Probe Microscopy	290
Chapter IV.	High Resolution Imaging of Bovine Catalase Micro-Crystals Using the Atomic Force Microscope (To Be Submitted to *Science*)	309
Summary:	Future Directions for Scanned Probe Microscopy in Biology	325

List of Figures

Introduction

Figure 1. A stylized representation of the scanning force microscope head and sample stage. 9

Figure 2. A montage of scanning electron micrographs tracing the evolution of cantilevers and stylii. 11

Chapter 1.

Figure 1. A block diagram of a digital control system for scanned probe microscopy. 26

Figure 2. A block diagram of a multiprocessor control and data acquisition system for scanned probe microscopy. 30

Figure 3. A block diagram of the scanned probe microscope control and data acquisition system. 37

Figure 4. A diagram of the piezoelectric ceramic drive electronics. 43

Figure 5. Measured time domain characteristics of the 420 V piezo drive electronics. 46

Figure 6. Measured frequency domain characteristics of the 420 V range piezo drive electronics. 48

Figure 7. A diagram of a single channel analog to digital converter for the scanned probe microscope control and data acquisition system. 52

Figure 8. Measured performance of the analog to digital converter section. 55

Figure 9. Evolution of the count distribution histogram with sample size. 58

Figure 10. An image of highly oriented pyrolytic graphite taken using the SPM control electronics presented in this article to control an ultra-high vacuum scanning tunneling microscope. 62

Figure 11. A block diagram of the SPM control and data acquisition system as it might be adapted for near field scanning optical microscopy. 66

Appendix A.

Figure 1. A block diagram of the scanned probe miroscope control system. 76

Figure 2. A block diagram of the TMS320C30 digital signal processor. 77

Figure 3. A block diagram of the TMS320C30 System Board. 79

Figure 4. DSP-Link/ NIM Bin Bus Timing Diagram. 83

Figure 5. Assembly drawing, connector pinout and schematics for the DSP interface / bus driver card. 85

Figure 6. The Modified NIM Connector Pinout. 92

Figure 7. The NIM Bin Bus Connector Pinout. 93

Figure 8. Modification of a single-wide NIM module backplane. 94

Figure 9. Modification of a double-wide NIM module backplane. 95

Figure 10. Printed circuit board mounting hole pattern for NIM modules. 96

Figure 11. Schematic diagram for low noise voltage regulators. 99

Figure 12. A map of the SPM control electronics address space. 101

Figure 13. Schematics for the DAC board. 108

Figure 14. Schematic diagrams for the high voltage piezoceramic driver and approach motor driver circuitry. 114

Figure 15. Schematics for the ADC module. 119

Figure 16. ADC module timing diagram. 126

Figure 17. Quadrant Photodiode Preamplifier. 142

Figure 18. Second Stage Amplifier Schematic. 143

Appendix B.

Figure 1. A block diagram of a digital control system for scanned probe microscopy. 150

Figure 2. A block diagram of a scanned force microscope control and data acquisition system. 153

Figure 3. Software algorithms used during one timer period while scanning. 159

Figure 4. Manual optimization of AFM feedback using step response curves. 168

Figure 5. An AFM tip-sample approach curve taken in air. 179

Chapter 2.

Figure 1. A diagram of the scanning force microscope head. 195

Figure 2. A diagram of the single mode optical fiber input optics. 200

Figure 3. A diagram of the laser diode input optics. 203

Figure 4. Images of micro-crystals of beef liver catalase. 206

Appendix C.

Figure 1. The AFM base. 213

Figure 2. The modified AFM base. 216

Figure 3. The SEM sample stub adapter. 217

Figure 4. The AFM base suspension ring. 218

Figure 5. Mechanical drawings of the AFM head. 222

Figure 6. Single mode fiber input telescope body. 229

Figure 7. Collimating lens retaining sleeve. 231

Figure 8. Laser diode input telescope body. 233

Figure 9. A top view of the assembled photodiode translator. 236

Figure 10. Photodiode mount. 237

Figure 11. Thrust plunger. 238

Figure 12. Right side adjustment screw bracket. 239

Figure 13. Left side thrust plunger bracket. 240

Figure 14. Top thrust plunger bracket. 241

Figure 15. Bottom adjustment screw bracket. 242

Figure 16. The telescope clamp. 244

Figure 17. The motor sleeve counterweight. 245

Chapter 3.

Figure 1. A comparison of solution deposition and chemical vapor deposition chemistry of bi- and tri - alkoxysilanes. 253

Figure 2. Comparison of surface topography resulting from different alkoxysilane deposition methods by scanning force microscopy. 256

Figure 3. Two synthetic routes to the isothiocyanate derivative of 3-aminopropyl alkoxysilane treated substrates. 263

Figure 4. A typical image taken with the scanning fluorimeter. 271

Figure 5. Image of a microcrystal of bovine catalase fixed to a 3-amino propyl alkoxysilane treated glass substrate obtained under water. 276

Figure 6. The chemical vapor deposition (CVD) apparatus. 281

Figure 7. Chemical structures of the small molecule fluorescent probes used to assay for various surface derivatives. 285

Appendix D.

Figure 1. Reaction flask type CVD apparatus. 294

Figure 2. Use of an Abderhalden drying apparatus forCVD. 298

Chapter 4.

Figure 1. Two views of a catalase tetramer. 312

Figure 2. AFM images of beef liver catalase micro-crystals. 314

Figure 3. A gray scale representation of the 2-dimensional power spectrum of the image shown in Fig. 2b. 317

Figure 4. A transmission electron micrograph of a Pt-C replica of a catalase micro-crystal sample. 319

List of Tables

Appendix B.

Table I. Formulas for Feedback Algorithms. 166

Chapter 3.

Table I. Stability of Fluorescence Intensity After Various Washes. 260

Table II. Isothiocyanate Derivatization of Aminopropyl Glass. 262

Table III. CVD of 3-Mercaptopropyl Trimethoxysilane. 266

Table IV. CVD of Alkoxysilylpropyl TMA Cl. 267

Table V. CVD Derivatization of SIlica. 269

Table VI. CVD Derivatization of Mica. 273

Appendix D.

Table I. Suppliers of Alkoxysilanes. 293

Table II. Parts for Reaction Flask Chemical Vapor Deposition Apparatus. 295

Table III. Equipment for Handling Air Sensitive Reagents. 296

Table IV. Parts for the Drying Apparatus Based Chemical Vapor Deposition Apparatus. 297

An Introduction to Scanning Force Microscopy

An Historical Perspective

Microscopy might be most broadly defined as the family of techniques which can be used to visualize objects too small to be seen with the naked eye. When considered in this light, microscopy encompasses the fields of electromagnetic microscopy, electron microscopy, scanned probe microscopy and other less familiar techniques. Since the 1600's, microscopy and biology have had a symbiotic relationship; originally light microscopes provided a new window into the world of microorganisms and efforts to view the tiny creatures spurred the development of more sophisticated instruments. This pattern holds true to the present day with advances in confocal light microscopy, pH and ion sensitive dyes, etc. being driven by the demands for superior methods to image inter- and intra-cellular processes and structures.

When one surveys the field of microscopy, several themes emerge. One of these has been the drive for increased resolution at almost any cost. In the 1870's Ernst Abbe elucidated the "fundamental" limit to resolution in light microscopy. This limit was due to diffraction caused by the electromagnetic wave nature of light. It was only after the introduction of the concept of wave-particle duality by Louis de Broglie in 1924 that it was realized that electron sources might provide a key to better resolution. Because electrons can be readily accelerated and focussed by electromagnetic fields, their wavelength can be decreased to any point at which diffraction effects do not pose a serious limit to resolution. As early as 1928 several investigators were actively engaged in the construction of electron microscopes. It was hoped that this new tool would readily permit visualization of biological specimens. However, the increased resolution offered by the electron microscope came at a cost; because electrons interact strongly

with matter, imaging has to be done in a vacuum. Also the cross section for electron absorbtion is fairly uniform for low atomic weight materials and consequently contrast on biological specimens requires enhancement. Additionally, electron induced sample damage proved to be substantial and efforts to minimize electron damage continue at present. Nonetheless, in 1934, Ladislaus Marton[1] became the first investigator to image a biological sample, a section of a plant leaf, in the electron microscope. Despite its inherent limitations, over the years, methods for imaging biological samples have been developed which have made the electron microscope a powerful tool for biologists.

Another theme occurring in microscopy is one which is shared in many areas of biology; new techniques and instruments reveal important details of biological systems which deepen our understanding of currently recognized problems and often also lead to the discovery of entirely new aspects of biology. Although there are many examples which illustrate this theme, perhaps the most compelling from the field of microscopy is the discovery of the cellular nature of animal and plant tissues. Although many attribute this erroneously to Schleiden and Schwann[2] in 1838, the existence of "cells" was documented in the mid-1600's by Hooke[3] and others. In any case, it was through the use of the then relatively new instrument, the light microscope, that these investigators were able to provide evidence supporting the cell doctrine and give a formal basis to the nascent field of cell biology. This discovery was so profound that it provides, along with evolutionary theory, one of the fundamental tenets of modern biology.

The last major theme that should be mentioned is one which is currently emerging. It is that digital imaging promises to revolutionize the way in which microscopy is done. With the advent of high speed electronic computers and the ability to directly acquire image data in digital form, many of the limitations of film can be avoided. Additionally, with image data in digital form the full suite of digital signal processing algorithms can be applied to the images. Algorithms are available to enhance contrast, deconvolve instrumental imperfections, etc. This not only allows the maximum amount of relevant information to be extracted from images, but also permits visualization of details which had been inaccessible to microscopists.

One of the most striking aspects of microscopy is that, after four hundred years, there is still no ideal technique which is well suited to the varied demands of biology. Conventional light microscopy has limited resolution and microscopical techniques which allow higher resolution, such as electron microscopy and X-ray crystallography, require placing the specimen in harsh environments or the examination of highly ordered specimens (crystals). As will be seen, scanned probe microscopes are not a panacea for these problems, but they provide a powerful addition to the biologist's armamentarium.

Scanned Probe Microscopy

Scanning force microscopy (SFM) is one of several recently invented scanned probe microscopies (SPMs). The founding member of the SPM family was the now familiar scanning tunneling microscope (STM).[4] Other members include magnetic force microscopy,[5] scanning charge microscopy,[6] scanning ion conductance microscopy,[7] scanning electrochemical microscopy[8] and near-field

scanning optical microscopy. [9] Although different contrast mechanisms are at work in each of these microscopies, they share three common elements: i) the ability to finely control the position of a probe; ii) the ability to measure a signal which depends on the probe-sample interaction; iii) a control mechanism which can use a distance dependent signal to coordinate the probe motion.

The prime attraction of the SPMs is the superior resolution that can be attained as compared to the techniques of light and electron microscopy. Soon after the invention of the STM, images were obtained in which atomic features are clearly resolved. [10] Such demonstrations of the resolution inherent in SPMs suggested that, with reasonable effort, high resolution images could be routinely obtained on a variety of samples, including perhaps samples of biological interest. Another strength of the SPMs lies in their ability to image in different environments (e.g., in air or under water). The promise of high resolution imaging of biological samples under physiologically relevant conditions has piqued the interest of structural biologists.

The simplest example of a scanned probe microscope is provided by the STM. In an STM the probe is a sharp tip usually composed of a platinum or tungsten alloy which has been fabricated by cold cleaving or electrochemical etching. The three-dimensional position of the tip is controlled by the use of piezo-electric crystal actuators. When imaging with the STM, an electrical potential is maintained between the tip and the sample. As the tip is brought into close proximity to the sample surface the probability of electrons tunneling across the potential barrier increases. The movement of electrons across the barrier constitutes a current which can be measured electronically. Because the probability of an electron tunneling across the barrier is exponentially dependent

on the distance between the tip and sample, the tunneling current provides a signal which is exquisitely sensitive to tip-sample separation. Sample topography is sensed by recording the excursions of the tip perpendicular to the sample surface, while maintaining a constant tunneling curent, as the tip is raster scanned over the sample surface.

The major factor limiting the application of STM to biology is the requirement of sample conductivity. Most biological samples are minimally conductive to electron flow and even if a biological sample can be imaged with the STM the lack of a clear contrast mechanism greatly complicates image interpretation. Additionally, there is some concern that typical STM imaging substrates (e.g., highly oriented pyrolytic graphite) may give rise to artifacts which resemble some of the more interesting biological specimens (e.g., DNA and other filamentous samples).[11,12]

In order to overcome the sample conductivity requirement of the STM, in 1985 Binnig, Quate and Gerber[13] invented the scanning force microscope (which until recently was called the atomic force microscope or AFM). In their original design, a cantilever was brought into contact with the sample surface and the deflection of the cantilever was monitored by an STM. Because the tunneling current between the STM tip and the back of the cantilever was difficult to control and prone to fluctuations induced by contamination of the tunneling junction, designs based on optical beam deflection[14] soon became popular.

The STM and scanning force microscope (SFM) are not the only members of the scanned probe microscope family that are of interest to biologists. In fact, two other SPMs, the scanning ion conductance microscope (SICM) and the near-

field scanning optical microscope (NSOM) will both give biologists new ways to look at cellular biology. With the SICM, high resolution images of ion flow at cell membranes should be possible, and in the limiting case, the currents from single ion channels may be imageable. NSOM also promises to be an exciting tool for biology. Its key advantage is the ability to attain lateral resolution on the order of 10 nm without sacrificing the advantages of light microscopy. This means that all of the techniques used to increase contrast and specifically mark biological structures applied in other forms of light microscopy are available for use with NSOM. Because the images produced by NSOM are heavily dependent on probe-sample separation, this technique offers, for relatively flat specimens, background signal rejection comparable to that obtained with confocal microscopy.

Before moving to the substance of this thesis, it is important to gain some familiarity with scanning force microscopy and some of the key factors controlling contrast generation in SFM images. Equally important is an understanding of the challenges involved in imaging biological samples by SFM. While many of the problems, and techniques for their solution, in this area are similar to those in electron and light microscopy, there are several factors which are peculiar to SFM.

Scanning Force Microscopy

As mentioned previously, the scanning force microscope consists of a cantilever whose deflection is recorded as it is raster scanned over a sample surface.[15] This rather minimalistic view of the microscope serves well; the nature of the cantilever is not specified, nor is the mechanism by which its

deflection is sensed, allowing many different embodiments to be envisioned. The implementation of a scanning force microscope (SFM) which was used in gathering the data presented in this thesis is shown in Figure 1.

At the heart of the SFM is the cantilever and stylus. Several versions of cantilevers are shown in Figure 2. This montage of cantilever images shows successive steps in the evolution of cantilevers and stylii. Originally cantilevers were hand fabricated (Fig. 2a) by bending wire or metallic foil into the appropriate shape and affixing tiny mirors with glue. To form a stylus often shards of diamond were also glued to the tip of the cantilever.
These cantilevers were not only time consuming to make, but they also left much to be desired in terms of performance. With these cantilevers resonant frequencies tended to be low and the spring constants were often too high. In addition, due to the nature of the fractured diamonds, one could never be assured of a pointed stylus.

The next step in the evolution of cantilevers for SFM was the use of micromachining techniques for their fabrication. [16] Progress occurred in two steps. The first micromachined cantilevers were made without a stylus. These were usually used at a steep angle so that the tip of the cantilever could be used as a stylus, rather than affixing a diamond shard as done previously. Shortly after this development, methods were established to produce cantilevers with integral pyramidal stylii. This type of cantilever is shown in Figure 2b and has been the style of cantilever predominately used to date. A higher magnification image of the integral stylus is shown in Figure 2c.

Figure 1. A stylized representation of the scanning force microscope head and sample stage. The head design used to gather the image data presented in this thesis provides a mechanism for scanning the cantilever over a stationary sample. The deflection of the cantilever is detected by the motion of the laser beam reflected from the back of the cantilever. By using a quadrant photodiode as the reflected beam position sensor the instrument can also be used to measure torsional motions of the cantilever (called by some lateral force microscopy). The details of the head design can be found in Chapter 2 and Appendix C of the thesis.

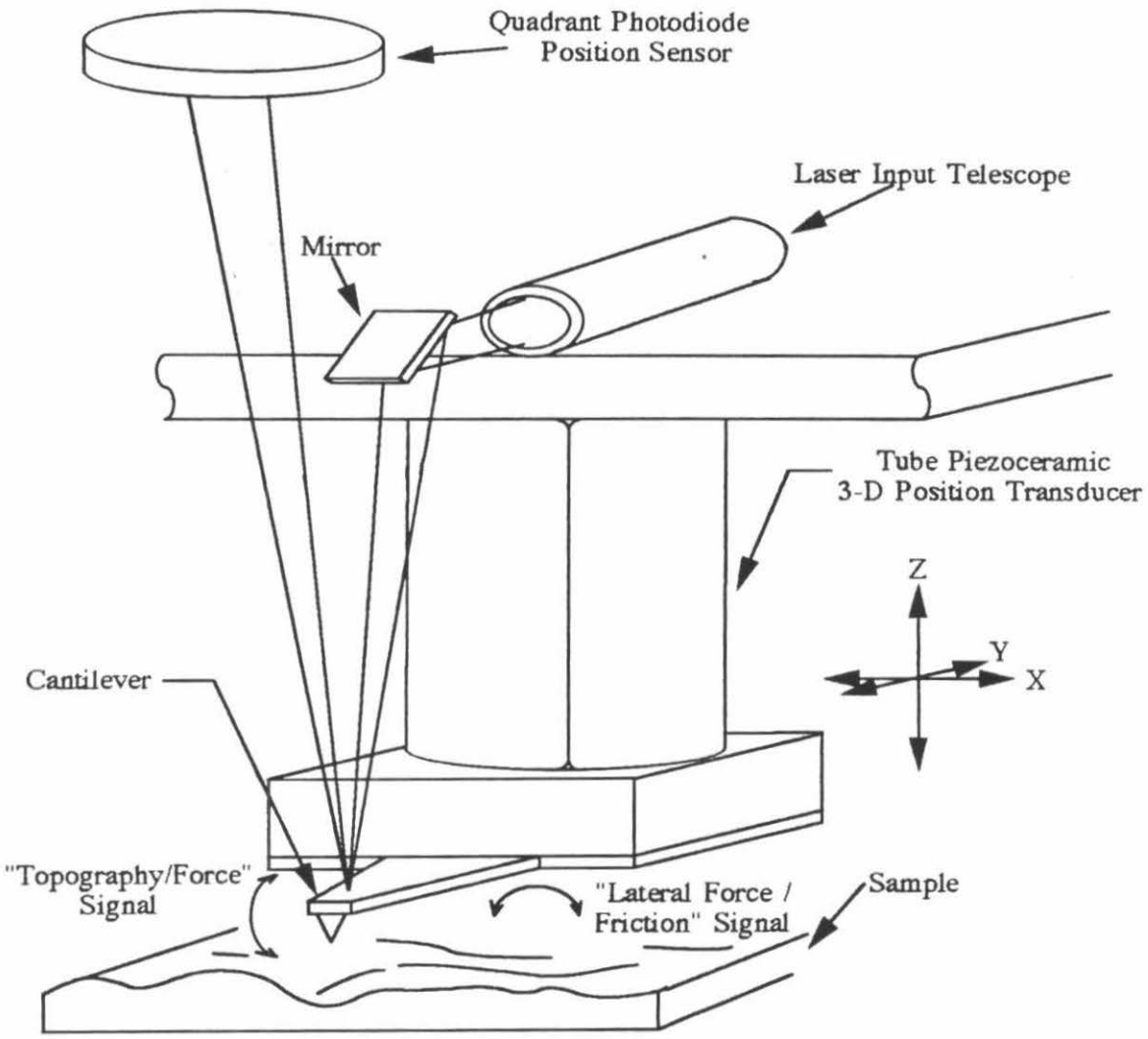
Quadrant Photodiode
Position Sensor
Laser Input Telescope
Mirror
Tube Piezoceramic
3-D Position Transducer
Z
Y
X
Cantilever
"Topography/Force"
Signal
"Lateral Force /
Friction" Signal
Sample

Figure 2. A montage of scanning electron micrographs tracing the evolution of cantilevers and stylii. a) a hand fabricated cantilever with a foil mirror and diamond shard stylus. b) a micromachined cantilever with integral pyramidal stylus. c) a view of the end of a micromachined cantilever with an integral stylus at higher magnification. d) an electron beam deposited tip at the apex an integral stylus attached to a micromachined cantilever (similar to the cantilever shown in parts b and c). e) micrograph of a micromachined cantilever fabricated by a process that produces sharp integral tips with good aspect ratios. f) a transmission electron micrograph of the apex of a stylus attached to a cantilever fabricated by the same process as the cantilever in part e. (Parts a and b of this Figure were supplied by courtesy of Dr. Jan Hoh).

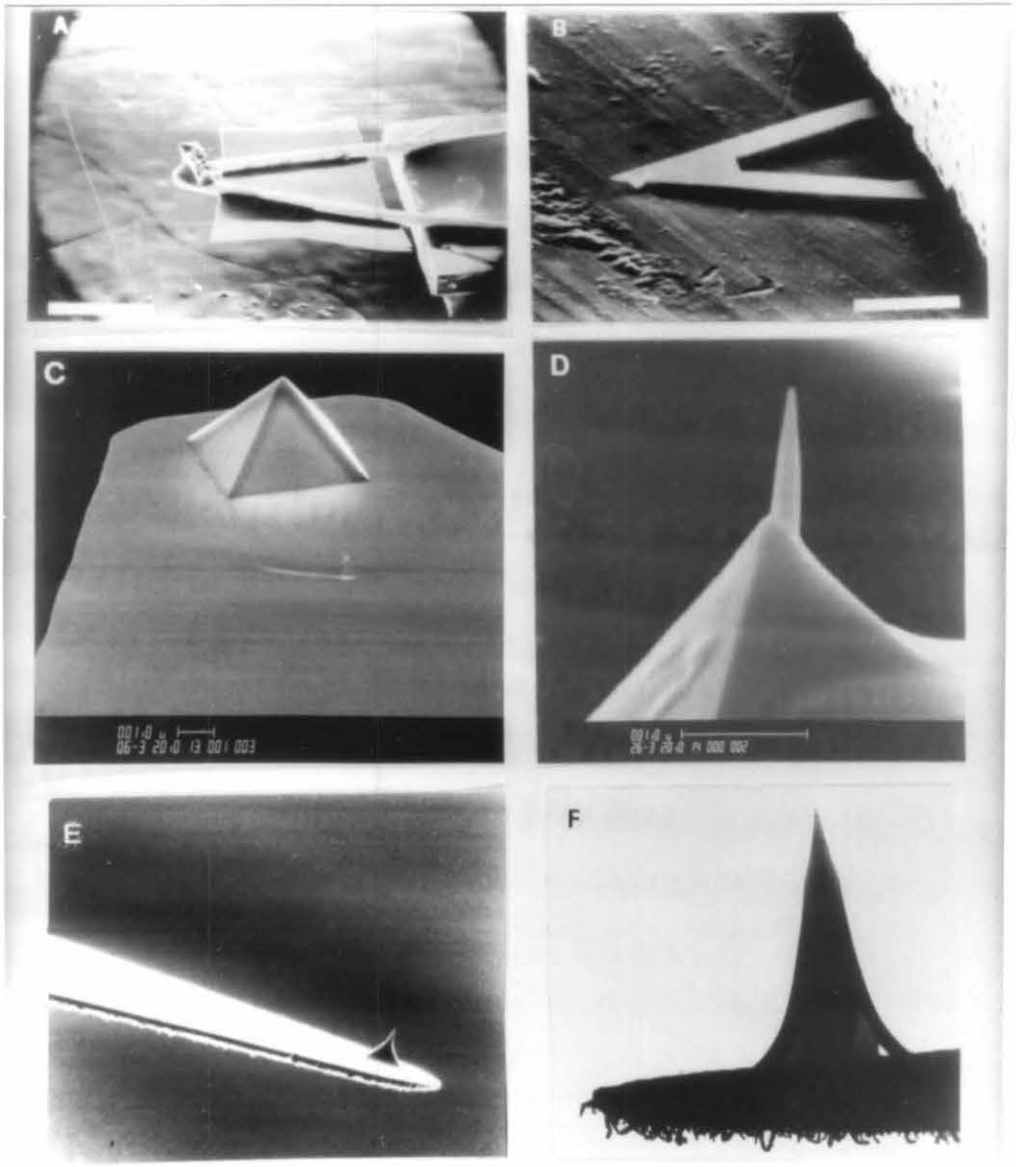
A
B
C
D
E
F

One of the drawbacks of pyramidal stylii is their aspect ratio (the ratio of height to width at the base). Because the angle between the faces of the pyramid is shallow, steep sample features are not accurately measured. Recently, several methods have been developed which permit the fabrication of high aspect ratio stylii to address this problem. Figure 2d shows a standard micromachined cantilever with an integral pyramidal stylus upon which an amorphous carbon deposit has been grown by electron beam deposition.[17,18] In the vernacular of the SFM field, this type of stylus is often referred to as an electron beam deposited (EBD) tip. Investigators often take one additional processing step and attempt to sharpen the EBD tips by annular ion milling.[19,20]

Figure 2e shows a cantilever with an integral stylus manufactured by a different micromachining process. This type of cantilever has just recently become commercially available. The two main advantages offered by this new fabrication scheme are that the stylii produced have much more attractive aspect ratios and the tips tend to be quite sharp. We have examined several of these tips by TEM and Figure 2f is a micrograph showing one of the better tips we have found.

Having just discussed some of the features of cantilevers and stylii it seems appropriate now to turn to their use. A description of the two major SFM imaging modes as well as an overview of tip-sample interaction and contrast generation mechanisms follows. In SFM it is cantilever deflection which is measured. This simple fact has been used to advantage, for example, in the scanning charge microscope, however this can also be troublesome in that surface forces which are unassociated with sample topography (e.g., meniscus forces) can result in substantial deflection of the cantilever. With SFM it is

possible to image samples in two different force regimes. The first regime utilizes the attractive forces that occur when two surfaces come into close proximity. By arranging instrument conditions so that the SFM is sensitive to the attaractive force beween the stylus apex and the sample,[21] contours of equal attractive force can be recorded as the cantilever is scanned. Because the attractive force decreases strongly with tip-sample separation this imaging mode can provide a sensitive measure of surface topography without having the tip and sample actually come into contact. Previously many investigators thought that while this non-contact or attractive mode imaging was less likely to damage the sample, it would fall far short of the desired lateral resolution attainable with the contact or repulsive imaging mode.

The contact or repulsive imaging mode is perhaps more intuitive than the non-contact mode and has certainly been more widely used. All of the data presented in this thesis was taken using contact mode imaging. During contact mode imaging the apex of the stylus is brought into contact with the sample while the deflection of the cantilever is monitored. One method used to image topography is to set the Z axis piezoactuator at some average value and to record the excursions in cantilever position as the scanning proceeds. This mode, called constant height or fast scan mode, is often used to examine samples at high magnification or at fast scan rates in order to eliminate thermal drift and low frequency mechanical vibration effects. The validity of the tacit assumption of uniform sample elasticity also needs to be considered when interpreting images taken in constant height mode. Another way to image a sample surface is to keep the cantilever deflection constant by altering the Z axis voltage during scanning. One thus traces out contours of equal repulsive force. Again, with the assumption that sample elasticity is uniform, the record of voltage applied to the

Z axis piezoactuator should be proportional to sample topography. Images acquired in this manner are called constant force or slow scan images.

It is appropriate to comment a little further concerning the nature of atomic contact in repulsive mode imaging. While there is no doubt that tip sharpness (measured as the radius of curvature) is essential for good image quality, sharpness is not the only factor that influences imaging. Among the other factors playing significant roles are tip and sample elasticity, chemical composition, interaction between charges on the tip and sample. An appealing view of tip-sample interaction is one where the materials that compose the tip and sample are infinitely stiff. This implies that they are entirely inelastic and can sustain tremendous stresses without deforming. The result of this model is that a point contact is possible between one atom at the apex of the tip and the various atoms composing the sample and that the resolution of the microscope is not limited by finite tip-sample contact area. As one might anticipate, this view proves to be somewhat naive and the real properties of materials with finite elasticity and bond strengths necessitate its modification. [22]

Special Problems in Imaging Biological Samples

In thinking about how some of the ideas discussed above might be applied in efforts to image biological materials one is immediately struck with the fact the many biological materials are highly deformable and that in order to effectively image biological samples forces applied to the sample by the stylus must be reduced as much as possible. It should also noted that, as tips become sharper, contact areas decrease and forces which might have previously been tolerated, now lead to serious sample distortion. Thus in attempts to obtain high resolution

images of compliant samples the requirement of sharper tips to improve resolution leads to increasingly stringent performance criteria for SFM instrumentation.

There have been several estimates of the tolerable forces while imaging biomaterials.[23,24] Because the reduction of imaging forces is central to attaining the goal of high resolution imaging of biological samples, commercial SPM instruments were evaluated for their ability to attain the conservative level of imaging forces in the 10^{-11} newton range. Because none of the commercially available instruments were able to meet this challenging level of performance these systems could not be used to repeatably image biological samples. This forced the design of an instrument which would routinely achieve imaging forces in the 10^{-11} newton range. The description of the instrument along with the methods used in designing and verifying the performance of this instrument occupy Chapters 1 and 2 as well as Appendicies A, B and C of this thesis.

Chapter 1 is focused on the design and evaluation of SPM control electronics whose performance exceeds the requirements for imaging biological samples. The noise performance of the custom designed control electronics is sufficient to eliminate the electronics as a potential noise source for the microscope. Having eliminated the electronics as a limiting factor, the next largest noise source is mechanical and acoustic vibration of the microscope stage and head. To reduce this noise source to the lowest possible level, a new microscope head was designed, which is the topic of Chapter 2. This head design eliminates all unnecessary components which may contribute noise.

Another problem encountered when one attempts to image biological samples by SPM is sample motion. Samples tend to exhibit both intramolecular motion and motion with respect to the imaging substrate. Biological samples tend to be particularly soluble in the solution environments which would be most relevant. Avoiding problems such as the detachment of samples adsorbed to the imaging substrate is particularly challenging in SPM. Because many of the methods previously used to immobilize samples degrade substrate surface smoothness and preclude high resolution imaging, alternative techniques were developed which allow sample immobilization without compromising substrate smoothness. The development of this covalent sample immobilization chemistry comprises Chapter 3.

The culmination of the effort described in Chapters 1-3 of this thesis can be found in Chapter 4 which describes the successful imaging of protein micro-crystals. Protein micro-crystals occupy a special position in scanning force microscopy; because they present such attractive features as scanning probe microscope samples, many attempts have been made to image protein crystals. To the best of our knowledge all of these attempts have fallen short of providing high resolution images of protein crystals. In Chapter 4 we present images with resolution comparable to that achievable by electron microscopy. In fact, even STM sudies of Pt-C replicas[25] do not show the resolution we are able to achieve with the SFM.

A Concluding Remark

The work presented in this thesis consitutes a reasonable and systematic effort to realize some of the potential of SFM for studying biological structures.

At the outset there seemed to be three major areas requiring attention before SFM could be realistically applied to biology: i) the SFM instrumentation required refinement to eliminate noise sources that made high resolution imaging on biological samples difficult; ii) methods for immobilizing biological samples on SPM compatible imaging substrates without compromising substrate properties were needed; and iii) further investigation of tip-sample interactions and the effect of tip sharpness on image quality was required. The first two factors have been addressed by the work in this thesis and the last factor is the focus of some ongoing effort.

The major question concerning many who might read this thesis is, does SFM have something to offer the biologist and if so, what? The best answer to this question is that SFM has a great deal to offer biologists. The two main categories of biological study to which the SFM can immediately contribute are: i) imaging biological structures in physiological conditions with resolution on the order of a few nanometers (high resolution); and ii) imaging cellular and organellar structures and processes in living specimens perhaps in "real time." SFM should also be able to advance the area of biophysics concerned with the study of molecular motors by allowing calibrated, direct measurements of forces generated by the motors. This is all said with the caveat that SFM, like any other field, is subject to artifact; however, the careful biologist will find SFM provides a novel and rewarding method for imaging biological samples.

References:

1. Marton, L. (1934). "Electron Microscopy of Biological Objects." *Nature* **133** (3372): 911.
2. Conklin, E. G. (1939). "Predecessors of Schleiden and Schwann." *Amer. Naturalist* **73**:538-46.
3. Hooke, R. (1665). Micrographia: Physiological description of minute bodies made by magnifying glasses with observations and inquiries thereupon. First edition published by the Royal Society, available in facsimile edition from Dover Books, New York, N. Y.
4. Hansma, P. K., V. B. Eiings, O. Marti, C. E. Bracker. (1988). "Scanning Tunneling Microscopy and Atomic Force Microscopy: Application to Biology and Technology." *Science* **242**:209-16.
5. Rugar, D. et al. (1990). "Magnetic force microscopy: General principles and application to longitudinal recording media." *J. Appl. Phys.* **68** (3):1169-1183.
6. Saurenbach, F. and B. D. Terris. (1992). "Electrostatic Writing and Imaging Using a Force Microscope." *IEEE Trans. on Industry Applications* **28** (1):256-260.
7. Prater, C., P. Hansma, M. Tortonese, C. Quate (1991). "Improved scanning ion-conductance microscope using microfabricated probes." *Rev. Sci. Instrum.* **62** (11):2634-38.
8. Bard, A., F. Fan, D. Pierce, P. Unwin, D. Wipf, F. Zhou. (1991). "Chemical Imaging of Surfaces with the Scanning Electrochemical Microscope." *Science* **254**:68-74.
9. Betzig, E. and J. K. Trautman (1992). "Near-field Optics: Microscopy, Spectroscopy and Surface Modification Beyond the Diffraction Limit." *Science* **257**:189-195.
10. Binnig, G., H. Rohrer, Ch. Gerber and E. Weibel. (1982). "Surface Studies by Scanning Tunneling Microscopy." *Phys. Rev. Lett.* **49**:57-61.
11. Clemmer, C. R. and T. P. Beebe. (1991). "Graphite: A Mimic for DNA and Other Biomolecules in Scanning Tunneling Microscope Studies." *Science* **251**:640-42.
12. Heckl, W. M. and G. Binnig. (1992). "Domain Walls on Graphite Mimic DNA." *Ultramicroscopy* **42**:1073-78.
13. Binnig, G., C. F. Quate and Ch. Gerber (1986). "Atomic Force Microscope." *Phys. Rev. Lett.* **56**:930-933.

14. Meyer, G. and N. M. Amer (1988). "Novel optical approach to atomic force microscopy." *Appl. Phys. Lett.* **53** (12):1045.

15. Rugar, D. and P. K. Hansma. (1990). "Atomic Force Microscopy." *Physics Today* Pages 23-30, October 1990.

16. Albrecht, T. R. (1989). "Advances in Atomic Force Microscopy and Scanning Tunneling Microscopy." Ph. D. Thesis, Stanford University, Stanford, CA 94305.

17. Keller, D. J. and C. Chih-Chung. (1992). "Imaging steep, high structures by scanning force microscopy with electron beam deposited tips." *Surface Science* **268**:333-339.

18. Lee, K. L., D. W. Abraham, F. Secord and L. Landstein. (1991). "Submicron Si trench profiling with an electron-beam fabricated atomic force microscope tip." *J. Vac. Sci. Technol.* **B9** (6):3562-3568.

19. Vasile, M. J. et al. (1991). "Scanning probe tips formed by focused ion beams." *Rev. Sci. Instrum.* **62** (9):2167-71.

20. Vasile, M. J. et al. (1991). "Scanning probe tip geometry optimized for metrology by focused ion beam ion milling." *J. Vac. Sci. Technol.* **B9** (6):3569-3572.

21. Albrecht, T. R., P. Grutter, D. Horne, D. Rugar. (1991). "Frequency modulation detection using high- Q cantilevers for enhanced force microscope sensitivity." *J. Appl. Phys.* **69** (2):668.

22. Landman, U., W. D. Luedtke, N. A. Burnham, R. J. Colton. (1990). "Atomistic Mechanisms and Dynamics of Adhesion, Nanoindentation and Fracture." *Science* **248**:454-461.

23. Persson, B. N. J. (1987). "The atomic force microscope: Can it be used to study biological molecules?" *Chem. Phys. Lett.* **141** (4):366.

24. Drexler, K. E. (1991). "Molecular tip arrays for molecular imaging and nanofabrication." *J. Vac. Sci. Technol.* **B9** (2):1394-97.

25. Zasadzinski, J. A. N. (1989). "Scanning Tunneling Microscopy with Applications to Biological Surfaces." *BioTechniques* **7** (2):174-187.

Chapter I

Hardware for Digitally Controlled Scanned Probe Microscopes*

* Manuscript in press, *Review of Scientific Instruments*.

Hardware for digitally controlled scanned probe microscopes

S.M. Clark, † D.R. Baselt, C.F. Spence, † M.G. Youngquist
and J. D. Baldeschwieler

A. A. Noyes Laboratory of Chemical Physics
Division of Chemistry
and
†Division of Biology
California Institute of Technology
Pasadena, CA 91125

ABSTRACT:

The design and implementation of a flexible and modular digital control and data acquisition system for scanned probe microscopes (SPMs) is presented. The measured performance of the system shows it to be capable of 14 bit data acquisition at a 100 kHz rate and a full 18 bit output resolution resulting in less than 0.02 Å rms position noise while maintaining a scan range in excess of 1 μm in both the X and Y dimensions. This level of performance achieves the goal of making the noise of the microscope control system an insignificant factor for most experiments. The adaptation of the system to various types of SPM experiments is discussed. Advances in audio electronics and digital signal processors have made the construction of such high performance systems possible at low cost.

INTRODUCTION:

Among the most promising applications of scanning probe microscopies (SPM) are those concerned with the study of biomaterials. Although progress has been made in this arena, [1-3] the routine imaging of biomolecules and biological tissues at nanometer-scale resolution has remained a challenge.

We believe there are at least two barriers to increased resolution during scanning force microscopy (SFM) on biological samples. The first barrier is the limitation on resolution imposed by the shape of the cantilever tip (stylus). [4] A rounded stylus tends to reduce lateral resolution and to limit tip excursions on highly sloped sample features. The second barrier is the pressure of the stylus on the sample which may degrade image quality by inducing or exacerbating sample motion and deformation. The force exerted on a sample depends not only on the physical forces involved in tip-sample interaction, but is also influenced by the system noise of the SFM. It is only possible to fully exploit tip-sample interactions and other factors which alter microscope resolution if the system noise of the microscope can be made an insignificant factor. The use of sharper styluses to increase resolution may also demand lower system noise to avoid sample distortion and damage, especially when imaging relatively soft samples. We believe that the use of low noise control systems, such as we describe here, is an important step toward realizing the potential of SFM for biology.

The qualities that we feel are most important for scanned probe microscopes to possess are high resolution, low noise and flexibility.

Although several commercial SPMs are available, few are able to achieve the resolution and noise performance that we require for our planned experiments. They can also be difficult to adapt to new approaches (e.g., concurrent optical fluorescence microscopy on biological samples, etc.). We have designed and constructed a high performance digital control and data acquisition system for SPMs in order to increase the resolution of SFM data on biological samples. In this system the output noise may be considered negligible for most experiments and should be adequate for SFM of biomaterials. Due to the modular approach taken, the system is highly flexible and is able to support a wide variety of experiments. With a minimal addition of electronics the system is capable of supporting scanning tunnelling microscopy (STM), near field scanning optical microscopy [5] (NSOM), scanning ion conductance microscopy [6] (SICM) and scanning electrochemical microscopy [7] (SECM) experiments. This system may be of interest to others due to its inherent flexibility, low cost and improved performance.

We will first discuss the ideas behind the use of a digital control system for SPM as well as some of the factors governing ultimate SPM sensitivity and their impact on the design goals for a high resolution SPM. We then present our instrument as one example of the implementation of a digital control system, concentrating on the design of the analog signal I/O section and performance verification of the circuitry as well as demonstrating the system's flexibility using its adaptation to NSOM as an example.

DIGITAL CONTROL FOR SCANNED PROBE MICROSCOPY:

The minimal set of tasks to be handled by an SPM control system are coarse approach to the sample, the control of a probe micropositioner (usually a piezoelectric ceramic transducer, hereafter referred to simply as a piezo), and the measurement of a signal which can be used to control the proximity of the probe to the sample. In addition to these elementary functions, the ability to control auxiliary devices and to synchronously acquire multiple types of data is highly desirable.

Discussions of several implementations of control systems for SPMs are available in the literature. [8-12] Our goals in the design of the present system were to increase performance by avoiding some of the compromises which had been made in other systems and increase system flexibility through a modular design approach using a digital signal processor (DSP). Despite the availability of DSPs in commercial SPMs, we are unaware of any detailed discussion of DSP based control systems as applied to SPMs. Hence, we will review some of the principles involved below.

In a digital control system for SPM (see Figure 1) the proximity signal (tunnelling current in STM, cantilever deflection in SFM, etc.) is measured by a sensor using analog signal processing electronics and digitized by an analog to digital converter (ADC). The digital value representing the signal is compared against a digital setpoint to obtain an error signal. This error signal is used to calculate a digital value representing the ideal voltage to be applied to the Z axis of the micropositioner. The algorithm used for this calculation comprises the Z feedback loop. This new Z value is converted into the actual

Figure 1. A block diagram of a digital control system for scanned probe microscopy. Two distinct types of signals occur in a digital control system: i) those which are time and amplitude continuous (analog signals) denoted f (t); and ii) those which are quantized in time and amplitude (digital signals) denoted g (kT). In a digital control system both the conversion resolution and the sampling rate effect the degree to which the digital control system approximates an analog control system[25]. Specialized mathmatical techniques which adress the digital nature of the signals are used to effectively analyze digital control systems and to insure their performance. In this figure noise is denoted by n regardless of its source.

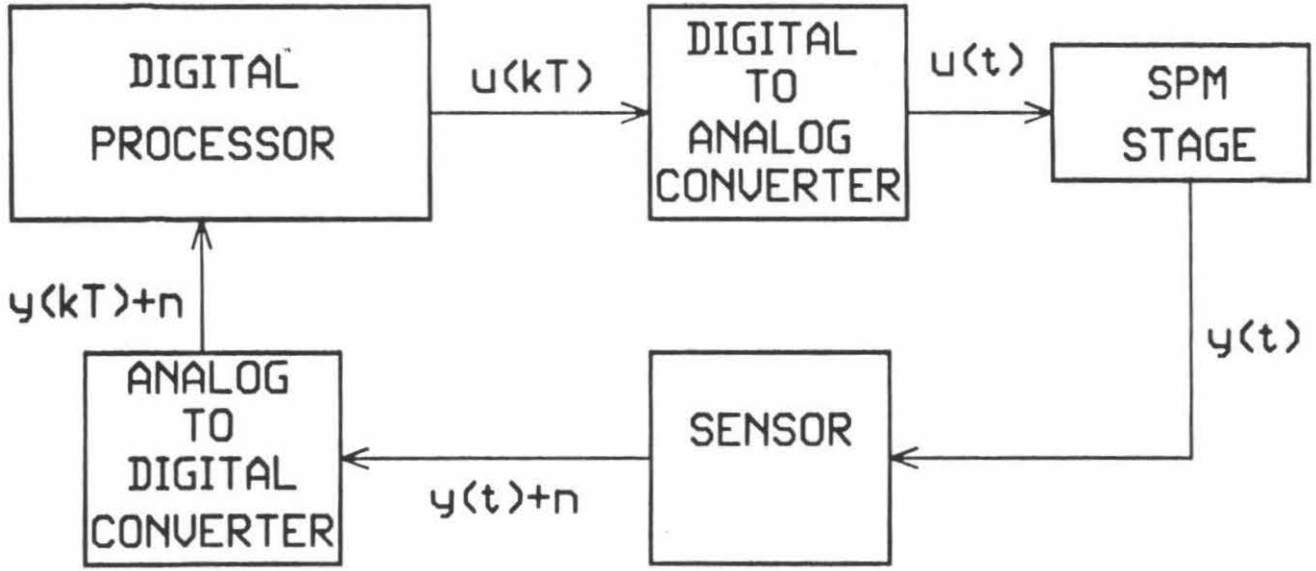
DIGITAL
PROCESSOR
u(kT)
DIGITAL
TO
ANALOG
CONVERTER
u(t)
SPM
STAGE
y(kT)+n
y(t)
ANALOG
TO
DIGITAL
CONVERTER
SENSOR
y(t)+n

Z voltage by a digital to analog converter (DAC) and amplified by a high voltage amplifier to provide the output voltage necessary to drive the micropositioner. Although it is possible to correct for nonlinearities inherent in the piezoelectric actuators through position feedback, [13] typically the voltages used to drive the micropositioner in the X and Y dimensions are generated in an open loop fashion (that is, they are calculated and sent to the X and Y DACs without measuring a control signal for them).

The major advantages offered by a DSP based control system are flexibility, improved performance (decreased scan times, increased noise immunity, etc.) and the possibility of easily using sophisticated techniques such as phase sensitive detection, optimal filtering, active damping, evolutionary feedback parameter optimization and so forth. The tremendous flexibility of a DSP based system arises from the generic nature of the analog I/O electronics combined with the ability to modify the control software. This allows the implementation of novel imaging modes or the adaptation of the system to control different devices with a minimum of hardware development thus saving both time and expense. Another advantage lies in the capabilities of the DSP itself. Because DSPs typically contain features such as single machine cycle multiplication and matrix manipulation facilities, they are particularly well suited to real-time computation and signal processing. They are much faster for these tasks than microcontrollers or other dedicated microprocessors. The last barrier to the use of DSPs for SPM control systems was removed with the advent of low cost, high performance DACs and ADCs for application in the audio frequency range.

Another key to system flexibility is to use a modular design approach. By breaking the system into generic components which can be controlled through a standard interface it is possible not only to simplify component design, but also to update easily the system configuration as requirements change. For more elaborate experiments, modules can simply be added which follow the standard communication protocol and which perform specialized functions.

As an illustration of the potential engendered by modular design, we show, in Figure 2, a block diagram of a multiprocessor architecture. This type of architecture allows task sharing between the central DSP and other embedded processors. In this system, "smart" DACs could serve to relieve the DSP of raster generation and other peripheral control tasks, these tasks being handled by embedded microprocessors (either DSPs or microcontrollers). Through the use of such "smart" DACs the system could be tailored to particular piezos and real time hysteresis and creep correction could be done. One way in which this might be achieved is by implementing the real time optical scan correction system of Barrett and Quate[13] using a digital servo loop. In such a design the optical beam displacement sensors would provide a measurement of the piezo displacement and the desired X-Y raster pattern becomes a 2-dimensional, time dependent reference input to the servo. The implementation of various types of control loops such as proportional - integral-differential (PID) control, optimal control or feedforward control could be easily done in the control software. A particularly attractive microcontroller for this application might be the Motorola MC68332 [14] due to its hardware interpolation feature which would allow rapid generation of smooth raster signals. The field programmable gate array (FPGA) shown in

Figure 2. A block diagram of a multiprocessor control and data acquisition system for scanned probe microscopy. This architecture allows task sharing between the central DSP and other embedded processors. In one version of such a system the central DSP would be used to execute the Z feedback loop and store image data, while the other processors could be used for raster generation, digital rotation, control of auxillary equipment (e.g., a scanning bipotentiostat, hybrid photomultiplier detectors, etc.).

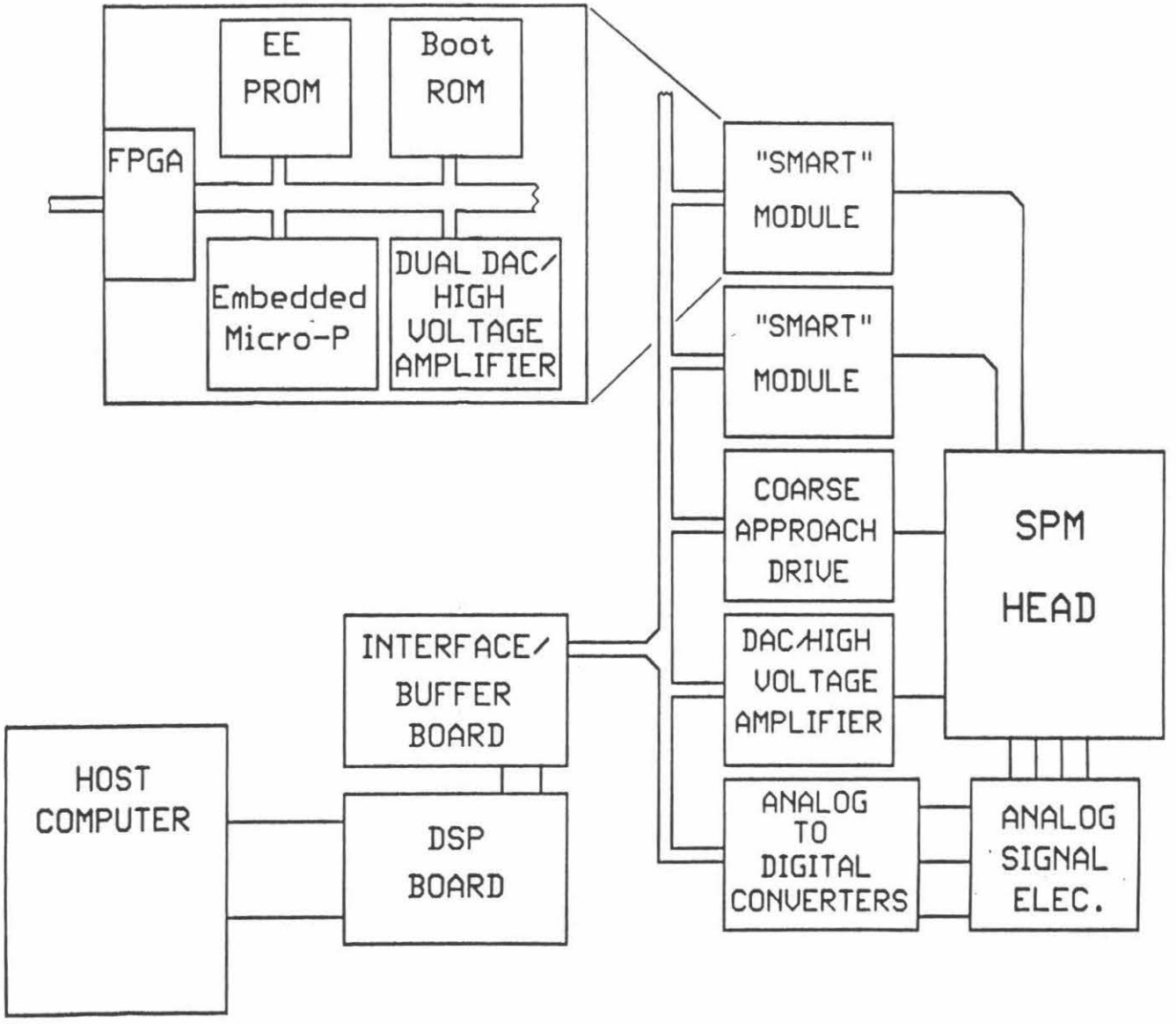
EE
PROM
Boot
ROM
FPGA
Embedded
Micro-P
DUAL DAC/
HIGH
VOLTAGE
AMPLIFIER
"SMART"
MODULE
"SMART"
MODULE
COARSE
APPROACH
DRIVE
SPM
HEAD
INTERFACE/
BUFFER
BOARD
DAC/HIGH
VOLTAGE
AMPLIFIER
HOST
COMPUTER
DSP
BOARD
ANALOG
TO
DIGITAL
CONVERTERS
ANALOG
SIGNAL
ELEC.

the diagram allows complex timing and logic functions to be handled easily and facilitates the interface between the processors. The "smart" module concept can be extended to more interesting applications such as microprocessor controlled scanning bipotentiostats for scanning electrochemical microscopy and so forth.

NOISE IN SPM:

The noise level of a SPM control system is a significant factor in its ability to meet experimental demands. To understand how noise influences SPM experiments, and to provide a framework for minimizing noise, one can divide noise sources into two categories, output noise and input noise. Output noise originates in the piezo drive electronics and can be minimized by the use of special low noise design techniques. Input noise is inherent in SPM measurements and cannot be reduced beyond a certain minimal level. We discuss both noise categories below.

Reduction of piezo drive output noise was one of our major design goals. Because the force applied by a cantilever is proportional to its deflection, noise on the Z axis output lying outside the servo bandwidth introduces uncontrollable force fluctuations which are undesirable (within the servo bandwidth the noise will be reduced by the feedback gain). Our specific design goal for the SFM was that the system noise contribution from the piezo drive electronics be slightly less than the mechanical noise contribution from the microscope stage and head; from calculation we expect the mechanical noise from thermal stage vibration to be ≈ 0.1 Å rms amplitude. We frequently use tubular piezos with a response of ≈ 50 Å/V,

hence our system can tolerate an output noise of 2 mV rms over a 100 kHz bandwidth while maintaining a 1μm scan range.

Resolution is another key consideration; ideally the cantilever could be positioned at any arbitrary deflection. The average incremental force applied by the stylus depends on the DAC output step size, with smaller steps providing finer control of the applied force. Typically, higher resolution DACs also exhibit lower output noise, so high resolution DAC circuitry provides a real advantage in terms of controlling forces for SPMs. Large zoom ratios are another feature gained by using high resolution DACs. The ability to zoom in on rare features initially found by scanning large areas can be crucial in systems without sample translators and greatly simplifies the use of any SPM.

In almost every experimental measurement, weak input signal detectability is limited by noise. In many cases interfering signals generated externally to the experiment may be excluded from the measurement by proper shielding and grounding; however, noise can be reduced only to a finite limit. This ultimate noise floor is the result of the thermal motion of charge carriers (Johnson noise) and the quantization of charge (shot noise). The voltage noise (rms) due to Johnson noise of a resistance, R, is given by [15]

$$V_n = \{4kTRB\}^{1/2}.$$

In this equation, T is the absolute temperature (K), B is the measurement bandwidth (Hz) and k is Boltzmann's constant (1.380662×10^{-23} JK^{-1}).

Just as Johnson noise from a source resistance presents a fundamental

limit for voltage measurements, shot noise presents a fundamental limit in the experimental measurement of currents. The shot noise (rms) for a current of average value <I> is [15].

$$i_n = \{ 2 q \langle I \rangle B \}^{1/2}$$

where again, B is the bandwidth of the measurement (Hz) and q is the electron charge (1.602189×10^{-19} C). The best measurements one can make are limited by noise at these levels. Only Johnson noise can be decreased by lowering the temperature of an experiment; however, both shot noise and Johnson noise can be reduced by limiting the detection bandwidth. By using techniques such as lock-in detection, bandwidths of a few Hertz can be readily obtained.

When one considers the effect of shot noise on STM experiments one finds that for a tunnelling current of 100 pA and a 10 kHz bandwidth the shot noise is 0.4 pA. Thus, the maximum signal to noise ratio for these conditions is ≈ 250. Similarly, for a 1 pA tunnelling current, in the same 10 kHz bandwidth, the best signal to noise ratio is less than 20. Often the effects of shot noise are not obvious in topography data from STM; this is due to the fact that high impedance amplifiers typically used as STM preamplifiers tend to have a limited frequency response, effectively limiting the bandwidth to $\approx$ 1 kHz or less. One might expect, however, that shot noise would play a more significant role in experiments done at high gap resistances, over large bandwidths, or in tunnelling spectroscopy.

Shot noise also limits optical beam deflection sensitivity for SFM. For a photodiode, <I> is given by $\langle I \rangle = P \, \emptyset$ where P is the optical power incident

on the photodiode and Ø is the spectral responsivity at the wavelength of interest. Under typical operating conditions in our SFM, <I> is ≈ 15 μA/ quadrant and i_n is ≈ 690 pA/ quadrant assuming a 100 kHz measurement bandwidth. Thus, in our SFM as presently used, current fluctuations of amplitude 2 i_n give rise to signals of ≈ 280 μV which roughly corresponds to a change of one ADC unit (±10 V full scale and 16 bit resolution). In the sense that our instrument can detect changes in photocurrent of amplitude 2 i_n, we can say that it is shot noise limited. Further increasing the gain of the difference amplifier, whose output is the deflection signal, provides larger signal amplitude, but does not increase signal to noise ratio.

To increase sensitivity further requires increasing the laser power on the photodiode, increasing the optical lever gain (i.e., the ratio of beam deflection distance to cantilever tip motion) or decreasing the measurement bandwidth. The laser power can easily be increased; however, as the light intensity on the cantilever increases so does the momentum transfered to the cantilever. The force exerted on the cantilever by photon pressure is given by

$$F = 2P/c,$$

where P is the laser power incident on the cantilever and c is the speed of light. Thus, for a helium-neon laser with 10% intensity noise, to keep laser noise induced force fluctuations below 10^{-11} N one is limited to less than ≈ 20 mW. On the other hand, the optical lever gain can be increased without compromising other aspects of the instrument's performance. However, optical lever gain is limited in practice by the mechanical design of the instrument both in terms of mechanical noise and ease of use.

To interpret the shot noise limit in terms of position sensitivity for an optical lever based SFM requires knowledge of the diameter of the reflected beam at the photodiode face and the optical lever gain. For the SFM head presently used, the beam diameter at the photodiode is ≈ 10 mm and the optical lever gain is ≈ 2,500 when using a 100 μm cantilever. Although the beam on the face of the photodiode has a Gaussian intensity profile, a worst case shot noise sensitivity value may be calculated by assuming a uniform intensity distribution. Using this approximation, with 20 mW incident on the photodiode the shot noise limit corresponds to a position sensitivity of ≈ 0.05 Å.

SYSTEM OVERVIEW:

The system which we have designed and are presently using for experiments is based on a single DSP. We opted to purchase a board level DSP and to focus effort on developing the algorithms and software for SPM control as well as the analog I/O described in this paper. As can be seen in Figure 3, the major components of the digital control and data acquisition system are the DSP, the piezo drivers, the analog signal processing section and the ADCs. Because the analog signal processing electronics are instrument specific they will not be discussed in detail here.

For our system we chose the Spectrum TMS320C30 DSP board[16] which uses a personal computer (PC) as the host. The PC also serves for software development and image processing and display tasks. Due to the noise level introduced onto the DSP board by the PC, we found the on-board analog I/O to be inadequate for our needs, hence our custom designed analog I/O uses

Figure 3. A block diagram of the scanned probe microscope control and data acquisition system. The NIM (Nuclear Instrumentation Module) Bin is indicated only schematically and all power supplies have been omitted for diagram clarity. Other host systems and alternative packaging could clearly be used (e.g., workstations and VXI Bus).

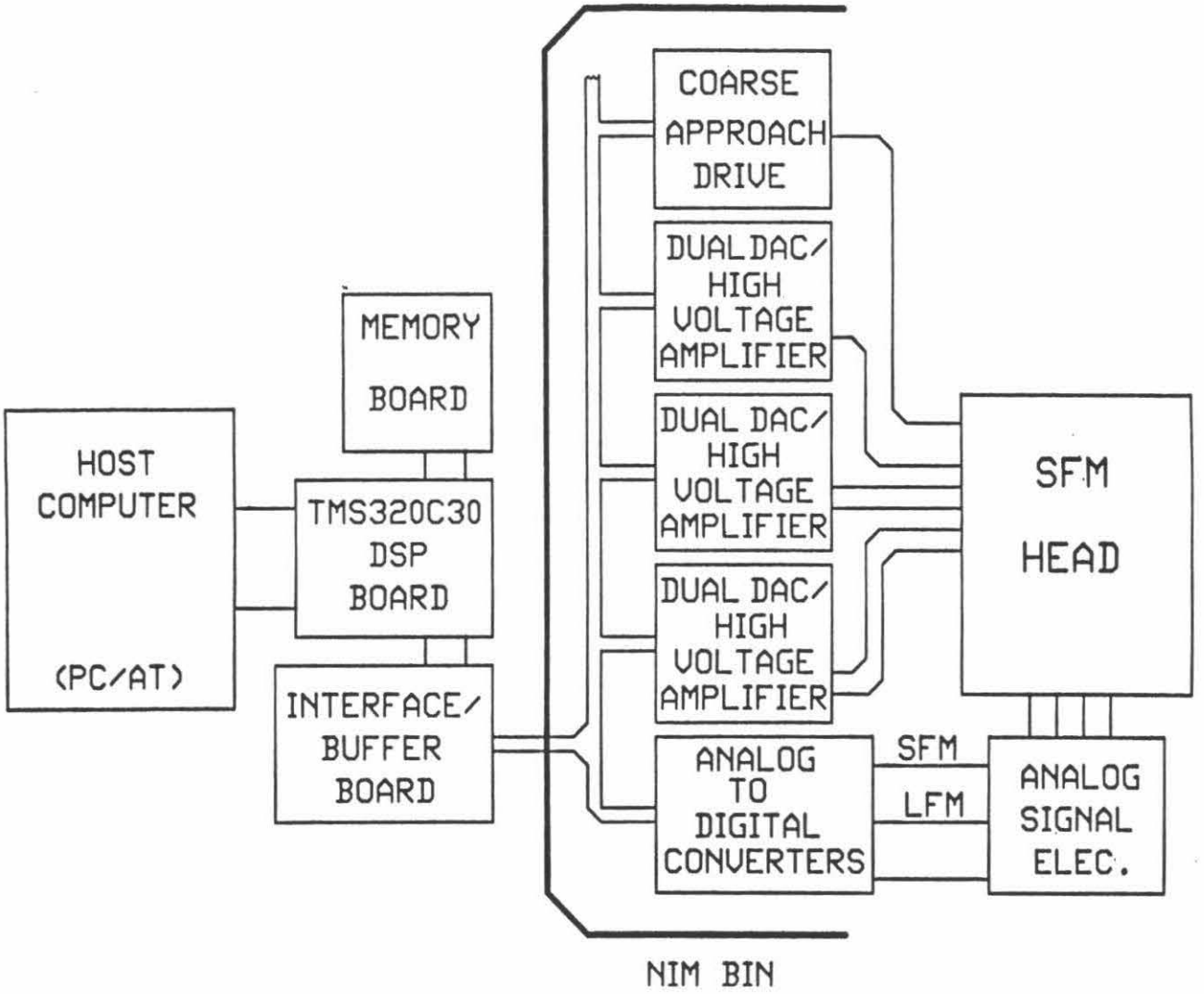
COARSE
APPROACH
DRIVE
DUAL DAC/
HIGH
VOLTAGE
AMPLIFIER
DUAL DAC/
HIGH
VOLTAGE
AMPLIFIER
DUAL DAC/
HIGH
VOLTAGE
AMPLIFIER
MEMORY
BOARD
HOST
COMPUTER
(PC/AT)
TMS320C30
DSP
BOARD
INTERFACE/
BUFFER
BOARD
ANALOG
TO
DIGITAL
CONVERTERS
SFM
LFM
ANALOG
SIGNAL
ELEC.
SFM
HEAD
NIM BIN

the external interface bus (DSP-Link).

For our laboratory the most cost effective method of packaging the analog I/O was to modify nuclear instrumentation module (NIM) bins by adding a digital backplane and to use commercially available NIM enclosures to house individual printed circuit boards. Using the NIM format forces design modularity and facilitates the exchange of modules between microscopes. We have buffered the DSP-Link signals and used these to drive directly the terminated digital backplane. This implementation of a generic high speed digital bus allows zero wait state communication between the NIM modules and the DSP; in fact, by using high speed bus drivers the present hardware could easily accommodate bus bandwidths in excess of 50 Mbytes/s. Other NIM bin modifications include the addition of an independent +5 volt linear power supply for powering the digital circuitry and the addition of high voltage power supplies.

SYSTEM COMPONENTS:

Digital Signal Processors

For most users the selection of a DSP for application in a SPM system will entail the selection of a board level component for a particular computational platform (personal computer, workstation, etc.). The major issues involved in the selection of a DSP board, such as floating point or integer operation, memory addressing capability and the quality of on-board I/O functions are discussed in Reference 17. Although the electronics

described in this paper will function with any DSP board having an external bus, processor speed is an important factor if fast scan rates are required. Processors that have fast clock rates allow either more operations to be performed in the feedback loop or faster sampling intervals. At the time this work was begun, a TMS320C30 DSP (Texas Instruments [18]) based board from Spectrum Signal Processing was chosen due to its ready availability and reasonable price. This board has a 33 MHz DSP clock rate which allows 150 instructions to be executed in the interrupt interval used in our system (10 μs). We find that the 100 kHz sampling rate easily permits a feedback servo bandwidth of 20 kHz and that 150 instructions are adequate for the implementation of the Z feedback loop and the scan raster generation. Since the time of our purchase, board level products suitable for SPM control based on several different DSPs have come onto the market providing a variety of sophisticated products to choose from.

If the capabilities of board level DSP products prove to be inadequate for a particular microscope design, one may be forced to design a DSP board from scratch. This is obviously not a trivial undertaking and should only be done as a last resort; however, some points merit consideration.

The first point is that the performance of the Z feedback loop and its complexity are constrained by the speed of the DSP. Secondly, because the feedback loop is a real-time process, only minimal time delay can be tolerated without compromising scan rate. There are two potential areas in which to gain performance: i) DSP speed, ii) relieving the DSP of tasks easily handled by less sophisticated processors. Other advantages gained by the design of a SPM specific DSP board are the ability to place substantial amounts of fast

memory and/or dual port memory on the board as well as the ability to use the serial data ports and external buses of the DSP to interface directly with the DACs and ADCs.

Piezoelectric Ceramic Drive Electronics

Because we require high resolution digital to analog converter (DAC) outputs we considered two ways to achieve high resolution: i) by using a single high resolution DAC ; and ii) by scaling the outputs of two or more lower resolution DACs and summing their outputs. Previously one would have been forced to implement the latter alternative, however, recently, tremendous progress has been made in the performance of low cost audio frequency DACs. With the availability of these components, the single DAC alternative becomes most attractive due to its simplicity.

Several manufacturers produce DACs which offer greater than 16 bit resolution with total harmonic distortion plus noise of less than -96dB. Typical of this class of DAC is the PCM58P-K from Burr-Brown [19] which we have used in our SPM system. This is an 18 bit serial-input, current-output DAC with an idle channel signal to noise ratio of +126 dB at bipolar zero. This DAC performs suitably in SPM applications in our laboratory; however, even higher performance DACs such as the PCM63P (Burr-Brown) have recently come on the market. The PCM63P offers 20 bit resolution with low noise and for new designs this type of DAC should also be considered.

For our system the selection of high voltage amplifiers to drive the piezos was uncomplicated due to the narrow field of parts to choose from.

Component level high voltage operational amplifiers suitable for SPM applications are available from primarily two companies, Apex Microtechnology [20] and Burr-Brown. The major considerations in judging a high voltage amplifier for use with piezoceramic scanners in SPM are i) total output voltage swing, ii) output noise and iii) current drive capacity. The current capability required of an amplifier is an important consideration because of the capacitance presented by the piezoceramic to the output of the amplifier. The output currents required of the amplifier to achieve a given output voltage slew rate may be found from $i = C\, dV/dt$. We used the PA85 from Apex because at the time it offered the greatest output voltage range at a suitable current capability.

Piezoelectric Ceramic Drive Performance

A schematic diagram of a piezo drive module is shown in Figure 4. The piezo drive electronics are composed of dual DACs and high voltage amplifiers. The interface logic consists of data and address buffers and address decoders. The address decoders are implemented in programmable array logic (PAL) devices. The control logic is also implemented in PALs and functions to provide the required clock and control signals for the DACs and the parallel to serial converters (shift registers).

The assembly is physically composed of two printed circuit boards mounted in a double width NIM module; one board contains the dual DAC circuitry and the other board contains the high voltage amplifiers. This division of the circuitry allows the use of the DAC section alone for low voltage applications (e.g., tip-sample bias generation) without having to

Figure 4. A diagram of the piezoelectric ceramic drive electronics. The piezo drive electronics are composed of dual DACs and high voltage amplifiers. The interface logic consists of data and address buffers and address decoders. The address decoders are implemented in programmable array logic (PAL) devices. The control logic is also implemented in PALs and functions to provide the required clock and control signals for the DACs and the parallel to serial converters (shift registers).

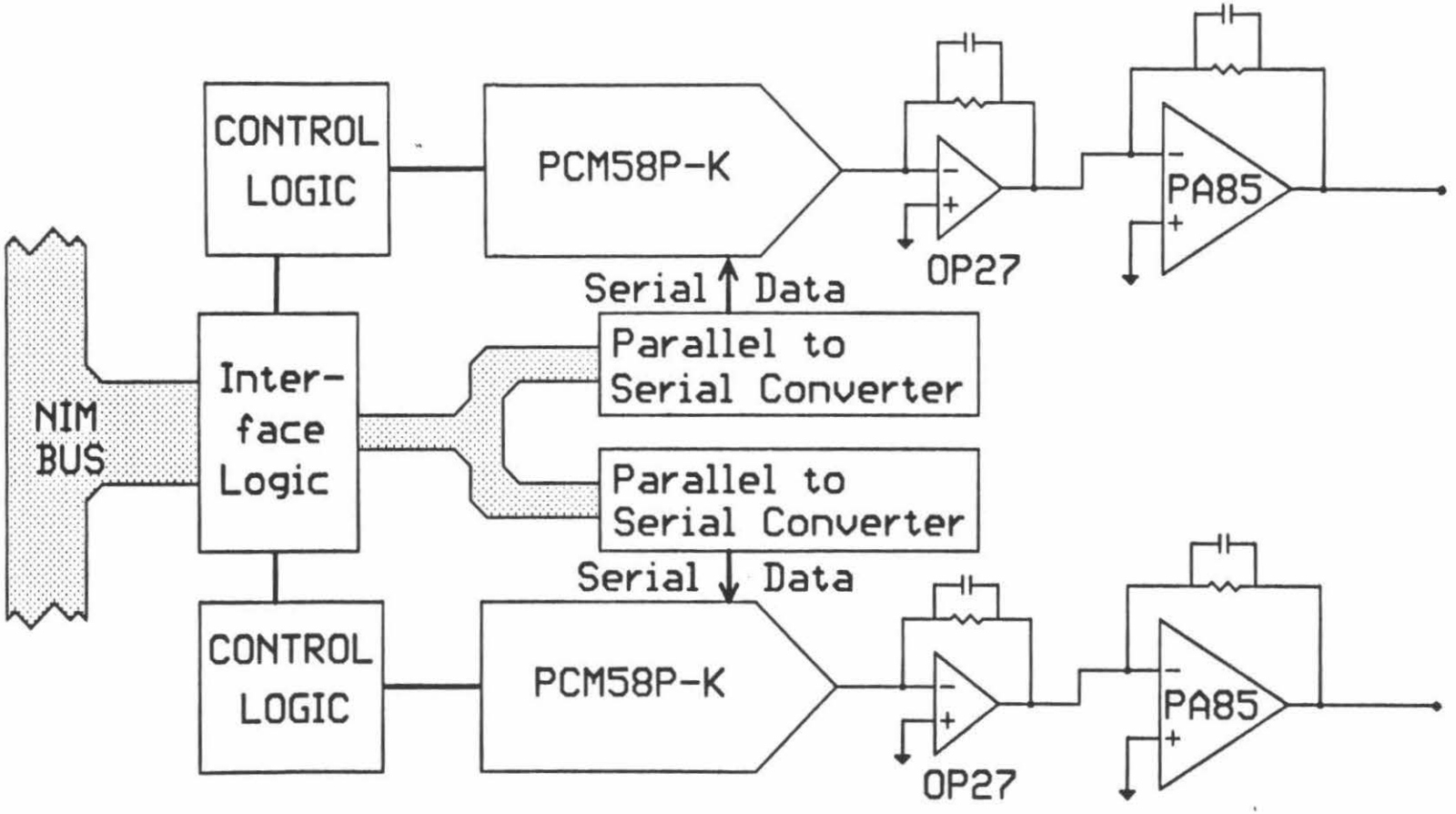
CONTROL
LOGIC
PCM58P-K
OP27
PA85
Serial
Data
Parallel to
Serial Converter
Parallel to
Serial Converter
NIM
BUS
Inter-
face
Logic
Serial
Data
CONTROL
LOGIC
PCM58P-K
OP27
PA85

fabricate special boards.

A theoretical analysis of the DAC/HV amplifier circuitry would predict that with a 420 V output range, the output noise of this section should be ≈ 100 μV rms in a 100 kHz bandwidth (discounting 1/f noise below about 10 Hz). Figures 5 & 6 present data to document the time domain and frequency domain performance of the DAC/HV amplifier section. As can be seen in the time domain traces of Figure 5, the broadband output noise of this section (without feedback) is 450 μV peak to peak (320 μV rms, or 0.016 Å rms for a microscope using a 50 Å/V piezo). This gives a measured dynamic range (maximum output signal/noise level of the output) of ≈ 118 dB.

In Figure 6 we show power spectra measured to judge if the harmonic distortion of the DAC/HV amplifier section would present a problem. To perform this test of the circuitry, digital representations of sine waves of various amplitudes and frequencies were generated and output via the piezo drive circuitry. The power spectra were measured using a Hewlett-Packard 3563A Control Systems Analyzer. An ideal spectrum would have a single peak (strictly speaking, a delta function) located at the frequency of the sine wave with no other features. Two aspects of these spectra are of particular interest; the broadband noise can again be seen to be negligible (the baseline of the spectra match the recording instrument noise floor) and the spectral purity of the output signals eliminates concerns that nonlinearity in the drive electronics might give rise to noise in the Z feedback loop or excite undesired resonances in the piezo tube.

Figure 5. Measured time domain characteristics of the 420 V range piezo drive electronics. The upper trace presents the average of 256 time traces taken by a digital storage oscilloscope (Tektronix 2440). The waveform amplitude is ≈ 5 mV (-98 dB) and its frequency is ≈ 1 kHz. This representation eliminates random noise (as it averages to zero) while maintaining any systematic features of the signal. The structure seen in the waveform is due to oscilloscope digitization and not individual DAC steps. The lower trace presents a single time trace of the same amplitude and frequency so that noise contribution may be seen. At this signal level the output consists of only three DAC steps but they are not visible due to the output low-pass filters.

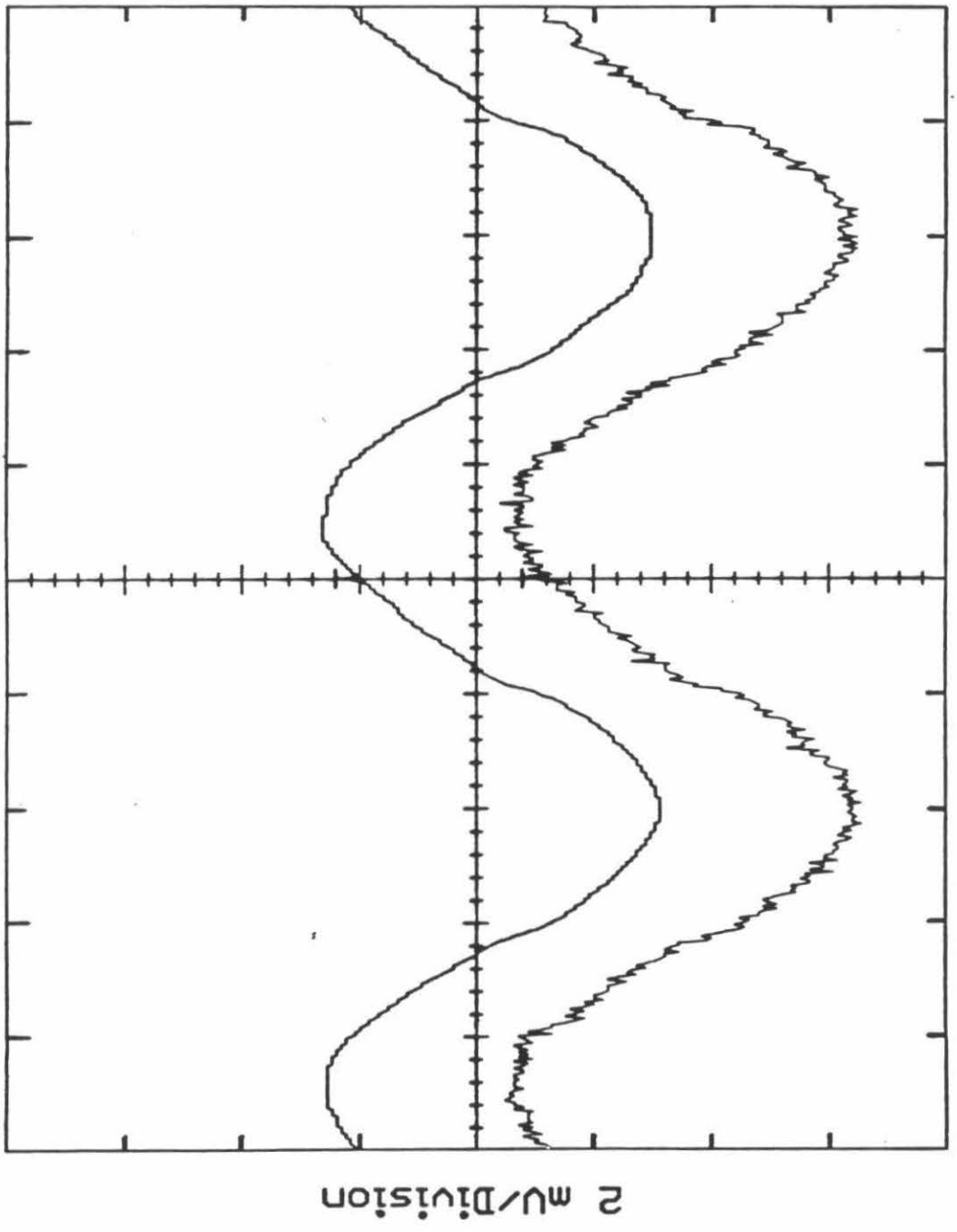
2 mV/Division
200 us/Division

Figure 6. Measured frequency domain characteristics of the 420 V range piezo drive electronics. Power spectra of the piezo drive electronics taken to assess the total harmonic distortion at various frequencies and signal amplitudes. The spectra were taken using a Hewlett-Packard 3563A Control Systems Analyzer. A resistor divider was used to scale the signal to avoid overloading the analyzer input circuitry. For all of the spectra, the analyzer was set to 50 time record averages. Note that the total dynamic range (maximum output signal/noise level of the output) of the piezo drive is ≈ 118 dB. A) -20 dB signal level spectra. The total harmonic distortion is <-75 dB. B) -80 dB signal level spectra. The total harmonic distortion is <-25 dB.

a)

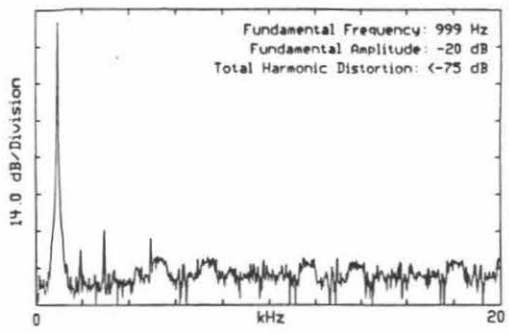
Fundamental Frequency: 999 Hz
Fundamental Amplitude: -20 dB
Total Harmonic Distortion: <-75 dB
14.0 dB/Division
0
kHz
20

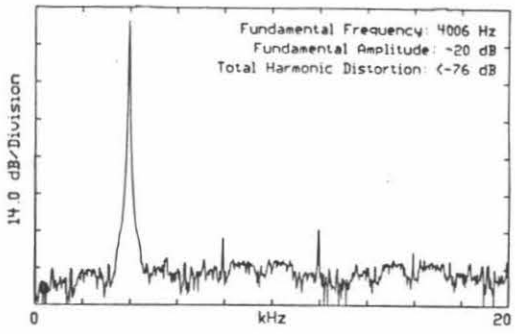
Fundamental Frequency: 4006 Hz
Fundamental Amplitude: -20 dB
Total Harmonic Distortion: <-76 dB
14.0 dB/Division
0
kHz
20

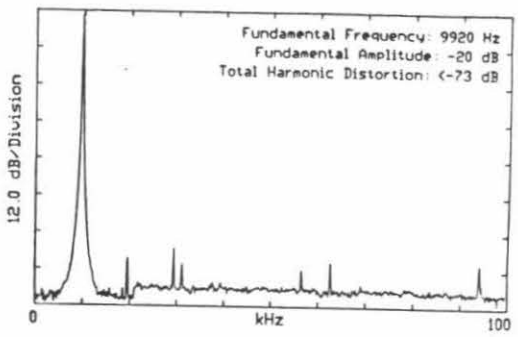
Fundamental Frequency: 9920 Hz
Fundamental Amplitude: -20 dB
Total Harmonic Distortion: <-73 dB
12.0 dB/Division
0
kHz
100

b)

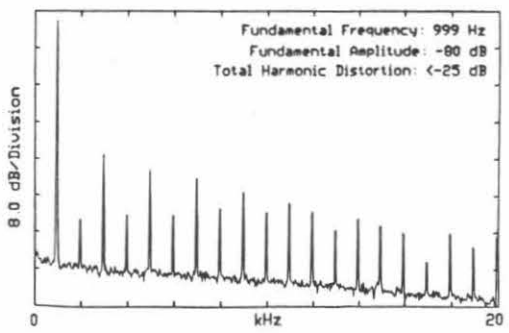
Fundamental Frequency: 999 Hz
Fundamental Amplitude: -80 dB
Total Harmonic Distortion: <-25 dB
8.0 dB/Division
0
kHz
20

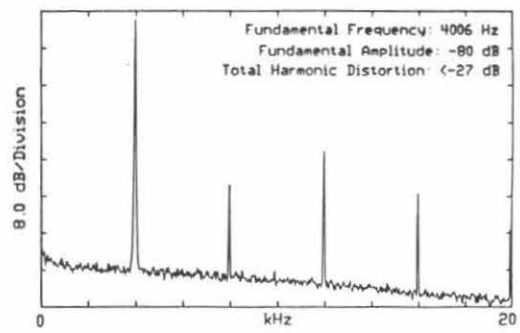
Fundamental Frequency: 4006 Hz
Fundamental Amplitude: -80 dB
Total Harmonic Distortion: <-27 dB
8.0 dB/Division
0
kHz
20

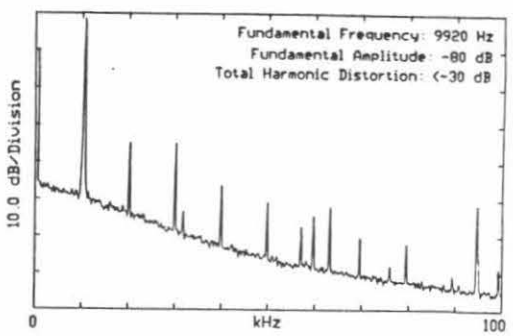
Fundamental Frequency: 9920 Hz
Fundamental Amplitude: -80 dB
Total Harmonic Distortion: <-30 dB
10.0 dB/Division
0
kHz
100

When examined together, the data of Figures 5 & 6 document a level of output performance which compares very favorably with completely analog SPM control systems and was previously unattainable with low cost digital systems. The outstanding performance of this circuitry strongly suggests that this section should function adequately for most SPM applications. In the event that this level of performance is inadequate, further reductions in the output noise level and signal purity may be obtained by using better high voltage power supplies in conjunction with better electrical shielding.

Analog to Digital Converters

In the area of analog to digital converters (ADCs), again striking progress has been made both in cost and performance. Recently several companies have introduced parts which offer 16 bit and greater resolution. Two architectures dominate the field: i) the delta/sigma type and ii) the successive approximation type. [21] We have found that the conversion time, defined as the time interval between the sampling of a signal at the start of the conversion process and the end of the conversion at which time the digital value is available for the servo loop to act on, typical of commercially available delta/sigma converters (on the order of 1 ms) would severely limit feedback loop bandwidth. Thus we have chosen the PCM78P from Burr - Brown, a 16 bit successive approximation converter which offers a 5 μs conversion time with better than -80 dB signal to noise ratio. Although the PCM78P claims 16 bit resolution, it is specified as having only 14 bit linearity and no missing codes at 14 bit resolution.

The other components which determine the performance of the ADC

individual ADCs. For SFM we use three of the ADCs; one for vertical cantilever deflection, one for torsional cantilever motion and one for total light intensity on the quadrant photodiode. An alternative scheme for SFM

section are the anti-aliasing filter and the track and hold amplifier. The practical criterion which must be met by the anti-aliasing filter is that signals in the frequency region above half the ADC sampling frequency must be attenuated to less than one least significant bit. We have found the APQ-25 series of passive filters from Toko America [22] to be more than suitable in this role. The particular part used in our system is a seven pole low-pass filter with a constant ≈ 35 μs group delay (the time taken for a signal to pass through the filter) throughout the passband and a nominal cutoff frequency of ≈ 30 kHz. Passive filters are preferred for low noise applications because passive components add a minimum of noise to the processed signal.

The track and hold amplifier used in conjunction with the ADC must be compatible with the desired system performance (i.e., a 12 bit track and hold will degrade the performance of a 16 bit ADC). As specified by Analog Devices,[23] the AD1154BW track and hold amplifier is compatible with our design goals. The AD1154BW is a true 16 bit, low cost track and hold amplifier with a 2 μs settling time. It performs well in our SPM.

ADC Section Performance

Figure 7 presents a schematic of a single ADC section. The four ADC sections contained on a single ADC board are housed in a double width NIM module. One convert command triggers the conversion start for all of the ADCs, thus avoiding any question concerning the phase relations of the individual ADCs. For SFM we use three of the ADCs; one for vertical cantilever deflection, one for torsional cantilever motion and one for total light intensity on the quadrant photodiode. An alternative scheme for SFM

Figure 7. A diagram of a single channel analog to digital converter for the scanned probe microscope control and data acquisition system. The resistor divider is included to correctly scale the input to the ADC and the operational amplifier (OPA627) serves to buffer the divider voltage from the dynamic 1.5 kΩ input impedance of the ADC. In the prototype system there are four such channels on the ADC board. The interface logic consists of data and address buffers and address decoders. The address decoders are implemented in programmable array logic (PAL) devices. The control logic is also implemented in PALs and functions to provide the required clock and control signals for the ADCs and the serial to parallel converters (shift registers).

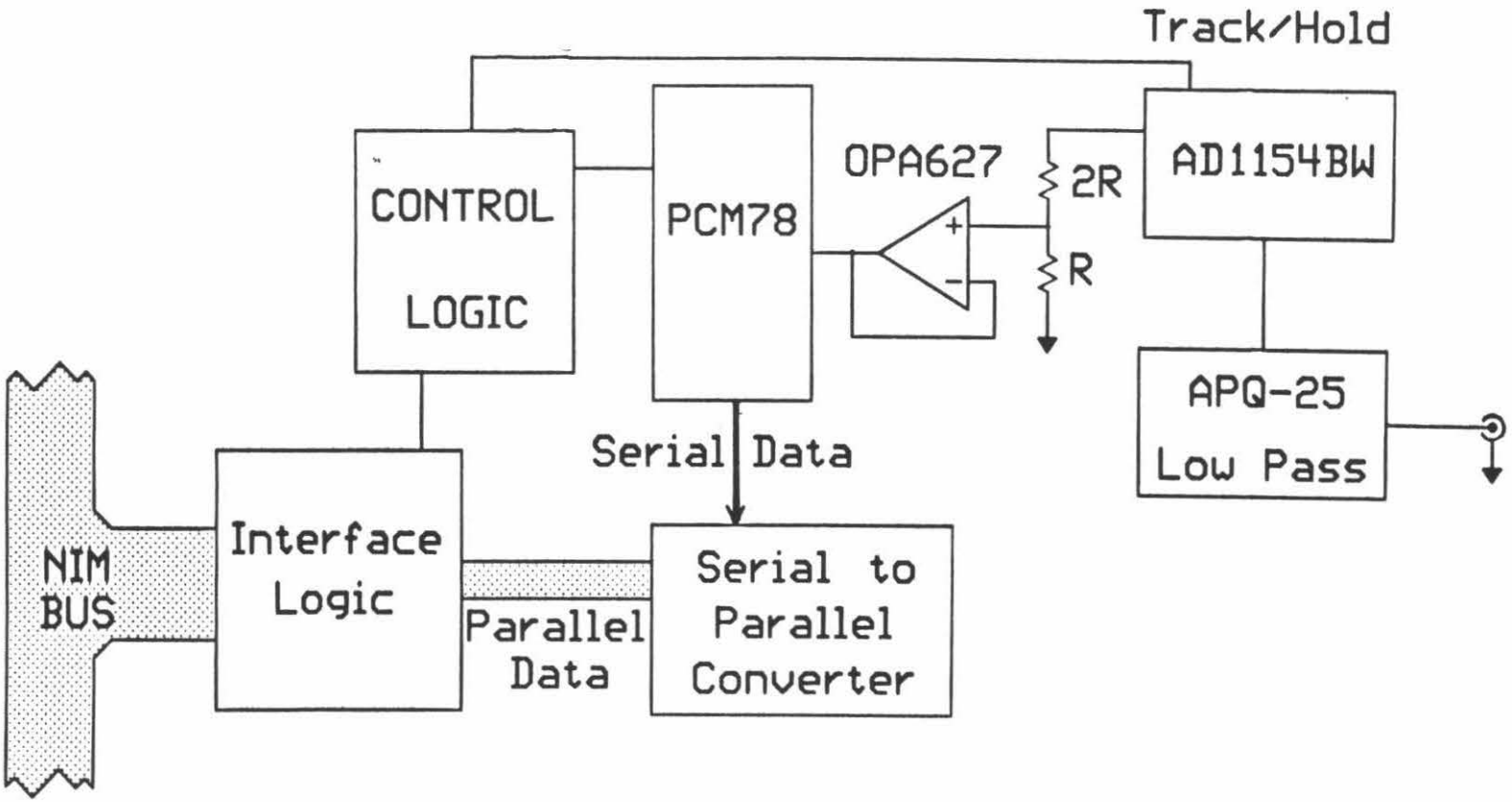
Track/Hold
CONTROL
LOGIC
PCM78
OPA627
2R
R
AD1154BW
APQ-25
Low Pass
Serial Data
NIM
BUS
Interface
Logic
Parallel
Data
Serial to
Parallel
Converter

is to directly digitize all four photodiode quadrant signals. This approach has the advantage that an almost perfect common mode signal rejection ratio can be obtained. In order to do the digital signal processing required by digitizing all of the quadrant signals the sampling interval would have to be lengthened and this might limit the Z feedback servo bandwidth. In our system we might have to increase the sampling interval from 10 μs to 15 μs to provide the required computational time.

The design goal for the ADC section was to achieve full 16 bit measurement capability with a ± 10 V input range at a sampling rate in excess of 100 kHz. This would give four times oversampling of the highest frequency signals of interest, thus meeting the requirements of the Z feedback loop and allowing high scan rates. The ADC section achieves a maximum conversion time of ≈ 6 μs allowing a sampling rate in excess of 150 kHz. At this sampling rate the ADC section yields 14 bit performance which is limited by ADC noise of 2 bits (4 ADC units or 1.2 mV referred to the ADC section input).

We have done a more detailed evaluation of the ADC circuitry for missing codes (at 12 to 16 bit resolution levels) and differential linearity [21] which is shown in Figure 8. To do the evaluation we use a low frequency linear bipolar ramp as the input waveform to the ADC. By using this waveform and acquiring data over many cycles of the ramp we should accumulate a significant number of samples at each of the ADC output codes. We then construct a histogram which has each of the output codes along the abscissa and the number of samples at each output code as the ordinate. For an ideal ADC this histogram would have an average number of samples in

Figure 8. Measured performance of the analog to digital converter section. A typical section of ADC ouput code histogram at three resolution levels. The same area of missing codes is presented in each of the histograms at a different resolution level so that the effects of rebinning would be clear. The sections of histograms shown were selected because they are illustrative of clusters of missing codes found in the ADC output. All of the histograms are derived from a data set consisting of 1000 time records.

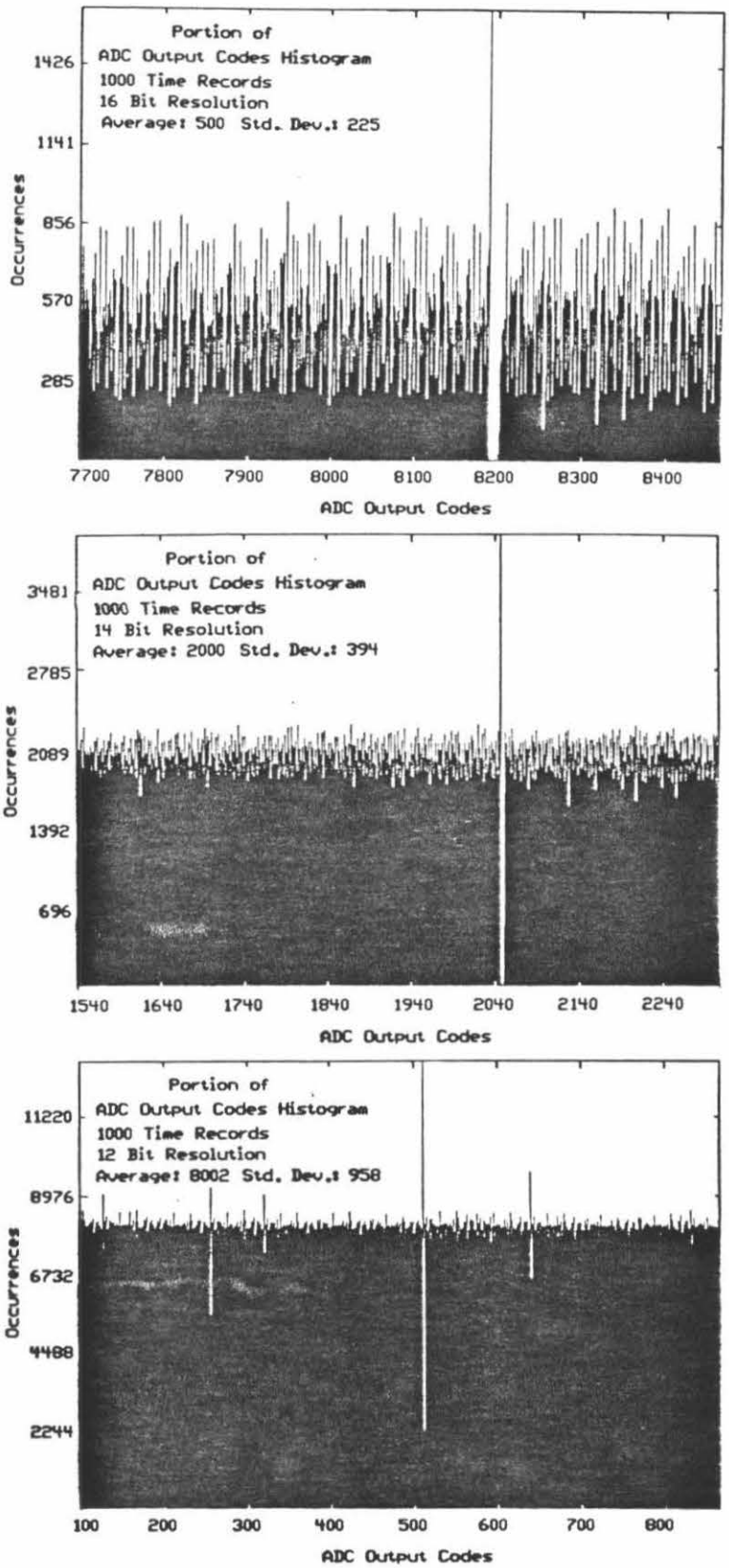
Portion of
ADC Output Codes Histogram
1000 Time Records
16 Bit Resolution
Average: 500 Std. Dev.: 225
Occurrences
1426
1141
856
570
285
7700 7800 7900 8000 8100 8200 8300 8400
ADC Output Codes
Portion of
ADC Output Codes Histogram
1000 Time Records
14 Bit Resolution
Average: 2000 Std. Dev.: 394
Occurrences
3481
2785
2089
1392
696
1540 1640 1740 1840 1940 2040 2140 2240
ADC Output Codes
Portion of
ADC Output Codes Histogram
1000 Time Records
12 Bit Resolution
Average: 8002 Std. Dev.: 958
Occurrences
11220
8976
6732
4488
2244
100 200 300 400 500 600 700 800
ADC Output Codes

each of the bins with the expected deviation from this being given by the square root of the number of samples expected in the bin. If the ADC has missing codes one would expect that there would be no samples falling within the bin for the missing code. Differential linearity may also be coarsely judged by this technique; bins which show deviation from the expected value of samples in the bin by more than the standard deviation can be judged to have a linearity problem. In Figure 8, two aspects of the histogram structure are noteworthy. First, we find that there are indeed bins with no samples and that if we reduce the effective ADC resolution by rebinning (i.e., to bin at 15 bit resolution we combine adjacent bins from the 16 bit histogram, etc.) it is only when we reach the twelve bit resolution level that there are no missing codes. Secondly, the histograms show significant deviations from ideal behavior in both periodic structure and deviation from the value expected in the bins.

One can view the number of counts in a bin as representative of the width of a bin (i.e., the voltage range resulting in a count being added to a particular bin). Adopting this view, one finds from Figure 8, that bins corresponding to missing codes often have very wide bins adjacent to them. Thus, if one regards the ADC output code histogram as constituting a type of transfer function for the ADC, one could increase ADC performance by post-processing data to normalize bin width (reduce differential linearity error to zero).

In order to summarize the differential linearity measurement we have constructed a second type of histogram, shown in Figure 9, called the count distribution histogram. In this histogram we display the number of counts in a bin (bin value) as the abscissa and the number of bins which contain that

Figure 9. Evolution of the count distribution histogram with sample size. These histograms demonstrate the general Poisson character of the count distribution histogram. The construction of the histograms from the binned data of Figure 9 is described in the text. In the histograms with larger numbers of samples one can see not only significant deviation from an ideal Poisson distribution, but also the multimodal character of the histogram. These data are indicative of the poor differential linearity of the PCM78P.

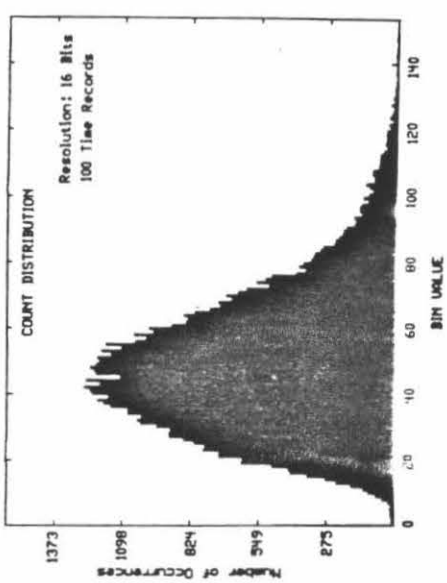
COUNT DISTRIBUTION
Resolution: 16 Bits
100 Time Records
Number of Occurrences
1373
1098
824
549
275
0
20
40
60
80
100
120
140
BIN VALUE

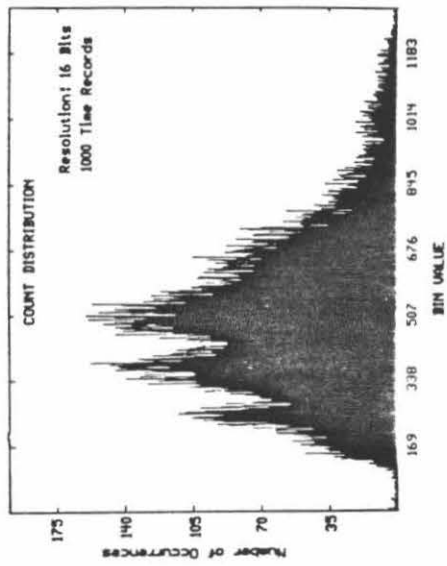
COUNT DISTRIBUTION
Resolution: 16 Bits
1000 Time Records
Number of Occurrences
175
140
105
70
35
169
338
507
676
845
1014
1183
BIN VALUE

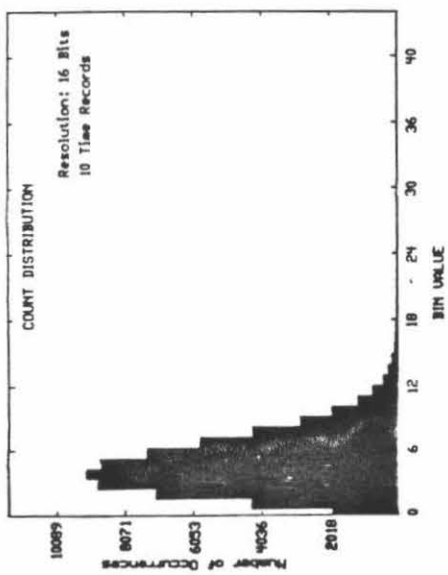
COUNT DISTRIBUTION
Resolution: 16 Bits
10 Time Records
Number of Occurrences
10069
8071
6053
4036
2018
0
6
12
18
24
30
36
40
BIN VALUE

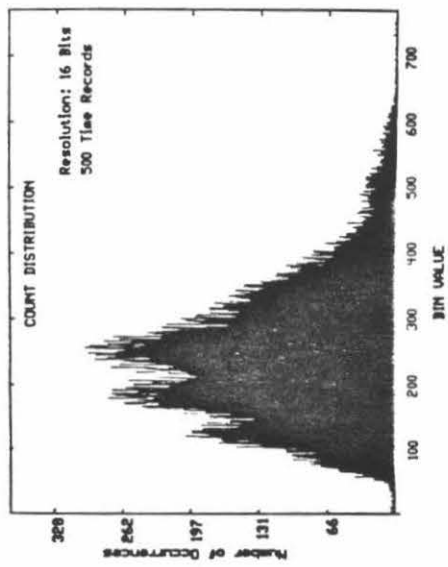
COUNT DISTRIBUTION
Resolution: 16 Bits
500 Time Records
Number of Occurrences
328
262
197
131
66
100
200
300
400
500
600
700
BIN VALUE

bin value as the ordinate. Again, if the ADC performance were ideal, this should produce a distribution with a single mode located at the average number of samples in a bin. The area of the histogram equals the total number of samples and the standard deviation of the distribution would be found from Poisson statistics to be the square root of the average number of samples expected in a bin. As can be seen in Figure 9, the stringency of this test technique varies with the number of samples. In the small sample cases, 10 and 100 time records, the distribution does not show significant departure from ideal behavior (i.e., the distributions show one mode and Poisson character). However, in the large sample cases there is a clear deviation from ideal. The appearance of multiple maxima in the distribution indicates that ADC bin widths are not uniform, but rather, their widths occur in clusters. The clustering of bin widths at values distinct from the mean necessarily implies differential nonlinearity. Although these test data indicate that the differential linearity of PCM78P leaves a great deal to be desired, we find in practice, that the signal to noise ratios of our SPM system are sufficiently large that missing codes and nonlinearities in the ADC circuitry do not seriously degrade instrument performance (e.g., four consecutive ADC codes for ± 10 V input range at 16 bit resolution corresponds to a "dead band" of ≈ 1.2 mV). For systems in which this is not the case, we believe that the diagnostic tests outlined above may prove useful in the selection of ADCs.

Although we are not able to achieve 16 bit performance, we would point out that a 14 bit performance level is tolerable for most SPMs, and that systems which offer performance superior to ours are much more expensive (by factors of 5-10). Also, as mentioned previously, the adaptation of the system to accommodate higher performance ADCs as they are required is

quite straightforward. One should also note that, for some SPM designs, high speed true 12 bit ADCs may be an optimal ADC choice.

SYSTEM PERFORMANCE:

To evaluate the ability of the system to control a SPM we have used the system in conjunction with several different types of microscope available in our laboratory. Perhaps the instrument which best illustrates the capability of the control system is the ultra-high vacuum scanning tunnelling microscope (UHVSTM). We have recently constructed a new scanner and sample translator assembly for the UHVSTM. The new scanner is capable of motions six times larger along the Z axis (2μm) and ten times larger in the X and Y dimensions (3μm) than our previous scanner. The new scanner was limited by the electronic noise of the control electronics which were previously used and could only achieve atomic resolution when the servo control voltage was limited to a 30 volt range. When using the control system described in this paper, atomic resolution was achieved with a full 380 volt control range; the imaging capability was limited in this case by the mechanical stability of the scanner assembly, rather than by the control electronics. Additionally, the modular design of the system and its standard communication interface allowed simple integration of control electronics for the sample translator.

The use of data from the UHVSTM to illustrate the system performance avoids some of the questions raised of STM in air, and tip sharpness can be evaluated by field ion microscopy in this microscope thus avoiding concerns common to SFM. In Figure 10 we show an image of highly oriented pyrolytic graphite (HOPG) taken with the UHVSTM

Figure 10. An image of highly oriented pyrolytic graphite (HOPG) taken using the SPM control electronics presented in this article to control an ultra-high vacuum (UHV) scanning tunnelling microscope. A physisorbed contaminant is seen on the inert graphite basal plane. The image is approximately 50 x 50 Å with 250 x 250 pixels acquired at 250 pixels/second. It is a constant current image (tunneling current ≈ 1nA) at a sample bias of -0.1V. The brightnes in the image is proportional to both topographic height and slope. For details of image processing see the text.

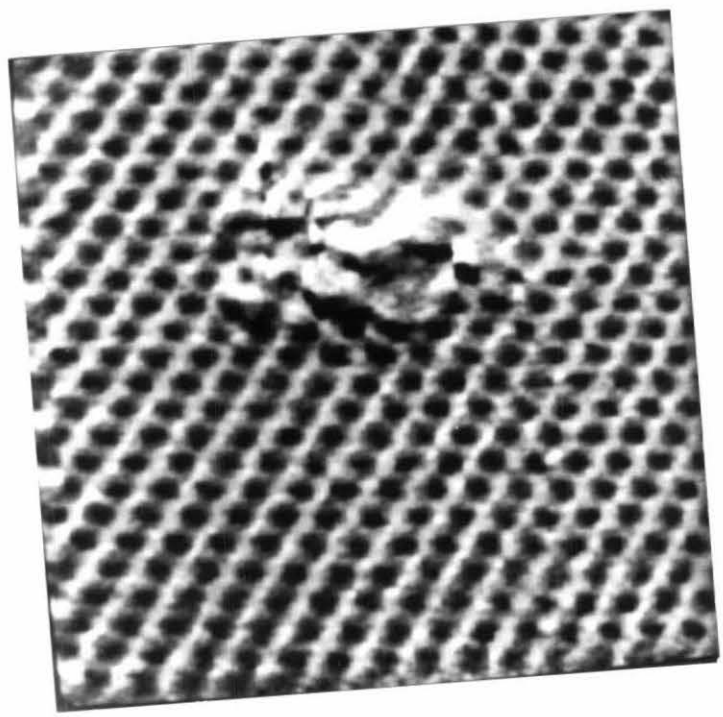

controlled by the digital control system. The data show atomic resolution as well as a physisorbed contaminant on the inert graphite basal plane. (During a subsequent scan, the contaminant was swept away mid-scan, thus affirming that it was weakly bound through physi- rather than chemisorption.) The image is approximately 50 x 50 Å with 250 x 250 pixels acquired at 250 pixels/second. It is a constant current image acquired at a tunnelling current of 1 nA with a -0.1 volt sample bias. The image is displayed with brightness proportional to both topographic height and slope. Tilt was removed by plane subtraction, and noise reduction was done through median filtering followed by smoothing with a binomially weighted sliding window 1 Å square (full width at half maximum) which is small compared to the 2.4 Å unit cell of HOPG.

ADAPTATION OF THE SPM CONTROL AND DATA ACQUISITION SYSTEM TO NEAR FIELD SCANNING OPTICAL MICROSCOPY:

Finally, as an example of the flexibility afforded by modular design we consider the adaptation of the system to near field scanning optical microscopy (NSOM). NSOM holds great potential for imaging biomaterials because it provides all of the advantages of optical microscopy with sub-wavelength resolution. As a field of microscopy, NSOM is still evolving rapidly. With the need to implement quickly various imaging modes and feedback schemes, the flexibility provided by a modular SPM control system could be a tremendous advantage.

The adaptation of the SPM control and data acquisition system to do NSOM is quite simple. In terms of the software, only minor reconfiguration is required. As for the hardware, the only additional requirement is that the instrument be able to detect very weak intensity light signals; thus there is a need for the ability to control and acquire data from photomultiplier tubes (PMTs). In Figures 11a & b we present a diagram of how the control of and data acquisition from a PMT might be done. Figure 11a shows a diagram of how a PMT control module could be added to the system. In Figure 11b we show a more detailed diagram of the contents of the PMT control module.

The relevant parameters for PMTs are the magnitude of the high voltage applied to the tube during use and the photocurrent that is generated. Currently, at least one manufacturer [24] supplies a hybrid photodetector which consists of a PMT, a PMT socket and a miniaturized switching mode power supply to provide the high voltage. The high voltage applied to the PMT may be varied by adjusting a low voltage control line via a DAC and the supply may be turned on and off by turning off the low voltage power to the detector. We have found these self-contained units to have excellent performance as well as being quite compact and convenient.

When photon counting is not required, acquisition of data from the PMT is easily done by using the standard current to voltage conversion circuit with a high input impedance amplifier. When using this type of circuit it is important to note that electrometer amplifiers tend to have significant output impedances and may require some buffering before the ADC input.

Figure 11. A block diagram of the SPM control and data acquisition system as it might be adapted for near field scanning optical microscopy. The major addition needed to perform NSOM experiments is the photomultiplier tube (PMT) control and data acquisition module. A) A diagram showing how the PMT module interfaces with the rest of the SPM system. B) A more detailed diagram of the PMT module itself showing conceptually how such a module might be implemented.

a)

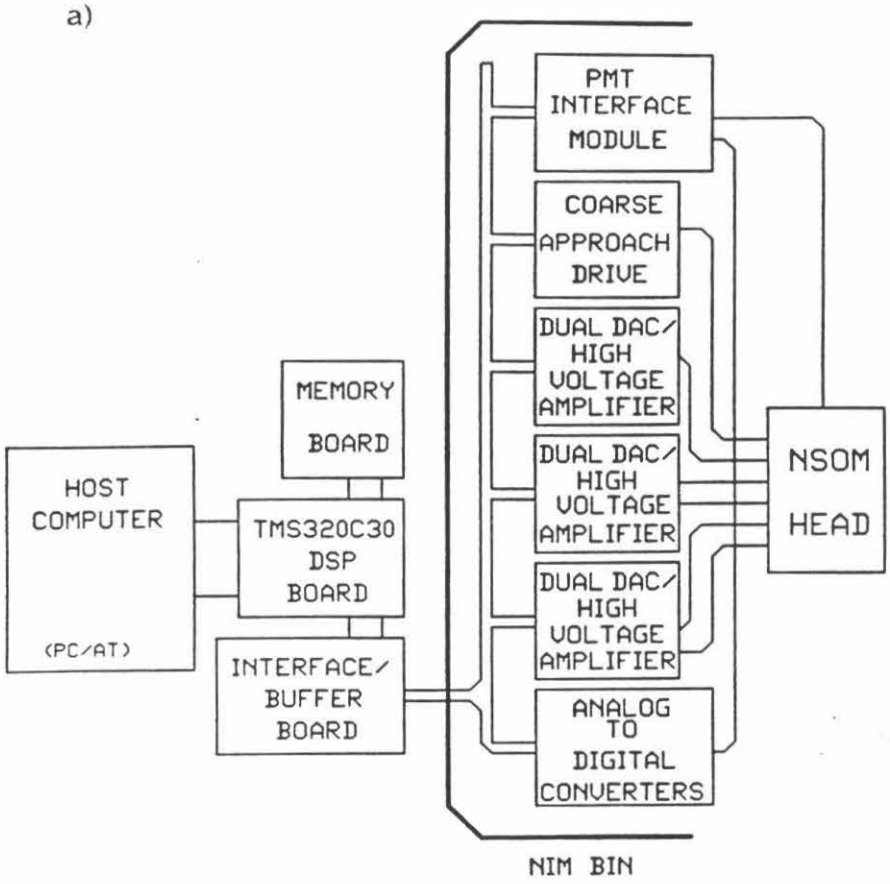
PMT
INTERFACE
MODULE
COARSE
APPROACH
DRIVE
DUAL DAC/
HIGH
VOLTAGE
AMPLIFIER
DUAL DAC/
HIGH
VOLTAGE
AMPLIFIER
DUAL DAC/
HIGH
VOLTAGE
AMPLIFIER
ANALOG
TO
DIGITAL
CONVERTERS
NSOM
HEAD
MEMORY
BOARD
HOST
COMPUTER
(PC/AT)
TMS320C30
DSP
BOARD
INTERFACE/
BUFFER
BOARD
NIM BIN

b)

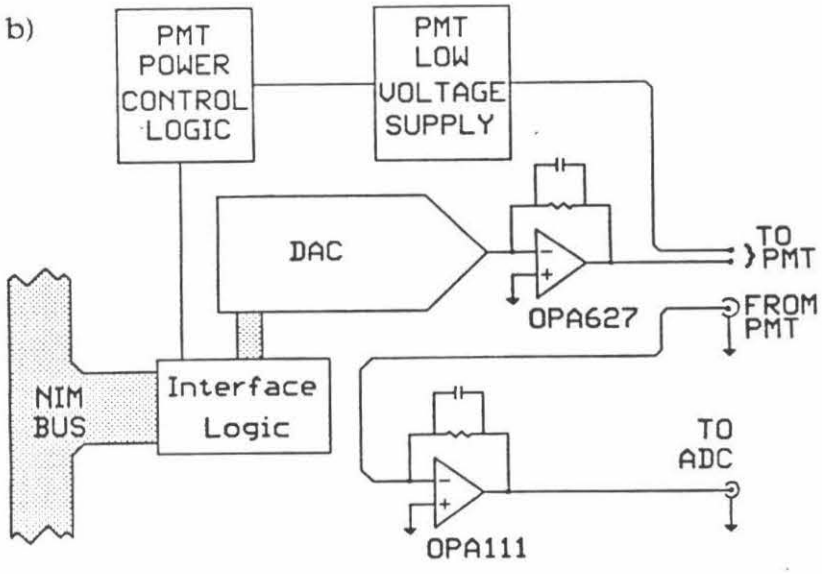
PMT
POWER
CONTROL
LOGIC
PMT
LOW
VOLTAGE
SUPPLY
DAC
TO
PMT
OPA627
FROM
PMT
NIM
BUS
Interface
Logic
TO
ADC
OPA111

The adaptation of the SPM control system for NSOM is as simple as the construction and installation of a module to interface with PMTs. With this type of module both integrated light intensity and light modulation detection could easily be done.

ACKNOWLEDGEMENTS:

The authors would like to thank Jean-Paul Revel for a critical reading of the manuscript. Financial support for this work was provided by Abbott Laboratories, Inc., the National Institutes of Health Training Grant GM07617 (SMC), the Ford Motor Company and a National Science Foundation Fellowship (DRB).

The authors will gladly supply more detailed documentation to interested readers.

REFERENCES

1. J.H. Hoh, R. Lal, S.A. John, J.-P. Revel, M.F. Arnsdorf, *Science* **253**, 1405 (1991).
2. H.G. Hansma, *et al.,, Science*, in press.
3. A. Engel *Annu. Rev. Biophys. Biophys. Chem.* **20**, 79 (1991).
4. C. Bustamante, J. Vesenka, C. Tang, W. Rees, M. Guthold, R. Keller, *Biochemistry* **31**, 22 (1992).
5. A. Lewis and K. Lieberman, *Anal. Chem.* **63** (11), 625 A (1991) and refrences therein.
6. C. Prater, P. Hansma, M. Tortonese, C. Quate, *Rev. Sci. Instrum.* **62** (11), 2634 (1991).
7. A. Bard, F. Fan, D. Pierce, P. Unwin, D. Wipf, F. Zhou, *Science* **254**, 68 (1991)
8. O. Marti, S. Gould, P.K. Hansma, *Rev. Sci. Instrum.* **59** (6), 836 (1988).
9. A. Brown and R.W. Cline, *Rev. Sci. Instrum.* **61**(5), 1484 (1990)
10. R.S. Robinson, T.H. Kimsey, R. Kimsey, *J. Vac. Sci. Technol.* **B9** (2), 631 (1991)
11. A.J. Hoeven, E.J. van Loenen, P.J.G.M. van Hooft, K. Oostveen, *Rev. Sci. Instrum.* **61**(6), 1668 (1990).
12. R. Piner and R. Reifenberger, *Rev. Sci. Instrum.* **60** (10), 3123 (1989).
13. R. C. Barrett and C. F. Quate, *Rev. Sci. Instrum.* **62**(6), 1393 (1991).
14. Motorola, Inc., P.O. Box 1466, Austin, TX 78767 USA.
15. A. Ambrozy, Electronic Noise (McGraw-Hill, New York, 1982).
16. Spectrum Signal Processing, Inc., #301 3700 Gilmore Way, Burnaby, B.C. V5G4M1, Canada.
17. D. Baselt, S. Clark, M. Youngquist, C. Spence, J. Baldeschwieler, in

preparation.

18. Texas Instruments, Inc., P.O. Box 655012, Dallas, TX 75265 USA.

19. Burr-Brown Corp., 6730 S. Tucson Blvd., Tucson, AZ 85734 USA.

20. Apex Microtechnology, Corp., 5980 N. Shannon Rd., Tucson, AZ 85741 USA.

21. D. Sheingold, ed., Analog-Digital Handbook (Prentice-Hall, Englewood Cliffs, New Jersey, U.S.A., 1986).

22. Toko America, Inc., 1250 Feehanville Dr., Mount Prospect, IL 60056 USA.

23. Analog Devices, Inc., One Technology Way, P.O. Box 9106, Norwood, MA 02062 USA.

24. Hamamatsu Photonics Corp., 360 Foothill Road, P.O. Box 6910, Bridgewater, N.J. 08807 USA.

25. G. Franklin and J. Powell, Digital Control of Dynamic Systems (Addison-Wesley, Menlo Park, CA, 1980).

Appendix A.

Design Details of the Digital Signal Processor Based Low Noise Control Electronics for Scanned Probe Microscopes

I. Introduction

II. System Overview
- A. General System Architecture
- B. The Modular External Analog I/O Concept

III. The DSP-Link/NIM Bus Interface
- A. The Master-Slave Relationship
- B. Details of DSP Link
- C. The Bus Driver/Interface Card

IV. The NIM Module Format

V. Ubiquitous Circuitry and General Design Comments

VI. The Key Modules
- A. The Digital to Analog Converter Module
- B. The High Voltage/Motor Driver Module
- C. The Analog to Digital Converter Module

VII. Miscellaneous Circuitry
- A. The Photodiode Preamplifier
- B. The "2 nd Stage" Amplifier

I. INTRODUCTION

The use of digital processor based control loops for instrument control and data acquisition applications has held promise for some time. The major advantage to be gained in such a system is flexibility. For some systems flexibility is a driving concern and so digital processor based systems were built despite their poorer noise performance, lower bandwidth and increased cost compared to their analog counterparts. While flexibility is clearly an advantage for scanned probe microscope (SPM) control systems, SPM applications cannot tolerate the compromises in the other areas; thus it is only recently, as high performance components which eliminate the need for compromise have become available, that DSP based control systems have been used for SPMs.

The design of digital signal processor based low noise control electronics for scanned probe microscopes has become possible through advances in two areas. The most important advance has been the availability of high performance digital signal processors such as the TMS320C30 from Texas Instruments and the 96020 from Motorola. These processors equip the system desginer with capabilities which were previously unimaginable. In this regard, DSPs should be thought of as an enabling technology for high bandwidth digital control loop design.

The second advance has been the availability of low cost, high performance audio frequency data conversion products. Their recent availability has allowed high performance systems, which were previously prohibitively expensive, to be realized at a small fraction of the cost. This has

greatly contributed to the impetus to design DSP based systems for data acquisition and control of scanned probe microscopes.

Another area in which progress has been instrumental is the commercial availability of high voltage operational amplifiers. High voltage amplifiers are required to drive the piezoceramic motion transducers used in scanned probe microscopy. Until recently high voltage amplifiers for this and ohter applications had to be designed from scratch using discrete components. Often the characterization and perfection of these amplifiers was laborious and required a skilled engineer. However, the advent of hybrid circuit high voltage operational amplifiers designed specifically for driving piezoceramics has greatly simplified this task.

The major strengths of the DSP based SPM control electronics, as mentioned in Chapter 1, are its modularity and flexibility. These attributes make it well suited to the general problem of data acquisition from and control of various scientific instruments and it is not difficult to see how the system could be used to control and acquire data from such diverse instruments as mass spectrometers, scanning electron microscopes, X-ray microprobe systems and so forth. The broad range of potential applications arises directly from the generic nature of the system; the ability to change voltages as arbitrary functions of time and to acquire data at high resolution and speed is central to many different instruments. With suitable "front - end" detectors and signal conditioning, the system can be adapted to a wide range of experiments in the physical, chemical and biological sciences. By using the personal computer as a host for a DSP based system, all of its benefits and limitations are incurred.

The process of creating an electronic control system for scanned probe microscopes entails several stages: i) the initial feasibility study; ii) selection of a system architecture; iii) evaluation of components for crucial system functions; iv) system design; v) detailed design of subassemblies; vi) fabrication and test of subassemblies and vii) system integration and system test. While all of these steps were accomplished at one time or another, this appendix presents only the end results of selected portions of this multi-step process. This is done in order to maintain a focus on the particular aspects of the system which show both its versatility and limitations. It is hoped that the reader will gain an appreciation of the types of experiments made possible by using the system and be given some vague direction as to which parts of the system to examine if it should become a limiting factor.

II. SYSTEM OVERVIEW

A. General System Architecture

Figure 1 shows a block diagram of the SPM control system. As can be seen from the Figure, there are three major sections to the control system; the host platform, the DSP board (and associated memory, etc.) and the analog input/output section. In our case, the choice of DSP board required the use of a PC host.

At the heart of the system lies the digital signal processor (DSP), in this case a TMS320C30 from Texas Instruments (Figure 2). Digital signal processors are microprocessors tailor made for real time signal processing. The major advantages presented by DSPs, as compared to other

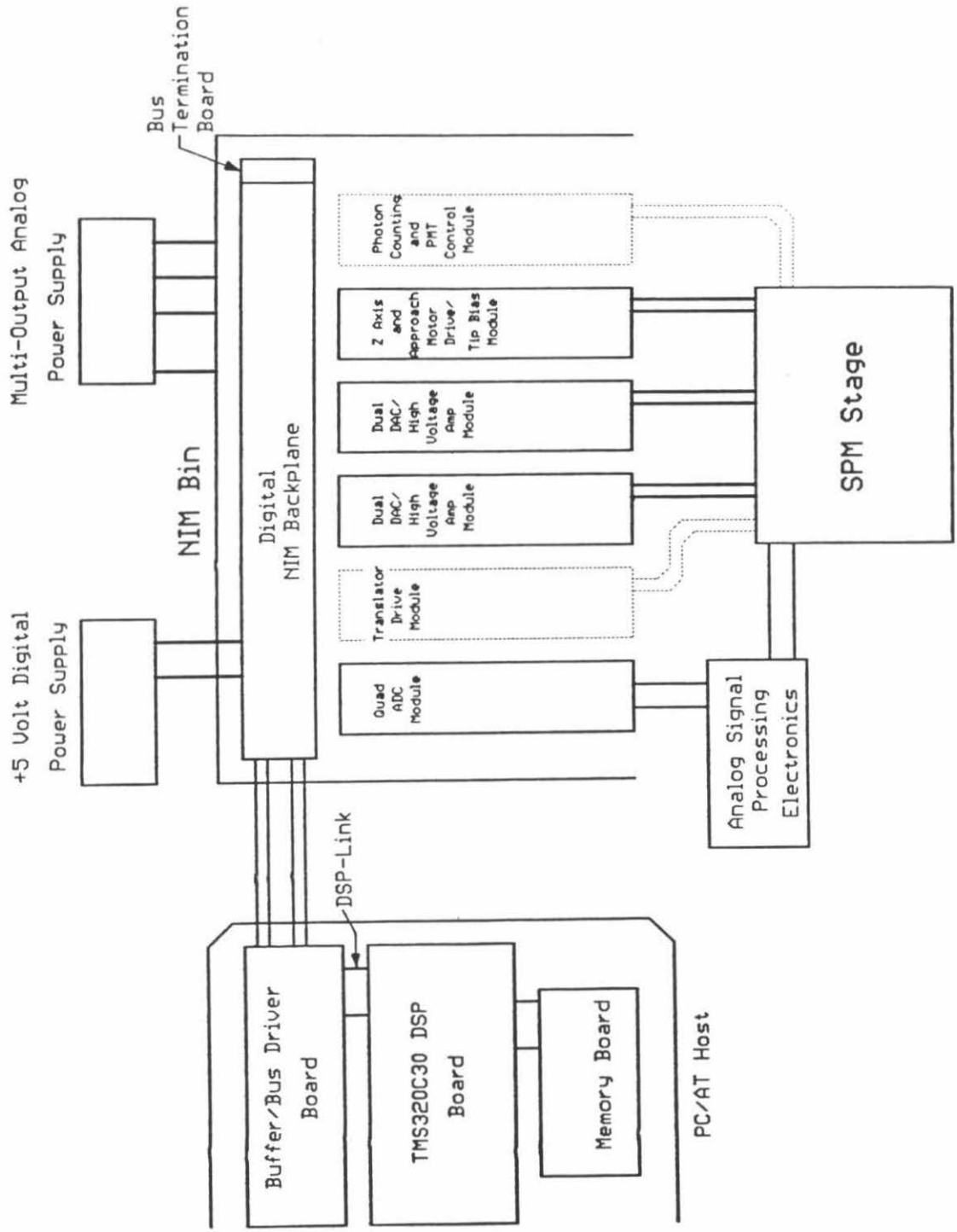

Figure 1. A block diagram of the scanned probe microscope control system.

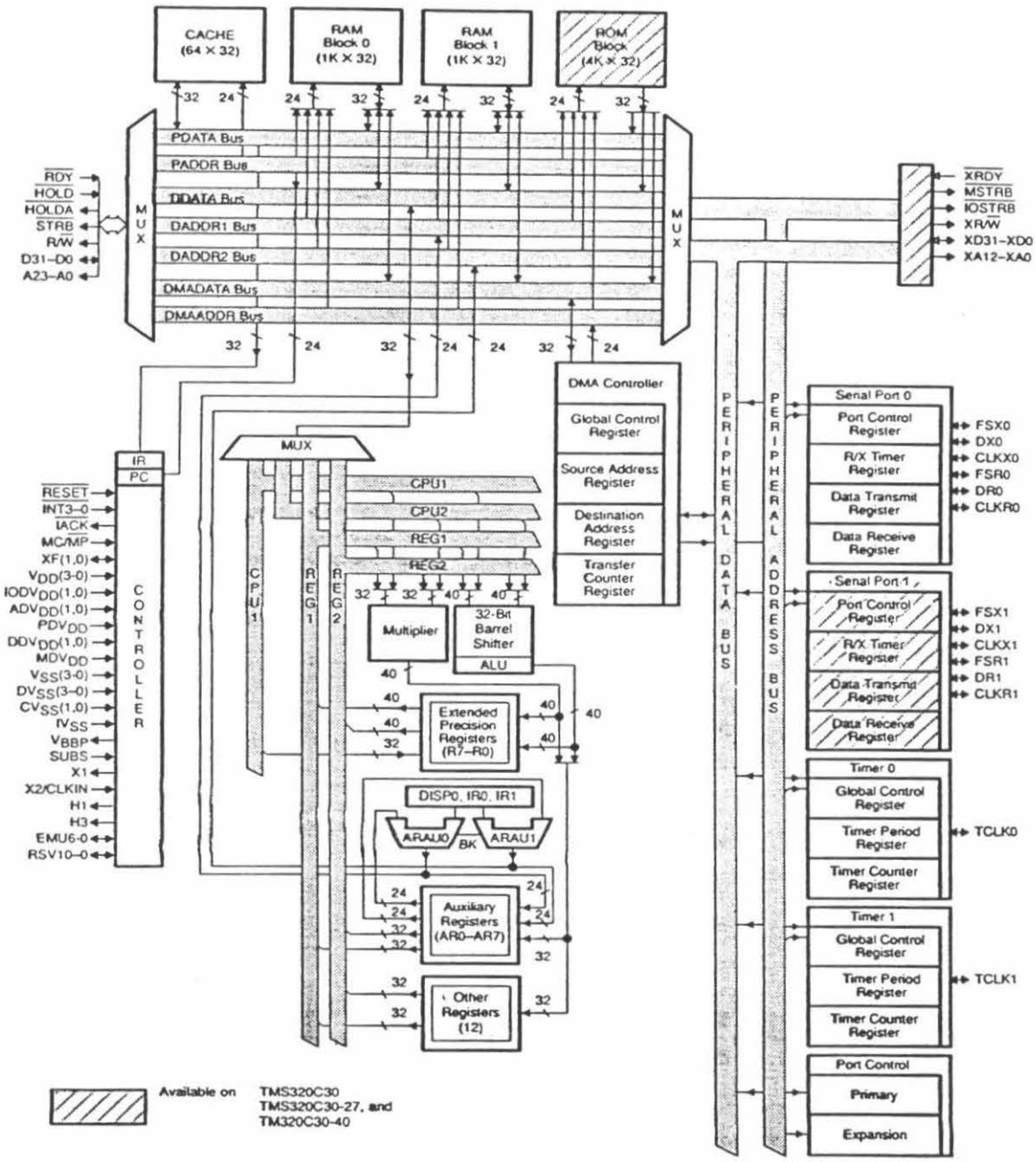

Figure 2. A block diagram of the TMS320C30 digital signal processor. (Reproduced from the TMS320C30 User's Guide 1991.)

microprocessors, for real time applications are their speed and reliable instruction cycle time as well as their ability to do single machine cycle multiplication and matrix manipulations. Often DSPs have additional features such as hardware registers that make the implemention of certain data structures (e.g., circular buffers) and algorithms markedly simpler than with other types of microprocessors. They also tend to have integral timers and clocks to generate or record events which occur at regular intervals.

In our system the TMS320C30 resides on a DSP board from Spectrum Signal Processing which occupies one of the plug-in card slots on the IBM PC/AT bus. A block diagram of the board is shown in Figure 3. The DSP communicates with the PC through the PC/AT bus and controls the analog I/O via the DSP-Link bus.

B. The Modular External Analog I/O Concept

In any system which requires analog I/O, there is a choice of where electronic components can be located. For many PC based systems placing a commercially available analog I/O card in the PC chassis is an attractive option. The major limitation encountered with this arrangement is that the electrical noise inherent in the computer chassis limits the effective dynamic range of the I/O section. In fact, we have found that internal (inside the computer chassis) analog I/O circuitry is limited to between 12-14 bits of dynamic range which is inadequate for the control of high resolution SPMs. To achieve dynamic range of 16 bits or more requires that the analog I/O circutry be placed outside of the computer chassis.

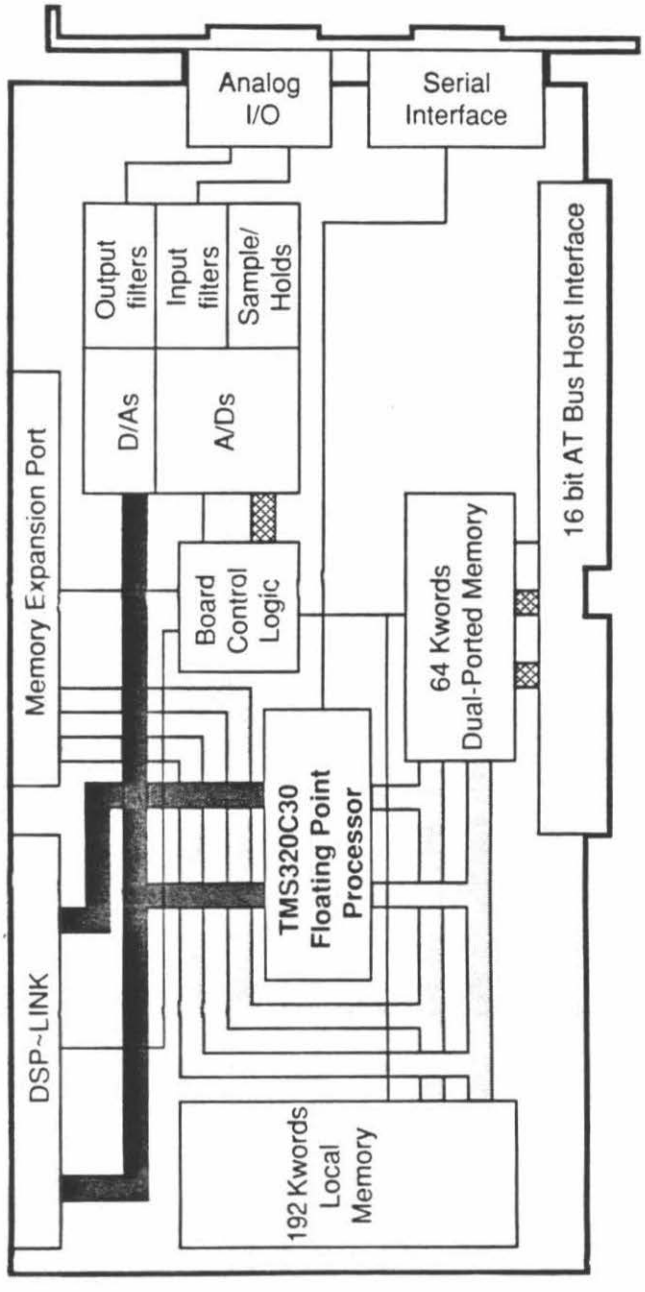

Figure 3. A block diagram of the TMS320C30 System Board

(Reproduced from the Spectrum Signal Processing catalog.)

Typically, external analog I/O has been implemented as a group of individual boxes which are connected in some fashion. This type of "architecture" tends to require that a new box be made for every additional function the system is to perform and that much redundant circuitry (e.g., power supplies, interfaces, etc.) be replicated for each box. A more satisfactory solution for SPMs is a modular approach to the I/O circuitry. We used a modified nuclear instrumentation module (NIM) bin to house modules which conform to a standard mechanical and electrical interconnection format. The details of this format will be discussed later, but the key point is that this format allows the flexibility of a modular design and reduces design overhead, facilitating the addition of new modules to the system and most importantly it allows housing of high performance circuitry.

III. The DSP-Link / NIM Bus Interface

In our system DSP-analog I/O communication is accomplished by using the DSP board external communications bus. For use in conjunction with external analog I/O we have buffered and extended this bus so that all modules in the NIM chassis can be directly connected to the bus. The manufacturer of the DSP board estalished a standard communications interface, called DSP-Link, for all of the DSP boards they market. The TMS320C30 board in particular supports only the most primative aspects of the DSP-Link standard.

A. The Master-Slave Relationship

DSP-Link establishes a master-slave relationship between the digital

signal processor and the other devices connected on the bus. This is the simplest type of interface and has a minimal set of bus operations. In a master-slave relationship the DSP controls all of the communications on the bus; to elicit action in a slave unit (e.g., initiate the conversion process in an analog to digital converter) the master writes a control signal to the unit. The unit has to hold its response until it is polled (usually be means of a read operation). With this type of bus structure multiple processors can be connected, however only one processor can play the role of master. Because of this there is no need for bus arbitration or collision avoidance mechanisms; all communications must pass through the master. This means that the primary operations on the bus are read and write and the data flow for these operations is defined with respect to the master (i.e., a write operation means that data is being transfered from the DSP to an external device).

B. Details of DSP-Link for the TMS320C30 System Board

The electrical signals comprising DSP-Link for the TMS320C30 boards are listed below. Only the subset of DSP-Link signals listed is supported by the TMS320C30 System and Processor boards. It should be noted that this set is different from those in the application note from Spectrum Signal Processing concerning the DSP-Link standard. For the TMS320C30 boards DSP-Link is mapped into memory space from address 800000 to 801FFF (hexadecimal). Each location occupies a 32-bit word in memory space, but only the most significant 16 bits are available on the DSP-Link connector. The signals on the DSP-Link connector are minimally buffered on the DSP board and cannot be used to drive long cables.

DSP-Link Signals and Their TMS320C30 Equivalents

DSP-Link Signal	TMS320C30 Signal	Function
D0-D15	XD16-XD31	Data Lines
A0-A12	XA0-XA12	Address Lines
IOE*	MSTRB*	Input/Output Enable
R/W*	IOR/W*	I/O Read/Write
INT0*	INT0*	Interrupt 0
INT1†	INT1†	Interrupt 1
IACK*	IACK*	Interrupt Acknowledge
FLAG_OUT	XF0	Flag Out
FLAG_IN	XF1	Flag In
CLK/2	H3	System Clock (÷ 2)
RESET*	RESET*	System Reset

* Denotes active low signals

† Denotes positive edge triggered signals

In addition to knowing the function of each of the interface signals it is important that signal timing also be defined. In Figure 4, on the next page, the bus timing for zero wait state write and read operations is shown. Occasionally bus timing must be slowed to accomodate the timing requirements of slower devices. This is done by the insertion of wait states. By adding wait states signal levels during write and read operations are held

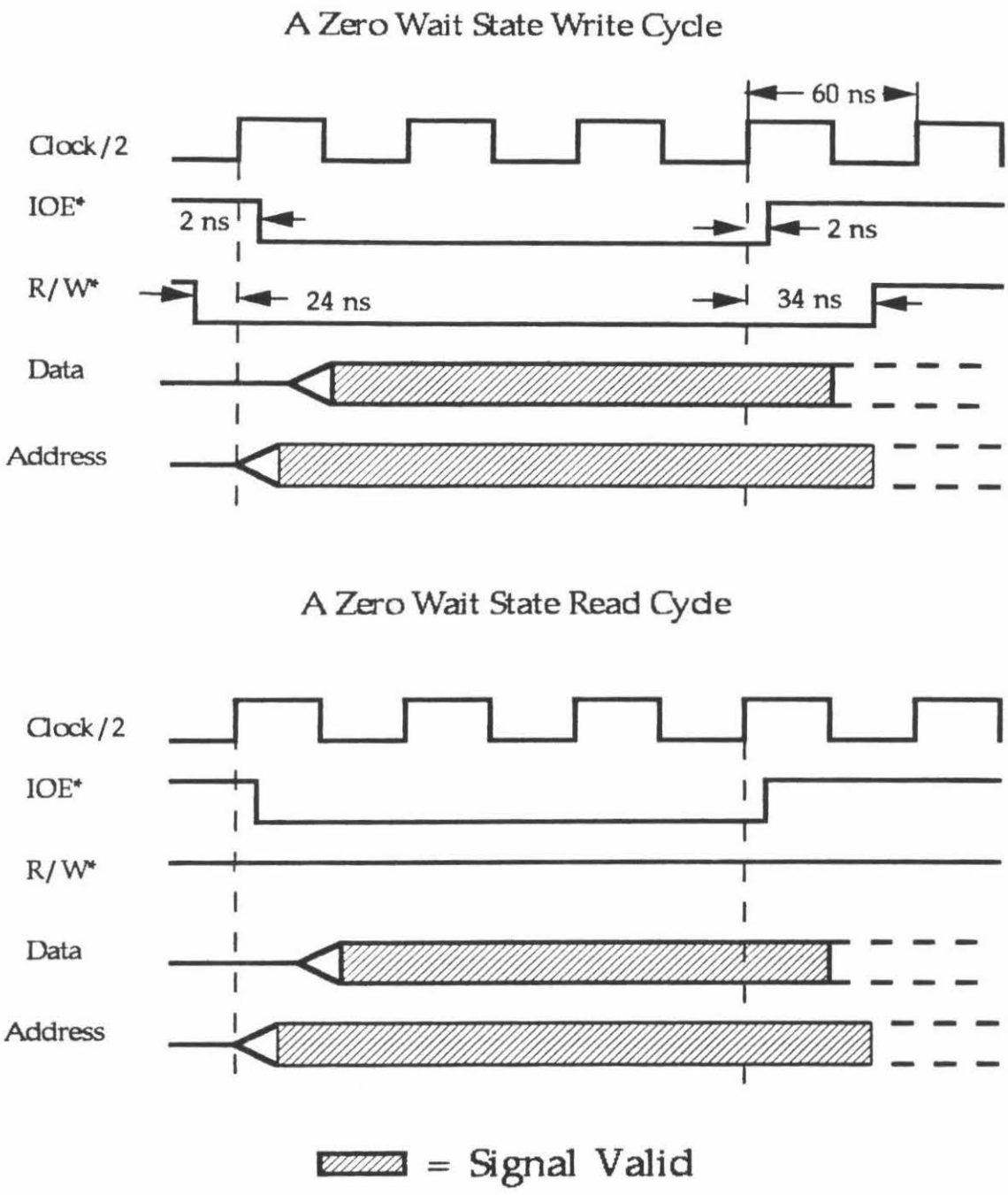

Figure 4. DSP-Link/NIM Bin Bus Timing Diagram

for an extended time. This hold time can be added in 60 ns increments and is software programable in the TMS320C30. During normal operation of our SPM the bus timing is set for one wait state.

C. The Bus Driver / Interface Card

As mentioned earlier, the circuitry on the TMS320C30 board does not have sufficient drive capability to transmit signals over long cables. Another aspect of the DSP-Link circuitry on the TMS320C30 board worth mentioning is that, because of some of the propagation delays on the board, the signal timing on the interface connector is not quite right. Additionally, the high speed nature of the bus signals makes impedance matching and proper line termination crucial. If inadequate attention is given to these issues the control system will work only marginally, if at all.

In order to supply the needed current to drive realistic cable lengths with edge rates in excess of 250 MHz, a card was designed which resides in the PC chassis beside the DSP board. This card has the standard full length AT bus profile and is called the DSP interface / bus driver card. The design and layout details for the card are given by the Figures on the next four pages.

The basic features of the DSP interface / bus driver card are that it functions as a bidirectional interface to the DSP and that the buffers provide proper drive and termination capabilities for the NIM bus. Refering to the schematics on the following four pages, the 74HCT240AN chips were chosen because they provide the required noise immunity and slower response time needed to remedy the timing problems on the DSP board. These parts

Figure 5. Assembly drawing, connector pinout and schematics for the DSP interface / bus driver card (pages 86-89).

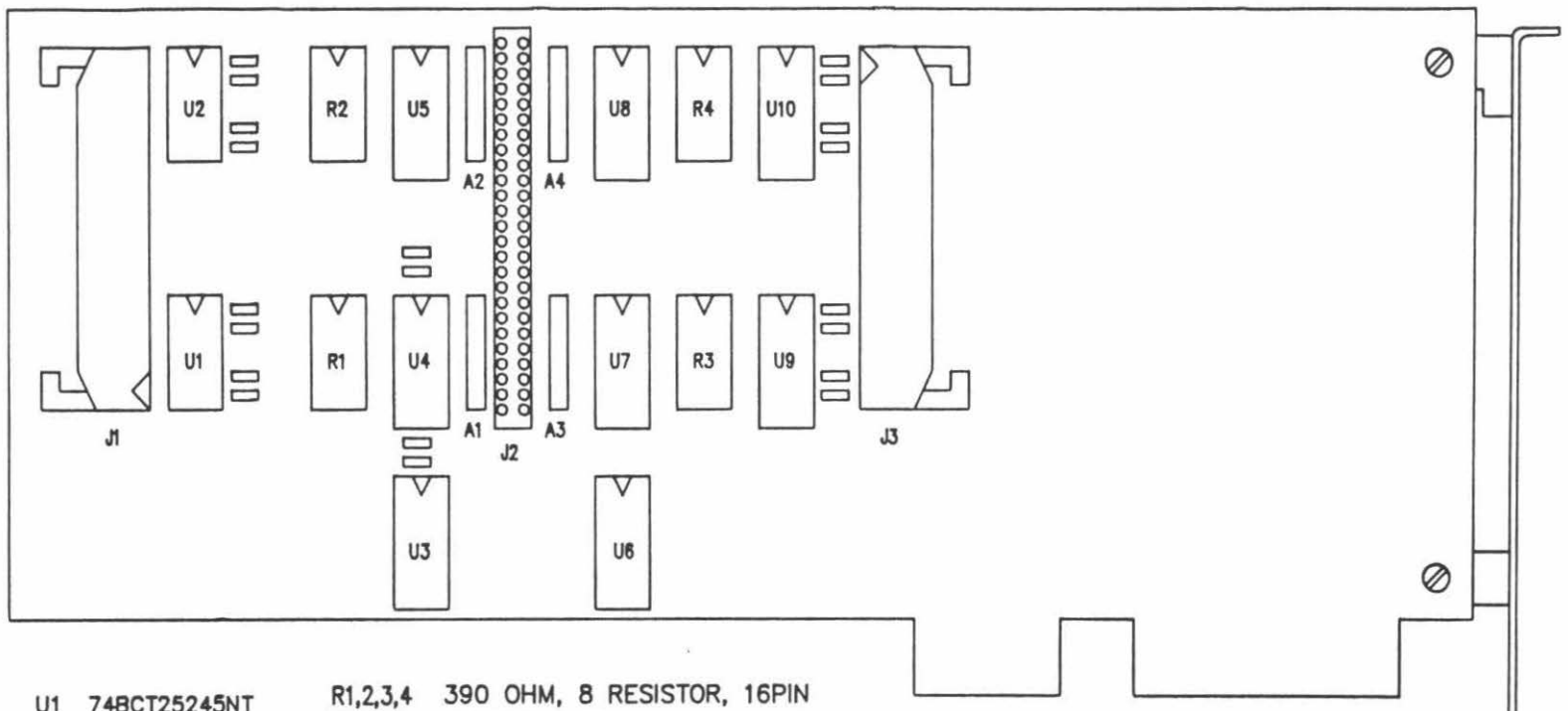

U1	74BCT25245NT	R1,2,3,4	390 OHM, 8 RESISTOR, 16PIN CERAMIC RESISTOR NETWORK
U2	74BCT25244NT		
U3	74HCT240AN	A1,2,3,4	SCHOTTKY DIODE ARRAY
U4	74HCT240AN		
U5	74HCT240AN	J1,J3	RIGHT ANGLE 50 PIN RIBBON CABLE CONNECTOR
U6	74HCT240AN		
U7	74HCT240AN	J2	STRAIGHT 50 PIN RIBBON CABLE CONNECTOR
U8	74HCT240AN		
U9	74BCT25245NT		
U10	74BCT25244NT		

THIS CARD HAS TWO OUTPUT CABLES WHICH ARE CONNECTED TO THE BUS ADAPTER CARD
ALL SIGNAL INPUTS TO THE 74HCT240AN'S ARE TERMINATED

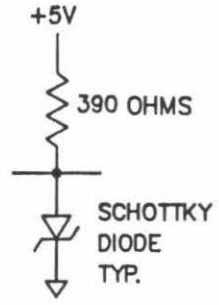

TYP. TERMINATION

DSP INTERFACE/BUS
DRIVER CARD

VCC	1	2	GND
A15	3	4	A14
A13	5	6	A12
A11	7	8	A10
A9	9	10	A8
GND	11	12	CLK/2
$\overline{\text{RESET}}$	13	14	FLAGOUT
FLAGIN	15	16	$\overline{\text{IACK}}$
INT1	17	18	$\overline{\text{INTØ}}$
$\overline{\text{WAIT}}$	19	20	$\overline{\text{READY}}$
$\overline{\text{GME}}$	21	22	$\overline{\text{IOE}}$
R/W*	23	24	GND
A7	25	26	A6
A5	27	28	A4
A3	29	30	A2
A1	31	32	AØ
GND	33	34	D15
D14	35	36	D13
D12	37	38	D11
D10	39	40	D9
D8	41	42	D7
D6	43	44	D5
D4	45	46	D3
D2	47	48	D1
DØ	49	50	GND

J2

DSP INTERFACE/BUS DRIVER CARD

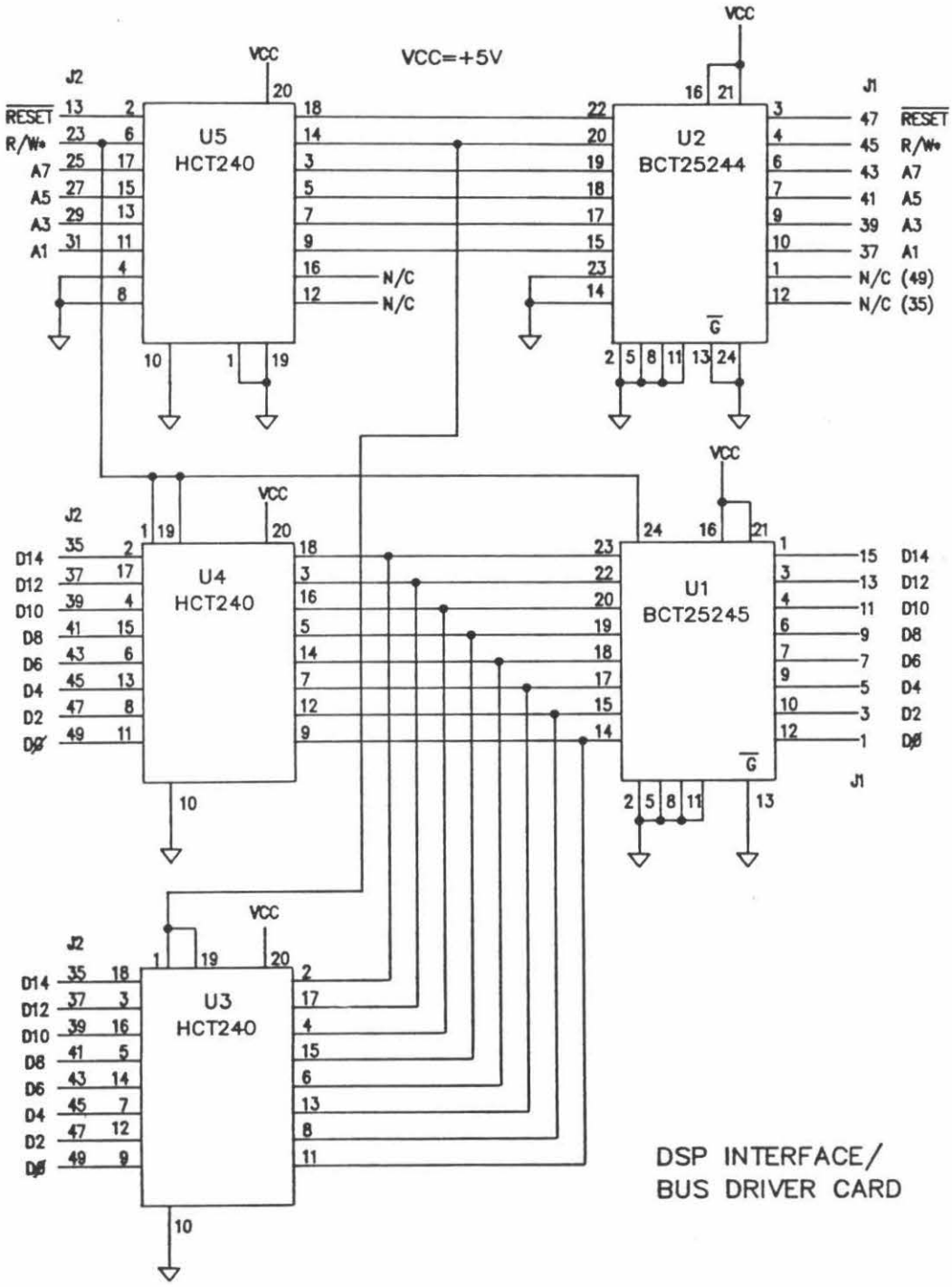
VCC=+5V
VCC
J2
J1
U5
HCT240
U2
BCT25244
U4
HCT240
U1
BCT25245
U3
HCT240
RESET
R/W*
A7
A5
A3
A1
N/C
D14
D12
D10
D8
D6
D4
D2
D0
G
DSP INTERFACE/
BUS DRIVER CARD

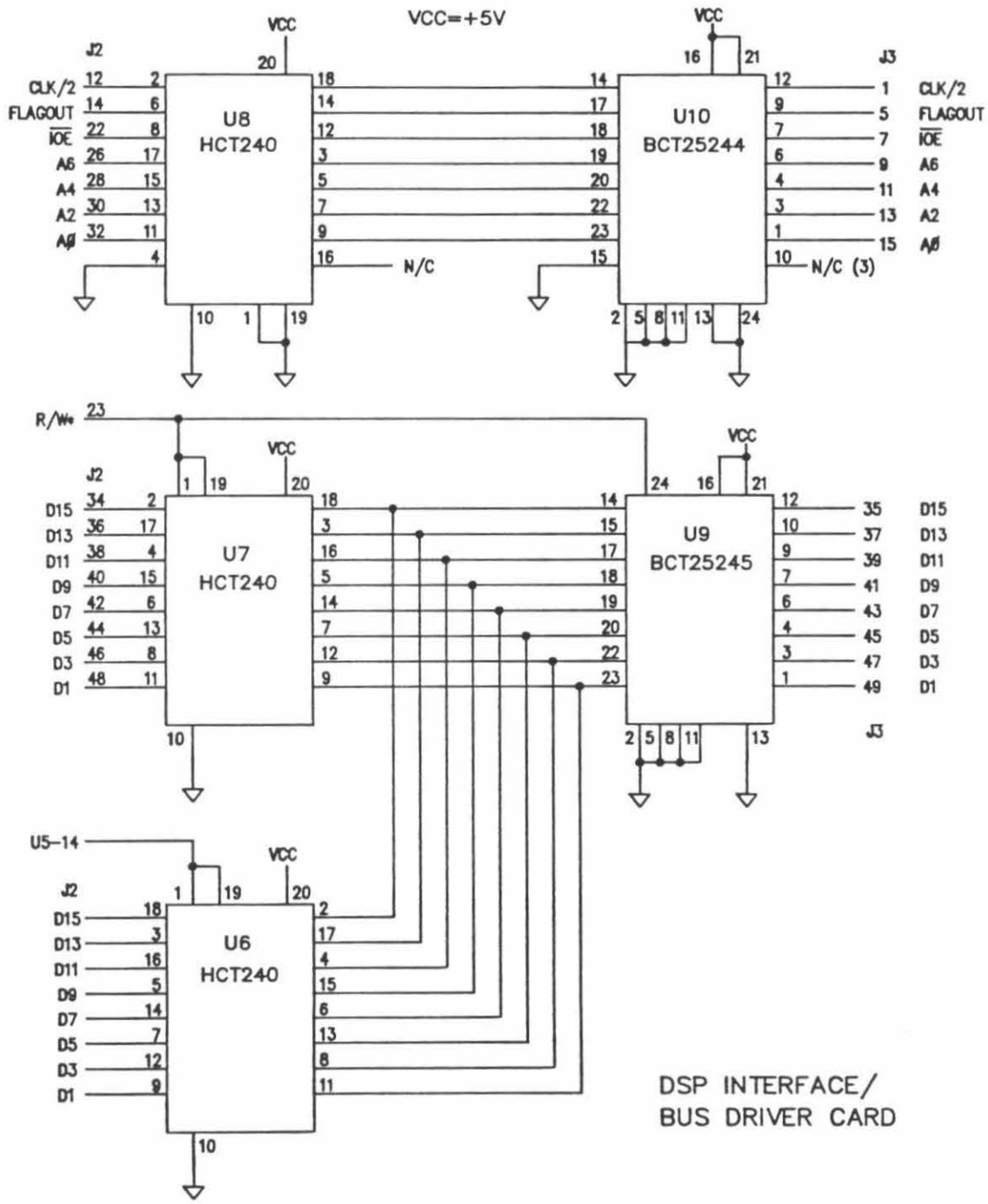
VCC=+5V
U8
HCT240
U10
BCT25244
U7
HCT240
U9
BCT25245
U6
HCT240
J2
J3
CLK/2
FLAGOUT
IOE
A6
A4
A2
A0
N/C
N/C (3)
R/W
D15
D13
D11
D9
D7
D5
D3
D1
U5-14
VCC
DSP INTERFACE/
BUS DRIVER CARD

provide inputs for the 74BCT25244NT line drivers. It should be noted that the termination networks present on this card are for the lines coming from the DSP. This termination should not be confused with the termination required at the end of the NIM bus.

IV. The NIM Module Format

The nuclear instrumentation module (NIM) format provides a standard for mechanical and electrical instrumentation packaging that dates back to the 1950's. Despite its age, the NIM format enables efficient, low-cost construction of modular intrumentation. With a few modifications (which of course violate the standard) a high-speed digital bus structure can be incorporated which allows computer control of the instrumentation modules at a cost far below that of other instrumentation packages (e.g., CAMAC or VXI).

The NIM system is based on the concept of an instrument mounting frame called a NIM bin. The NIM bin incorporates a central power supply and is used to house NIM units all of which conform to the same mechanical height and depth dimensions. Because the NIM bin has twelve slots for modules, any particular unit can occupy between one and six of the slots.

The central linear power supplies which are standard for NIM bins provide ±24 volt, ± 12 volt and + 6 volt regulated power for the units. For our application we wanted to also supply +5 volt, ± 15 volt and ± 210 volt power for the modules, so power supplies for these voltages were added to the NIM bin. The addition of these power supplies to the module slots required that

the standard NIM backplane connector pinout be modified. This modified pinout is shown on the next page (Figure 6).

For use with our DSP controlled architecture, an extension of the DSP - Link interface was directly appended to the NIM bin. This bus, which we call the NIM bus, occupies a substantial portion of the previously unused area in the upper half of the NIM unit back panel. The bus is physically composed of a multilayer printed circuit board which runs the length of the NIM bin and has 96 pin DIN connectors for every NIM slot. The bus is terminated by a resistor network which resides on a small board at the end of the NIM bus. The pinout of the 96 pin DIN conector is shown on the next page. The pinout was chosen so that it would provide a low impedance digital ground for the digital circuits in the modules. The center pins of most of the rows of the connector are ground and they are electrically connected to the ground plane (center layer) of the NIM bus.

The remainder of the information presented in Figures 7-9 gives the practical information needed to actually modify a commercially purchased NIM single wide or double wide unit so that it can be used in conjunction with the modified NIM bins made for scanning probe microscopy. The first two drawings show how to modify the back panel of single and double wide modules so that they will accept the NIM bus connector and the third drawing gives pertinent dimensions for mounting a printed circuit board inside the module.

Figure 6. The Modified NIM Connector Pinout

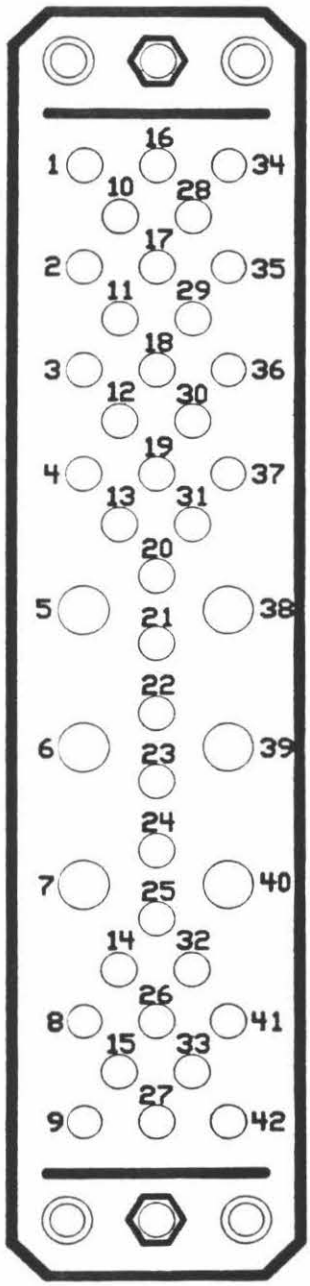

PIN	Assignment
1	+3 Volts DC
2	±3 Volt Ground
3	- 3 Volts DC
10	+5 Volts DC
11	±5 Volt Ground
12	- 5 Volts DC
16	+12 Volts DC
17	±12 Volts Ground
18	- 12 Volts DC
23	+ High Voltage
25	H. V. Ground
27	- High Voltage
28	+24 Volts DC
29	± 24 Volt Ground
30	- 24 Volts DC
33	117 VAC Hot
34	+15 Volts DC
35	± 15 Volt Ground
36	- 15 Volts DC
41	117 VAC Neutral
42	Chassis Ground

Unused Pins: 4-9, 13-15, 19-22, 24, 26, 31, 32, 37-40

Figure 7. The NIM Bin Bus Connector Pinout

Signal Name		96 Pin Connector			Signal Name	
+ 5 Volt Power		A1	B1	C1	+ 5 Volt Power	
+ 5 Volt Power		A2	B2	C2	+ 5 Volt Power	
Digital Ground		A3	B3	C3	Digital Ground	
Digital Ground	(2)	A4		C4	Not Used	(1)
Address Line 14	(4)	A5		C5	Address Line 15	(3)
Address Line 12	(6)	A6		C6	Address Line 13	(5)
Address Line 10	(8)	A7		C7	Address Line 11	(7)
Address Line 08	(10)	A8		C8	Address Line 09	(9)
Clock/2	(12)	A9		C9	Digital Ground	(11)
Flag_Out	(14)	A10		C10	Reset*	(13)
IACK*	(16)	A11		C11	Flag_In	(15)
Int0*	(18)	A12		C12	Int1†	(17)
Ready*	(20)	A13		C13	Wait*	(19)
IOE*	(22)	A14		C14	GME*	(21)
Digital Ground	(24)	A15		C15	R/W*	(23)
Address Line 06	(26)	A16		C16	Address Line 07	(25)
Address Line 04	(28)	A17		C17	Address Line 05	(27)
Address Line 02	(30)	A18		C18	Address Line 03	(29)
Address Line 00	(32)	A19		C19	Address Line 01	(31)
Data Line 15	(34)	A20		C20	Digital Ground	(33)
Data Line 13	(36)	A21		C21	Data Line 14	(35)
Data Line 11	(38)	A22		C22	Data Line 12	(37)
Data Line 09	(40)	A23		C23	Data Line 10	(39)
Data Line 07	(42)	A24		C24	Data Line 08	(41)
Data Line 05	(44)	A25		C25	Data Line 06	(43)
Data Line 03	(46)	A26		C26	Data Line 04	(45)
Data Line 01	(48)	A27		C27	Data Line 02	(47)
Digital Ground	(50)	A28		C28	Data Line 00	(49)

Numbers in parentheses are pin numbers for the 50 pin header on the back of the board. Note that NIM Bin Bus Pins A1-C1 & A2-C2 are all +5 Volt Digital Power and Pins A3-C3 and B4-B32 are Digital Ground. Pins numbered greater than 28 are not used.

Figure 8. Modification of a single-wide NIM module backplane

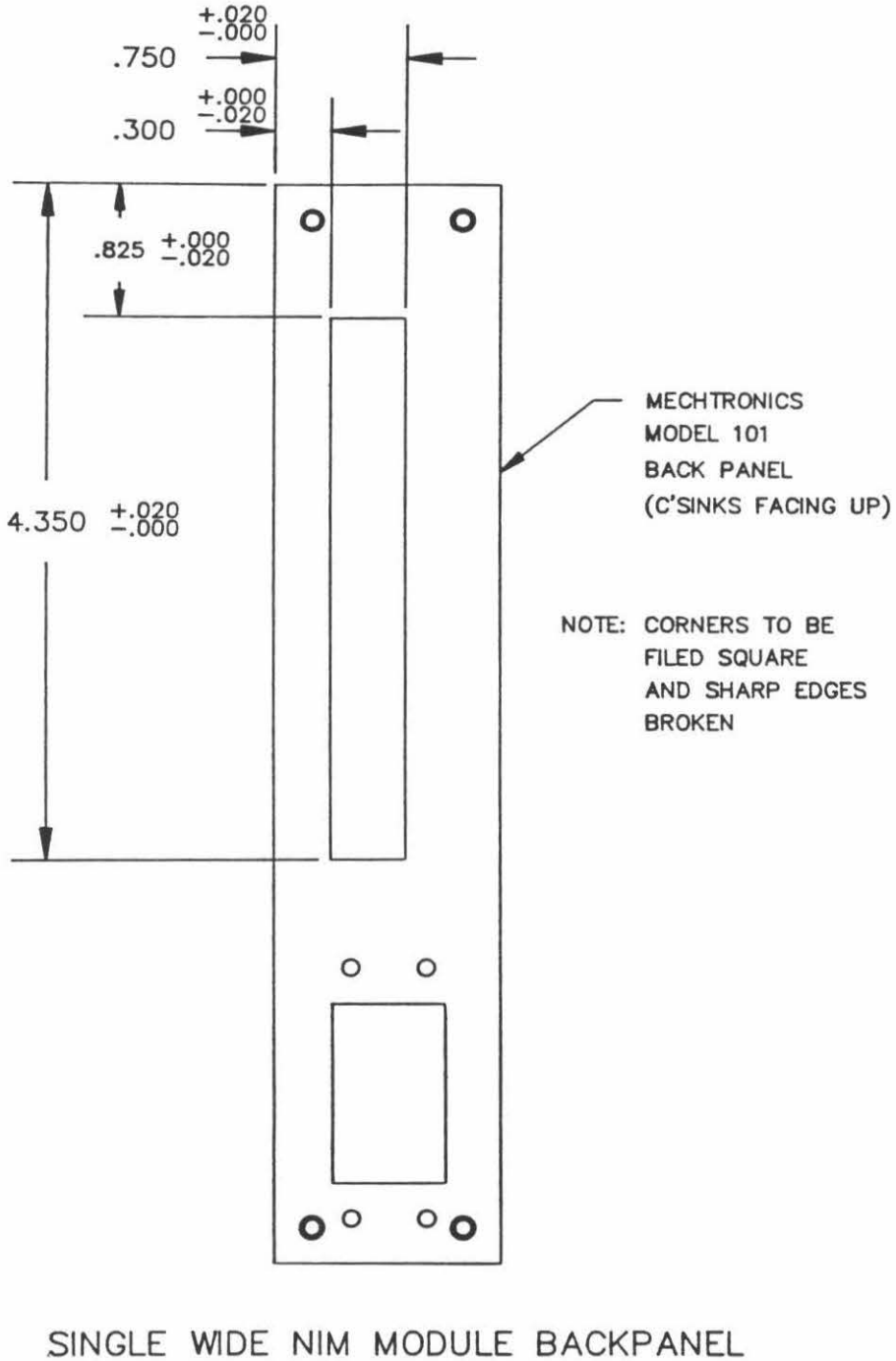

Figure 9. Modification of a double-wide NIM module backplane

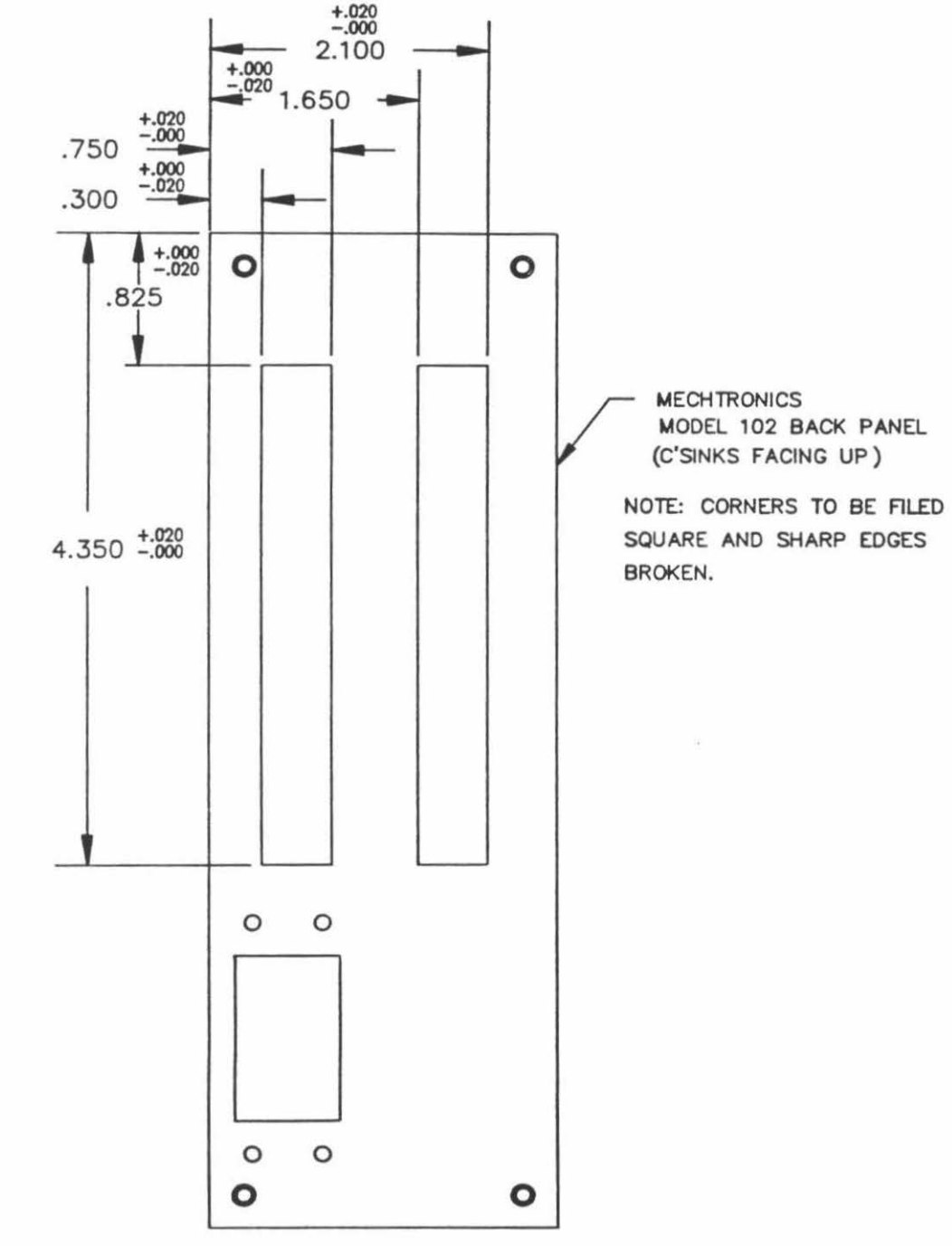

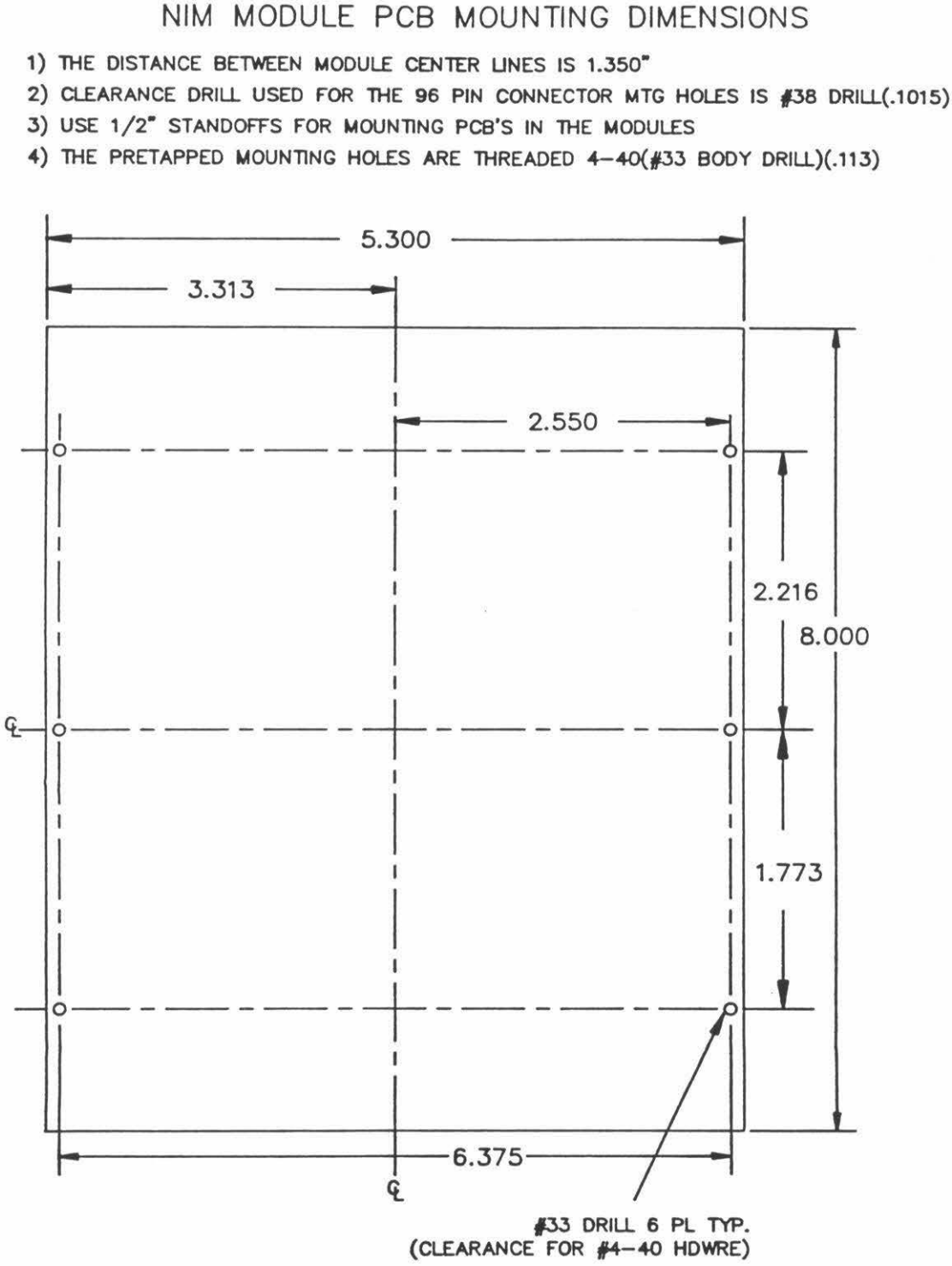

Figure 10. Printed circuit board mounting hole pattern for NIM modules.

V. General Design Comments and Ubiquitous Circuitry

The design of high performance SPM control electronics requires not only that adequate components be selected but also that care be taken in the way they are used. This aspect of design, the detailed manner in which the components are connected, can make the difference between a costly design which does not perform well and an inexpensive design whose performance is state of the art. An attempt to cover any substantial portion of the field of low noise electronic design would be beyond the scope of this discussion, however there are several points which require attention due to their utility in the use and design of modules for SPM control. The examples below are mentioned because it is hoped that they will be useful to others who wish to augment or modify the SPM control electronics to suit their particular experimental needs.

Perhaps the most crucial aspect of the low noise electronic design for SPMs was the grounding of the various circuitry sections. In the SPM control electronics almost fanatical attention was paid to seperating analog and digital grounds and in making sure that return currents from driven loads were confined to particular paths. One example of this can be found on the digital to analog converter (DAC) boards. If one examines the back side of the board some thin coaxial cables run from the shift register outputs to the serial data inputs of the DACs. These are not mistakes in board layout; the coaxial cable was used to provide a seperate return path for the current of the serial data signal. One may also notice a resistor network attached to the same pin at the DAC. It should be obvious that this serves to terminate the serial data line and prevent ringing and undershoot.

In addition to grounding considerations, shielding plays a major role in the SPM circuitry. All of the printed circuit boards were designed as multilayer boards and the additional layers were used not only as signal layers, but also as ground and power planes and to serve as integral shielding. Even so, an extra layer of shielding was required between the DAC board and the high voltage board, to prevent some of the digital clock signals from being picked up by the high voltage circuitry.

Among the various circuits used in the SPM control electronics there are some which fit best into the category of ubiquitous circuits. This group includes circuits which are used in more than one particular type of module. The two types of circuit which fall in this group are the low noise power supplies and the programmable logic for the interface circuitry.

As one might expect, it is difficult to demand superior noise performance from devices powed by noisy power sources. Thus it was found neccessary to build low noise, low impedance output power supplies on each of the printed circuit boards. The schematic for the low noise power supplies may be found on the next page (Figure 11). At the heart of the supply is a low noise, ultra-stable voltage reference from Burr-Brown the REF-10KM. This integrated circuit provides a nominal voltage of +10.000 ± 0.005 volts with less than 1ppm/°C thermal drift. It has a truly impressive output noise specification of 6 μV peak to peak in the frequency range from 0.1 to 10 Hz. In the power supply reference circuit the output of the REF-10KM is low pass filtered at 1.6 Hz and buffered by a low noise operational amplifier, the OP27. This provides a stable 10.00 volt reference voltage for the other portions of the

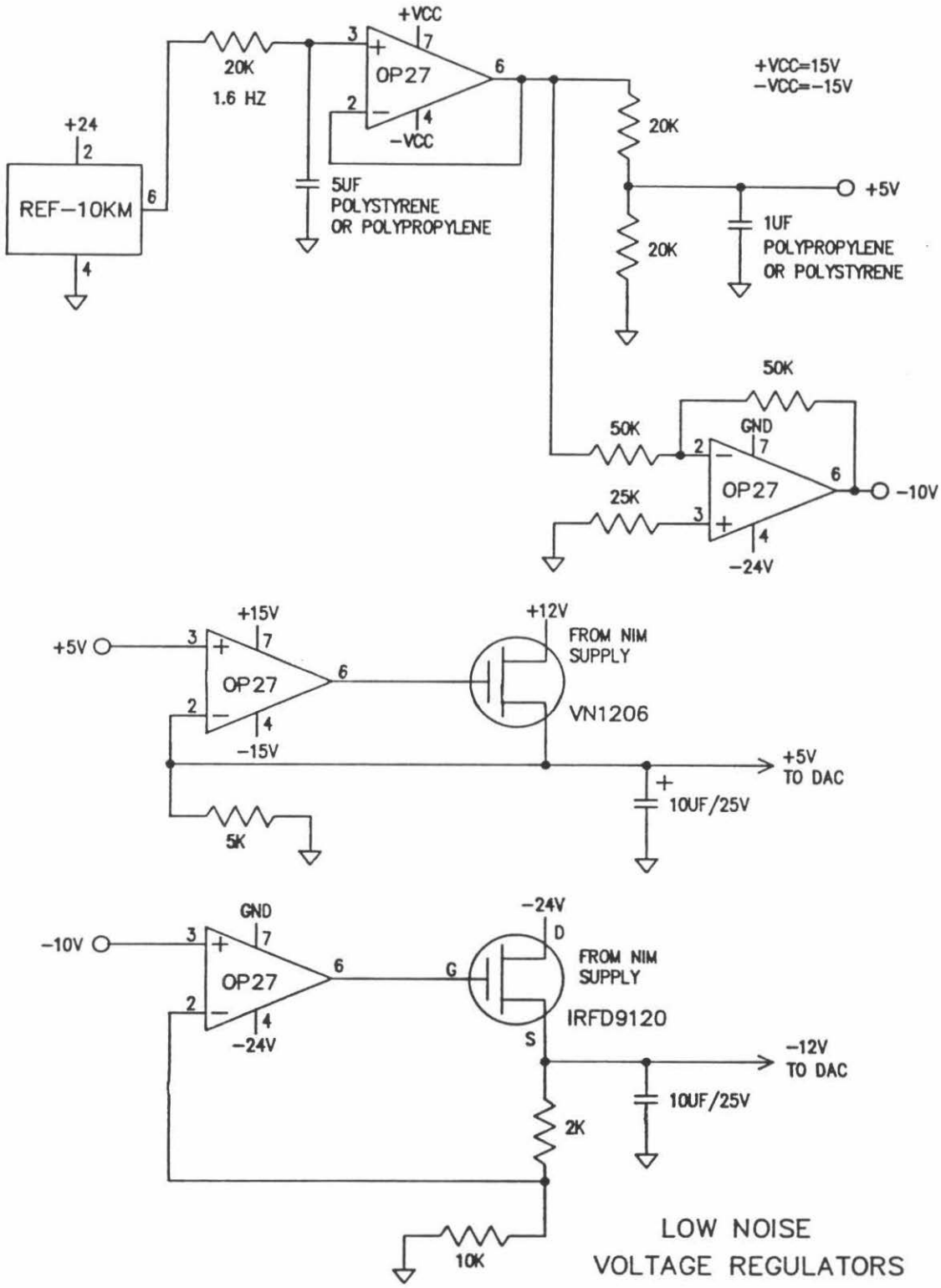

Figure 11. Schematic diagram for low noise voltage regulators.

power supply circuitry. The remainder of the power supply circuitry uses low noise amplifiers as error amplifiers with their output controlling a series pass element (the power FETs). The performance of these voltage regulators is quite good and they have an output impedance of less than 0.001 Ohm from dc to 10 kHz. The high frequency (> 10 kHz) performance could undoubtedly be improved by substituting OPA627 amplifiers for the OP27s which drive the FETs. As the circuit stands, however, its performance is more than adequate for powering the DACs and ADCs of the SPM control electronics.

The second type of circuit which is found in any module that is controlled by the DSP is the interface and address decoding logic circuitry. The interface logic has been included on the drawings for each of the other modules and so only the address decode logic will be discussed here.

The address space for the SPM control electronics is shown in Figure 12 on the next page. The significance of this table is that each device on the NIM bus must have a unique address. The object of the address decode logic is to enable the correct circuitry to respond to read and write operations on the NIM bus. As can be seen from the previous diagram describing these operations, the DSP activates the read/write* and input/output enable* signals and asserts an address on the bus. Then within 60 ns data is passed on the bus. This means that by the time the data state becomes valid the logic in each of the modules on the bus must decode the address and take the appropriate action (e.g., load a buffer with a value from a shift register, etc.). To accomplish this, while maintaining flexibility the address decoders have been implemented in programmable array logic devices.

Figure 12. A map of the SPM control electronics address space.

Address	Device†	Address	Device
00	DAC A LSB	20	CONVERT
01	DAC A MSB	21	ADC A
02	DAC B LSB	22	ADC B
03	DAC B MSB	23	ADC C
04	DAC C LSB	24	ADC D
05	DAC C MSB	25	
06	DAC D LSB	26	
07	DAC D MSB	27	
08	DAC E LSB	28	
09	DAC E MSB	29	
0A	DAC F LSB	2A	
0B	DAC F MSB	2B	
0C		2C	
0D		2D	
0E		2E	
0F		2F	
10		30	
11		31	
12		32	
13		33	
14		34	
15		35	
16		36	
17		37	
18		38	
19		39	
1A		3A	
1B		3B	
1C		3C	
1D		3D	
1E		3E	
1F		3F	

* Addresses are offsets in hexadecimal from the base address 800000 hexadecimal. The first 256 addresses (8 least significant address lines) are decoded by the PALs in the modules.
† Devices or signals.

Programmable array logic (PALs) devices are integrated circuits which can be configured by the user to perform any of a number of logic functions. The PALs are programmed by the sequential applicaton of sets of voltages on the pins of the device. This is most convieniently done using a PAL programmer, a special piece of equipment designed just for this purpose. When using this machine the designer's task becomes one of adequately defining the desired functionality and properly testing the resulting configured device.

To describe the desired device characteristics several "silicon compilers" have been written and come into usage. Some examples of these are PALASM (PAL Assembler), CUPL and ABEL. The output of all of these programs is a file type readable by the programming equipment called a JEDEC file. If everything has gone properly the JEDEC file will contain all the information needed to configure ("blow") the PAL and to test it. When we initially started this work we were using the CUPL language, but as the project matured we began using the ABEL language.

As examples of how address decoders are implemented with ABEL, the next four pages contain listings of the ABEL files we used to blow the address decoders in the present SPM control electronics. We have not taken the space to list all the accessory files and ABEL output generated during an address decoder programming session.

```
module DAC_ADDR_DECODE_1
title 'AFM DAC ADDRESS DECODER by      S. Clark and C. Spence'
Declarations          DAC_DECODER device  'P22V10';

" Inputs
        A7,A6,A5,A4,A3,A2,A1,A0          pin 1,2,3,4,5,6,7,8;
        IOE                              pin 9;
        VCC                              pin 24;
        GND                              pin 12;

" Outputs
        LOAD_A_LSBS                      pin 16;
        LOAD_DAC_A                       pin 18;
        LOAD_B_LSBS                      pin 20;
        LOAD_DAC_B                       pin 22;

        H,L,X  = 1,0,.X.;
        ADDRESS = [A7,A6,A5,A4,A3,A2,A1,A0];

equations

        !LOAD_A_LSBS  = !IOE & (ADDRESS == ^h00);
        !LOAD_DAC_A   = !IOE & (ADDRESS == ^h01);
        !LOAD_B_LSBS  = !IOE & (ADDRESS == ^h02);
        !LOAD_DAC_B   = !IOE & (ADDRESS == ^h03);

test_vectors

([ADDRESS ->
  LOAD_A_LSBS,LOAD_DAC_A,LOAD_B_LSBS,LOAD_DAC_B])

^h00    -> [L,H,H,H];      ^h01    -> [H,L,H,H];      ^h02    -> [H,H,L,H];
^h03    -> [H,H,H,L];      ^h04    -> [H,H,H,H];      ^h05    -> [H,H,H,H];
^h06    -> [H,H,H,H];      ^h07    -> [H,H,H,H];      ^h08    -> [H,H,H,H];
^h09    -> [H,H,H,H];      ^h0A    -> [H,H,H,H];      ^h0B    -> [H,H,H,H];
^h0C    -> [H,H,H,H];      ^h0D    -> [H,H,H,H];      ^h0E    -> [H,H,H,H];
^h0F    -> [H,H,H,H];      ^h10    -> [H,H,H,H];      ^h11    -> [H,H,H,H];
^h12    -> [H,H,H,H];      ^h13    -> [H,H,H,H];      ^h14    -> [H,H,H,H];
^h15    -> [H,H,H,H];      ^h16    -> [H,H,H,H];      ^h17    -> [H,H,H,H];
^h18    -> [H,H,H,H];      ^h19    -> [H,H,H,H];      ^h1A    -> [H,H,H,H];
^h1B    -> [H,H,H,H];      ^h1C    -> [H,H,H,H];      ^h1D    -> [H,H,H,H];
^h1E    -> [H,H,H,H];      ^h1F    -> [H,H,H,H];      ^h20    -> [H,H,H,H];
^h21    -> [H,H,H,H];      ^h22    -> [H,H,H,H];      ^h23    -> [H,H,H,H];
^h24    -> [H,H,H,H];

end DAC_ADDR_DECODE_1
```

```
module DAC_ADDR_DECODE_2
title 'AFM DAC ADDRESS DECODER TWO  by      S. Clark and C. Spence'
Declarations          DAC_DEC2 device  'P22V10';

"Inputs
        A7,A6,A5,A4,A3,A2,A1,A0          pin 1,2,3,4,5,6,7,8;
        IOE                              pin 9;
        VCC                              pin 24;
        GND                              pin 12;

"Outputs
        LOAD_A_LSBS                      pin 16;
        LOAD_DAC_A                       pin 18;
        LOAD_B_LSBS                      pin 20;
        LOAD_DAC_B                       pin 22;

        H,L,X  = 1,0,.X.;
        ADDRESS = [A7,A6,A5,A4,A3,A2,A1,A0];

equations

        !LOAD_A_LSBS  = !IOE & (ADDRESS == ^h04);
        !LOAD_DAC_A   = !IOE & (ADDRESS == ^h05);
        !LOAD_B_LSBS  = !IOE & (ADDRESS == ^h06);
        !LOAD_DAC_B   = !IOE & (ADDRESS == ^h07);

test_vectors

(ADDRESS ->
 LOAD_A_LSBS,LOAD_DAC_A,LOAD_B_LSBS,LOAD_DAC_B])

^h00    -> [H,H,H,H];      ^h01    -> [H,H,H,H];      ^h02    -> [H,H,H,H];
^h03    -> [H,H,H,H];      ^h04    -> [L,H,H,H];      ^h05    -> [H,L,H,H];
^h06    -> [H,H,L,H];      ^h07    -> [H,H,H,L];      ^h08    -> [H,H,H,H];
^h09    -> [H,H,H,H];      ^h0A    -> [H,H,H,H];      ^h0B    -> [H,H,H,H];
^h0C    -> [H,H,H,H];      ^h0D    -> [H,H,H,H];      ^h0E    -> [H,H,H,H];
^h0F    -> [H,H,H,H];      ^h10    -> [H,H,H,H];      ^h11    -> [H,H,H,H];
^h12    -> [H,H,H,H];      ^h13    -> [H,H,H,H];      ^h14    -> [H,H,H,H];
^h15    -> [H,H,H,H];      ^h16    -> [H,H,H,H];      ^h17    -> [H,H,H,H];
^h18    -> [H,H,H,H];      ^h19    -> [H,H,H,H];      ^h1A    -> [H,H,H,H];
^h1B    -> [H,H,H,H];      ^h1C    -> [H,H,H,H];      ^h1D    -> [H,H,H,H];
^h1E    -> [H,H,H,H];      ^h1F    -> [H,H,H,H];      ^h20    -> [H,H,H,H];
^h21    -> [H,H,H,H];      ^h22    -> [H,H,H,H];      ^h23    -> [H,H,H,H];
^h24    -> [H,H,H,H];

end DAC_ADDR_DECODE_2
```

```
module DAC_ADDR_DECODE_3
title 'AFM DAC ADDRESS DECODER THREE  by   S. Clark and C. Spence'
Declarations          DAC_DEC3 device  'P22V10';

"Inputs
        A7,A6,A5,A4,A3,A2,A1,A0          pin 2,1,4,3,6,5,8,7;
        IOE                              pin 9;
        VCC                              pin 24;
        GND                              pin 12;

"Outputs
        LOAD_A_LSBS                      pin 16;
        LOAD_DAC_A                       pin 18;
        LOAD_B_LSBS                      pin 20;
        LOAD_DAC_B                       pin 22;

        H,L,X  = 1,0,.X.;
        ADDRESS = [A7,A6,A5,A4,A3,A2,A1,A0];

equations

        !LOAD_A_LSBS  = !IOE & (ADDRESS == ^h08);
        !LOAD_DAC_A   = !IOE & (ADDRESS == ^h09);
        !LOAD_B_LSBS  = !IOE & (ADDRESS == ^h0A);
        !LOAD_DAC_B   = !IOE & (ADDRESS == ^h0B);

test_vectors

(ADDRESS ->
 [LOAD_A_LSBS,LOAD_DAC_A,LOAD_B_LSBS,LOAD_DAC_B])

^h00   -> [H,H,H,H];      ^h01   -> [H,H,H,H];      ^h02   -> [H,H,H,H];
^h03   -> [H,H,H,H];      ^h04   -> [H,H,H,H];      ^h05   -> [H,H,H,H];
^h06   -> [H,H,H,H];      ^h07   -> [H,H,H,H];      ^h08   -> [L,H,H,H];
^h09   -> [H,L,H,H];      ^h0A   -> [H,H,L,H];      ^h0B   -> [H,H,H,L];
^h0C   -> [H,H,H,H];      ^h0D   -> [H,H,H,H];      ^h0E   -> [H,H,H,H];
^h0F   -> [H,H,H,H];      ^h10   -> [H,H,H,H];      ^h11   -> [H,H,H,H];
^h12   -> [H,H,H,H];      ^h13   -> [H,H,H,H];      ^h14   -> [H,H,H,H];
^h15   -> [H,H,H,H];      ^h16   -> [H,H,H,H];      ^h17   -> [H,H,H,H];
^h18   -> [H,H,H,H];      ^h19   -> [H,H,H,H];      ^h1A   -> [H,H,H,H];
^h1B   -> [H,H,H,H];      ^h1C   -> [H,H,H,H];      ^h1D   -> [H,H,H,H];
^h1E   -> [H,H,H,H];      ^h1F   -> [H,H,H,H];      ^h20   -> [H,H,H,H];
^h21   -> [H,H,H,H];      ^h22   -> [H,H,H,H];      ^h23   -> [H,H,H,H];
^h24   -> [H,H,H,H];

end DAC_ADDR_DECODE_3
```

```
module ADC_ADDR_DECODE
title 'AFM PCM78 ADDRESS DECODER by  S. Clark and C. Spence'
Declarations
        ADC_DECODER device  'P22V10';

"Inputs
        A7,A6,A5,A4,A3,A2,A1,A0          pin 1,2,3,4,5,6,7,8;
        IOE                              pin 9;
        VCC                              pin 24;
        GND                              pin 12;

"Outputs
        CONVERT                          pin 16;
        READ_A                           pin 17;
        READ_B                           pin 19;
        READ_C                           pin 21;
        READ_D                           pin 23;
        OE                               pin 15;

        H,L,X  = 1,0,.X.;
        ADDRESS = [A7,A6,A5,A4,A3,A2,A1,A0];

equations
        CONVERT   = !IOE & (ADDRESS == ^h20);
       !READ_A    = !IOE & (ADDRESS == ^h21);
        !READ_B   = !IOE & (ADDRESS == ^h22);
        !READ_C   = !IOE & (ADDRESS == ^h23);
        !READ_D   = !IOE & (ADDRESS == ^h24);
       !OE      = !IOE & ((ADDRESS <= ^h24) & (ADDRESS => ^h21));
test_vectors
(ADDRESS -> [CONVERT,READ_A,READ_B,READ_C,READ_D,OE])

^h20 -> [H,H,H,H,H,H];   ^h21 -> [L,L,H,H,H,L];    ^h22 ->[L,H,L,H,H,L];
^h23 -> [L,H,H,L,H,L];   ^h24 -> [L,H,H,H,L,L];    ^h00 -> [L,H,H,H,H,H];
^h01 -> [L,H,H,H,H,H];   ^h02 -> [L,H,H,H,H,H];    ^h03 -> [L,H,H,H,H,H];
^h04 -> [L,H,H,H,H,H];   ^h05 -> [L,H,H,H,H,H];    ^h06 -> [L,H,H,H,H,H];
^h07 -> [L,H,H,H,H,H];   ^h08 -> [L,H,H,H,H,H];    ^h09 -> [L,H,H,H,H,H];
^h0A -> [L,H,H,H,H,H];   ^h0B -> [L,H,H,H,H,H];   ^h0C -> [L,H,H,H,H,H];
^h0D -> [L,H,H,H,H,H];   ^h0E -> [L,H,H,H,H,H];    ^h0F -> [L,H,H,H,H,H];
^h10 -> [L,H,H,H,H,H];   ^h11 -> [L,H,H,H,H,H];    ^h12 -> [L,H,H,H,H,H];
^h13 -> [L,H,H,H,H,H];   ^h14 -> [L,H,H,H,H,H];    ^h15 -> [L,H,H,H,H,H];
^h16 -> [L,H,H,H,H,H];   ^h17 -> [L,H,H,H,H,H];    ^h18 -> [L,H,H,H,H,H];
^h19 -> [L,H,H,H,H,H];   ^h1A -> [L,H,H,H,H,H];   ^h1B -> [L,H,H,H,H,H];
^h1C -> [L,H,H,H,H,H];   ^h1D -> [L,H,H,H,H,H];    ^h1E -> [L,H,H,H,H,H];
^h1F -> [L,H,H,H,H,H];
end ADC_ADDR_DECODE
```

IV. The Key Modules

In the SPM control electronics there are three key modules: i) the digital to analog converter (DAC) module; ii) the high voltage amplifier module and iii) the analog to digital converter (ADC) module. The function of the DAC and ADC modules is evident; the function of the high voltage amplifier module is to take input from the DACs and amplify the voltage to provide adequate voltages to drive the piezoceramic transducer elements. Although the high voltage modules are conceptually distinct from the DACs and warrant a separate discussion, they are physically located in the same NIM unit as the DACs because of their dependence on low noise signals from the DACs.

A. The Digital to Analog Converter Module

The DAC module schematic is shown on the following two pages. On the first page the interface circuitry and control logic is shown. The second page contains the shift registers and the DACs themselves. The circuit operates by accepting up to twenty four bit digital words from the NIM bus. Because the NIM data bus is only sixteen bits wide the transfer of more than sixteen bit words requires two write operations. The circuit is designed so that the least significant word must be written first followed by the most significant word. This was done so that a single sixteen bit transfer can be accomplished without requiring the insertion of wait states. Once the shift registers (the 74LS165s) have been loaded with data the control logic shifts the data into the serial input of the DACs.

Figure 13. Schematics for the DAC board.

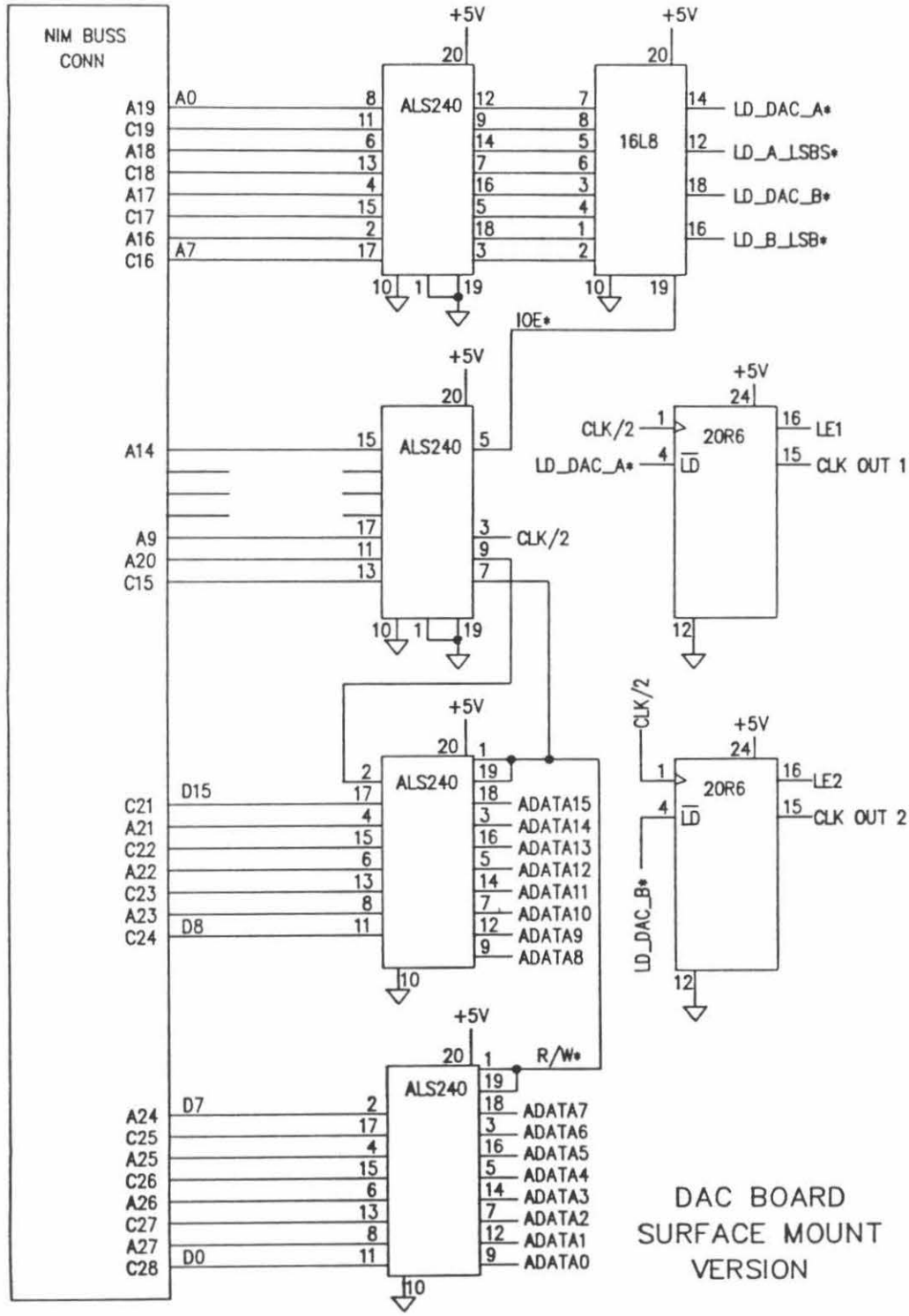

NOTES: 1. DECOUPLING ON ALL DIGITAL IC'S– 2.2UF ELECTROLYTIC AND .1UF CERAMIC – NOT SHOWN
2. ANALOG SECTION AND ITS POWER SUPPLIES SHOWN ONLY CONCEPTUALLY – SEE SHEET 2
3. TERMINATION NETWORKS ON PCM58 INPUTS NOT SHOWN

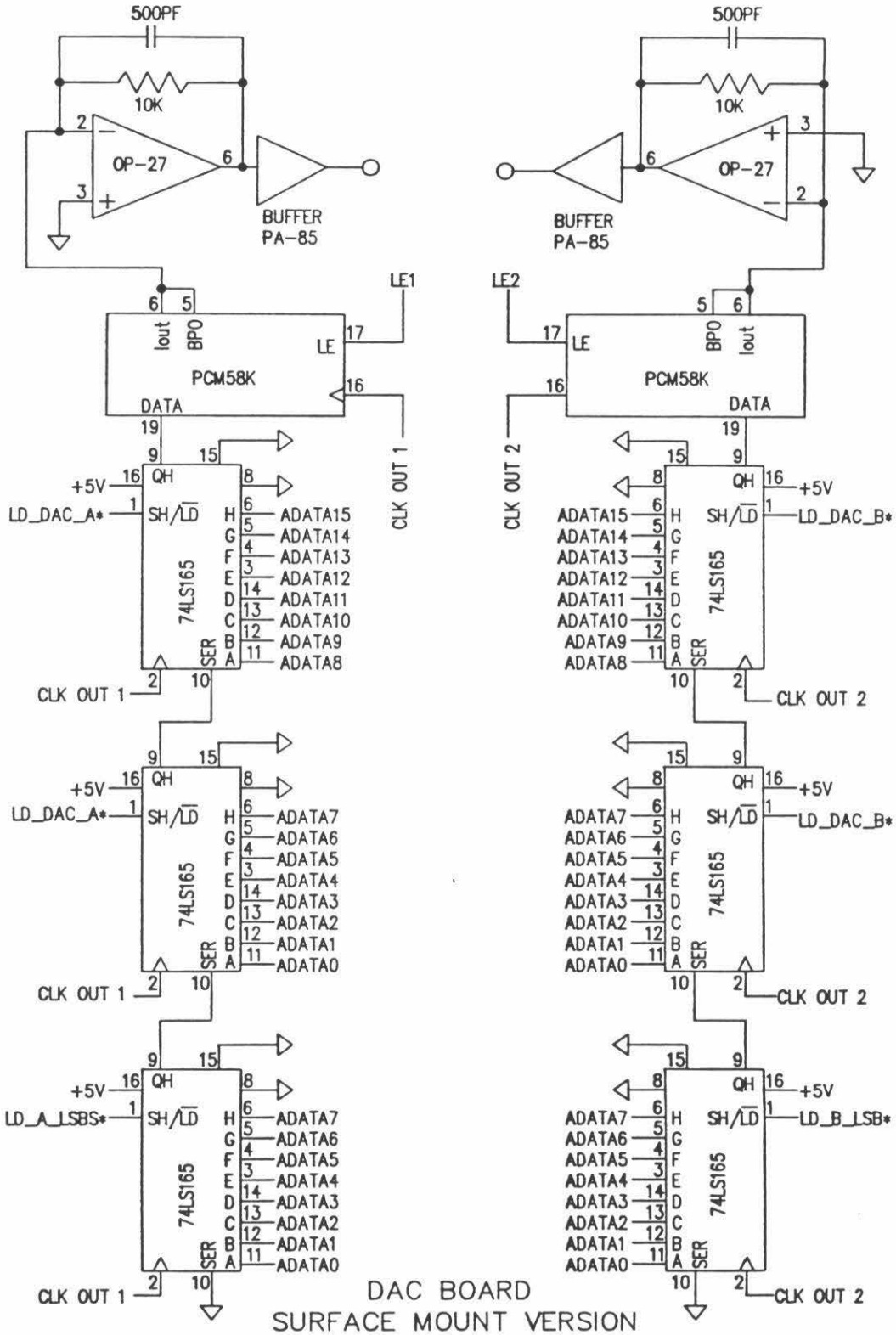

DAC BOARD
SURFACE MOUNT VERSION

The control logic functions to coordinate the passage of data from the shift registers into the DACs. Because the PCM58K is an eighteen bit serial input DAC, the control logic gates the system clock allowing eighteen clock pulses to pass to the shift registers after the most significant word has been written. The CUPL file for the control PALs (20R6s) is given on the next two pages. These files were written using a state machine description of the desired PAL configuration. The other PAL (16L8), which serves as an address decoder, was described previously in the section on address decoders.

The performance of this circutry in conjunction with the high voltage amplifiers was already covered in Chapter I.

B. The High Voltage Amplifier Module

As mentioned previously, the function of the high voltage ampifier module is to amplify the DAC output voltage to a level suitable to drive the piezoceramic transducers. For this purpose, the PA85 hybrid power operational amplifier is ideally suited. The PA85 has a 450 volt biploar power supply range and is capable of supplying in excess of 200 mA of current to the piezo elements. Another attractive feature of the PA85 for SPM drive applications is its low noise; it is rated as having a typical voltage noise, referred to the input, of 1 μV rms in a 100 kHz bandwidth.

In the piezoceramic drive circuit, the PA85 is operated at a nominal gain of 18.75; thus the total output voltage range is 375 volts. While the PA85 can accommodate higher voltages, the output range was chosen so that the

```
/*   PAL LOGIC DESCRIPTION FILE PAL2.PLD: 18 BIT COUNTER */
Name PAL2;
Partno     XX;
Date       12/11/90;
Revision   1.0;
Designer   S. Clark/D. Baselt;
Company    XX;
Assembly   DAC Board;
Location   U4 and U5;

/*************************************************************/
/*   This PAL functions as the control logic for the         */
/*   shift registers and the PCM58P-K current output DAC.    */
/*   Because the PCM58 is an 18 bit serial input DAC the     */
/*   control logic needs to generate the clock pulses for    */
/*   the shift registers as well as an inverted clock and    */
/*   the LE signal for the DAC.                              */
/*************************************************************/
/*   Allowable Target Device Types:     20R6, 22V10          */
/*************************************************************/

/*   Inputs     */

Pin  1     =     CLK;
Pin  2     =     CLK_IN;
Pin  4     =     !LOAD;

/*   Outputs    */

Pin  15    =     CLK_OUT;          /* GATED CLOCK */
Pin  16    =     Q4;               /* DOUBLES AS LATCH ENABLE */
Pin  17    =     Q3;
Pin  18    =     Q2;
Pin  19    =     Q1;
Pin  20    =     Q0;
Pin  21    =     CLK_ENABLE;
Pin  22    =     INV_CLK_OUT;      /* INVERTED GATED CLOCK */

/*   Declarations and Intermediate Variable Definitions */

FIELD count     =     [Q4..Q0]; /* DECLARE COUNTER BIT FIELD*/
```

```
/*   Logic Equations      */

CLK_OUT         =     CLK_IN & !CLK_ENABLE;
INV_CLK_OUT     =     !CLK_IN & !CLK_ENABLE;

SEQUENCE  count       {

PRESENT    00     IF LOAD NEXT 01;
                  DEFAULT NEXT 00;
                  OUT CLK_ENABLE.D;
PRESENT    01     IF !LOAD NEXT 02;
                  DEFAULT NEXT 01;
                  OUT CLK_ENABLE.D;
PRESENT    02     NEXT 03;
PRESENT    03     NEXT 04;
PRESENT    04     NEXT 05;
PRESENT    05     NEXT 06;
PRESENT    06     NEXT 07;
PRESENT    07     NEXT 08;
PRESENT    08     NEXT 09;
PRESENT    09     NEXT 0A;
PRESENT    0A     NEXT 0B;
PRESENT    0B     NEXT 0C;
PRESENT    0C     NEXT 0D;
PRESENT    0D     NEXT 0E;
PRESENT    0E     NEXT 0F;
PRESENT    0F     NEXT 10;
PRESENT    10     NEXT 11;
PRESENT    11     NEXT 12;
PRESENT    12     NEXT 13;
PRESENT    13     NEXT 14;
PRESENT    14     NEXT 15;
                  OUT CLK_ENABLE.D;
PRESENT    15     NEXT 00;
                  OUT CLK_ENABLE.D;
PRESENT    16     NEXT 00;              /* UNUSED STATES */
PRESENT    17     NEXT 00;
PRESENT    18     NEXT 00;
PRESENT    19     NEXT 00;
PRESENT    1A     NEXT 00;
PRESENT    1B     NEXT 00;
PRESENT    1C     NEXT 00;
PRESENT    1D     NEXT 00;
PRESENT    1E     NEXT 00;
PRESENT    1F     NEXT 00;
}
```

Figure 14. Schematic diagrams for the high voltage piezoceramic driver and approach motor driver circuitry.

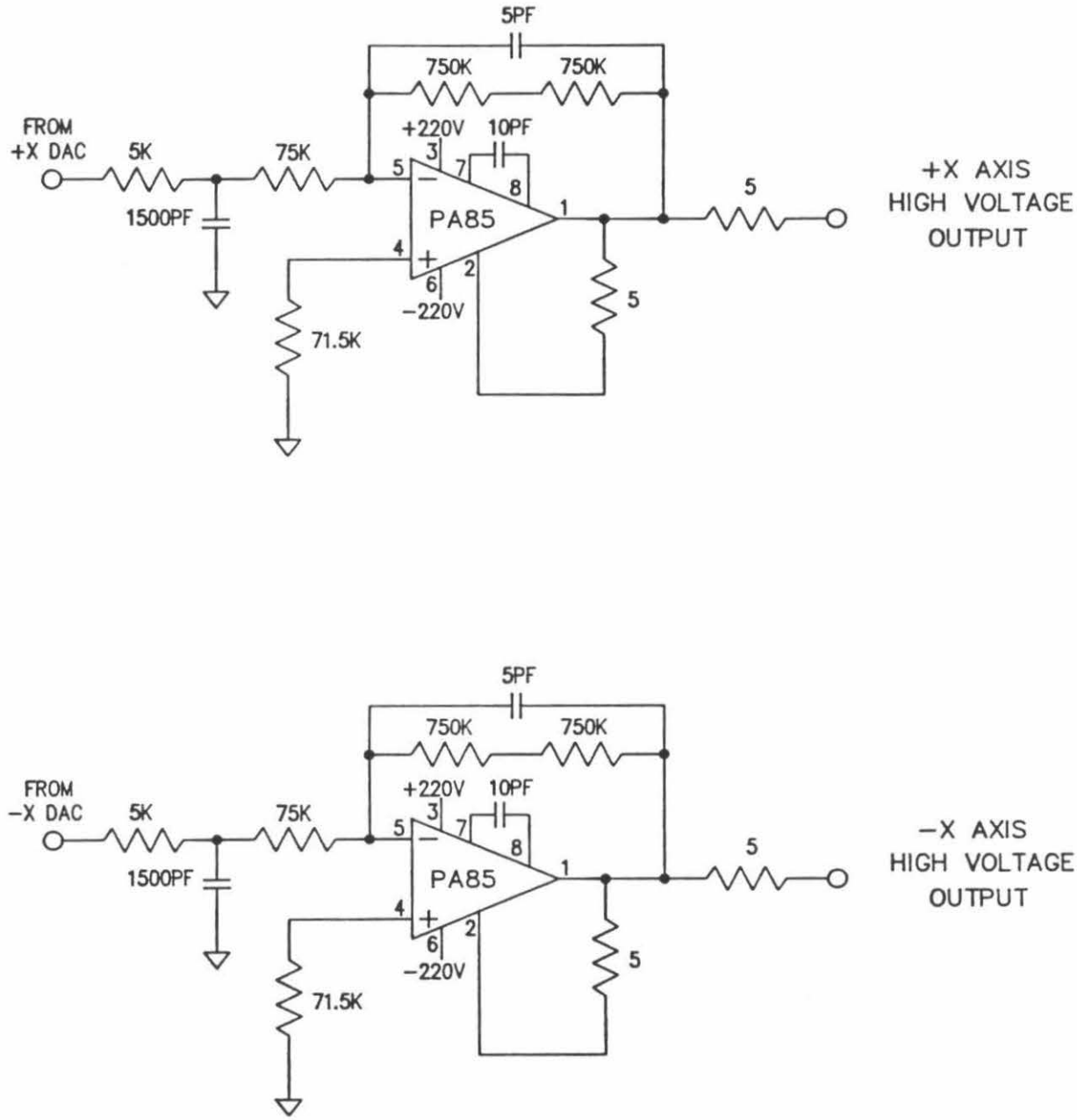

+X/-X AXIS DRIVE BOARD

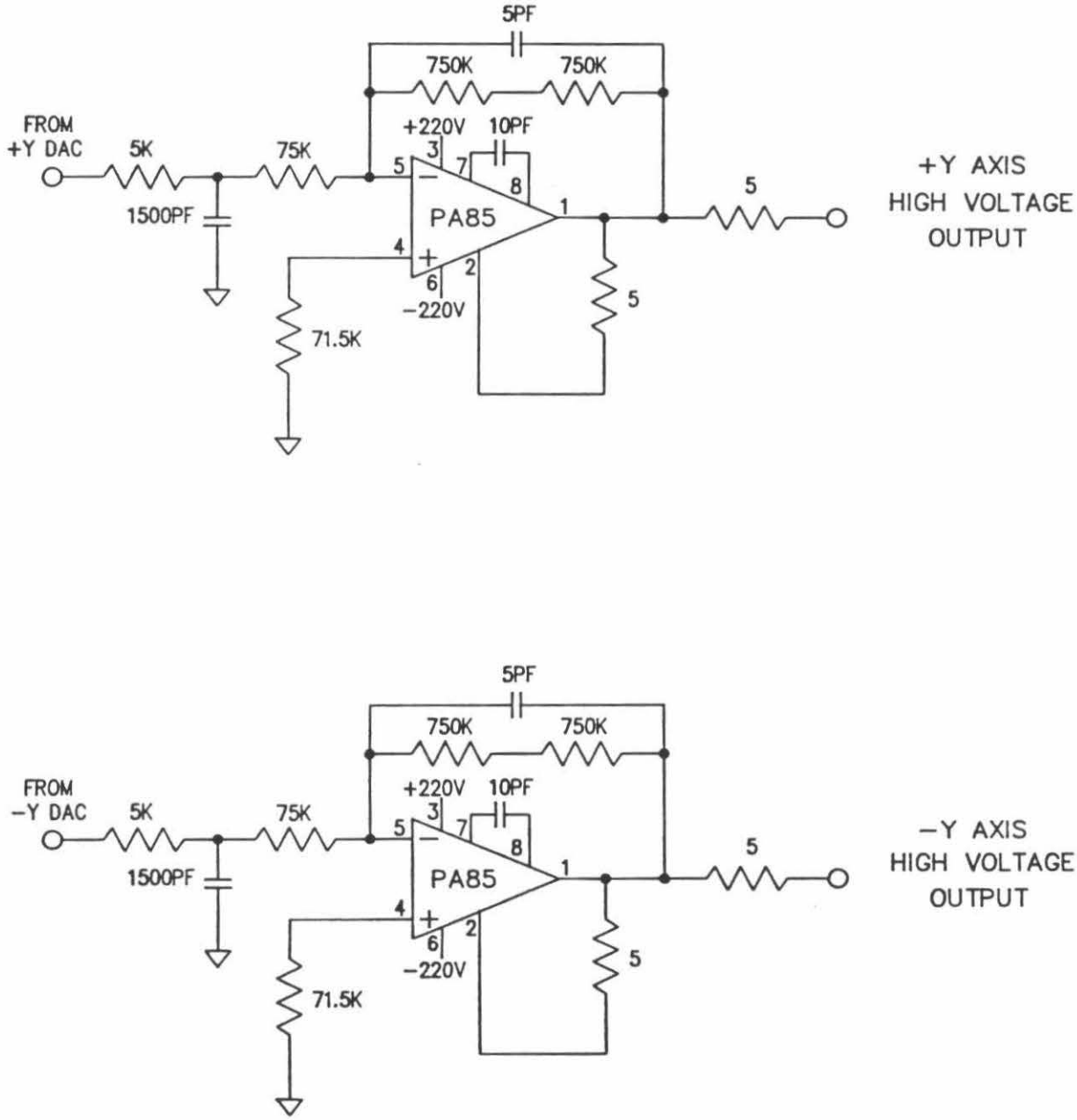

+Y/−Y AXIS DRIVE BOARD

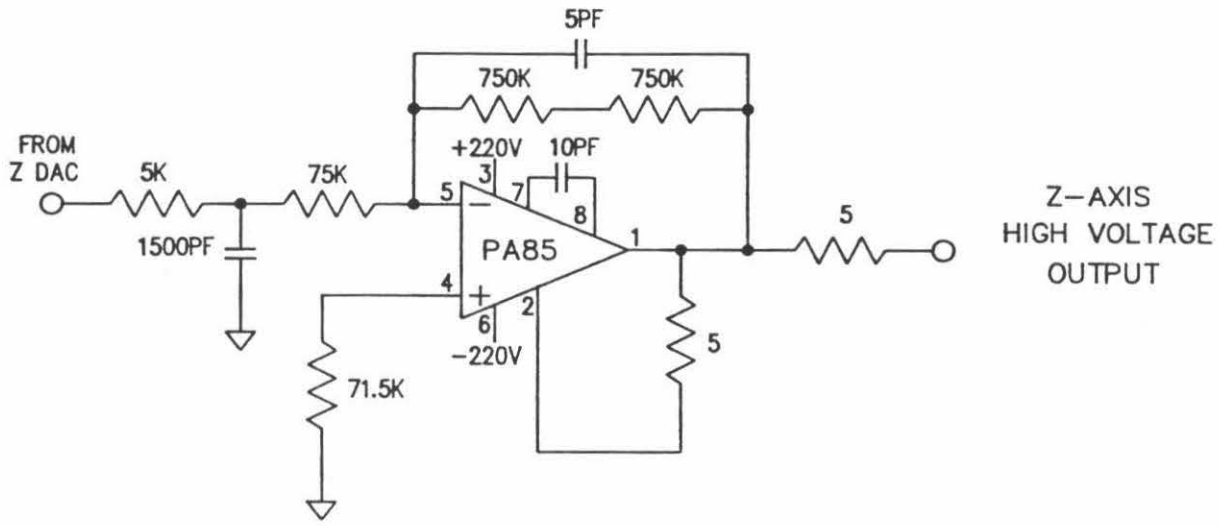

NOTE: ALL RESISTORS ARE 1/4W, 1%.
ALL RESISTOR VALUES ARE IN OHMS.

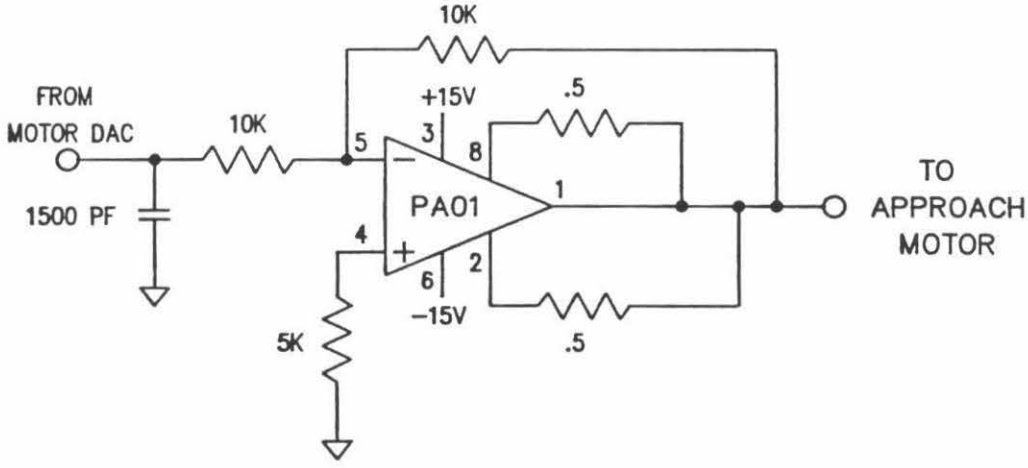

Z-AXIS/APPROACH MOTOR DRIVE BOARD

voltages applied to the tube piezo would not be likely to exceed the voltage gradient rating of the piezo material.

The designer has the option of driving each of the five piezo electrodes independently or driving them in a hardware coordinated fashion. At the time this circuitry was designed the flexibility available with the independent drive scheme seemed quite attractive. This led to a design in which two DAC and high voltage modules are housed together in a double wide NIM unit. The unit has two outputs, one for each of the opposing electrodes of the piezo tube. This scheme leaves one electrode, namely Z, as the odd one out. By combining the Z high voltage stage with a lower voltage power amplifier to drive the approach motor we were able to utilize the last dual DAC / high voltage module as a Z axis / approach motor drive module. The schematic for this module is shown in the third schematic of this section.

C. The Analog to Digital Converter Module

The last key module is one which provides the means for the DSP to recieve data from the external world. Because the DSP can process only digital data and the signals generated by the SPM stage are analog the needed device is an analog to digital converter (ADC). Many of the considerations involved in the selection and evaluation of ADCs were discussed in Chapter 1, so they need not be repeated here. For use with a quadrant photodetector, a quad ADC module was designed. This module takes four signal inputs and samples and converts them in parallel. The inputs range of the ADCs is ± 10 volts and the ADCs can maintain the full sixteen bit conversion at sampling rates in excess of 125 kHz. Figure 15 shows the schematics for the ADC

Figure 15. Schematics for the ADC module.

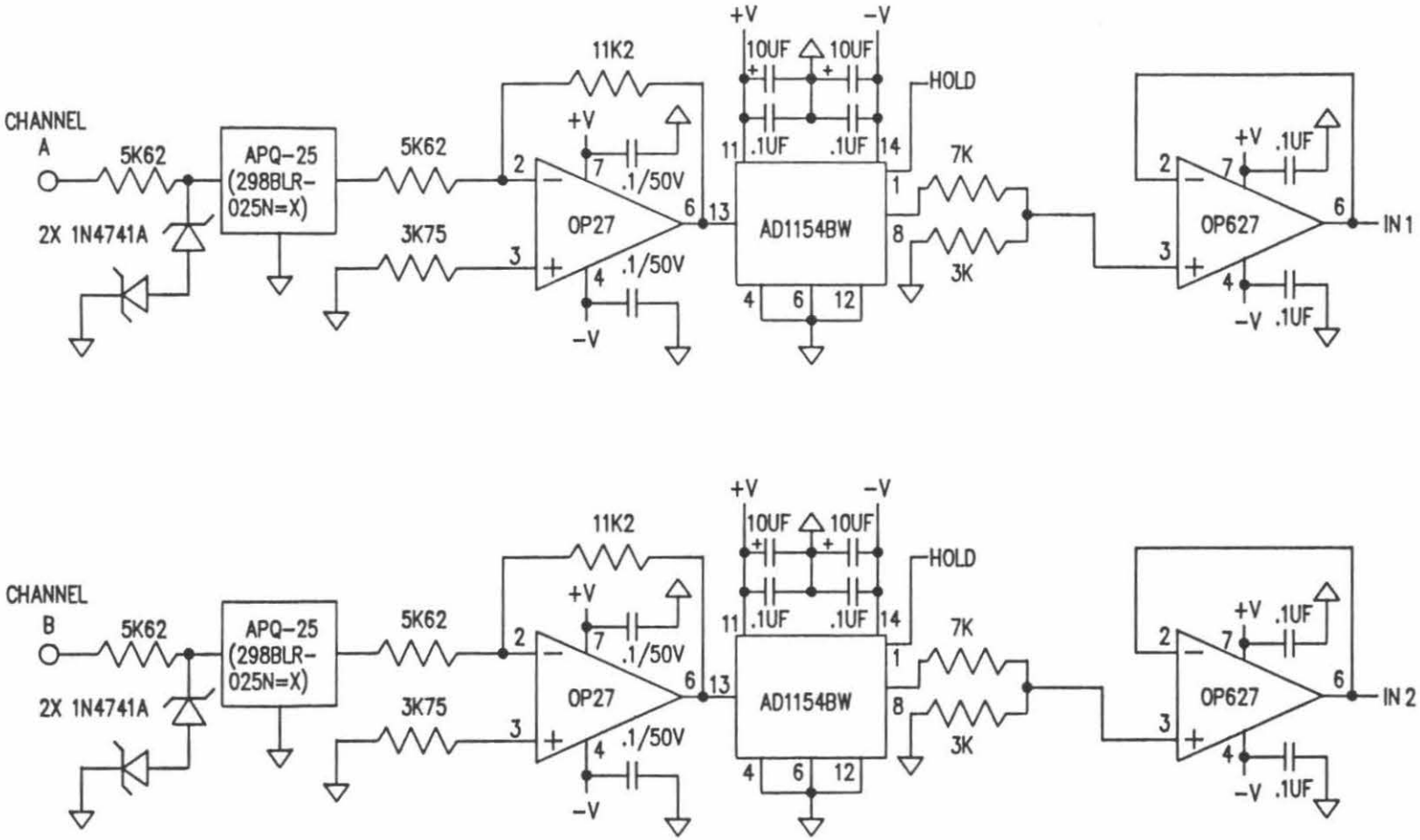

A/D CONVERTER BOARD

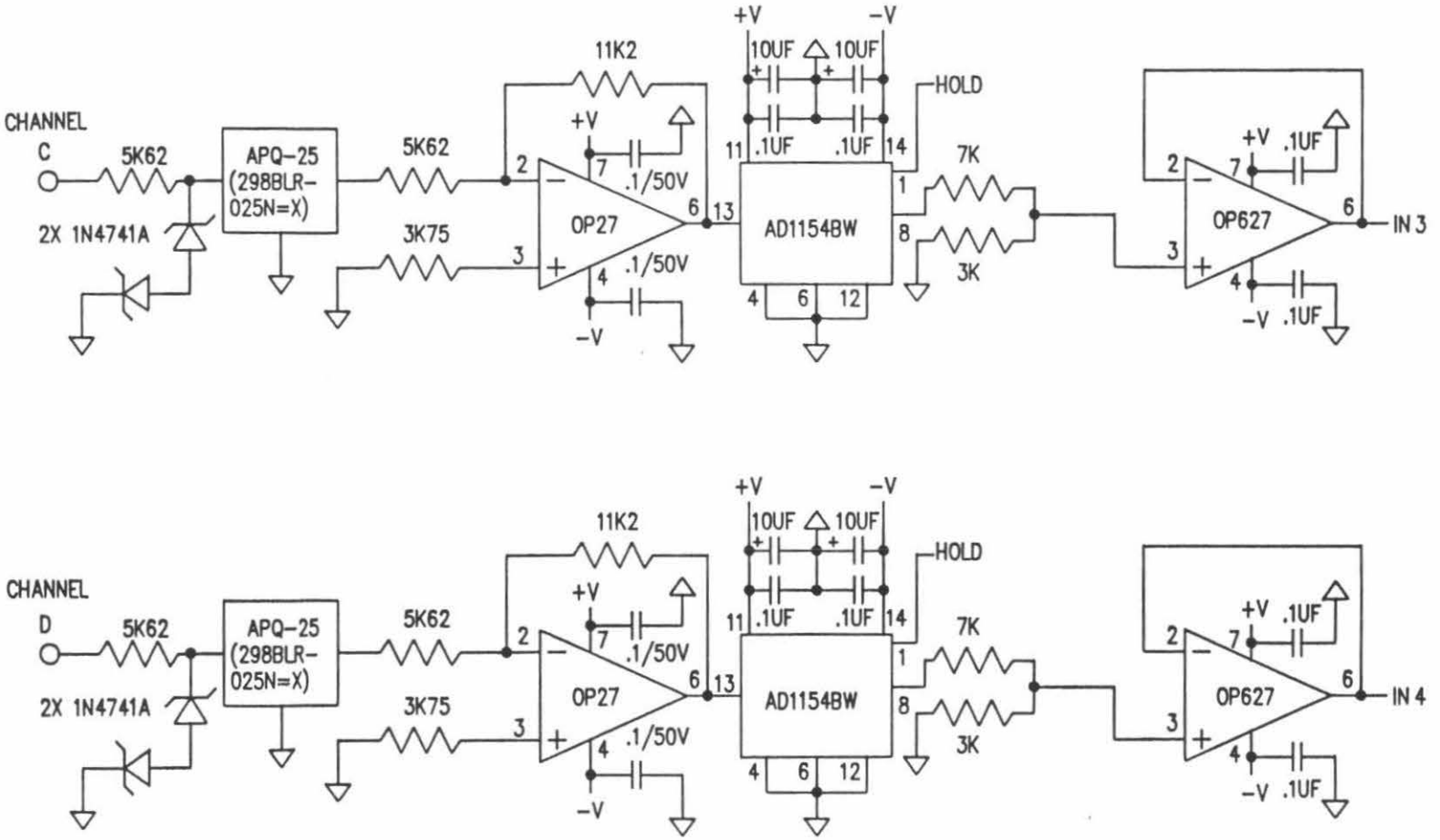

A/D CONVERTER BOARD

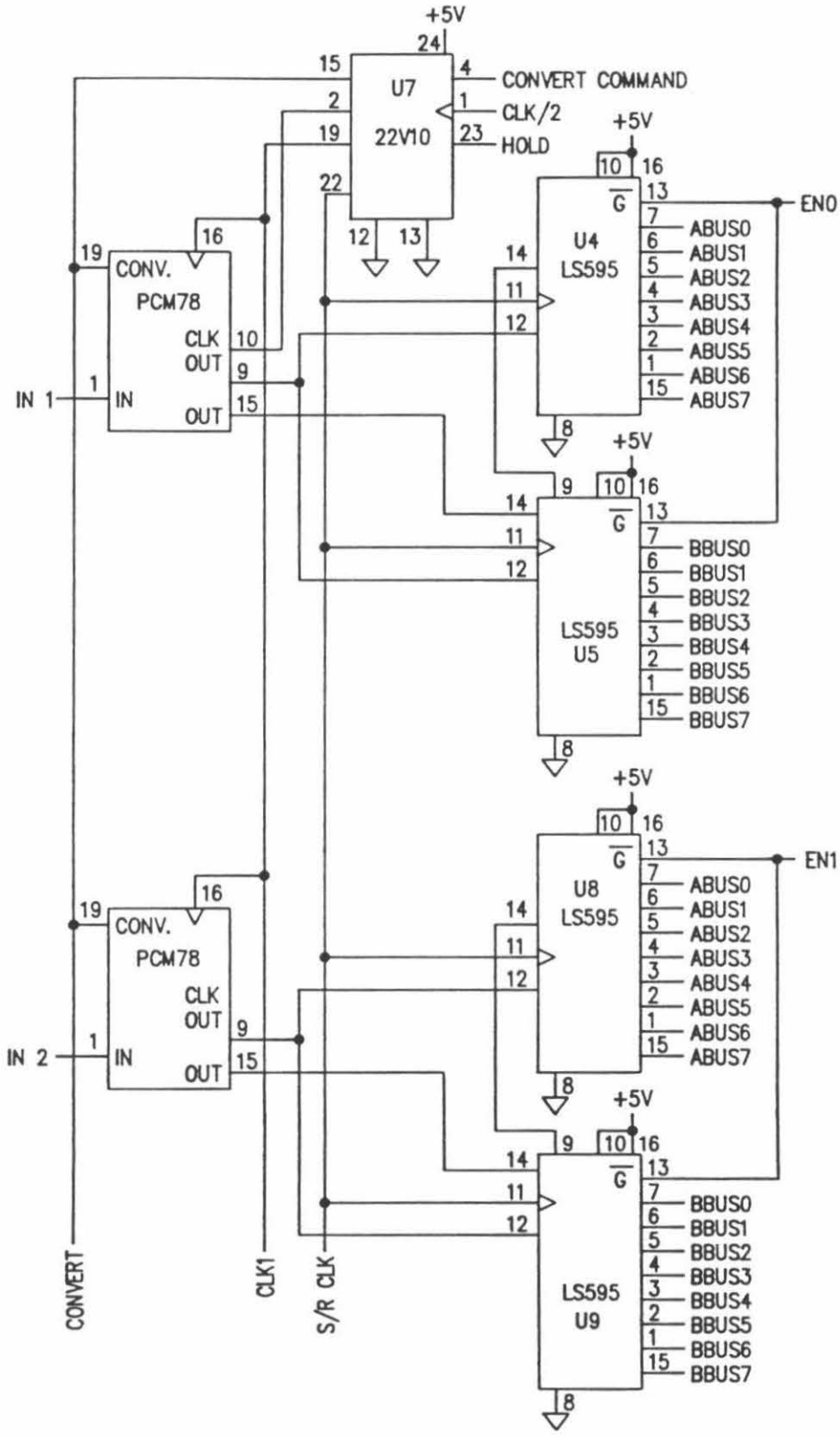

A/D CONVERTER BOARD

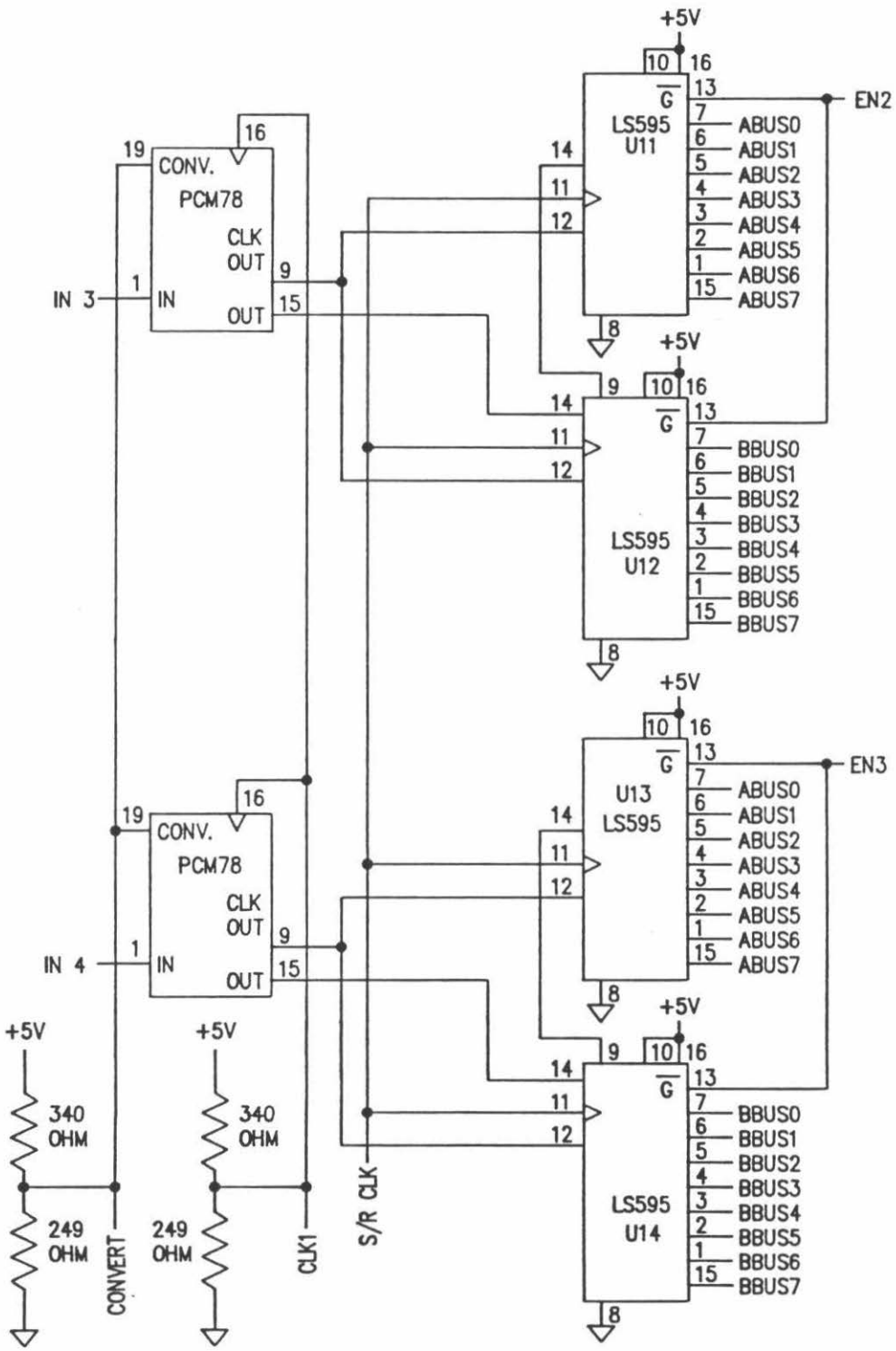
A/D CONVERTER BOARD
+5V
CONV.
PCM78
CLK OUT
IN
OUT
IN 3
IN 4
LS595
U11
U12
U13
U14
G
ABUS0
ABUS1
ABUS2
ABUS3
ABUS4
ABUS5
ABUS6
ABUS7
BBUS0
BBUS1
BBUS2
BBUS3
BBUS4
BBUS5
BBUS6
BBUS7
EN2
EN3
340 OHM
249 OHM
CONVERT
CLK1
S/R CLK

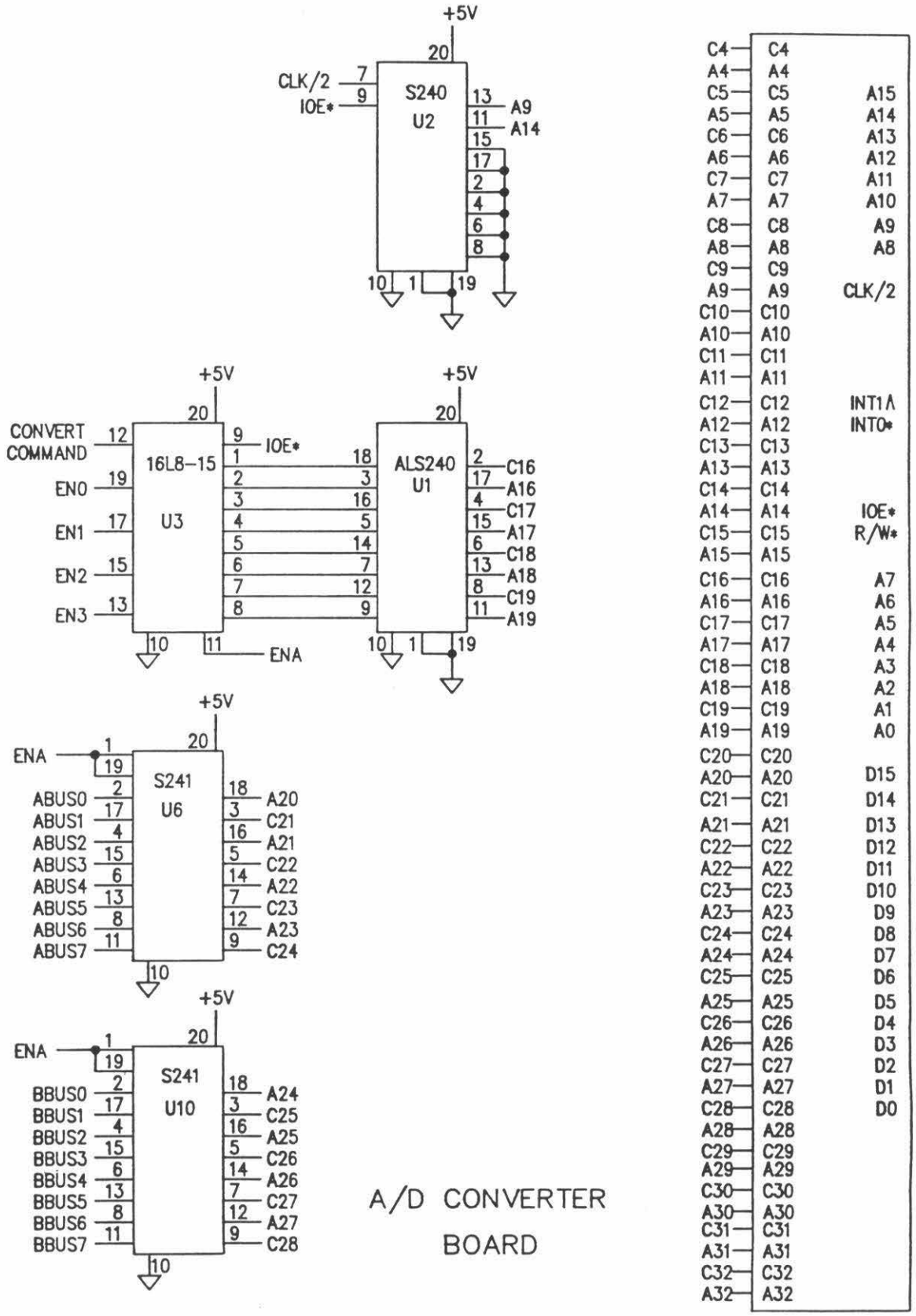

A/D CONVERTER BOARD

module. The first two pages show the four analog channels of the ADC module while the following three pages show the control and interface logic for this module.

The analog portion is simply comprised of circuitry which provides input overvoltage protection, scales the input and provides for anti-alias filtering. It should be noted that because the anti-aliasing filter is a seven pole low pass with a cutoff of 33 kHz signals above 20 kHz may be subject to substantial phase shifts in addition to the standard ≈ 25 μs group delay. The low noise power supplies were used in this section to provide power for the signal conditioning amplifiers as well as the sample and hold amplifier.

The control and interface logic for the ADC module is shown on the next three pages. The PCM78PK is a successive approximation type ADC with a serial data output format. Because the NIM bus is a parallel data bus the serial data from the PCM78PK must be converted into parallel data. This is accomplished by the 74LS595 serial input parallel output shift registers with internal latches. The parallel output of these circuits can then be used as inputs for the bus driver circuitry.

Perhaps the ADC circuitry and the functionality required of the control logic can best be understood by describing the sequence of events during a conversion cycle. Figure 16 shows a graphical representation of the sequence of signals during the conversion process. To start a conversion cycle the DSP performs a write operation to address 800020 hexadecimal. A write operation to this address is interpreted by the ADC address decoder circuit as a convert command and the convert output of the address decoder goes from ground to

Figure 16. ADC module timing diagrams.

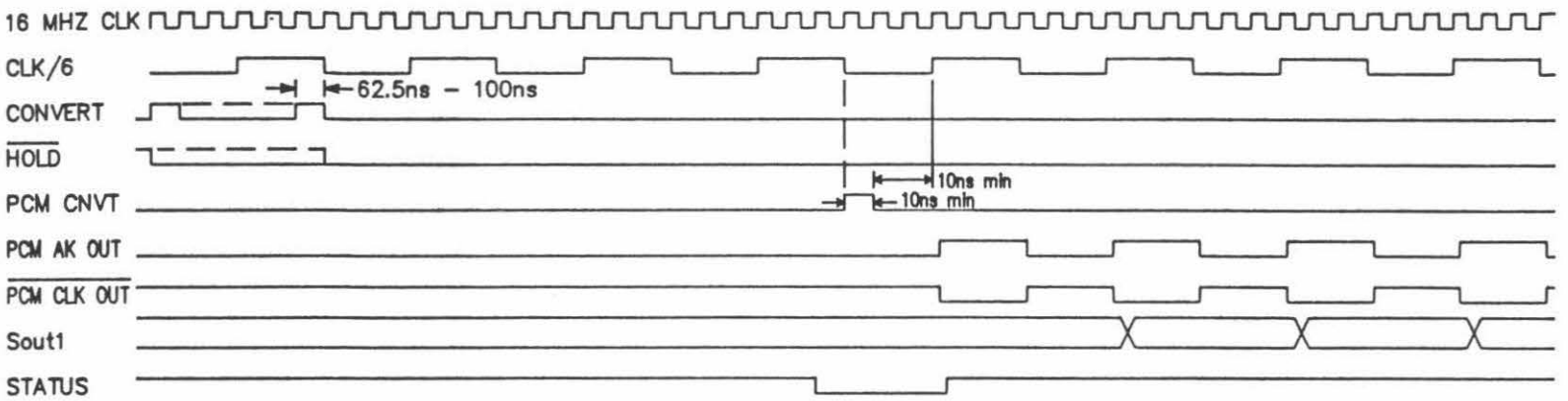

TIMING DIAGRAM 1

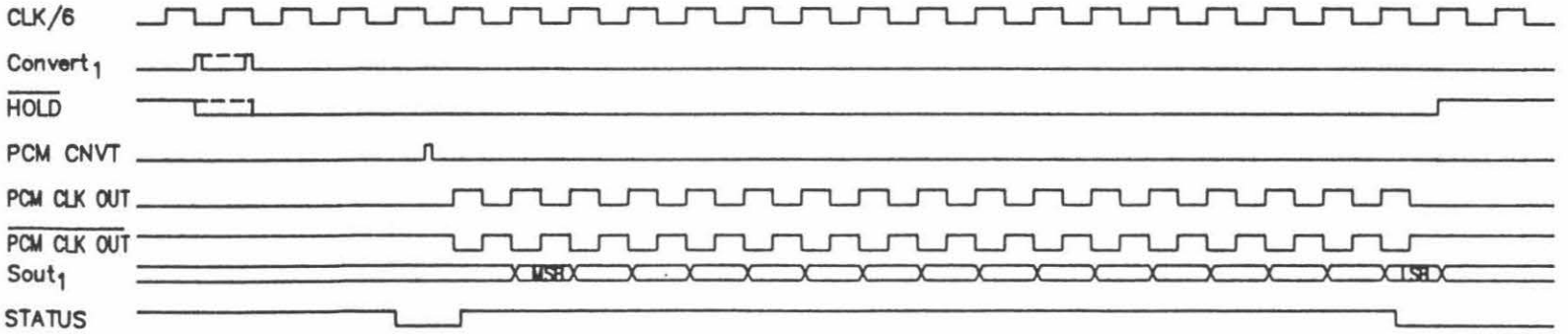

TIMING DIAGRAM 2

a TTL hi level for the remainder of one clock cycle. This convert pulse triggers the ADC control logic, which has been programmed into the PALCE22V10 PAL. The first thing that the control logic must do is assert the hold signal to the track and hold amplifier (THA). When this is done the THA shifts from the track mode (in which it has been following the input signal) to the hold state in which it presents at its output the input signal voltage at the instant the hold signal was issued. It takes up to 4 µs for the output of the THA to stabilize to the sixteen bit level, thus it is important that the hold signal be issued immediately at the start of a conversion cycle. Because successive approximation ADCs start the conversion process at the most significant bit (MSB), if the ADC input has settled to within one MSB the ADC output will be an accurate representation of the ADC input. This same criteria holds true for all of the bit levels in the ADC; so if the converter is slower than the settling time of the THA and the THA hold signal sufficiently preceeds the start of ADC conversion, the ADC will consistently give the correct result.

As much as 1.5 µs after the THA hold signal has been issued, the convert command signal for the PCM78PK is generated by the control logic. This pulse enables the PCM78PK internal conversion circuitry which is clocked by the gated clock coming from the control logic. As the successive approximation register determines each bit of the digital code corresponding to the input voltage the bits become available on the serial output pin of the ADC. The same clock serves the ADC conversion circuitry and the two shift registers which accept the serial data from the ADC insuring that the data is captured properly. At the end of the conversion cycle the status line of the ADC, which has been held high during the conversion process, makes a

transition to the low state. This signal is used by the 74LS595s to shift the data contained in the string of flip-flops composing the shift register itself into the internal latches which can be read in parallel by the bus driver circuits. The data is held in these internal latches until the DSP executes a read operation for one of the addresses between 800021 and 800025 hexadecimal. When the read command for one of these addresses is issued, the address decoder sends an enable signal to the appropriate pair of 74LS595s and also enables the NIM bus driver circuitry which asserts the digital word resulting from the previous ADC cycle onto the NIM bus. Because the DSP can execute many instructions in the time required for one ADC cycle, the most efficient sequence of events for a feedback loop tends to be: i) start an ADC conversion cycle; ii) write new values to the various DAC addresses; iii) calculate new DAC values based on the previous ADC information; iv) read new ADC values; v) return to the begining of the loop.

It may not be immediately obvious how to generate a PAL from the timing diagrams for the ADC control logic. In order to illustrate this we have included the ABEL file and its associated documentation and JEDEC files. In this example we have used the ability of ABEL to accept input in the form of truth tables to create a description of the functionality of the desired PAL. The logic required for control of the PCM78PK and its associated circuits was found to be too complex for a standard 20R8 PAL and so it was programmed into a PALCE22V10. One other point worth mentioning is that recently low cost field programmable gate arrays (FPGAs) have become available. These integrated circuits can serve as arrays of PALs; it is likely that all of the digital logic used on each of the DAC and ADC modules, including the shift registers and bus drivers, could be incorporated in one FPGA for each type of module.

```
module PCM78_22
title 'PCM78 state machine        by      S. Clark and C. Spence'
Declarations  PCM78PAL device  'P22V10';

"Inputs
        CLKIN16, PCLK, EXCNVT           pin 1,2,4;
        GND                             pin 12;
        VCC                             pin 24;

"Outputs
        PCLKO                           pin 22;
        PCNVT                           pin 15 ISTYPE 'com';
        HOLD                            pin 23 ISTYPE 'com';
        Q0, CLK4, Q2, Q3, Q4, Q5, Q6    pin 20,19,18,17,16,14,21 ISTYPE 'reg';
        H, L, X = 1, 0, .X;

equations

        PCLKO       = !PCLK;

 truth_table([Q6.fb, Q5.fb, Q4.fb, Q3.fb, Q2.fb, CLK4.fb, Q0.fb, EXCNVT]:>
            [Q6, Q5, Q4, Q3, Q2, CLK4, Q0]->[HOLD, PCNVT])

            [0,0,0,0,0,0,0,0]:>[0,0,0,0,0,0,0]->[H, L];
            [0,0,0,0,0,0,0,1]:>[0,0,0,0,0,0,1]->[L, L];
            [0,0,0,0,0,0,1,X]:>[0,0,0,0,0,1,0]->[L, L];
            [0,0,0,0,0,1,0,X]:>[0,0,0,0,0,1,1]->[L, L];     "1
            [0,0,0,0,0,1,1,X]:>[0,0,0,0,1,0,0]->[L, L];
            [0,0,0,0,1,0,0,X]:>[0,0,0,0,1,0,1]->[L, L];
            [0,0,0,0,1,0,1,X]:>[0,0,0,0,1,1,0]->[L, L];
            [0,0,0,0,1,1,0,X]:>[0,0,0,0,1,1,1]->[L, L];     "2
            [0,0,0,0,1,1,1,X]:>[0,0,0,1,0,0,0]->[L, L];
            [0,0,0,1,0,0,0,X]:>[0,0,0,1,0,0,1]->[L, L];
            [0,0,0,1,0,0,1,X]:>[0,0,0,1,0,1,0]->[L, L];
            [0,0,0,1,0,1,0,X]:>[0,0,0,1,0,1,1]->[L, L];     "3
            [0,0,0,1,0,1,1,X]:>[0,0,0,1,1,0,0]->[L, L];
            [0,0,0,1,1,0,0,X]:>[0,0,0,1,1,0,1]->[L, H];
            [0,0,0,1,1,0,1,X]:>[0,0,0,1,1,1,0]->[L, L];
            [0,0,0,1,1,1,0,X]:>[0,0,0,1,1,1,1]->[L, L];     "4
            [0,0,0,1,1,1,1,X]:>[0,0,1,0,0,0,0]->[L, L];
            [0,0,1,0,0,0,0,X]:>[0,0,1,0,0,0,1]->[L, L];
            [0,0,1,0,0,0,1,X]:>[0,0,1,0,0,1,0]->[L, L];
            [0,0,1,0,0,1,0,X]:>[0,0,1,0,0,1,1]->[L, L];     "5
            [0,0,1,0,0,1,1,X]:>[0,0,1,0,1,0,0]->[L, L];
            [0,0,1,0,1,0,0,X]:>[0,0,1,0,1,0,1]->[L, L];
            [0,0,1,0,1,0,1,X]:>[0,0,1,0,1,1,0]->[L, L];
```

```
[0,0,1,0,1,1,0,X]:>[0,0,1,0,1,1,1]->[L,L];      "6
[0,0,1,0,1,1,1,X]:>[0,0,1,1,0,0,0]->[L,L];
[0,0,1,1,0,0,0,X]:>[0,0,1,1,0,0,1]->[L,L];
[0,0,1,1,0,0,1,X]:>[0,0,1,1,0,1,0]->[L,L];
[0,0,1,1,0,1,0,X]:>[0,0,1,1,0,1,1]->[L,L];      "7
[0,0,1,1,0,1,1,X]:>[0,0,1,1,1,0,0]->[L,L];
[0,0,1,1,1,0,0,X]:>[0,0,1,1,1,0,1]->[L,L];
[0,0,1,1,1,0,1,X]:>[0,0,1,1,1,1,0]->[L,L];
[0,0,1,1,1,1,0,X]:>[0,0,1,1,1,1,1]->[L,L];      "8
[0,0,1,1,1,1,1,X]:>[0,1,0,0,0,0,0]->[L,L];
[0,1,0,0,0,0,0,X]:>[0,1,0,0,0,0,1]->[L,L];
[0,1,0,0,0,0,1,X]:>[0,1,0,0,0,1,0]->[L,L];
[0,1,0,0,0,1,0,X]:>[0,1,0,0,0,1,1]->[L,L];      "9
[0,1,0,0,0,1,1,X]:>[0,1,0,0,1,0,0]->[L,L];
[0,1,0,0,1,0,0,X]:>[0,1,0,0,1,0,1]->[L,L];
[0,1,0,0,1,0,1,X]:>[0,1,0,0,1,1,0]->[L,L];
[0,1,0,0,1,1,0,X]:>[0,1,0,0,1,1,1]->[L,L];      "10
[0,1,0,0,1,1,1,X]:>[0,1,0,1,0,0,0]->[L,L];
[0,1,0,1,0,0,0,X]:>[0,1,0,1,0,0,1]->[L,L];
[0,1,0,1,0,0,1,X]:>[0,1,0,1,0,1,0]->[L,L];
[0,1,0,1,0,1,0,X]:>[0,1,0,1,0,1,1]->[L,L];      "11
[0,1,0,1,0,1,1,X]:>[0,1,0,1,1,0,0]->[L,L];
[0,1,0,1,1,0,0,X]:>[0,1,0,1,1,0,1]->[L,L];
[0,1,0,1,1,0,1,X]:>[0,1,0,1,1,1,0]->[L,L];
[0,1,0,1,1,1,0,X]:>[0,1,0,1,1,1,1]->[L,L];      "12
[0,1,0,1,1,1,1,X]:>[0,1,1,0,0,0,0]->[L,L];
[0,1,1,0,0,0,0,X]:>[0,1,1,0,0,0,1]->[L,L];
[0,1,1,0,0,0,1,X]:>[0,1,1,0,0,1,0]->[L,L];
[0,1,1,0,0,1,0,X]:>[0,1,1,0,0,1,1]->[L,L];      "13
[0,1,1,0,0,1,1,X]:>[0,1,1,0,1,0,0]->[L,L];
[0,1,1,0,1,0,0,X]:>[0,1,1,0,1,0,1]->[L,L];
[0,1,1,0,1,0,1,X]:>[0,1,1,0,1,1,0]->[L,L];
[0,1,1,0,1,1,0,X]:>[0,1,1,0,1,1,1]->[L,L];      "14
[0,1,1,0,1,1,1,X]:>[0,1,1,1,0,0,0]->[L,L];
[0,1,1,1,0,0,0,X]:>[0,1,1,1,0,0,1]->[L,L];
[0,1,1,1,0,0,1,X]:>[0,1,1,1,0,1,0]->[L,L];
[0,1,1,1,0,1,0,X]:>[0,1,1,1,0,1,1]->[L,L];      "15
[0,1,1,1,0,1,1,X]:>[0,1,1,1,1,0,0]->[L,L];
[0,1,1,1,1,0,0,X]:>[0,1,1,1,1,0,1]->[L,L];
[0,1,1,1,1,0,1,X]:>[0,1,1,1,1,1,0]->[L,L];
[0,1,1,1,1,1,0,X]:>[0,1,1,1,1,1,1]->[L,L];      "16
[0,1,1,1,1,1,1,X]:>[1,0,0,0,0,0,0]->[L,L];
[1,0,0,0,0,0,0,X]:>[1,0,0,0,0,0,1]->[L,L];
[1,0,0,0,0,0,1,X]:>[1,0,0,0,0,1,0]->[L,L];
[1,0,0,0,0,1,0,X]:>[1,0,0,0,0,1,1]->[L,L];      "17
[1,0,0,0,0,1,1,X]:>[1,0,0,0,1,0,0]->[L,L];
```

[1,0,0,0,1,0,0,X]:>[1,0,0,0,1,0,1]->[L,L];
[1,0,0,0,1,0,1,X]:>[1,0,0,0,1,1,0]->[L,L];
[1,0,0,0,1,1,0,X]:>[1,0,0,0,1,1,1]->[L,L]; "18
[1,0,0,0,1,1,1,X]:>[1,0,0,1,0,0,0]->[L,L];
[1,0,0,1,0,0,0,X]:>[1,0,0,1,0,0,1]->[L,L];
[1,0,0,1,0,0,1,X]:>[1,0,0,1,0,1,0]->[L,L];
[1,0,0,1,0,1,0,X]:>[1,0,0,1,0,1,1]->[L,L]; "19
[1,0,0,1,0,1,1,X]:>[1,0,0,1,1,0,0]->[L,L];
[1,0,0,1,1,0,0,X]:>[1,0,0,1,1,0,1]->[L,L];
[1,0,0,1,1,0,1,X]:>[1,0,0,1,1,1,0]->[L,L];
[1,0,0,1,1,1,0,X]:>[1,0,0,1,1,1,1]->[L,L]; "20
[1,0,0,1,1,1,1,X]:>[1,0,1,0,0,0,0]->[L,L];
[1,0,1,0,0,0,0,X]:>[1,0,1,0,0,0,1]->[L,L];
[1,0,1,0,0,0,1,X]:>[1,0,1,0,0,1,0]->[L,L];
[1,0,1,0,0,1,0,X]:>[1,0,1,0,0,1,1]->[H,L]; "21
[1,0,1,0,0,1,1,X]:>[1,0,1,0,1,0,0]->[H,L];
[1,0,1,0,1,0,0,X]:>[0,0,0,0,0,0,0]->[H,L];
[1,0,1,0,1,0,1,X]:>[0,0,0,0,0,0,0]->[H,L];
[1,0,1,0,1,1,0,X]:>[0,0,0,0,0,0,0]->[H,L]; "22
[1,0,1,0,1,1,1,X]:>[0,0,0,0,0,0,0]->[H,L];
[1,0,1,1,0,0,0,X]:>[0,0,0,0,0,0,0]->[H,L];
[1,0,1,1,0,0,1,X]:>[0,0,0,0,0,0,0]->[H,L];
[1,0,1,1,0,1,0,X]:>[0,0,0,0,0,0,0]->[H,L]; "23
[1,0,1,1,0,1,1,X]:>[0,0,0,0,0,0,0]->[H,L];
[1,0,1,1,1,0,0,X]:>[0,0,0,0,0,0,0]->[H,L];
[1,0,1,1,1,0,1,X]:>[0,0,0,0,0,0,0]->[H,L];
[1,0,1,1,1,1,0,X]:>[0,0,0,0,0,0,0]->[H,L]; "24
[1,0,1,1,1,1,1,X]:>[0,0,0,0,0,0,0]->[H,L];
[1,1,0,0,0,0,0,X]:>[0,0,0,0,0,0,0]->[H,L];
[1,1,0,0,0,0,1,X]:>[0,0,0,0,0,0,0]->[H,L];
[1,1,0,0,0,1,0,X]:>[0,0,0,0,0,0,0]->[H,L];
[1,1,0,0,0,1,1,X]:>[0,0,0,0,0,0,0]->[H,L];
[1,1,0,0,1,0,0,X]:>[0,0,0,0,0,0,0]->[H,L];
[1,1,0,0,1,0,1,X]:>[0,0,0,0,0,0,0]->[H,L];
[1,1,0,0,1,1,0,X]:>[0,0,0,0,0,0,0]->[H,L];
[1,1,0,0,1,1,1,X]:>[0,0,0,0,0,0,0]->[H,L];
[1,1,0,1,0,0,0,X]:>[0,0,0,0,0,0,0]->[H,L];
[1,1,0,1,0,0,1,X]:>[0,0,0,0,0,0,0]->[H,L];
[1,1,0,1,0,1,0,X]:>[0,0,0,0,0,0,0]->[H,L];
[1,1,0,1,0,1,1,X]:>[0,0,0,0,0,0,0]->[H,L];
[1,1,0,1,1,0,0,X]:>[0,0,0,0,0,0,0]->[H,L];
[1,1,0,1,1,0,1,X]:>[0,0,0,0,0,0,0]->[H,L];
[1,1,0,1,1,1,0,X]:>[0,0,0,0,0,0,0]->[H,L];
[1,1,0,1,1,1,1,X]:>[0,0,0,0,0,0,0]->[H,L];
[1,1,1,0,0,0,0,X]:>[0,0,0,0,0,0,0]->[H,L];
[1,1,1,0,0,0,1,X]:>[0,0,0,0,0,0,0]->[H,L];

```
[1,1,1,0,0,1,0,X]:>[0,0,0,0,0,0,0]->[H,L];
[1,1,1,0,0,1,1,X]:>[0,0,0,0,0,0,0]->[H,L];
[1,1,1,0,1,0,0,X]:>[0,0,0,0,0,0,0]->[H,L];
[1,1,1,0,1,0,1,X]:>[0,0,0,0,0,0,0]->[H,L];
[1,1,1,0,1,1,0,X]:>[0,0,0,0,0,0,0]->[H,L];
[1,1,1,0,1,1,1,X]:>[0,0,0,0,0,0,0]->[H,L];
[1,1,1,1,0,0,0,X]:>[0,0,0,0,0,0,0]->[H,L];
[1,1,1,1,0,0,1,X]:>[0,0,0,0,0,0,0]->[H,L];
[1,1,1,1,0,1,0,X]:>[0,0,0,0,0,0,0]->[H,L];
[1,1,1,1,0,1,1,X]:>[0,0,0,0,0,0,0]->[H,L];
[1,1,1,1,1,0,0,X]:>[0,0,0,0,0,0,0]->[H,L];
[1,1,1,1,1,0,1,X]:>[0,0,0,0,0,0,0]->[H,L];
[1,1,1,1,1,1,0,X]:>[0,0,0,0,0,0,0]->[H,L];
[1,1,1,1,1,1,1,X]:>[0,0,0,0,0,0,0]->[H,L];

end PCM78_22
```

A Sample Documentation File Produced by ABEL 4.00

```
ABEL 4.00 -Device Utilization Chart Fri Nov 22 14:12:27 1991

PCM78 state machine by   S. Clark and C. Spence

    ==== P22V10 Programmed Logic ====

PCLKO     = (!PCLK);

HOLD      = (!EXCNVT & !Q6.FB & !Q5.FB & !Q4.FB
          & !Q3.FB & !Q2.FB & !CLK4.FB & !Q0.FB
          # Q6.FB & Q4.FB & CLK4.FB
          # Q6.FB & Q4.FB & Q2.FB
          # Q6.FB & Q4.FB & Q3.FB
          # Q6.FB & Q5.FB );

Q0.D      = (Q6.FB & Q4.FB & Q2.FB
          # Q6.FB & Q4.FB & Q3.FB
          # Q6.FB & Q5.FB
          # !EXCNVT & !Q6.FB & !Q5.FB & !Q4.FB
          & !Q3.FB & !Q2.FB & !CLK4.FB
          # Q0.FB ); " ISTYPE 'INVERT'

CLK4.D    = (Q6.FB & Q4.FB & Q2.FB
          # Q6.FB & Q4.FB & Q3.FB
          # Q6.FB & Q5.FB
          # CLK4.FB & Q0.FB
          # !CLK4.FB & !Q0.FB ); " ISTYPE 'INVERT'

Q2.D      = (Q6.FB & Q4.FB & Q2.FB
          # Q6.FB & Q4.FB & Q3.FB
          # Q6.FB & Q5.FB
          # Q2.FB & CLK4.FB & Q0.FB
          # !Q2.FB & !Q0.FB
          # !Q2.FB & !CLK4.FB ); " ISTYPE 'INVERT'
```

```
Q3.D      = (Q6.FB & Q5.FB
          # Q3.FB & Q2.FB & CLK4.FB & Q0.FB
          # Q6.FB & Q4.FB
          # !Q3.FB & !Q0.FB
          # !Q3.FB & !CLK4.FB
          # !Q3.FB & !Q2.FB ); " ISTYPE 'INVERT'

PCNVT     = (!Q6.FB & !Q5.FB & !Q4.FB & Q3.FB & Q2.FB
          & !CLK4.FB & !Q0.FB );

Q4.D      = (!Q5.FB & !Q4.FB & Q3.FB & Q2.FB & CLK4.FB &
Q0.FB
          # !Q6.FB & !Q4.FB & Q3.FB & Q2.FB & CLK4.FB & Q0.FB
          # !Q5.FB & Q4.FB & !Q3.FB & !Q2.FB
          # !Q6.FB & Q4.FB & !Q0.FB
          # !Q6.FB & Q4.FB & !CLK4.FB
          # !Q6.FB & Q4.FB & !Q2.FB
          # !Q6.FB & Q4.FB & !Q3.FB ); " ISTYPE 'BUFFER'

Q5.D      = (!Q6.FB & Q5.FB & !Q0.FB
          # !Q6.FB & !Q5.FB & Q4.FB &Q3.FB & Q2.FB
          & CLK4.FB & Q0.FB
          # !Q6.FB & Q5.FB & !CLK4.FB
          # !Q6.FB & Q5.FB & !Q2.FB
          # !Q6.FB & Q5.FB & !Q3.FB
          # !Q6.FB & Q5.FB & !Q4.FB ); " ISTYPE 'BUFFER'

Q6.D      = (!Q6.FB & Q5.FB & Q4.FB & Q3.FB & Q2.FB
          & CLK4.FB & Q0.FB
          # Q6.FB & !Q5.FB & !Q3.FB & !Q2.FB
          # Q6.FB & !Q5.FB & !Q4.FB ); " ISTYPE 'BUFFER'
```

==== P22V10 Chip Diagram ====

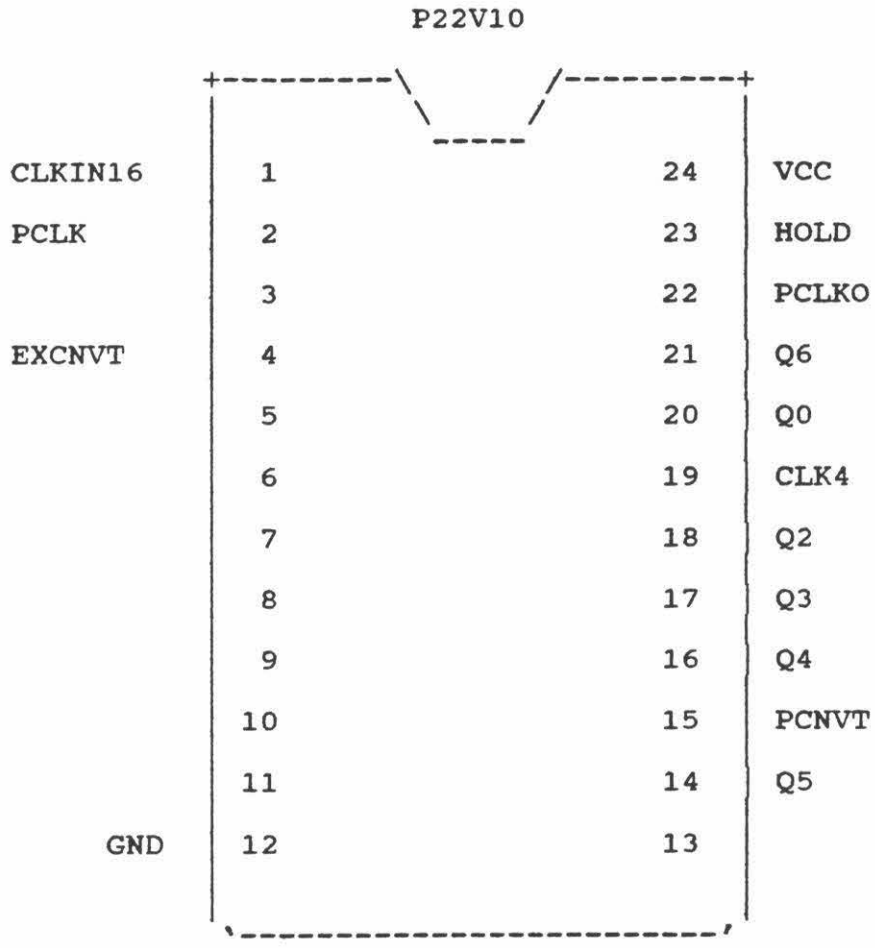

SIGNATURE: N/A

==== P22V10 Resource Allocations ====

Device Resources	Resource Available	Design Requirement	Part Util.	Unused
Dedicated input pins	12	2	2	10(83%)
Combinatorial inputs	12	2	2	10(83%)
Registered inputs	-	0	-	-
Dedicated output pins	-	10	-	-
Bidirectional pins	10	0	10	0 (0%)
Combinatorial outputs	-	3	-	-
Registered outputs	-	7	-	-
Reg/Com outputs	10	-	10	0 (0%)
Two-input XOR	-	0	-	-
Buried nodes	-	0	-	-
Buried registers	-	0	-	-
Buried combinatorial	-	0	-	-

==== P22V10 Product Terms Distribution ====

Signal Name	Pin Assigned	Terms Used	Terms Max	Terms Unused
PCLKO	22	1	10	9
HOLD	23	5	8	3
Q0.REG	20	5	14	9
CLK4.REG	19	5	16	11
Q2.REG	18	6	16	10
Q3.REG	17	6	14	8
PCNVT	15	1	10	9
Q4.REG	16	7	12	5
Q5.REG	14	6	8	2
Q6.REG	21	3	12	9

==== List of Inputs/Feedbacks ====

Signal Name	Pin	Pin Type
PCLK	2	INPUT
EXCNVT	4	INPUT

==== P22V10 Unused Resources ====

Pin Number	Pin Type	Product Terms	Flip-flop Type
3	INPUT	-	-
5	INPUT	-	-
6	INPUT	-	-
7	INPUT	-	-
8	INPUT	-	-
9	INPUT	-	-
10	INPUT	-	-
11	INPUT	-	-
13	INPUT	-	-

==== I/O Files ====

Module: 'pcm78_22'

Input files
===========
ABEL PLA file: pcm78_22.tt3
Vector file: pcm78_22.tmv
Device library: P22V10.dev

Output files
============
Report file: pcm78_22.doc
Programmer load file: pcm78pal.jed

A Sample JEDEC File Produced by ABEL 4.00

```
ABEL 4.00 Data I/O Corp. JEDEC file for: P22V10 V9.0

Created on: Fri Nov 22 14:12:27 1991

PCM78 state machine by   S. Clark and C. Spence

*
QP24* QF5828* QV0* F0*
X0*
NOTE Table of pin names and numbers*
NOTE PINS CLKIN16:1 PCLK:2 EXCNVT:4 GND:12
          VCC:24 PCLKO:22 PCNVT:15 HOLD:23*
NOTE PINS Q0:20 CLK4:19 Q2:18 Q3:17 Q4:16 Q5:14 Q6:21*
L0044 1111111111111111111111111111111111111111111111*
L0088 1111111110110101110110110110110111111011111*
L0132 1111111111101111101111111111110111111111111*
L0176 1111111111101111111111011111111011111111111*
L0220 1111111111101111111111111011110111111111111*
L0264 1111111111101111111111111111111111111101111*
L0440 1111111111111111111111111111111111111111111*
L0484 1111101111111111111111111111111111111111111*
L0924 1111111111111111111111111111111111111111111*
L0968 1111111110110110110110110110111101111101111*
L1012 1111111111101111111111011101111111111011111*
L1056 1111111111101111111111111111101111111011111*
L1496 1111111111111111111111111111111111111111111*
L1540 1111111111101111111111011111111011111111111*
L1584 1111111111101111111111111011110111111111111*
L1628 1111111111101111111111111111111111111101111*
L1672 1111111110110111110110110110111111111011111*
L1716 1111111111111101111111111111111111111111111*
L2156 1111111111111111111111111111111111111111111*
L2200 1111111111101111111111011111111011111111111*
L2244 1111111111101111111111111011110111111111111*
L2288 1111111111101111111111111111111111111101111*
L2332 1111111111111101110111111111111111111111111*
L2376 1111111111111110111011111111111111111111111*
L2904 1111111111111111111111111111111111111111111*
L2948 1111111111101111111111011111111011111111111*
```

```
L2992 11111111111011111111111111011110111111111111*
L3036 11111111111011111111111111111111111111101111*
L3080 11111111111111011101110111111111111111111111*
L3124 11111111111111101111111011111111111111111111*
L3168 11111111111111111110111011111111111111111111*
L3652 11111111111111111111111111111111111111111111*
L3696 11111111111011111111111111111111111111101111*
L3740 11111111111111011101110111011111111111111111*
L3784 11111111111011111111111111111110111111111111*
L3828 11111111111111101111111111101111111111111111*
L3872 11111111111111111110111111101111111111111111*
L3916 11111111111111111111111011101111111111111111*
L4312 11111111111111111111111111111111111111111111*
L4356 11111111111111011101110111011101111111011111*
L4400 11111111110111011101110111011101111111111111*
L4444 11111111111111111111111011101110111111011111*
L4488 11111111110111101111111111111111011111111111*
L4532 11111111110111111111011111111111011111111111*
L4576 11111111110111111111111011111111011111111111*
L4620 11111111110111111111111111111011101111111111*
L4884 11111111111111111111111111111111111111111111*
L4928 11111111110111101110111011101110111111011111*
L5368 11111111111111111111111111111111111111111111*
L5412 11111111110111101111111111111111111111101111*
L5456 11111111110111011101110111011101111111011111*
L5500 11111111110111111111011111111111111111101111*
L5544 11111111110111111111111011111111111111101111*
L5588 11111111110111111111111111011111111111101111*
L5632 11111111110111111111111111111011111111101111*
L5808 11111000000000101110*
C0E95*
8BF8
```

This would not only save a tremendous amount of printed circuit board space, but also simplify board layout and reduce digital noise while increasing speed.

VII. Miscellaneous Circuitry

It was implied earlier in the discussion of the ADC module that the original design intention was to directly digitize the signals from the four quadrants of the quadrant photodiode. Two points remain to be made in this area: i) what generates the signal from the photodiode and ii) if the signals are not directly digitized, what processing occurs before the ADC inputs.

The first point is easily addressed by presentation of the quadrant photodiode preamplifier circuit in Figure 17. The preamplifier is physically composed of a small multilayer printed circuit board which resides directly on top of the photodiode. The board is supplied with regulated power (± 22 volts) from a power supply housed in the "second stage amplifier" chassis. There is an on board bipolar voltage regulator to supply the transimpedance amplifiers with the ± 15 volts they require. The preamplifiers are comprised of two dual low noise operational amplifiers (OPA2107s) used in a transimpedance (current to voltage) mode. The outputs from these amplifiers are sent via coaxial cables to the "second stage amplifier."

The function of the second stage amplifier is to perform the summing and differencing of the preamplifier outputs needed to form signals corresponding to X and Y beam motions on the face of the quadrant photodiode. A schematic of this circuit is shown in Figure 18.

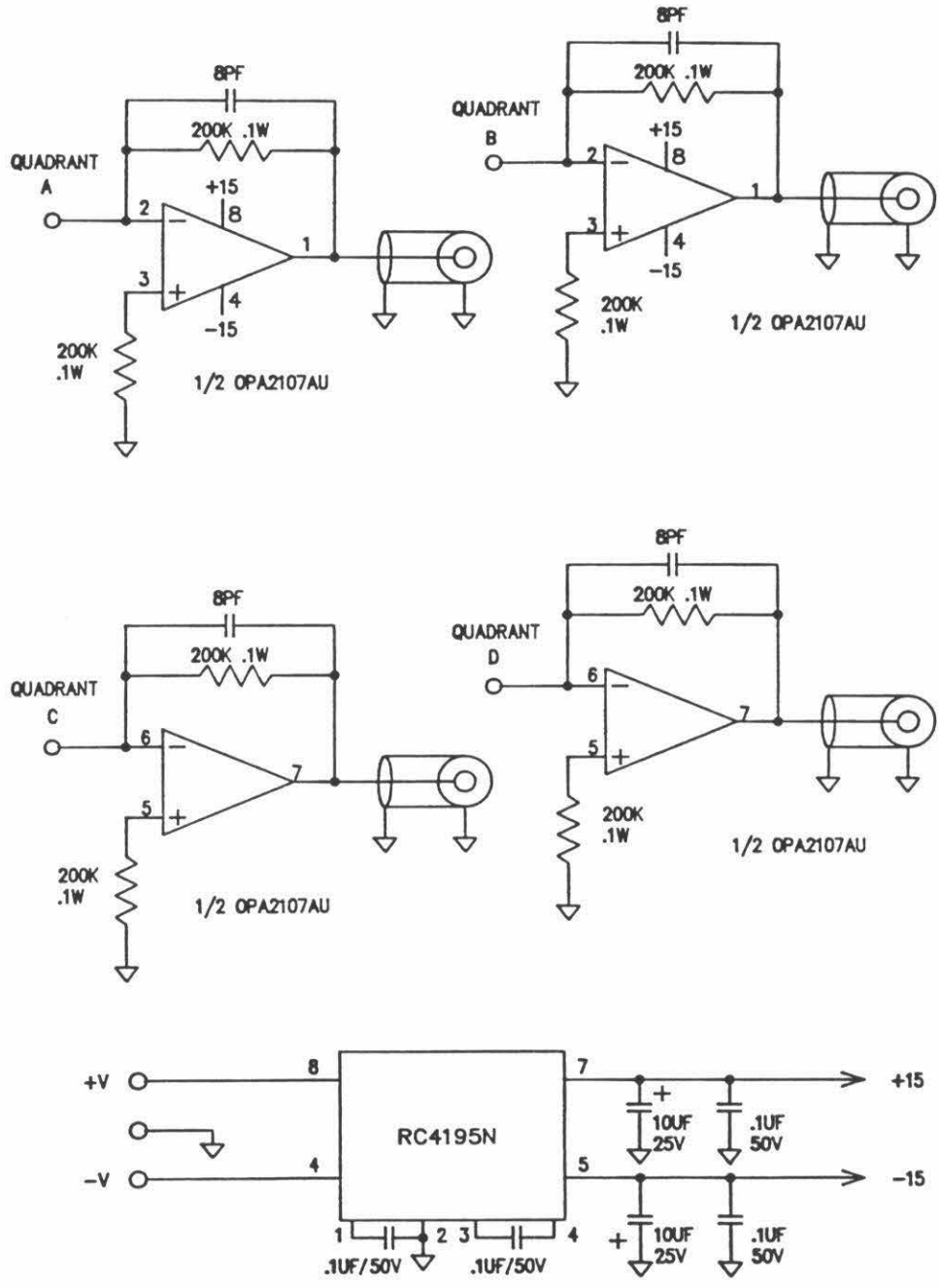

Figure 17. QUADRANT PHOTODIODE PREAMPLIFIER

Figure 18. Second stage amplifier schematic.

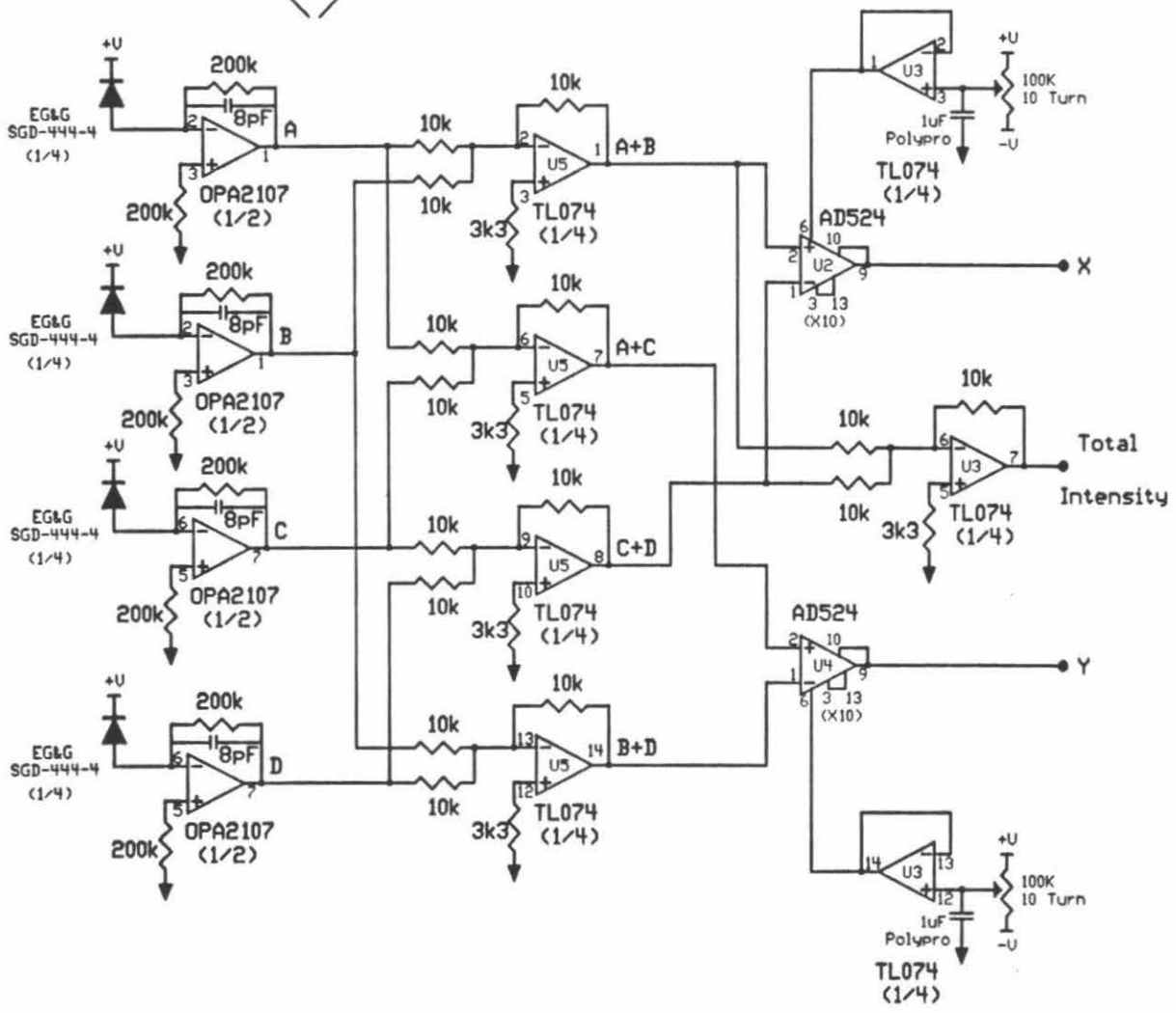
PREAMP
SECOND STAGE AMP
EG&G SGD-444-4 (1/4)
+U
200k
8pF
A
B
C
D
OPA2107 (1/2)
10k
3k3
TL074 (1/4)
A+B
A+C
C+D
B+D
AD524
U2
U4
(X10)
X
Y
Total Intensity
U3
U5
100K 10 Turn
1uF Polypro
-U

(This figure also includes the photodiode preamplifier to make the connection between the two circuits clearer.) This circuit includes features such as pin programmable gain at the intrumentation amplifiers (AD524s) where the X and Y signals are formed as well as a variable output offset.

While the second stage amplifier works adequately, it is certainly more desireable to directly digitize the signals from the photodiode preamplifiers. If this were done, a nearly infinite common mode rejection ratio could be obtained and a digital automatic gain control could be implemented as well as gaining the ability to directly measure laser intensity noise and eliminate it from the measurement. This tack was not taken because the number of DSP instructions needed to perform the required calculations would be excessive and that the feedback loop bandwidth would suffer.

Appendix B.

Digital Signal Processor Control of Scanned Probe Microscopes*

* The software for the scanned probe microscope control electronics is the work of David Baselt, and this Appendix is adapted from a manuscript prepared by the authors listed on the following page. This material is included to allow a more complete understanding of the control electronics and their operation.

Digital Signal Processor Control of Scanned Probe Microscopes

David R. Baselt, Steven M. Clark†, Michael G. Youngquist, Charles F. Spence†
and John D. Baldeschwieler

A. A. Noyes Laboratory of Chemical Physics
Division of Chemistry and Chemical Engineering
and
†Division of Biology
California Institute of Technology
Pasadena, CA 91125

ABSTRACT

Software for a digital signal processor based scanned probe microscope (SPM) control system is described. The SPM control system consists of a commercial digital signal processor board, interfaced to analog I/O and run by the control system software. All of the SPM control functions are implemented in software allowing unprecedented flexibility without sacrificing performance. The system is capable of supporting a wide variety of SPM experiments including tunneling, force and nearfield optical microscopy. We discuss implementations of feedback, raster generation (including hysteresis correction, compensation for sample tilt and scan rotation), automatic tip-sample approach and a digital lock-in amplifier. We also present an instruction parser architecture which significantly enhances the control system.

I. INTRODUCTION

Since the invention of the scanning tunneling microscope in 1981,[1] a new branch of microscopy has emerged. Scanned probe microscopy (SPM), as it has come to be known, now encompasses more than twenty different modalities of sample imaging via their interaction with a rastered probe.[2] While the physics underlying the microscopies is diverse, they all share basic requirements for microscope control and data acquisition. To perform SPM a probe must be positioned near a sample and (usually) rastered while various signals are measured as functions of probe position, input parameters (e.g., tip-sample bias in STM), and/or time. The primary experimental differences which must be addressed by an SPM control system are input signal generation and sensor linearity, Z-feedback response rate and the number of data types recorded at each sampling interval.

Digital signal processor (DSP) boards which enable straightforward implementation of digital control systems have recently become available. By using these boards it is possible to assemble an effective and flexible SPM control system. The key advantages of such a system are its inherent flexibility, modularity, improved noise immunity and relatively low cost (10-30% of commercial SPM systems). Additionally, functions which may be too complex or cumbersome to implement using hardware can often be added by modifying the DSP control software. Despite the common use of DSPs for SPM control in commercial instruments, we are unaware of any detailed treatment of DSP based SPM control systems in the literature.[3-13]

In this paper we describe the software for a DSP based SPM control system assembled using board level components. In its most basic form the control system generates the XY raster, performs the Z-feedback and records SPM data. We present algorithms for these functions as well as more advanced features such as digital oscilloscope and lock-in amplifier emulations. To give the context in which the software operates, we begin with an overview of the basic hardware requirements of the system and discuss some of the considerations involved in component selection.

II. HARDWARE OVERVIEW

In a digital control system for SPM (see Figure 1) the proximity signal (tunneling current in STM, cantilever deflection in SFM, etc.) is measured by a sensor using analog signal processing electronics and digitized by an analog to digital converter (ADC). This ADC reading of the sensor output (referred to as C) is compared against a digital setpoint to obtain an error signal. The error signal is used to calculate a digital code representing the ideal voltage to be applied to the Z axis of the piezoelectric micropositioner (hereafter referred to as the piezo). The algorithm used for this calculation comprises the Z feedback loop. This new Z code is converted into the actual Z voltage (later referred to as Z), which moves the piezo in a direction perpendicular to the sample surface, by a digital to analog converter (DAC). The DAC output is amplified by a high voltage amplifier to provide the output voltage necessary to drive the piezo. The raster voltages used to drive the piezo in the X and Y dimensions are typically generated in an open loop fashion (that is, they are calculated and sent to the X and Y DACs without measuring a control signal for them); however closed loop XY positioning offers the capability to correct imperfections in the piezo

Figure 1. A block diagram of a digital control system for a scanned probe microscope. Two distinct types of signals occur in a digital control system: i) those which are time and amplitude continuous (analog signals) denoted $f(t)$; and those which are quantized in time and amplitude (digital signals) denoted $g(kT)$. In a digital control system both the conversion resolution and the sampling rate effect the degree to which the digital control system approximates an analog control system.[21,22] Specialized mathematical techniques which address the digital nature of the signals are used to effectively analyze digital control systems and insure their performance. In this figure noise from any source is denoted by the variable n.

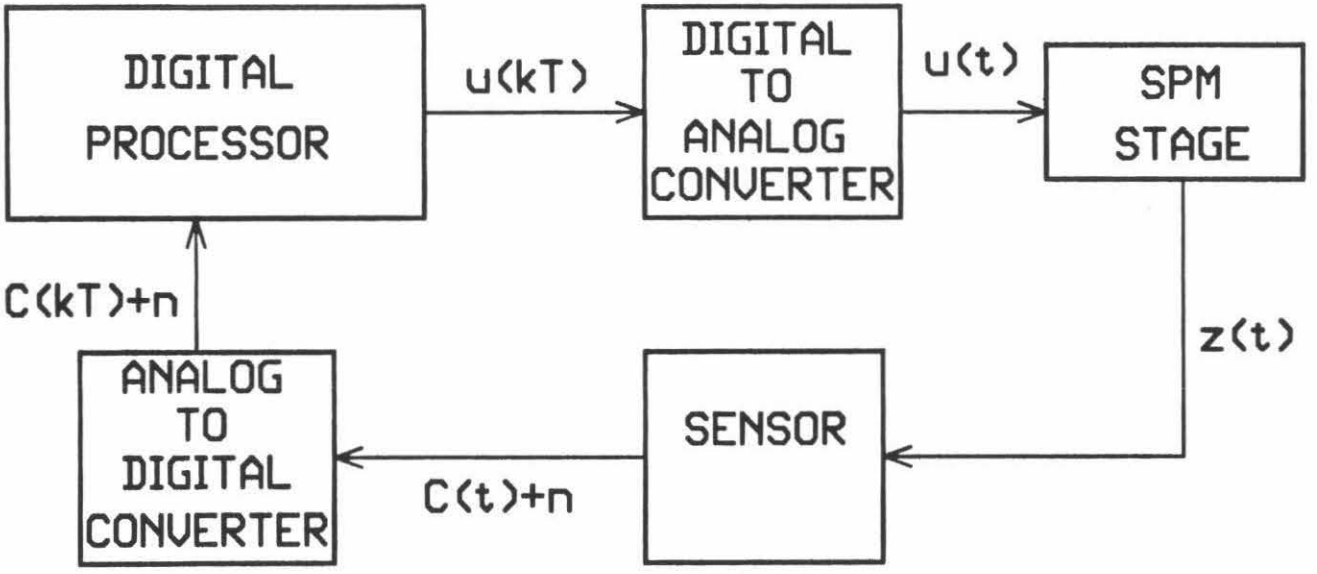
DIGITAL
PROCESSOR
u(kT)
DIGITAL
TO
ANALOG
CONVERTER
u(t)
SPM
STAGE
C(kT)+n
z(t)
ANALOG
TO
DIGITAL
CONVERTER
SENSOR
C(t)+n

response.[14] In this paper we have adopted the convention that X refers to the fast raster voltage and Y to the slow raster voltage.

DSPs are particularly well suited for the real-time computation and signal processing tasks necessary for implementing a digital SPM. They typically contain features such as single cycle multiplication, matrix manipulation facilities and clock speeds of 20 Mhz and greater. Thus, DSPs are much faster for these tasks than microcontrollers or other dedicated microprocessors. Another point should be made about DSPs; because they are independent processors they can perform operations concurrently with the host processor. In many cases a DSP can be used to accelerate tasks to be performed by a host, but for instrument control it is often more useful to load a program which the DSP runs independently of the host platform. One way to optimally exploit this dual processor architecture is to divide tasks into two sets, instrument control to be run by the DSP and user interface to be run by the host system.

Since board level DSP coprocessor products are now commercially available for a variety of host computer platforms, the ability to use DSPs for controlling SPMs is a practical alternative for those constructing their own SPM. A basic system, illustrated by the scanned force microscope schematic of Figure 2, consists of the DSP board, its host computer and the analog I/O circuitry. The two major considerations involved in the selection of processors are whether floating point or integer DSPs are to be used and how much memory should be directly addressable by the DSP. Additionally, the selected DSP board must be compatible with the intended analog I/O and the host computer. For the system that we have built, a TMS320C30 system board[15] was chosen. This board uses a 80386 IBM PC\AT compatible computer as its host.

Figure 2. A block diagram of a scanned force microscope control and data acquisition system. The system shown uses a PC/AT computer as the host for the digital signal processor board and has external analog I/O. All electronic details have been ommitted for clarity. Other host systems and analog I/O packaging schemes could clearly be used (e.g., workstations and VXI Bus).

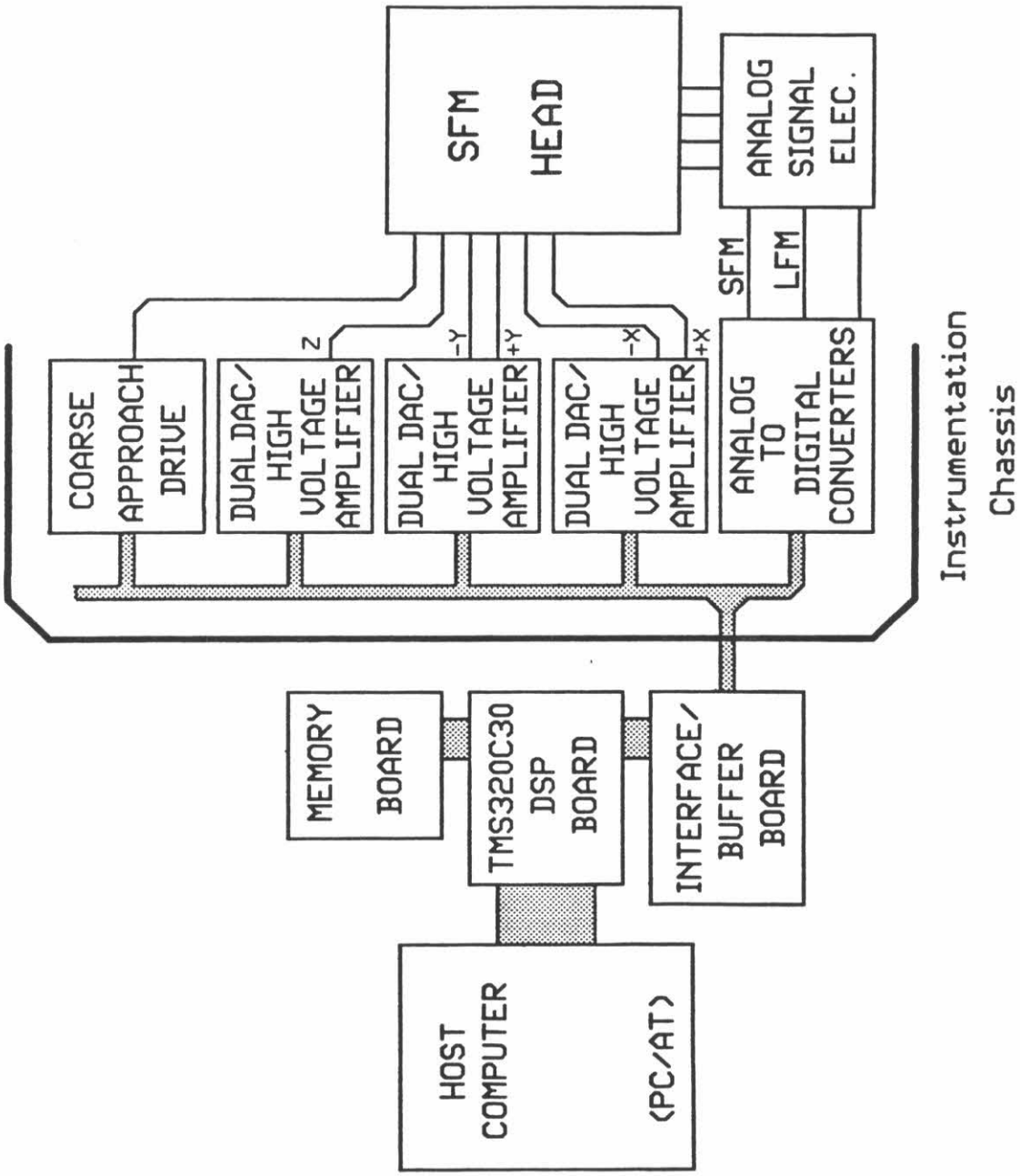
SFM HEAD
ANALOG SIGNAL ELEC.
SFM
LFM
COARSE APPROACH DRIVE
DUAL DAC/ HIGH VOLTAGE AMPLIFIER
Z
DUAL DAC/ HIGH VOLTAGE AMPLIFIER
-Y
+Y
DUAL DAC/ HIGH VOLTAGE AMPLIFIER
-X
+X
ANALOG TO DIGITAL CONVERTERS
Instrumentation Chassis
MEMORY BOARD
TMS320C30 DSP BOARD
INTERFACE/ BUFFER BOARD
HOST COMPUTER (PC/AT)

The decision as to the type of DSP to be used, floating point or integer, depends on the time available to write software and the proficiency of the programmer. While integer DSP based boards are typically less expensive, they require strict attention to underflow and overflow conditions during algorithm implementation. Most of the algorithms presented in this paper can be implemented on integer DSPs, however floating point DSPs simplify the programming task by alleviating underflow/overflow concerns.

The amount of DSP memory required is another matter of programming convenience. Our particular system is capable of generating data at rates of 1.2 Mbytes/sec. Although storing data on the host computer, a PC, at this rate is an inexpensive option, it requires extensive knowledge of PC hardware and 80x86 assembly language programming. Therefore, we chose a DSP board with enough memory for on-board image storage. For on-board image storage a minimum of 250 Kwords is recommended and 2 Mwords is not excessive. The TMS320C30[16] has a 16 Mword directly addressable memory space and not the segmented memory space of the 80x86 processors when run under DOS. The TMS320's straightforward memory structure greatly decreases analysis time and simplifies programming especially for image manipulation routines. While purchasing DSP on-board memory is significantly more expensive, the programming simplicity it provides makes it cost effective.

The last major area that must be addressed during the hardware design phase of the construction of an SPM control system is the type of analog I/O to be used. There are three major alternatives to consider: i) the use of DSP on-board analog I/O, ii) the use of off-board analog I/O, and iii) the construction of custom designed analog I/O.

While the use of DSP on-board analog I/O provides the most convenient alternative, this advantage often comes at the price of resolution and noise performance. On-board analog I/O sections may be susceptible to noise generated by the host computer and the DSP itself; hence, even if the board contains high resolution parts (e.g., full 16 bit ADCs) the system performance can be compromised to the 10 to 12 bit level. During the initial stages of system construction, we found the use of on-board I/O to be very helpful because it allowed software development to proceed in parallel with custom hardware design. For those who need the flexibility obtainable with a DSP based system, but do not need particularly high final performance the use of on-board analog I/O may be the optimal alternative.

Almost the same degree of convenience of on-board I/O can be achieved through the use of off-board analog I/O. This type of I/O circuitry is available as board level products internal or external to the host from many different manufacturers.[17] We prefer to use boards external to the host computer in order to keep the I/O section out of the noisy host environment and separately powered, while maintaining the ability to directly connect to the DSP board. Internal board level products usually suffer from the same host induced noise as do on-board I/O. However, some properly shielded and carefully powered products are available which can obtain 16-bit performance and boards of this type are strongly recommended if external I/O cannot be used.

One last issue of importance in the selection of any analog I/O product is the type of analog to digital converter used. Board level products containing delta-sigma converters[18] should not be used for control loop applications. While these converters provide high resolution, good noise immunity and high sample

rates, their long group delay (on the order of 1ms) precludes their use in feedback loops. Successive approximation converters [18] and their variants are preferred for high resolution, servo loop applications because their short conversion times and low group delay times do not require a sacrifice in feedback loop bandwidth.

As the final analog I/O alternative, one must also consider custom built I/O. By designing and constructing custom I/O, true state-of-the-art performance can be achieved. The major drawback to this alternative is the cost in terms of development time. The process of custom I/O development from conceptual design through testing and debugging of the final hardware can occupy an experienced engineer for several months. For those seriously considering this choice, some of the issues involved in the design of a custom I/O section are covered in Reference 19.

III. SOFTWARE

The major advantage offered by a DSP based instrument control system is flexibility. Because the software is responsible for all instrument control functions, many of the instrument's fundamental features can be tailored and optimized through simple software changes. The dual processor architecture described in this paper naturally lends itself to a division of software tasks in which instrument control functions are handled by the DSP program and the user interface by a separate PC program.

A. TIMING CONSIDERATIONS

Most SPM control functions occur in "real-time" and so they require consistent and predictable timing to function properly. This is true not only of

the feedback loop, where a regular sampling interval is crucial to predictable loop performance, but also for raster generation and modulation imaging. Because DSPs are specifically designed for "real-time" signal processing, they often have built-in timers which make it easy to reliably time control functions. These timers are usually programmable and can be used to generate processor interrupts. An interrupt is a signal which stops the execution of the current program the processor is running and starts the execution of another specific program (the interrupt service routine or ISR). For example, by having the ISR perform a function such as read an ADC and return control to a main program one can record data from an ADC at regular intervals.

In our control system we set one of the built-in timers of the DSP to trigger once every 10-15 µs, depending on the experiment in progress. This timer period serves as the fundamental clock by which all the time dependent functions of the SPM operate. Once per timer period, the XY raster is advanced, the ADCs are read, the feedback loop calculations are performed, and image data is updated (see Figure 3). In our software this set of functions comprises the ISR. After the ISR has been executed, the software calculates the next X and Y positions, sends data to the host for display and waits for the timer to generate the next interrupt. By using this scheme, control functions are timed to the accuracy of the DSP clock.

The total time required for the "once-per-timer-period" tasks must be less than the timer period. It is desirable to keep the timer period as short as possible. Because the system cannot take more than one data point per timer period, a

Figure 3. Software algorithms used during one timer period while scanning. Every 10 μs the DSP timer triggers an interrupt, causing the execution of the interrupt service routine (ISR). The software is written so that interrupts only occur after all the operations in the previous ISR call have been completed and the DSP is executing the waiting loop in the scan subroutine. Several portions of the DSP software are not shown: data storage, which occurs less than once per timer period; tip-sample approach routine, which is not used while scanning; and the user interface.

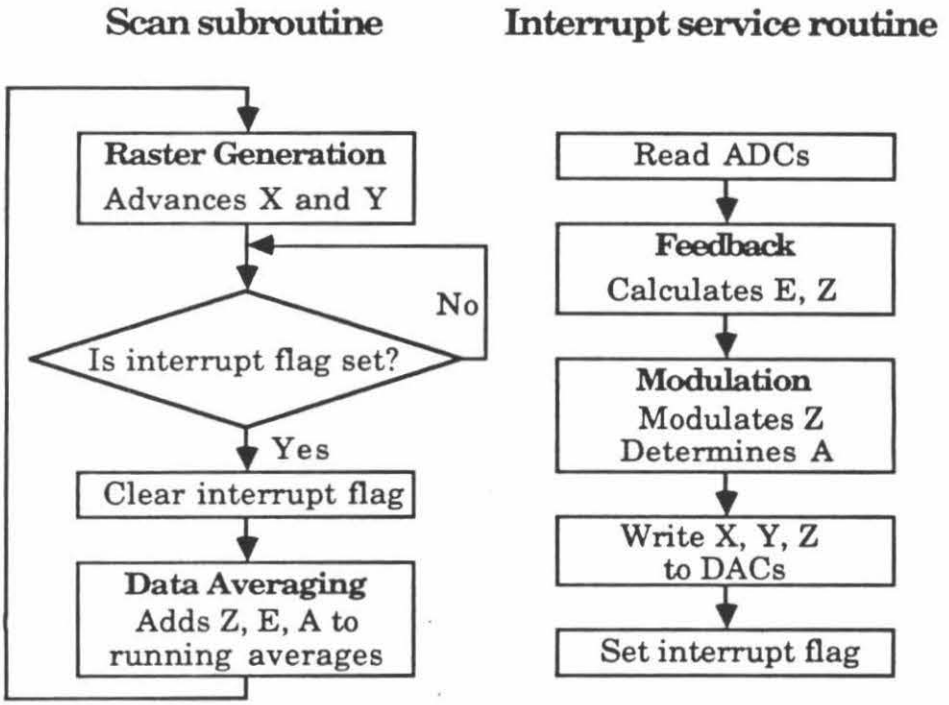
Scan subroutine
Interrupt service routine
Raster Generation
Advances X and Y
No
Is interrupt flag set?
Yes
Clear interrupt flag
Data Averaging
Adds Z, E, A to
running averages
Read ADCs
Feedback
Calculates E, Z
Modulation
Modulates Z
Determines A
Write X, Y, Z
to DACs
Set interrupt flag

shorter period means that faster scans are possible and that more oversampling can be done on slower scans. Additionally, the optimum response rate of the feedback (i.e., its ability to follow the topography of the sample surface) depends in part on the timer period. However, the period cannot be arbitrarily short since the period cannot be less than the ADC conversion time, typically 5-10 µs for 16 bit ADC's. With our DSP a 10 µs period, which allows 166 instruction cycles, is enough for basic SPM operation. If many time-consuming features (i.e., several types of modulation imaging at once, numerous data channels, etc.) are used simultaneously, up to a 15 µs timer period may be needed.

B. FEEDBACK

One of the greatest advantages of the DSP-based architecture is that it enables software emulation of analog feedback. Analog feedback is capable of superb servo loop performance in many applications and would be preferred for feedback in a SPM except that hardware implementations of analog servos tend to be difficult to optimize in real time. By using digital feedback it is possible to vary feedback parameters over a wide range from within the software. This allows the feedback loop response to be optimized for each combination of tip and sample which can be cumbersome in exclusively analog systems. Another advantage gained by using digital feedback is the simplified implementation of more advanced functions such as spectroscopy, digital modulation, and sample tilt compensation.

The fundamental function of the feedback loop is to maintain the sensor output voltage at a constant level (the "setpoint") specified by the user. The loop does this by continually adjusting Z, as determined by the algorithm which

composes the loop. The feedback algorithm determines the sign and the magnitude of Z to compensate for any difference between C and the setpoint. If the adjustment to Z is made based on the previous Z values, the loop is a feedback loop. On the other hand, if Z is adjusted in anticipation of what the next value of Z should be (based on some model or other information) the loop is referred to as a feedforward loop. In our software we use a feedback loop to maintain constant C on a local basis, however sample tilt compensation is done using feedforward correction.

Feedback Algorithms

Several different types of feedback loops can be implemented using DSPs, but only a few are appropriate for use as a control loop for SPM. Among the types of feedback we have found most useful are integral and proportional-integral-differential (PID) feedback. Although a feedback loop based on an optimal feedback design approach may provide superior performance for atomic force microscopy (AFM), we were interested in a control loop which is generally applicable to various types of SPM; we have found that PID feedback works well for both STM and AFM. In order to simplify the discussion of feedback algorithms we begin by examining the principles involved in the integral feedback loop.

Integral feedback

Perhaps the simplest feedback algorithm can be constructed as follows: Measure the sensor output and determine its deviation from the setpoint (the "error"). Assume that changing Z produces a proportional change in the sensor

output (i.e., the sensor is linear). To reduce the error, Z should then be changed by an amount proportional to the error. This can be expressed mathematically as:

$$E_{(kt)} = C_{(kt)} - S$$

$$Z_{(k+1t)} = Z_{(kt)} + IE_{(kt)},$$

where

t = the timer interval

k = an integer index which increases by one every interrupt cycle

$E_{(kt)}$ = the error signal sampled at interval kt

$C_{(kt)}$ = the ADC reading of the sensor output at interval kt

S = the user specified digital setpoint

$Z_{(kt)}$ = the voltage applied to the Z piezo electrode at interval kt

I = the user specified integral feedback gain.

Because the output depends only on the previous values of Z (in the sense that new Z values are found from the rectangular approximation integral of the input C) this is an integral feedback algorithm. The major advantage to an integral feedback loop is that it eliminates steady-state error (an offset from the setpoint which is time independent) in the servo. This is an important capability, but it comes at the price of speed. Since the new Z is a sort of rolling average of previous Z values, the integral feedback loop can be seen to act as a low-pass filter which tends to slow the servo response to transients.

One of the major assumptions made for the integral feedback loop was that the sensor response is linear . This is not always the case and, in fact, one of the most notable exceptions is when the sensor is a tunneling probe. Although integral feedback has been used successfully with such nonlinear sensors, many

users prefer to first linearize the tunneling current output with a logarithmic amplifier or in the instrument control software.

The integral feedback loop also serves to illustrate some of the other points concerning the general features of feedback. The first point to be made is that the feedback can be turned off simply by setting the gain (I) to zero. In this case the new Z value is equal to the old Z value and thus Z remains at the last Z value before the feedback was turned off. Another feature of feedback can be seen by considering the effect of too large a gain setting. In this case small errors cause large corrections in Z; if there are time delays in the loop, such as the ADC conversion delay, the phase delay through the anti-aliasing filter or the finite response time of the SPM stage, the loop will tend to overcompensate errors. This leads to oscillations in both the sensor signal and in the feedback response. The requirement of loop stability imposes an upper bound on the rate at which a feedback loop can respond to perturbations. For SPM this means that while scanning, changes in topography can only be followed well if they lie within the bandwidth of the feedback loop. To attain the best performance possible from the feedback loop the gains should be set as high as possible without causing the loop to oscillate; this makes the loop bandwidth as high as possible and increases the accuracy with which topography is followed.

One should also note that, because the integral feedback loop acts as a low-pass filter, there will be information in the sensor signal that is lost in the Z output. This means that by storing exclusively either the Z output (which is proportional to larger scale image features) or the sensor output (which contains information regarding smaller scale structures) one inherently filters the data in some ill defined manner. Others have noted this distinction between the

information in the sensor output and that in the Z output and have created a "new imaging" mode based on recording the fluctuations in the sensor output while maintaining the feedback in the regular manner.[20] While this does give better lateral resolution, it does so at the expense of height information. Thus it may arguably be best to store both types of data and combine them later in post-processing of the data. If this is done no information is lost and a better representation of the sample may be obtained.

PID feedback

It is possible to improve on some of the limitations of an integral feedback loop by using a more sophisticated algorithm such as proportional-integral-differential feedback. Through the addition of the proportional and differential terms one can increase the speed of the transient response and reduce overshoot and ringing respectively. In our laboratory we use PID feedback because it is easily implemented in a DSP based system and it is a robust algorithm that has proved useful in a wide variety of applications.

Conceptually, PID feedback sums the outputs of three separate feedback loops (Table I). Proportional feedback allows quick response to small features, and is used to increase the bandwidth of the loop, but will not address the problem of steady-state error. Integral feedback, described above, eliminates steady-state error, but does so at the expense of bandwidth and increased overshoot in the transient response. Differential feedback tends to reduce oscillations and overshoot in the transient response, but tends to amplify high frequency noise. By combining all three types of feedback one can tap the

strengths of each of the algorithms and arrive at a feedback loop which provides good performance.

Table I. Formulas for Feedback Algorithms

Proportional Feedback	$Z_t = P\,E_t$
Integral Feedback (Trapezoidal Approx.)	$Z_t = Z_{t-1} + I(E_t + E_{t-1})$
Derivative Feedback	$Z_t = D(E_t - E_{t-1})$
P-I-D Feedback	$Zt = P\,E_t + Z_{t-1} + I(E_t + E_{t-1}) + D(E_t - E_{t-1})$

An operational formula for PID feedback (using a trapezoidal approximation integral) is:

$$Z_{(k+1)t} = Z_{kt} + a\,E_{(k+1)t} + b\,E_{kt} + c\,E_{(k-1)t},$$

where $a = P+I+D$; $b = -P+I-2D$; and $c = D$

P = proportional gain I = integral gain D = differential gain

In our software P, I, D and S are set by the user; a, b and c are calculated by the PC. In our experience with AFM and STM, setting P a factor of 10 to 100 times higher than I provides optimum feedback.

Because differential feedback tends to amplify high frequency noise, we use it sparingly. In quiet systems, it does reduce oscillations, but most instruments do not suffer if it is not used. If differential feedback is omitted, the last term in the feedback equation can be dropped, saving processor instruction cycles.

Like integral feedback, the PID algorithm assumes a linear sensor response. Also like integral feedback, increasing any of the gains too much will cause oscillation, but if the gains are properly set, the response of the system is significantly better than if integral feedback alone is used.

Other Feedback Algorithms.

As mentioned previously, a variety of still more sophisticated algorithms exist[21,22] (optimal feedback, for example), but they generally require a mathematical model of the SPM stage response, including the characteristics of the tip-sample interaction. These algorithms enjoy only limited use for SPM because the sensor response can change unpredictably as the sample is scanned or when a different sample is imaged. PID feedback is perhaps the best feedback applicable for SPM because of its ability to tolerate a variety of system characteristics.

Optimizing feedback gains

If one endeavors to optimize the feedback gains by looking only at image quality, it is unlikely that a true optimum will be found. While it is true that image quality depends on the feedback gains, image quality is not a very sensitive measure of loop response. Step response curves, which indicate the response of the loop to a perturbation, provide a much more sensitive indicator of gain optimization and a more convenient way to adjust feedback gains.

To generate step response curves, such as shown in Figure 4, the setpoint is changed by an amount ΔS and the error signal is displayed for a few

Figure 4. Manual optimization of AFM feedback using step response curves. Curve A) Integral feedback only: I = 0.002, P = D = 0. Curve B) Raising I to 0.003 increases response rate but also increases the amount of overshoot (or oscillation). Curve C) Setting P to 0.03 increases response rate and decreases overshoot. The feedback now settles in about 0.25 ms (this corresponds to one data point or less if there are 250 points / scan line and the scan rate is 8 lines / second or less). For all of the curves $\Delta S = 50$ Å.

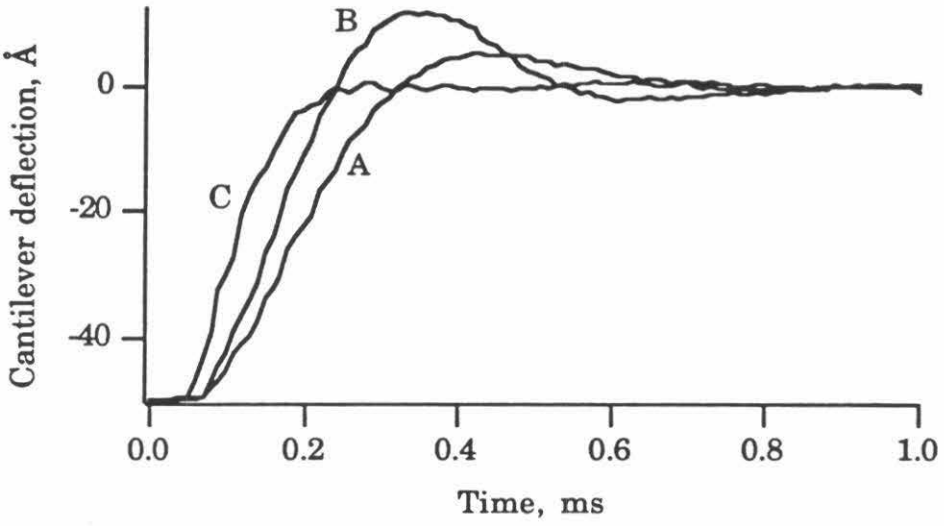
B
C
A
0
-20
-40
Cantilever deflection, Å
0.0
0.2
0.4
0.6
0.8
1.0
Time, ms

milliseconds afterward while the feedback adjusts to the new setpoint. (Due to the finite response time of the scanner, changing Z does not produce a real step response curve). The feedback behaves the same during a step response measurement as it would if a step were encountered on the sample and both the tip and the sample were perfectly sharp. By using step response curves, the feedback gains can be optimized either manually or automatically. Manual Optimization.

To manually optimize the feedback (see Figure 3), a step response curve is generated and the user adjusts P,I and D to reduce rise time and oscillations. In order to judge whether the new gain settings have decreased rise time and minimized overshot and oscillations another step response curve is generated. This process is repeated until the step response shows an optimal response. On our AFMs and STMs, if tip and sample are good, the feedback settles (as determined by visual inspection of the step response curves) within 20-50 feedback cycles. This means that the feedback will settle within one data point or less if the scan has 250 points per line and a rate of 4-10 lines/second. Thus, the feedback accurately follows topography as long as the error signal is within the loop bandwidth.

Automatic optimization.

The step response curve provides a quantitative measure of loop performance and allows automatic optimization of the feedback gains. The optimizer uses the standard deviation of the step response curve compared to an ideal step response as an indicator of loop performance. By using an "evolutionary" algorithm optimal feedback gains can be automatically found.

During automatic optimization nine "mutations" of the "parent" gain factors P,I and D are generated by multiplying them by random numbers between 0.9 and 1.1. A step response curve is then generated for the parent and each mutation, and the curve with the lowest standard deviation is found. The corresponding set of feedback gains become the parent values for the next round of optimization. The entire algorithm is repeated 10-20 times. The evolutionary optimizer works well when the initial PID gains are reasonable and the instrument is not excessively noisy. However, the evolutionary optimization tends to put the feedback on the verge of oscillation. Although this indicates that the feedback is optimized, it also means that if conditions change slightly the instrument may start to oscillate. Therefore we usually reduce P,I and D by about 1% after optimization.

C. SCANNING

In its most basic form, the scan subroutine generates the XY raster and stores incoming data. Useful extensions to the scanning subroutine can provide the ability to rotate the scan, "tilt" the scan and correct for scanner imperfections such as hysteresis and creep.

Basic Scanning

To generate a raster scan pattern digitally, X is repeatedly ramped between selected minimum and maximum values and Y is advanced after each cycle in X. For the XY raster to be useful for SPM both the minimum and

maximum values in each scan direction must be adjustable. This variability allows "magnification" and the area scanned to be changed.

Data Averaging

In our software, the scan rate is adjusted by varying the number of timer periods spent at each data point. To keep the scanner motion smooth, the raster advances after each period, rather than after each data point. Furthermore, the data recorded for each point represents an average value over the timer periods spent at that point. Thus data is not discarded at slower scan rates, but averaged to yield improved signal to noise ratio. To illustrate these ideas consider the following example. Assume that a scan has 250 data points per line in each direction. A typical scan rate of 4-10 lines per second then corresponds to 20 to 50 feedback cycles per data point. The maximum scan rate is 200 lines/second, or 1 feed back cycle per data point. Faster rates would yield fewer than one ADC reading per data point, effectively reducing the number of data points per scan line.

Raster Algorithm

The raster algorithm must avoid two potential pitfalls: 1) cumulative roundoff errors which appear in recursive algorithms; and 2) scan size and rate limitations which can arise in integer based algorithms. The following formula, implemented on a floating point DSP, generates an X raster without these problems. All variables are floating point numbers; a conversion to integer values is done before writing to the DAC.

$$X_t = X_o + t\,\Delta X,$$

where

X_o = starting point of the scan

t = time measured in timer periods

X_t = X position during timer period t

ΔX = X raster increment value (to be added with each timer period).

Although a raster can be generated using fewer instruction cycles, the above formula greatly simplifies programming, especially when implementing some of the features described below. An additional feature of this algorithm is that the term $t\,\Delta X$ eliminates the cumulative error which would result if $X_t = X_{t-1} + \Delta X$ were used.

Scan Rotation

An advantage of DSP raster generation is that the scan direction can be digitally rotated. Rotation is helpful in aligning the scan orientation to match long or narrow features so that the greatest possible pixel density can be acquired over the feature. Rotation is also necessary for AFM, in which friction between the tip and sample can adversely affect the feedback unless the scan direction is aligned perpendicular to the long axis of the cantilever.[23]

Since digital scan rotation is done in software, it is unlike analog scan rotation which requires dedicated hardware construction. Our implementation of digital rotation, which requires only ten instruction cycles, does not introduce additional noise into the scan, and is easily added to the basic scan routine. The algorithm requires advancing both X and Y during each timer period:

$$X'_t = X'_0 + t\,\Delta X'$$
$$Y'_t = Y'_0 + t\,\Delta Y',$$

where

$$X'_0 = (X_0 - X_c)\cos\phi + X_c - (Y - Y_c)\sin\phi - Y_c$$
$$Y'_0 = (X_0 - X_c)\sin\phi + X_c + (Y - Y_c)\cos\phi - Y_c$$
$$(X_c, Y_c) = \text{center of rotation}$$
$$\Delta X' = \Delta X \cos\phi$$
$$\Delta Y' = \Delta X \sin\phi$$
$$\phi = \text{rotation angle.}$$

The center of rotation is generally the center of the image. However, if the user pans (translates) the image when the rotation is nonzero, the center of rotation should not move with the image. Otherwise the image will pan in the wrong direction.

Sample Tilt Compensation

Compensation for sample tilt can be used to augment normal Z axis feedback or as a substitute for feedback. When sample tilt compensation is used with feedback, images of highly sloped samples can be improved by adding a raster to Z during scanning. This helps the feedback follow sample tilt in X by anticipating what the next Z value should be and adding a correction. As we commented earlier, this can be thought of as a type of slow feedforward correction scheme and acts to keep the errors which require feedback correction

small. As implemented in our software this algorithm takes about 5 instruction cycles. The mathematical expression for the algorithm is:

$$Z_t = Z_{t-1} + \Delta Z$$

The slope of the raster ΔZ is determined by the PC from analysis of the most recent image, and is inverted with each change in scan direction. Tilt correction is especially useful for "fast scan" imaging, in which the feedback gains are reduced and topography is recorded as fluctuations in sensor output. Unlike the XY raster, finite word length does not cause a problem with the Z raster because the feedback loop corrects for small errors.

Not all SPMs generate signals that are able to be directly used to control probe-sample proximity. The nearfield scanning optical microscope (NSOM) stands out as an example of a microscope which has no inherent feedback mechanism. To maintain reasonable tip-sample separation while scanning, these instruments require sample tilt compensation in both X and Y. In our work with NSOM we have replaced the feedback loop with the following algorithm (all variables are floating point quantities):

$$Z_t = i\,X_t + j\,Y_t + k.$$

The factors i,j and k are determined by the user from inspection of image sharpness. Although we are planning to add a feedback mechanism (lateral shear force feedback) to the NSOM in the future, the ability to use sample tilt compensation in place of feedback has proved very valuable for instrument development.

Hysteresis removal

Hysteresis and creep are two imperfections in piezoelectric scanner response which manifest themselves as important artifacts in most SPMs. Hysteresis occurs because the position of a piezoceramic scanner is not a linear function of the applied voltage; the piezo position depends on previously applied voltages. The nonlinearity caused by hysteresis can be as great as 25% of the scanner range.

Another imperfection seen in piezoceramics is creep, which often smears the first few lines of SPM images after panning or zooming. Creep is the continued mechanical motion of the piezo in spite of static electrode voltages. It can be compensated for while scanning and is an ideal candidate for being eliminated by feedback control of X and Y positioning. Because our systems do not have active XY positioning, we have not attempted to remove creep.

Hysteresis can be removed in four ways: i) using feedback in the X and Y dimensions; ii) generating the XY raster with a lookup table; iii) generating the XY raster with a nonlinear function and iii) warping the image after it is acquired. Although the first option is perhaps the optimal solution for both hysteresis and creep, we have not yet had the opportunity to upgrade our instruments to incorporate XY feedback. Because of its simplicity and ease of implementation, we have chosen to do hysteresis correction as a post image acquisition step.

Lookup table method

To compensate for hysteresis , an XY raster generation algorithm can be used to generate a nonlinear raster. This raster can be stored as a lookup table and new X and Y values read from the table before the first timer period of each data point. To provide for other motion periods the DSP can interpolate between lookup table entries. Because hysteresis depends on the recent scan motion history of the scanner, the same nonlinear raster cannot be used for all scans.

Nonlinear function method

A somewhat simpler method which requires more processor time is to generate a linear raster and then modify X and Y using a nonlinear function. The coefficients of the function have to change each time the X raster reverses direction. Unlike lookup tables, nonlinear functions do not permit complex high-order corrections, but for most scanners this type of correction scheme is adequate.

Post-processing method

Difficulties can arise when combining the above methods with features such as scan rotation. The method we have chosen simplifies programming by putting hysteresis correction in the PC software. The user-selected scan size and location is modified by the PC to correct for hysteresis. Hysteresis within the scan is eliminated by the image display software, which plots the data points in positions determined from measurements of the hysteresis characteristics of the scanner. The post-processing method has the disadvantage that, after processing, pixel density and scan rate are not constant throughout the scan.

tip-sample separation. The motor speed is proportional to a voltage set by a DAC. Generally, before starting the approach, the feedback has been turned off and Z set somewhere near the middle of the scanner range. The engage routine sets a DAC to start the motor and then waits for the sensor signal to cross the setpoint. When it does, the feedback is started and the motor shut off.

The engage routine also writes each ADC reading during the approach to a circular buffer. The sensor output for a few milliseconds after achieving feedback can then be plotted, a useful feature which helps the user check for false

Other artifacts

Other artifacts such as thermal drift, overall image curvature, and XY nonorthogonality can also be removed by the DSP and active feedback, but we remove them during image display.

D. TIP-SAMPLE APPROACH

The DSP subroutine which controls the approach of the tip and sample varies depending on the specific approach mechanism. We have designed two subroutines for application with either continuous approach or discontinuous approach mechanisms. We have used both subroutines successfully on various instruments in our laboratory.

Continuous approach

In a continuous approach, a motor slowly turns a screw which determines tip-sample separation. The motor speed is proportional to a voltage set by a DAC. Generally, before starting the approach, the feedback has been turned off and Z set somewhere near the middle of the scanner range. The engage routine sets a DAC to start the motor and then waits for the sensor signal to cross the setpoint. When it does, the feedback is started and the motor shut off.

The engage routine also writes each ADC reading during the approach to a circular buffer. The sensor output for a few milliseconds after achieving feedback can then be plotted, a useful feature which helps the user check for false

Figure 5. An AFM tip-sample approach curve taken in air. At t = -2 ms the tip and sample are already in contact with the cantilever deflected downward and the motion of the approach motor is pushing the cantilever up. When the cantilever deflection reaches its setpoint (zero deflection in this case), the feedback is started and the motor is shut off. Since the motor has rotational inertia, it takes about 35 ms to come to rest, and so the cantilever deflection does not immediately settle to the setpoint.

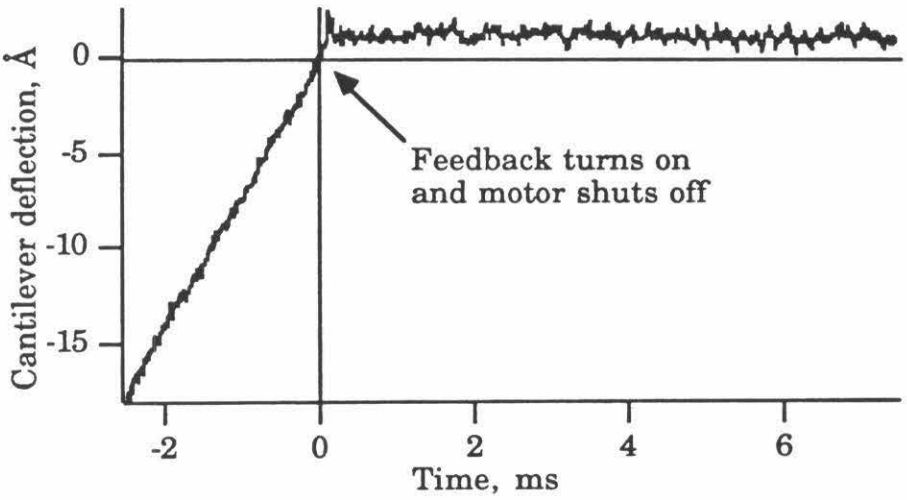
Cantilever deflection, Å
0
-5
-10
-15
Feedback turns on
and motor shuts off
-2
0
2
4
6
Time, ms

engages and tip crashes. Using engage plots such as the one in Figure 5, we have found that simply turning the feedback on when the sensor crosses the setpoint (as opposed to first withdrawing the tip) does not generally cause tip crashes in either STM or AFM.

Discontinuous approach

In a discontinuous approach, an inchworm, stepper motor, or some other device reduces the gap between the tip and sample in well defined increments, faster than the feedback can respond. The scanner must be set such that tip and sample are at their greatest separation before the approach mechanism takes a step. After each step, the feedback is turned on. If Z goes out of range, tip-sample separation is still too great and the cycle is repeated.

E. MODULATION MEASUREMENTS

In a modulation image, the dependence of an input on an output is determined at each point in the scan. For example, in STM, measuring the dependence of tunneling current on Z gives a barrier height image.[24] The dependence of tunneling current on V gives a density of states image.[25] In AFM, the dependence of cantilever deflection on Z gives an elasticity image.[26] Such modulation images can provide valuable information about the physical properties of a sample and give some indication of sample composition. Two types of modulation imaging which have been described in the literature include the difference method[25] and lock-in detection.

Modulation imaging is generally performed using a lock-in amplifier which can cost as much as the construction of an entire air STM. With DSP-systems software emulations of lock-in amplifiers are possible. Such emulations do not require any additional equipment and, within the bandwidth of interest for SPM, achieve signal to noise ratios similar to those of lock-in amplifiers. In fact, in our laboratory we have replaced our lock-in amplifiers with the emulation described below.

Difference method

One of the simplest ways to take a digital Z modulation measurement is to stop the XY raster momentarily and add a small change to Z, taking the difference between the input signal before and after the change in Z. This method is effective, but because no averaging (bandwidth limiting) is done, it does not achieve the optimum signal to noise ratio.

Lock-in detection

For lock-in detection of dC/dZ, a sinusoidal modulation is added to Z at an amplitude and frequency chosen by the user (typically the amplitude is ≈ 1Å and the frequency ≈ 1kHz). Neither the XY raster nor the feedback is interrupted for the modulation. The modulation frequency is set high enough and the feedback gains low enough so that the modulation is outside the bandwidth of the feedback loop. One can express this as:

$$Z'_t = Z_t + Hm_t,$$

where

$$m_t = \sin(\frac{2\pi t}{p})$$

H = peak to peak modulation amplitude

t = time measured in timer periods

p = modulation period measured in timer periods.

Assuming a linear sensor response, the magnitude of the error signal at the modulation frequency is given by:

$$A = \sqrt{A_0^2 + A_{90}^2}$$

$$A_0 = \frac{4}{np} \sum_{t=1}^{np} E_t m_t$$

$$A_{90} = \frac{4}{np} \sum_{t=1}^{np} E_t m_{t+\frac{p}{4}},$$

where:

A = peak to peak magnitude of the error signal

A_0 = amplitude of the component of the error signal in phase with the Z modulation

A_{90} = amplitude of the component of the error signal in quadrature with the Z modulation

n = number of modulation periods per data point.

The factor 4/np provides a peak to peak normalization of the amplitudes (assuming sinusoidal response).

The optimal division of tasks is to have the DSP store A_0 and A_{90} without the normalization factors, and have the PC normalize and take the square root. Note that n must be an integer for the algorithm to work; i.e., there must be an

integral number of modulation periods per data point. If a 1 kHz modulation frequency is used the fastest possible scan rate is one period or 1 ms per data point, corresponding to 2 lines/second at 250 point /line. Signal to noise is improved if slower scan rates are used; five or ten periods per point is not unreasonable if the SPM stage has the thermal stability required for such slow imaging.

The above algorithm uses every ADC reading taken during the modulation to yield better signal to noise ratios than difference algorithms which take only two readings per modulation. In addition, the XY raster is not stopped and the feedback is not turned off during the measurement thus avoiding glitches that degrade the data which occur when the feedback or raster are restarted.

The in phase and in quadrature components contain complementary information in a modulation image and so both A_0 and A_{90} should be stored if there will be a need to reconstruct phase as well as magnitude information. However, for basic elasticity or barrier height imaging we have found it sufficient to record only A_0; the 90 ° component provides negligible additional information at the modulation frequencies we use. By not recording the 90 ° component we reduce the amount of processor time required for modulation imaging from 25 to 18 instruction cycles and also halve the amount of data which needs to be stored for each modulation image.

Measurement of the second derivative

Digital control systems lend themselves particularly well to spectroscopy experiments.[13] Current-voltage tunneling spectroscopy can benefit from the measurement of both first and second derivative of current with respect to voltage.[27] The first derivative can be measured as described above; the second derivative can be measured simultaneously by detecting components of the error signal at twice the modulation frequency:

$$A_0 = \frac{4}{np} \sum_{t=1}^{np} E_t m_{2t}$$

$$A_{90} = \frac{4}{np} \sum_{t=1}^{np} E_t m_{2t+\frac{p}{4}}.$$

We have found that this technique performs satisfactorily when used in conjunction with the instruments in our laboratory.

F. OTHER DSP FUNCTIONS

Other DSP routines are needed to ramp the X,Y and Z voltages to specified values, move the coarse positioning translators, and measure a step response (by setting the step size to zero, the step response routine can double as a digital oscilloscope). Finally, there needs to be a main menu which calls the other routines in response to PC instructions.

G. THE USER INTERFACE

The user interface takes instructions from the user, sends data to the DSP, and displays data from the DSP. Implementation of the latter two functions is highly system dependent and does not effect instrument performance. However, the architecture of the instruction parser can contribute greatly to the utility and convenience of an instrument. The instruction parser consists of an input subroutine and a menu. The input subroutine takes instructions from the keyboard. The menu consists of a number of "if" statements, one for each possible instruction.

Input Subroutine

The input subroutine can be easily written to accept up to several hundred instructions, then feed them to the parser one by one. The SPM system is then effectively user programmable, greatly increasing its flexibility and making it possible for the system to perform simple experiments unattended. Conditional instructions, loop and branch instructions, and the ability to define macros which recall stored text files of instructions further increase the utility of the user interface.

The Instruction Parser

The user interface is most flexible if each basic operation of the SPM corresponds to an individual instruction. For example, it should be possible to set any of the DACs to a specified voltage from the parser. Conversely, all instructions should be as basic and low level as is reasonable. Commonly used functions, stored as macros, can then be built up from several instructions in such a way that they can be modified to suit the instrument and the operator.

The utility of this approach is illustrated by the ability to acquire a sequence of scans unattended. On instruments with a sample translator, macros can be written to translate, engage and scan repetitively. A sequence of scans with varying conditions or of different areas can be taken automatically. Strings of lithography operations can be performed. Among the macros we find most useful are those to implement circular image buffers, jog the tip-sample approach mechanism up or down until the sample is centered in the piezoceramic range and set parameters for various types of scans.

The macro driven parser simplifies use of the operating system since the beginning user need only know three or four macros to take images. It also makes the system more flexible because a more advanced user can build up low level commands into custom functions. Additionally, the availability of low-level commands is especially useful for testing new instruments, during which the need to perform unexpected operations often arises.

In addition to the word type instruction input, it should also be possible to change feedback and scan parameters with mouse or single keystroke commands while scanning. Real-time parameter updates not only make the software easier to use, but are invaluable for determining what effect various parameters have on image quality.

Another parser function we have found useful is an electronic logbook which keeps a record of important events (approaches, saves, etc.). The events are recorded when the various macros write to the logbook file (i.e., the approach

macro records sample tilt, current overshoot, etc.). Such a logbook can be of great help when analyzing data.

IV. CONCLUSION

A DSP based control system can be constructed quickly and inexpensively, or given sufficient time and money, can be developed into a state of the art SPM control system. With a DSP based system, it is possible to implement in software features such as scan rotation, modulation imaging and hysteresis correction, which would be difficult or expensive to implement with analog techniques. Consisting of just one or two components, a DSP board with integrated or separate analog I/O, the system has an overall conceptual simplicity. This simplicity leads to flexibility which permits a single system to support a wide variety of experiments and adapt to the changing demands of the SPM field.

The authors will gladly provide more detailed information on the algorithms discussed in this appendix to interested readers.

ACKNOWLEDGEMENTS

Financial support for this work was provided by Ford Motor Company, Abbott Laboratories, Inc., Topometrix, Inc., a National Science Foundation predoctoral followship (DRB), a National Institutes of Health Training Grant (GM07617) (SMC) and a Department of Education fellowship (MGY).

REFERENCES

1. G. Binnig, Ch. Gerber and C.F. Quate, *Phys. Rev. Lett.* **56**, 930 (1986).
2. C. F. Quate, "Scanned Probe Microscopies", pp. 1-8, American Institute of Physics Conference Proceedings #241, H. Kumar Wickramasinghe , Ed. 1992.

   H. Kumar Wickramasinghe, "Scanned Probes Old and New", pp 9-22, American Institute of Physics Conference Proceedings #241, H. Kumar Wickramasinghe , Ed. 1992.
3. O. Marti, S. Gould, P.K. Hansma, *Rev. Sci. Instrum* **59** (6), 836 (1988).
4. A. Brown, R.W. Cline, *Rev. Sci. Instrum* **61** (5).1484 (1990).
5. R.S. Robinson, T.H. Kimsey, *J. Vac. Sci. Technol.* **B9** (2), 631 (1991).
6. A.J. Hoeven, E.J. van Loenen, P.J.G.M. van Hooft, K. Oostveen, *Rev. Sci. Instrum* **61** (6), 1668 (1990).
7. R. Piner, R. Reifenberger, *Rev. Sci. Instrum* **60** (10), 3123 (1989).
8. S. Park, C.F. Quate, *Rev. Sci. Instrum* **58** (11), 2010 (1987).
9. A. Hammiche, Y. Wei, I.H. Wilson, R.P. Webb, *Rev. Sci. Instrum* **62** (2), 3010 (1991).
10. R. Erlandsson, R. Wigren, L. Olson, *Microsc. Microanal. Microstruct.* **1** (5/6), 471 (1991).
11. H. Halling, R. Moeller, A. Schummers, *IEEE Trans. Nuc. Sci.* **36** (1),634 (1989).
12. A. Schummers, H. Halling, K.H. Besocke, G. Cox, *J. Vac. Sci. Technol.* **B9** (2), 615 (1991).
13. D.P. DiLella, J.H. Wandass, R.J. Colton, C.R.K. Marrian, *Rev. Sci. Instrum* **60** (6), 997 (1989).
14. R. C. Barrett and C. F. Quate, *Rev. Sci. Instrum* **62** (6), 1393 (1991).

15. Spectrum Signal Processing, Inc., #301 3700 Gilmore Way, Burnaby, B.C. V5G4M1, Canada.

16. Texas Instruments, P.O. Box 1443, Houston, TX 77001.

17. For example, Data Translation, 100 Locke Drive, Marlboro, MA 01752.

18. D. Sheingold, ed., Analog-Digital Handbook (Prentice-Hall, Englewood Cliffs, New Jersey, U.S.A., 1986).

19. S.M. Clark, D.R. Baselt, C.F. Spence, M. G. Youngquist, J.D. Baldeschwieler, *Review of Scientific Instruments*, in press.

20. C. A. Putman, et al., in Proceeding of the SPIE Volume 1639, Scanning Probe Microscopies, edited by S. Manne, pp. 198-204.

21. Victor J. Bucek, Control Systems (Prentice-Hall, Englewood Cliffs, New Jersey, U.S.A., 1989).

22. G. Franklin and J. Powell, Digital Control of Dynamic Systems (Addison-Wesley, Menlo Park, CA, U.S.A., 1980).

23. A.J. den Boef, *Rev. Sci. Instrum* **62** (1), 88 (1991).

24. R. Wiesendanger, L. Eng, H.R. Hidber, P. Oelhafen, *Surf. Sci.* **189**, 24 (1987).

25. M.P. Everson, L.C. Davis, R.C. Jaklevic, W. Shen, *J. Vac. Sci. Technol.* **B9** (2), 891 (1991).

26. P. Maivald *et al*, paper presented at STM ' 90.

27. P.K. Hansma, ed., Tunneling Spectroscopy , Plenum, New York (1982).

Chapter II

A High Performance Scanning Force Microscope Head Design*

* Manuscript submitted to *Review of Scientific Instruments*

A high performance scanning force microscope head design

Steven M. Clark and John D. Baldeschwieler[†]

Division of Biology

and

[†]A. A. Noyes Laboratory of Chemical Physics

Division of Chemistry

California Institute of Technology

Pasadena, CA 91125

ABSTRACT:

A stable and highly sensitive scanning force microscope head design is presented. The head provides an implementation of the optical lever detection method in which mechanical vibration noise has been minimized.

INTRODUCTION:

Since its inception in 1985, the atomic force microscope[1] (also known as the scanning force microscope or SFM) has held great promise for imaging nonconducting samples with sub-nanometer resolution. Early attempts to image relatively inelastic samples such as graphite, crystals of ionic salts, and semiconductors yielded atomic resolution data. This data provided reason to believe that SFM might be applied easily to the study of biomaterials. However, as more compliant samples were examined, it became clear that several factors limit resolution on elastic samples. Among these factors are: i) unavoidable forces involved in tip-sample interaction; ii) tip shape; iii) sample motion, both scan induced and thermal; and iv) instrument and detection noise. Progress has been made in all of these areas; for example, imaging with both sample and cantilever immersed in liquid to reduce meniscus forces,[2] electron beam deposition of tips to increase tip sharpness,[3] imaging with specially prepared substrates to increase sample adhesion during imaging,[4] as well as efforts to image at low temperature to eliminate Brownian motion of the sample.[5] Other investigators have focused on sources of instrument noise and their reduction.[6] This paper describes a design to reduce mechanical noise and increase the stability of an SFM stage so that it exceeds the requirements for imaging biomaterials.

Establishing the force level acceptable for biomolecular imaging is difficult; it depends on the sample, preparation procedures, imaging environment, and other factors. Theoretical discussions of tolerable forces for biological samples advocate applied forces in the 10^{-10} to 10^{-11} N range.[7,8] We have used the more conservative 10^{-11} N figure as a design goal for the SFM stage

presented. One consequence of this force criterion is that, for stiff micromachined cantilevers (which have spring constants ≈ 1 N/m) motions larger than 0.1 Å are unacceptable. We have designed a SFM head that achieves stability and vibrational amplitudes less than this level. The body of this paper describes the design of the SFM head and discusses the most important factors considered during the design process.

DESIGN OVERVIEW:

A diagram of the SFM head is shown in Figure 1. Most commercial instruments are designed such that the sample is attached to the scanning element and moved while the probe remains stationary (except for small vertical deflections). In contrast, with our design the cantilever is scanned in a raster fashion over the stationary sample. This configuration was chosen for two reasons; first, it allows the head to be used in a "stand alone" mode in which it is used without the base, allowing the investigation of samples which are too large to be mounted on the SFM base. Second, in the case of samples on transparent substrates, it allows optical accessibility from the other side of the sample. This type of architecture allows the head to be used on an inverted epifluorescence type of microscope by using the microscope stage as the SFM base, thus making possible direct correlation between sample features in fluorescence microscopy and SFM.

MECHANICAL DESIGN:

The ideas at the foundation of the mechanical design are few and simple. They are: i) minimize the number of parts, ii) keep structures small and

Figure 1. A diagram of the scanning force microscope head. This simplified diagram of the SFM head indicates the relative positions of important components. For clarity, the base and the head support (approach) screws have been omitted.

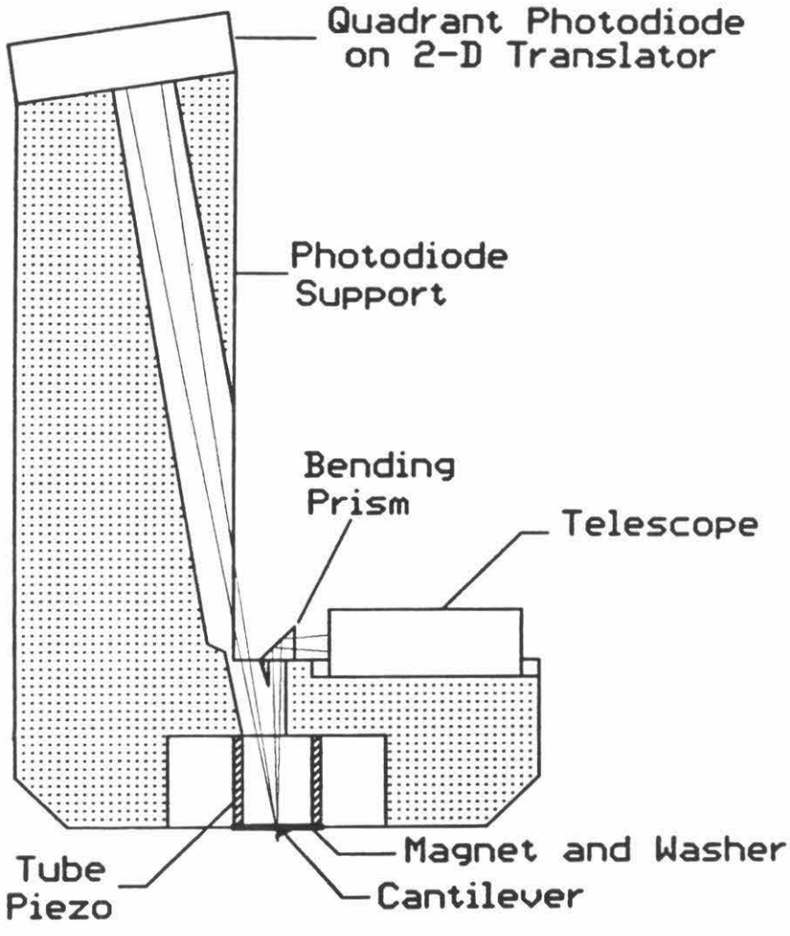

to the head. The electrodes are etched back from the edges of the tube to create a small area (a strip .005" wide on both ends of the piezo) of insulating ceramic material. This prevents electrical shorting and allows the piezo to be directly

places severe constraints on the input

must be focused to a small enough spot that the entire beam is incident on the back of the cantilever, even during large lateral motions; ii) the focused spot must have a depth of focus large enough to accommodate the full range of cantilever motion in the Z axis; and iii) the pointing stability of the input beam must be excellent to avoid introducing noise into the SFM experiment. This last

mechanically stiff, and iii) make sure that vibrations induced by seismic and acoustic disturbances are common mode to the structure. There was no effort made to use dissipative materials in the design because the philosophy was to eliminate excitation sources through acoustic shielding and vibration isolation as required, rather than design a system with low Q resonances in which vibrations might still enter the region of experimental interest.

The SFM head consists of only one major part, the head itself, which serves as a stiff platform to rigidly couple the input telescope, the piezo tube and the detector. This makes most motions induced by acoustic and seismic stimuli common mode to the structure and minimizes their effect.

To achieve our second design goal we used parts of small physical dimensions and mounted them in a rigid fashion. The only partial exception is the photodetector support which takes the form of a post with a 1/2" diameter bore for the return beam path from the cantilever. Although this structure is large, it is integral to the head and quite stiff. The frequencies of its lowest resonant modes are well above the regions of experimental interest. Despite attempts to excite transverse vibrations of the photodiode support, we have been unable to observe its motion. This leads one to believe that resonant motion of the support is, in fact, negligible.

The piezo tube is mounted in such a way as to avoid compliant coupling to the head. The electrodes are etched back from the edges of the tube to create a small area (a strip .005" wide on both ends of the piezo) of insulating ceramic material. This prevents electrical shorting and allows the piezo to be directly

glued to both the head and the magnet which holds the cantilever assembly, thus avoiding the use of layers of insulating materials which may be elastic.

The cantilever support consists of a small steel wedge soldered to a steel washer. The cantilever die is positioned near the wedge such that the beam reflected from the back of the cantilever is centered in the bore of the photodiode support. During the optical alignment process the die is held and positioned by means of a vacuum chuck with a multi-axis adjustment fixture. Once the proper cantilever position has been found the die is glued to the wedge to fix its position. While this procedure is somewhat cumbersome, it allows for the compensation of cantilever warpage or other changes in the position of the return beam (such as those from a liquid cantilever environment). In practice we find that the alignment time taken for this instrument is about the same as that required for mounting and aligning tips in the commercial instruments we have used. The elimination of optical adjustments in the beam paths is the major compromise in ease of use which has been made in order to eliminate potential sources of mechanical noise.

OPTICAL DESIGN:

Although the scanned cantilever architecture has attractive features, it places severe constraints on the input optics. These constraints are: i) the beam must be focused to a small enough spot that the entire beam is incident on the back of the cantilever, even during large lateral motions; ii) the focused spot must have a depth of focus large enough to accommodate the full range of cantilever motion in the Z axis; and iii) the pointing stability of the input beam must be excellent to avoid introducing noise into the SFM experiment. This last

constraint was found to be particularly important in previous SFM head designs constructed in our laboratory. In some cases instrument performance was compromised by thermal drift of components in the input beam path. In order to demonstrate the flexibility of this head design we have used two different light input schemes.

The object of the first input scheme, shown in Figure 2, is to remove heat sources from the head. To accomplish this we removed the laser from the head assembly by using a single mode optical fiber to couple the laser output to the input optics. In addition to avoiding thermal transients, as might be induced by an integral laser diode, this scheme also provides good vibration isolation and allows the use of different lasers.

The use of a single mode fiber (SMF) for the input beam dictates that a telescope be provided to focus the beam onto the cantilever. The SMF has a 4 μm diameter core and a numerical aperture of ≈ 0.1. The desired beam diameter incident on the back of the cantilever is ≈ 10 μm, the depth of focus must be > 2 μm and the focus must lie ≈ 1.5 cm from the front surface of the second lens. These figures impose a maximum lateral magnification of two and demand diffraction limited performance of the telescope. This was achieved through the use of two achromats; the first collimates the output of the fiber and optimally matches the collimated beam diameter to the second lens, and the second serves to focus the beam on the cantilever. Ray traces of the telescope predict the $1/e^2$ spot diameter at the cantilever position (1.2 cm from the last surface) to be 10 μm and the depth of focus to be ≈ 25 μm. These figures agree with the results of a Gaussian optical analysis of the system which give the spot diameter as 10 μm and a depth of field of ≈ 30 μm.

Figure 2. A diagram of the single mode optical fiber input optics. The telescope is composed of two achromats. It uses a connectorized single mode optical fiber as input and focuses the light to a ≈ 10 μm diameter spot at ≈ 1.2 cm from the output lens. This provides a spot of the required dimensions and, because the telescope has no local heat source, the position of the spot is extremely stable.

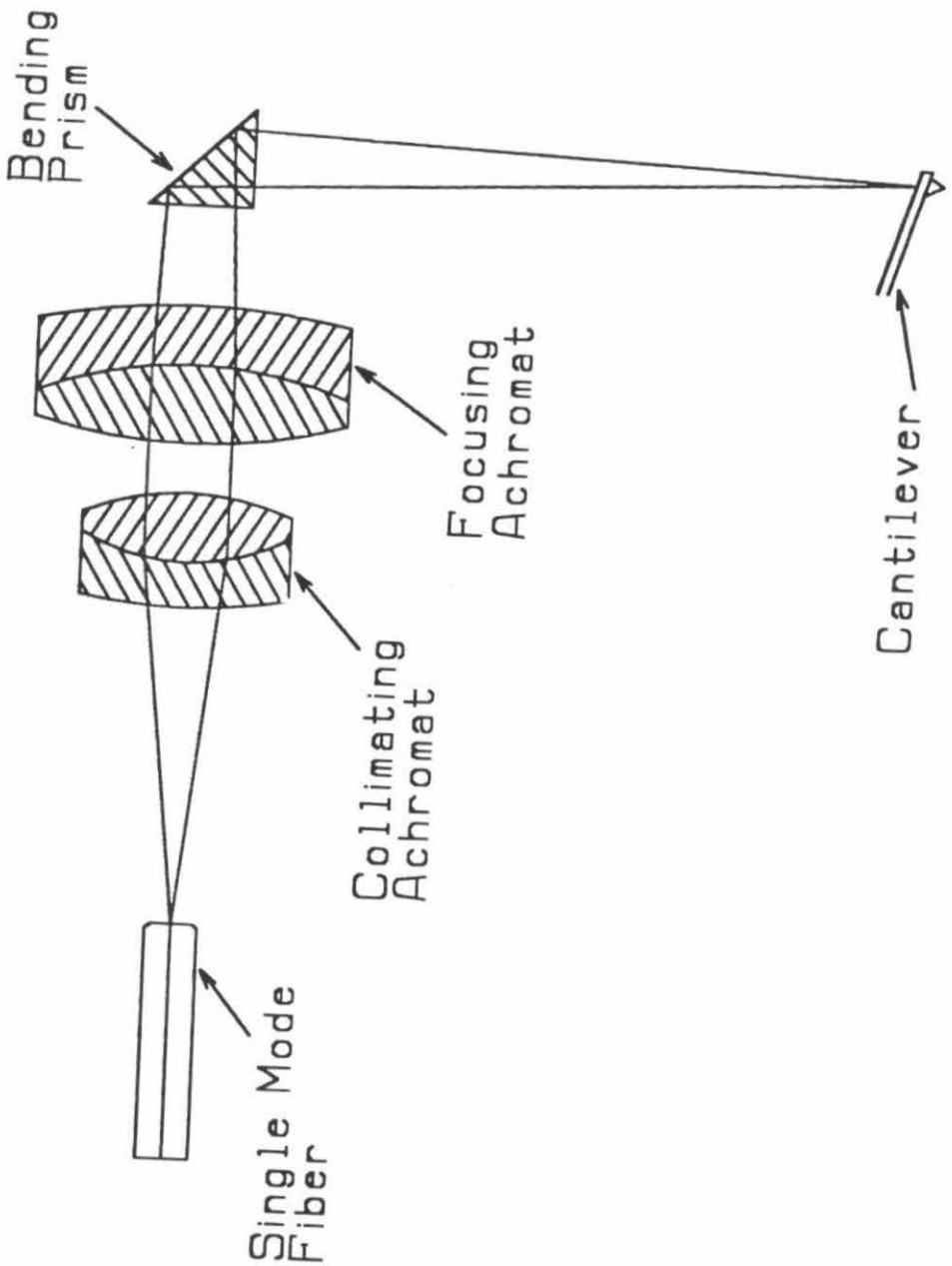
Bending
Prism
Focusing
Achromat
Collimating
Achromat
Single Mode
Fiber
Cantilever

The telescope rests in a "vee" groove machined into the head that serves to constrain its motions except axial rotation and translation. After optimizing the spot diameter on the cantilever by axial translation of the telescope, a small spring clamp holds it in position. This "semi-kinematic" mounting provides very stable and repeatable positioning of the telescope even during focus adjustment. The only other optical component in the input beam path is the bending prism which deflects the beam, by total internal reflection, so that it is coaxial with the piezoelectric ceramic tube. (Because the acceptance angle of the prism exceeds the beam convergence angle, the criterion for total internal reflection is met by all rays.) A prism was chosen for this application instead of a mirror because it does not require a mount if glued directly to the head and so provides an inherent stability in defining the optical path. The input optics perform satisfactorily as judged by the apparent beam diameter and stability as viewed on the cantilever at 40 X magnification and by the Gaussian spot reflected from the cantilever.

The second light input configuration uses an integral laser diode. This scheme, shown in Figure 3, is conceptually the same as that first used for SFM by Meyer and Amer,[9] and is often found in commercial instruments. In our implementation a collimated laser diode "bullet" is used as a light source and the output of the "bullet" is focused onto the cantilever by an achromat. From ray traces of this system we estimate the focused spot to be elliptical with a major axis of $\approx$ 20 µm and a minor axis of $\approx$ 10 µm.

As with any optical lever based SFM, the beam reflected from the back of the cantilever provides a sensitive measure of cantilever deflection. In this design, a quadrant photodiode is used to sense the position of the reflected beam and provides both torsional and vertical deflection signals. The fine positioning

Figure 3. A diagram of the laser diode input optics. Light from a visible laser diode pen is focused onto the back of the cantilever by an achromat. Only one lens is required because the output of the laser diode pen is collimated. The focused spot at the cantilever is elliptical with a major axis of ≈20 μm and a minor axis of ≈ 10 μm. In our implementation of this scheme the laser diode pen mounts directly in the lens housing and this assembly is substituted for the telescope assembly.

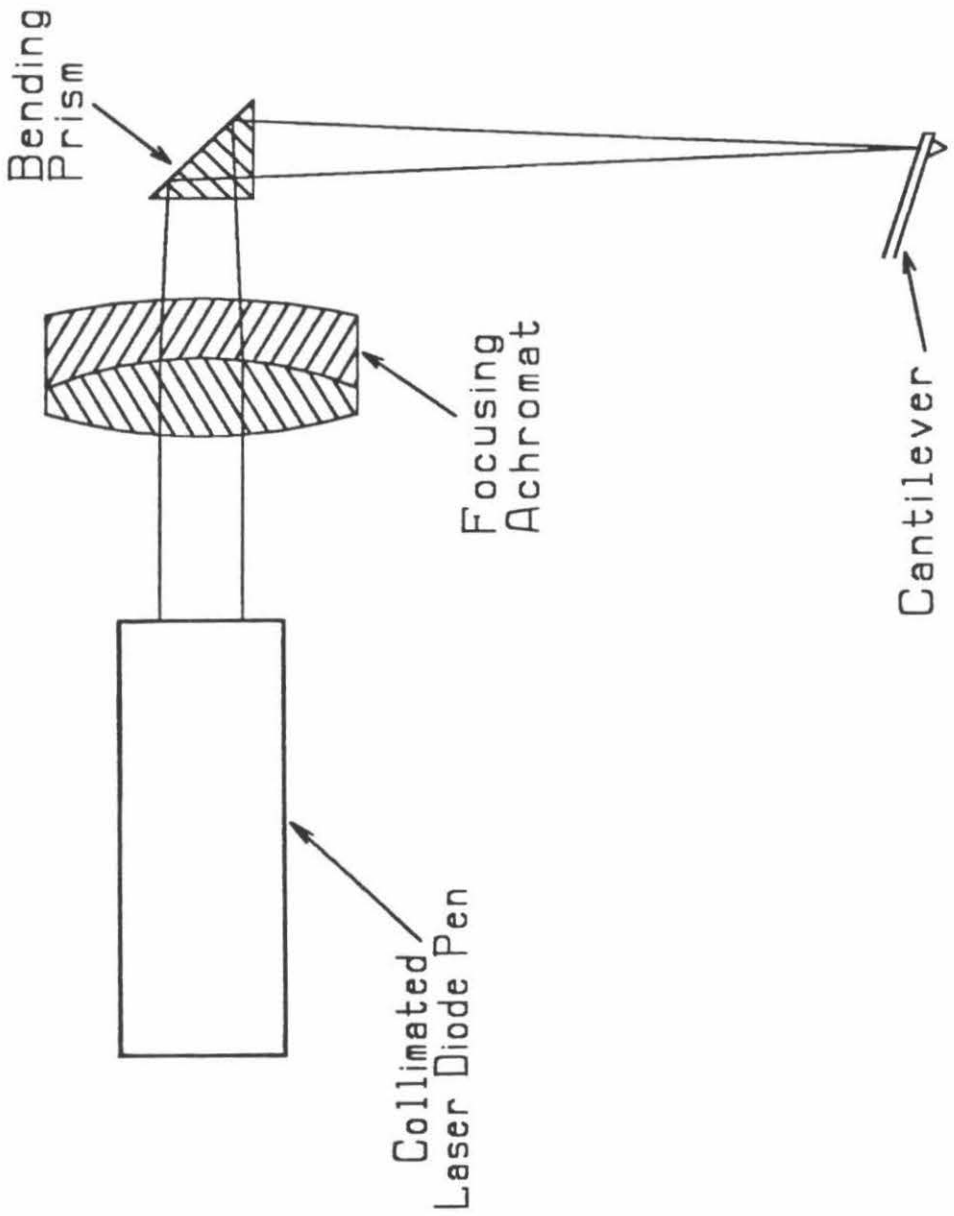
Bending
Prism
Focusing
Achromat
Cantilever
Collimated
Laser Diode Pen

of the photodiode can be adjusted by means of a two-dimensional short travel translator mechanism. There are no optical elements between the cantilever and the photodiode. Thus the only source of beam motion is the motion of the cantilever (disregarding pointing noise of the input optics which is negligible). The optical lever gain has been made as large as possible to provide maximal sensitivity and increases the signal to noise ratio. The reflected beam from the cantilever is divergent, because it is focused on the cantilever, and it is this divergence which places a practical limit on the path length from the cantilever to the photodiode. To allow the path to be as long as possible, a large photodiode is used to collect all of the return beam. The photodiode we use has a ≈ 12 mm aperture allowing a path length of ≈ 12 cm from the back of the cantilever to the face of the photodiode. In addition to enabling large optical lever gain, the increased size of the beam at the detector alleviates any concerns about local saturation of the photodiode active surface. Because the bandwidth we require is less than ≈ 100 kHz, the photodiode is used in the photovoltaic mode to minimize noise.

PERFORMANCE OF THE HEAD:

In order to demonstrate the capability of the head design, in Figure 4 we show images of a micro-crystal of bovine catalase. Imaging of protein micro-crystals requires that only small forces be applied to the sample; thus they provide a good test of the performance of the SFM head design. The first image, Figure 4a, shows a low magnification scan (1.5 µm x 1.5 µm) taken in air of a single protein micro-crystal. The plate morphology of the crystal is similar to that of other larger crystals found in the sample by light and electron microscopy (data not shown). In several places large defects in the crystal (e.g., concavities in

Figure 4. Images of micro-crystals of beef liver catalase. These images were taken in air with an electron beam deposited "super" tip. Both images were acquired using forces of ≈ .1 nN and have a sampled resolution of 250 x 250 pixels. They are displayed with brightness proportional to both topographical height and slope after tilt was removed by plane subtraction. a) A low magnification image (1.5μm x 1.5 μm scan range) of a single micro-crystal of beef liver catalase on a glass substrate. The crystal has a plate morphology with obvious defects in its surface. b) A higher magnification image (340 nm x 300 nm range) of a region of the same catalase micro-crystal. In this image the ≈ 10 nm period of the crystal is visible, however the resolution is inadequate to visualize the tetrameric structure of the individual catalase molecules which comprise the crystal.

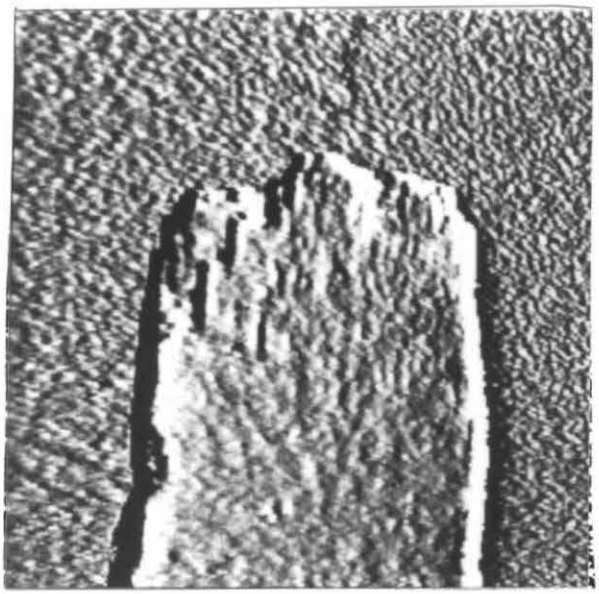

Figure 4a.

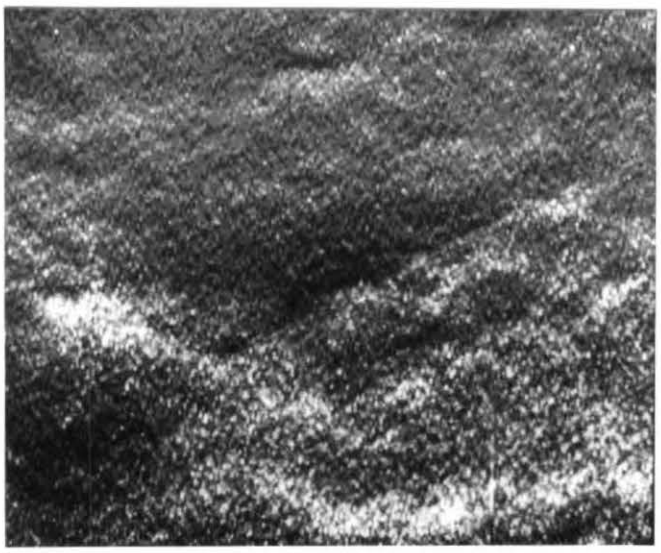

Figure 4b.

the surface) can be seen. In Figure 4b, a higher magnification image is shown in which the crystalline repeat can be seen. The characteristic dimension of the repeat is ≈ 10 nm, which agrees well with literature values.[10-12] Although catalase has a tetrameric structure, this image does not exhibit adequate resolution for these features to be seen. The images of Figure 4 were taken in air at a sampled resolution of 250 x 250 pixels using a commercial cantilever with an electron beam deposited tip. The force applied to the sample, as calculated from cantilever deflection, cantilever geometry and materials constants, was less than 1 nN for both of the images shown.

The authors will gladly provide more detailed documentation to interested readers.

ACKNOWLEDGMENTS:

The authors wish to thank Charles F. Spence for stimulating discussions and Dr. Jean-Paul Revel and Michael G. Youngquist for a critical reading of the manuscript. Financial support for this work was provided by Abbott Laboratories, Inc, the National Institutes of Health (Training Grant GM07617) and the United States Public Health Service (Training Grant HG00021).

REFERENCES :

1. G. Binnig, Ch. Gerber and C.F. Quate, *Phys. Rev. Lett.* **56**, 930 (1986).
2. H. G. Hansma, *et al*, *Science* **256**, 1180 (1992).
3. Y. Akama, E. Nishimura, A. Sakai and H. Murakami, *J. Vac. Sci. Technol.* **A8** (1), 429 (1990).
4. C. Bustamante, et al., *Biochemistry* **31**, 22 (1992).
5. C. B. Prater, et al., *J. Vac. Sci. Technol.* **B9** (2), 989 (1991).
6. S. M. Clark, *et al*, in press, *Review of Scientific Instruments*.
7. B. N. J. Persson, *Chem. Phys. Lett.* **141**, 366 (1987).
8. K. E. Drexler, *J. Vac. Sci. Technol.* **B9** (2), 1394 (1991).
9. G. Meyer and N. M. Amer, *Appl. Phys. Lett.* **53** (12), 1045 (1988).
10. M.R.N. Murthy *et al*, *J. Mol. Biol.* **152**, 465 (1981).
11. I. Fita *et al*, *Acta Cryst.* **B42**, 497 (1986).
12. T. Furuno, K. Ulmer and H. Sasabe, *Microscopy Research and Technique* **21**, 32 (1992).

Appendix C.

Design Details of the Scanned Force Microscope Head

I. Overview

II. Assemblies and Components

A. Base Assembly

B. Head Assembly

- The Head
- Telescope for Single Mode Fiber Input
- Telescope for Collimated Laser Diode Input
- Photodiode Translator
- Parts From Commercial Suppliers

I. Overview

In Chapter II many of the ideas which gave rise to this head design were discussed, but much of the practical detail required for its manufacture was omitted. In this Appendix we present a list of purchased parts and the drawings required to fabricate the head. We also briefly touch on some of the strengths and weaknesses of the design in light of the experience gained in using the head to image biological materials.

Due to its "stand-alone" architecture, the head can be easily separated both physically and conceptually into two parts, the base and the head itself, which will each be discussed in turn.

II. Assemblies and Components

A. The SFM Base Assembly

The SFM base, as presently used, consists of three pieces: i) the base; ii) a sample support and iii) the base suspension ring assembly. The base is shown in Figure 1. It was originally machined from Invar, however stainless steel would probably also perform adequately. The base has a 1.100" diameter bore in the center which was originally meant to accommodate an optical microscope objective lens. This was to be used for concurrent epifluorescence / SFM or for flash photolysis of caged precursors of biologically active compounds (e.g., caged ATP). This base has no sample clips because scan induced sample motion was a concern; samples are fastened to the base with adhesive. This method of fastening samples does offer good support, which

Figure 1. The AFM base.

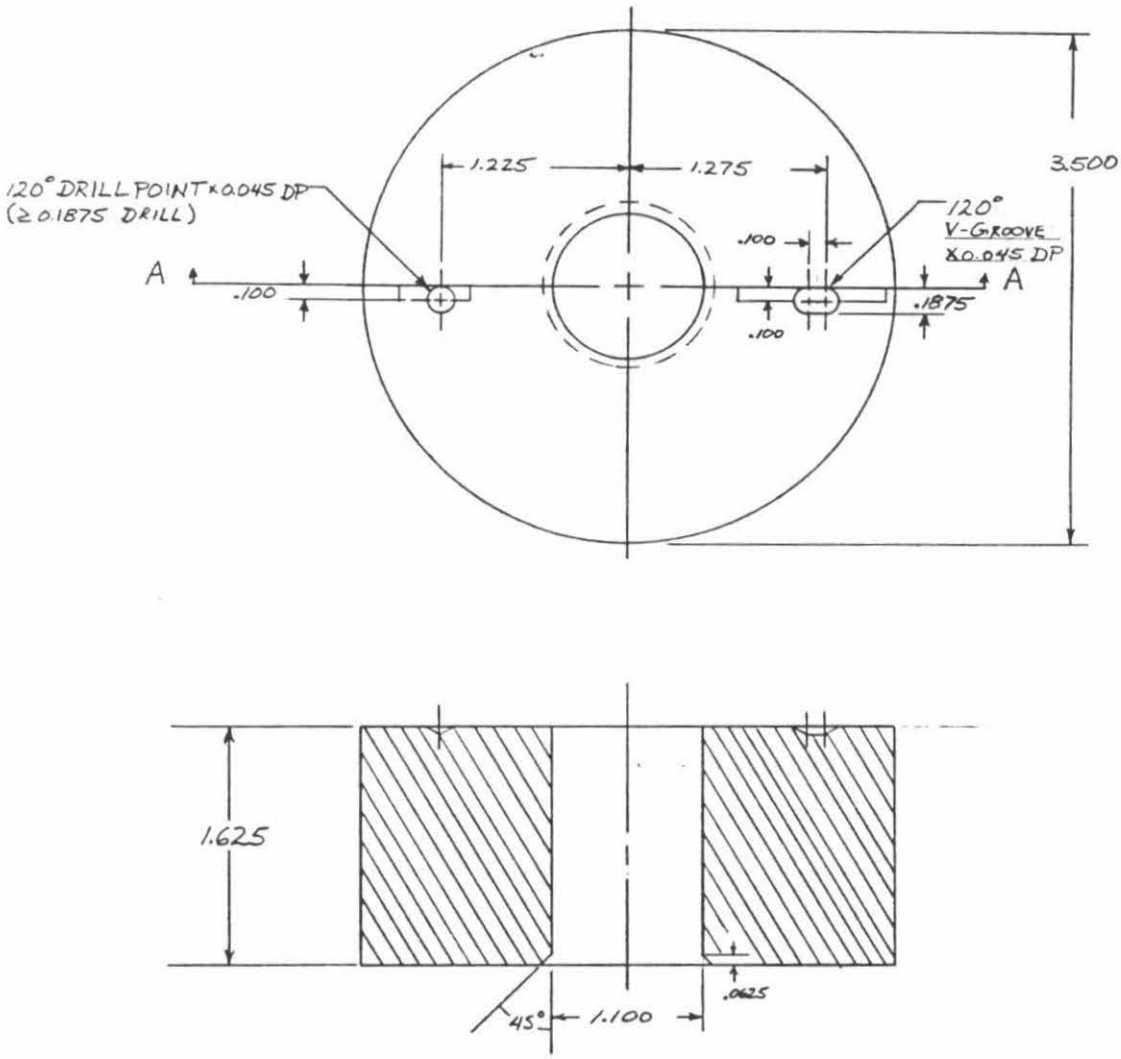

SECTION A-A

AFM BASE

SCALE 1:1 MATERIAL: INVAR

TOLERANCES: .XXX = ±0.002"

is crucial to avoid excessive vibration, however it does not allow for sample translation.

After using the base for some time, it became clear that it would be useful to be able to examine specimens which were mounted on scanning electron microscope (SEM) sample stubs to allow direct comparison of SFM and SEM data. To accomplish this, the base was modified as shown in Figure 2 and a sample adapter, shown in Figure 3, was made. The SEM stub mounts directly into the adapter via the hole in the center of the top surface. The adapter can either be allowed to rest on the modified base or it can be tensioned against the base using a suitable washer and screw. When allowed to simply rest on the base, the adapter is free to rotate. Because the adapter is slightly eccentric (due to machining imperfections) it can be used as a "poor - man's" sample translator.

Isolation from both seismic and acoustic noise sources can be important for high resolution imaging by SFM. To isolate the SFM head from seismic excitations a suspension ring was fabricated. A drawing of the ring is shown in Figure 4. When suspending the SFM head it is important to arrange for the suspension points to be above the center of gravity of the entire head assembly. This was achieved by using 3" long 1/4-20 eyebolts which were threaded into the suspension ring. Lock nuts were used to keep the eyebolts from turning. To provide a long pendulum, Silastic (surgical rubber) tubing was used to suspend the head assembly from the ceiling of the laboratory. In many cases this type of seismic vibration isolation has performed quite well; several other laboratories use similar schemes to isolate their microscopes. Often the suspension take the form of a massive platform

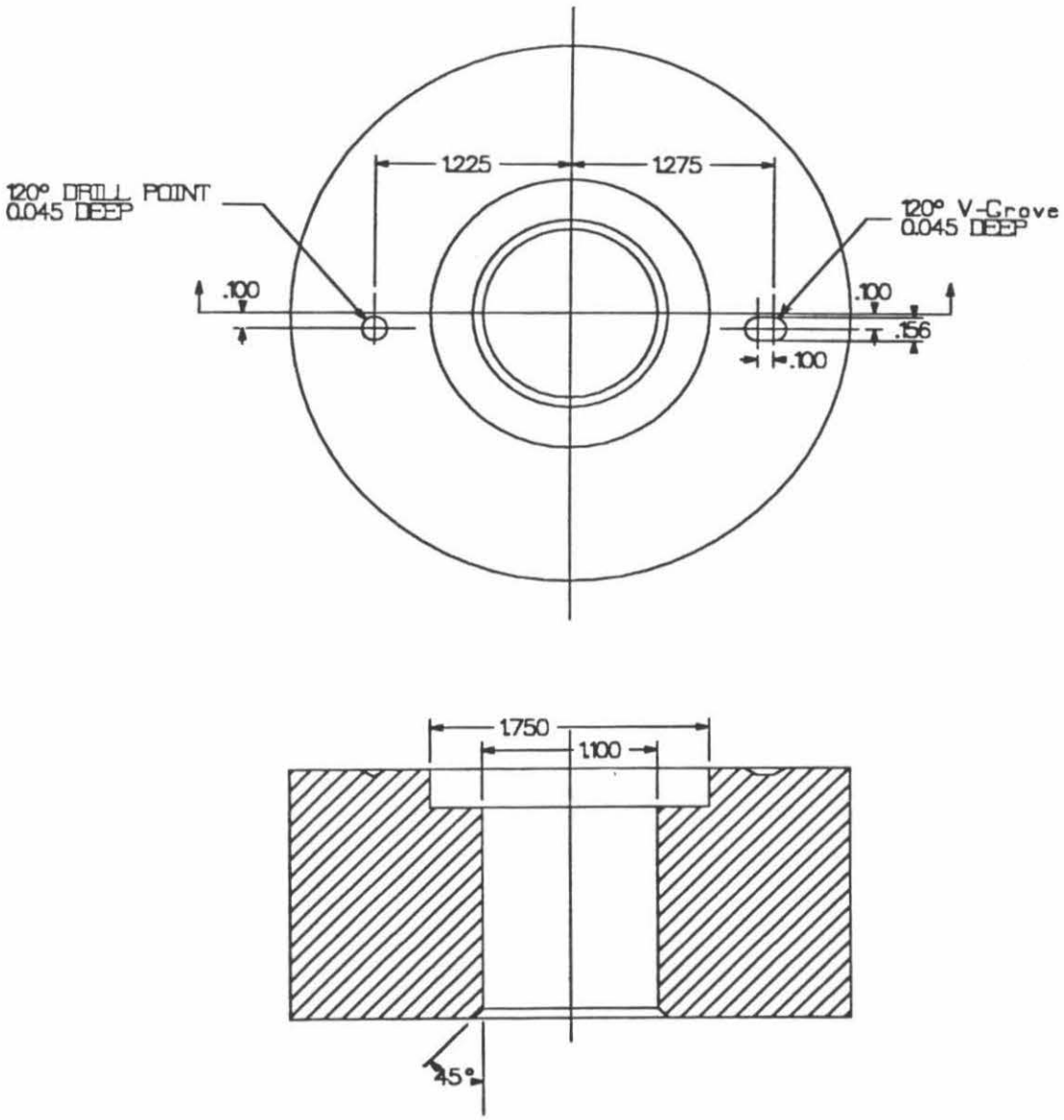

Figure 2. The modified AFM base.

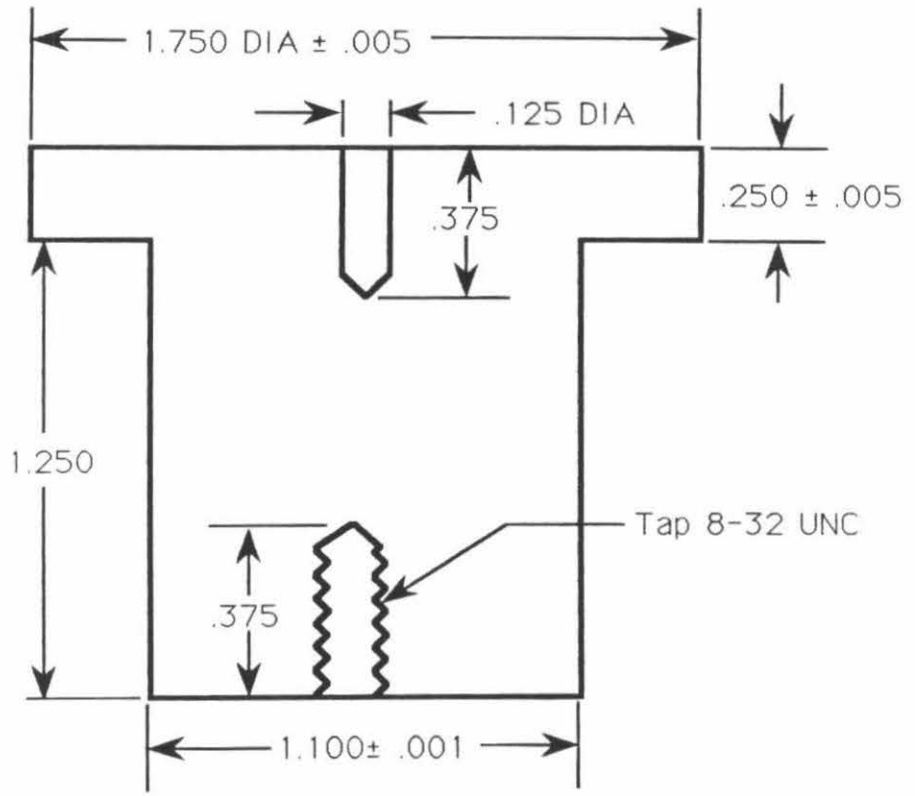

Figure 3. The SEM sample stub adapter.

Figure 4. The AFM base suspension ring.

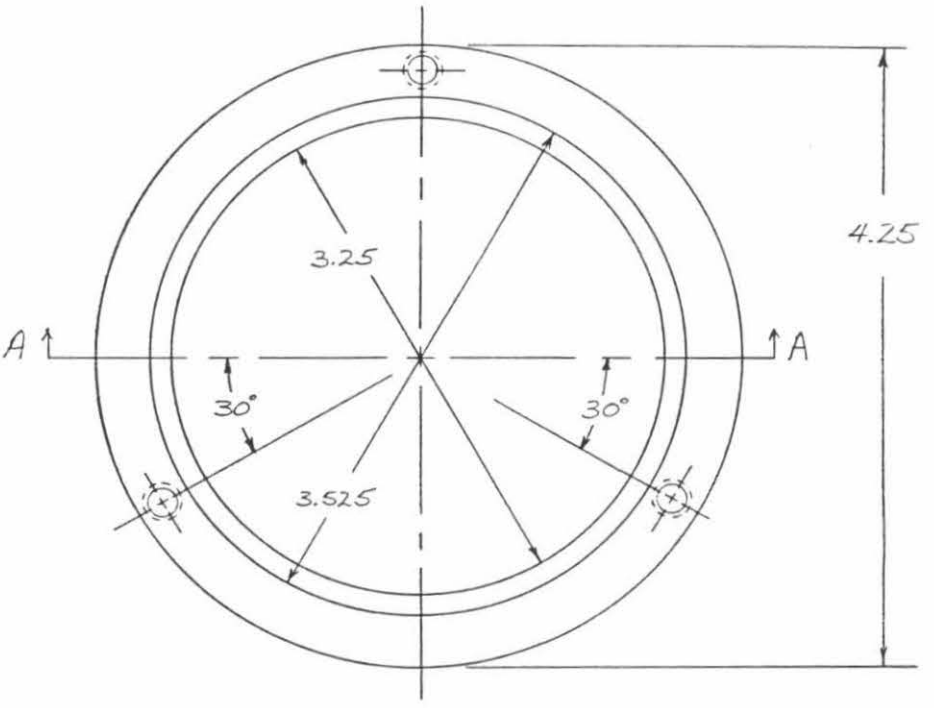

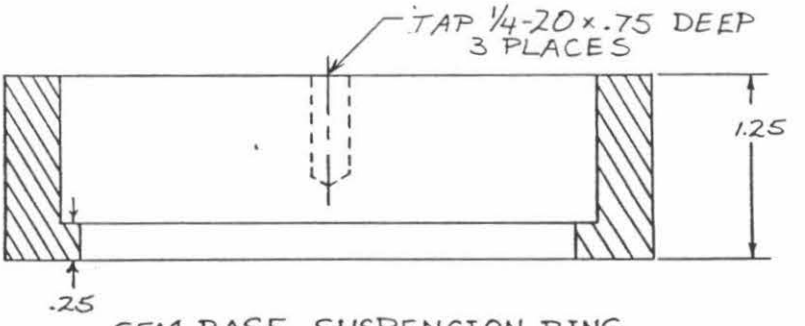

SFM BASE SUSPENSION RING

MATERIAL: 2024 ALUMINUM

.XX = ±0.010" .XXX = ±0.005"

FINISH: TYPE II BLACK ANODIZE

suspended by elastic supports with an enclosure on the platform to provide acoustic isolation for the instrument.

Recently, due to concerns about air currents effecting instrument performance, we have stopped suspending the SFM head assembly. In the current configuration, the base rests on a lead plate which is supported by rubber pencil erasers (Pink Pearl) on a pneumatically suspended vibration isolation table. With the head assembly on the table, it is possible to place a box over it to provide acoustic isolation and to restrict air movement. In this scheme, the suspension ring provides mechanical clearance for the head of the screw which tensions the SEM stub adapter.

Perhaps the most useful modification to the SFM base which could be made is the incorporation of a sample translator. This would be especially beneficial for imaging biological specimens where one typically examines relatively large portions of a sample in search of particular structure. A typical example of this might be the search for double stranded DNA molecules which have been deposited at dilute concentration. A translation mechanism also allows one to gather many images of a surface and thereby gain a "feel" for the sample. This capability is quite advantageous when working out sample preparation methods.

We have not yet had an opportunity to use the SFM head in conjunction with an epifluorescence optical microscope, however a prototype stage for a Nikon Diaphot microscope has been fabricated. By using this stage, concurrent optical microscopy and SFM can be done. This approach

should prove invaluable in attempts to obtain SFM data on biological samples.

B. The SFM Head Assembly

- The Head

The SFM head assembly consists of the SFM head, an input telescope assembly, the photodiode translator assembly and miscellaneous parts. The machine drawings for the fabrication of the head are shown in Figures 5a-e. The head was fabricated from aluminum using both conventional and electrical discharge machining methods. The main features of this design are its low cost, its lack of adjustments and its simplicity.

The assembly of the head requires that the input telescope be assembled and installed on the head and that the piezo tube be prepared and installed. The preparation of the piezo tube was covered in Chapter II and only a couple of details need to be mentioned before moving to the telescope.

In preparing the piezo itself, we have found that after the quadrants have been etched back from the ends of the tube it is convenient to solder the electrode wires to the tube and then coat the tube with clear polyurethane (this is available in spray cans at hobby stores). The coating serves to electrically insulate the piezo and to keep moisture and chemicals out of the piezo material. After the coating has dried, the ends of the tube are scraped clean of the coating to provide a solid contact surface for both the head and the magnet which retains the cantilever and its mounting washer.

Figure 5. Mechanical drawings of the AFM head (pages 223-227).

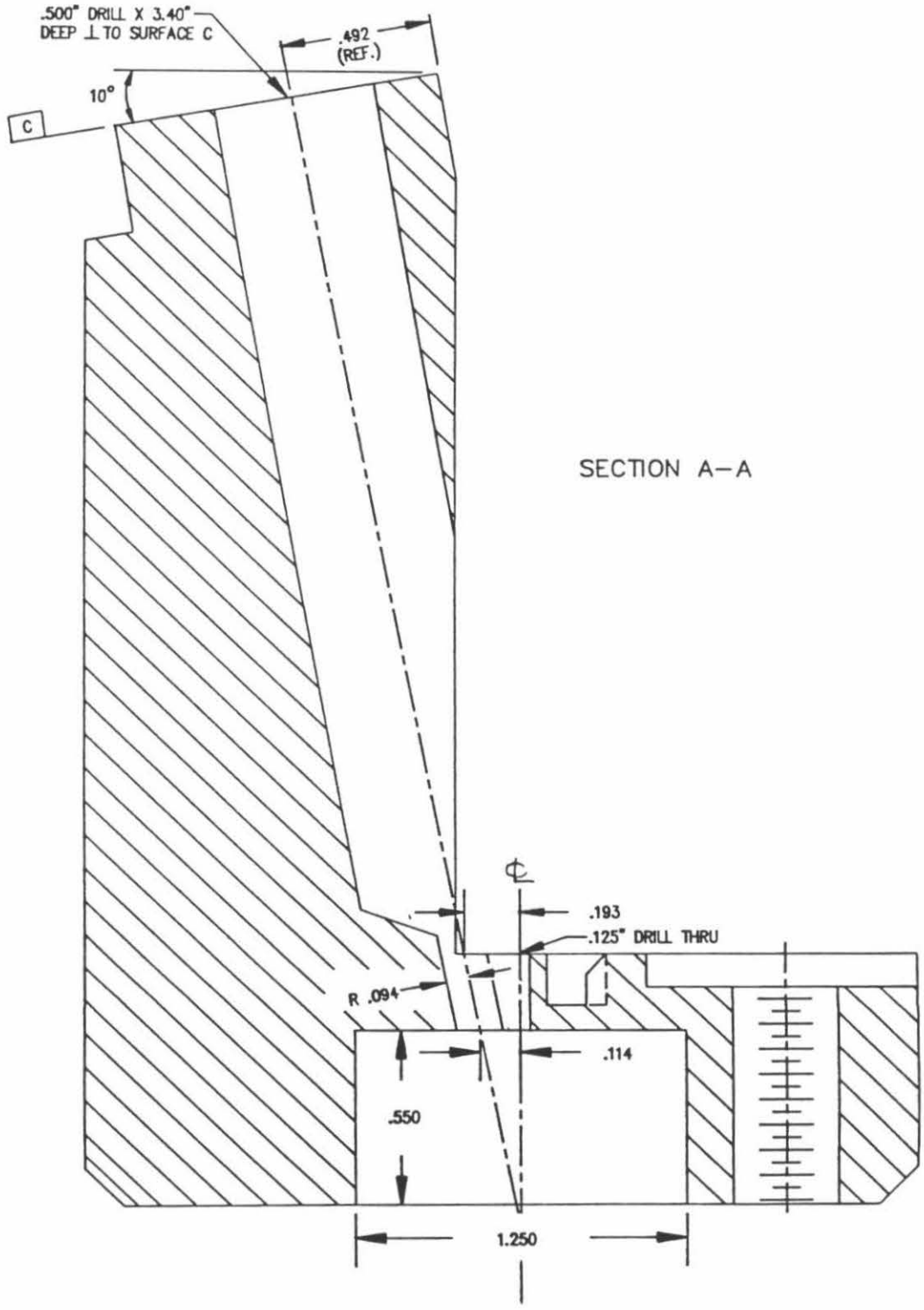
.500" DRILL X 3.40"
DEEP ⊥ TO SURFACE C
.492
(REF.)
10°
C
SECTION A–A
℄
.193
.125" DRILL THRU
R .094
.114
.550
1.250

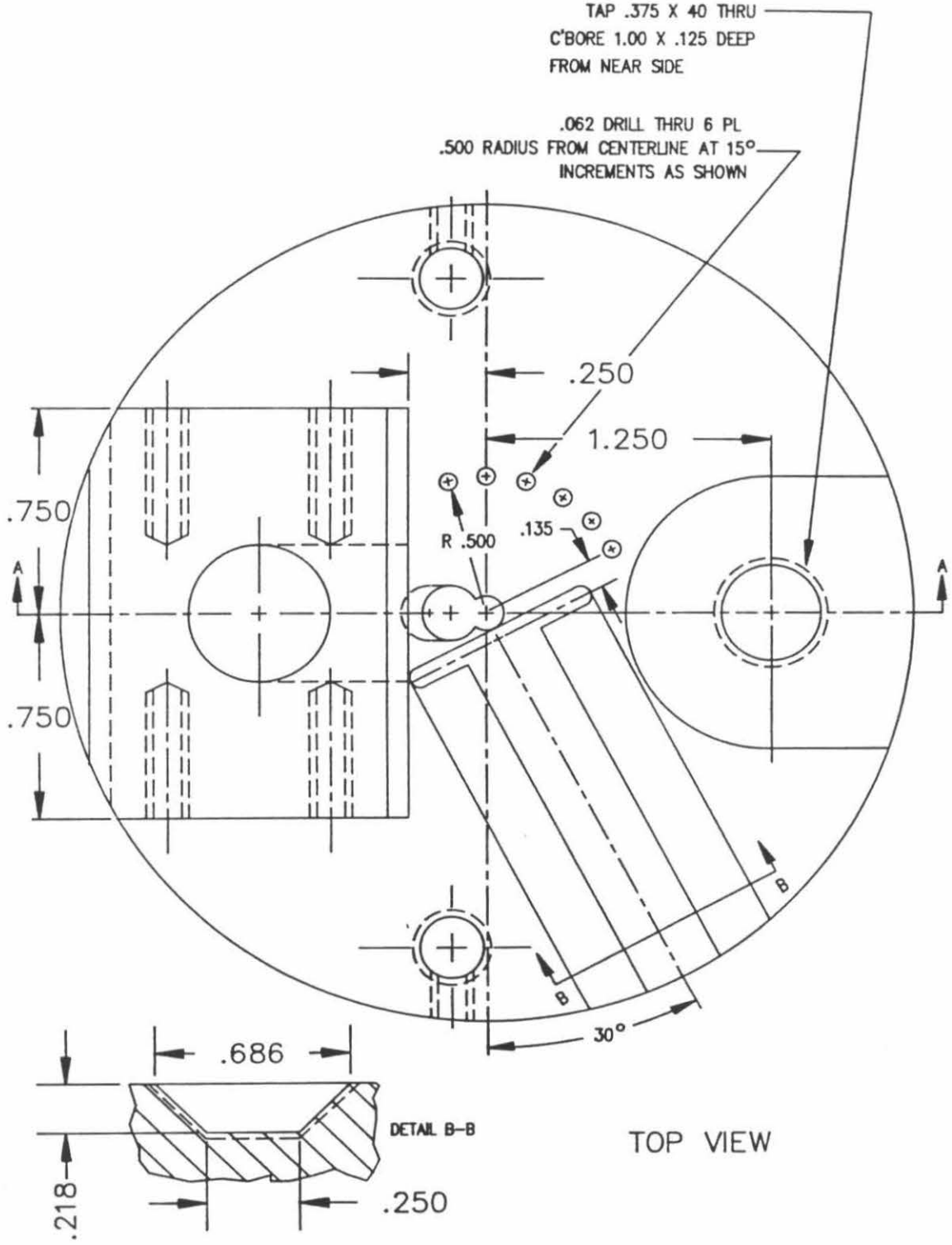
TAP .375 X 40 THRU
C'BORE 1.00 X .125 DEEP
FROM NEAR SIDE
.062 DRILL THRU 6 PL
.500 RADIUS FROM CENTERLINE AT 15°
INCREMENTS AS SHOWN
.250
1.250
.750
.750
R .500
.135
A
A
B
B
30°
.686
.218
.250
DETAIL B-B
TOP VIEW

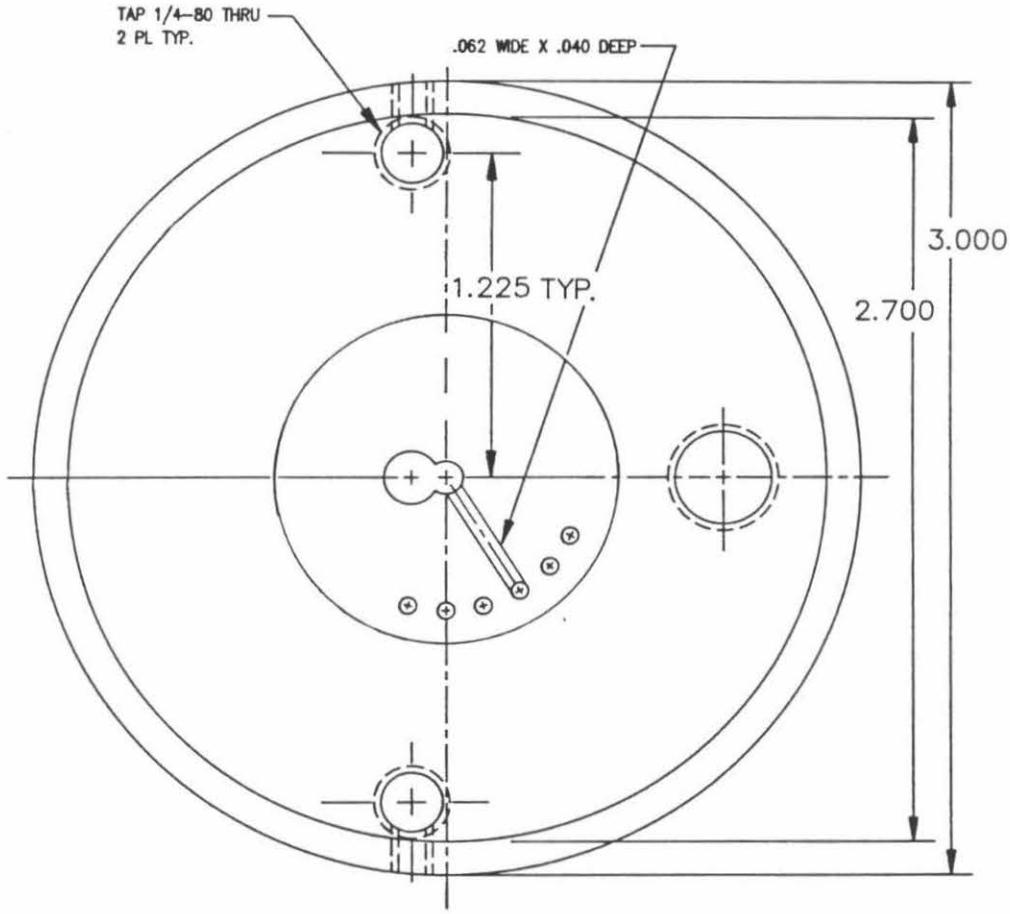

BOTTOM VIEW

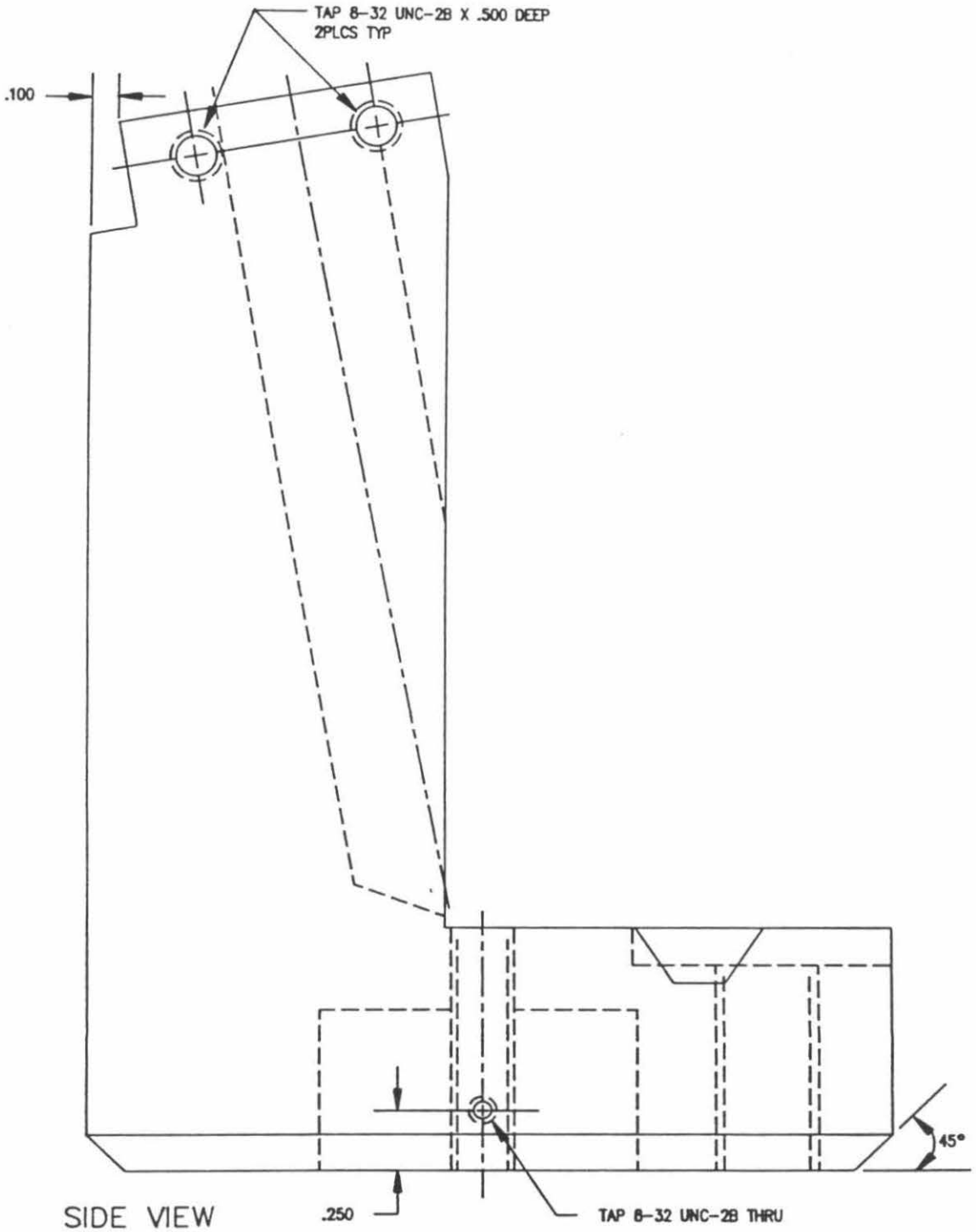
TAP 8-32 UNC-2B X .500 DEEP
2PLCS TYP
.100
45°
.250
TAP 8-32 UNC-2B THRU

SIDE VIEW

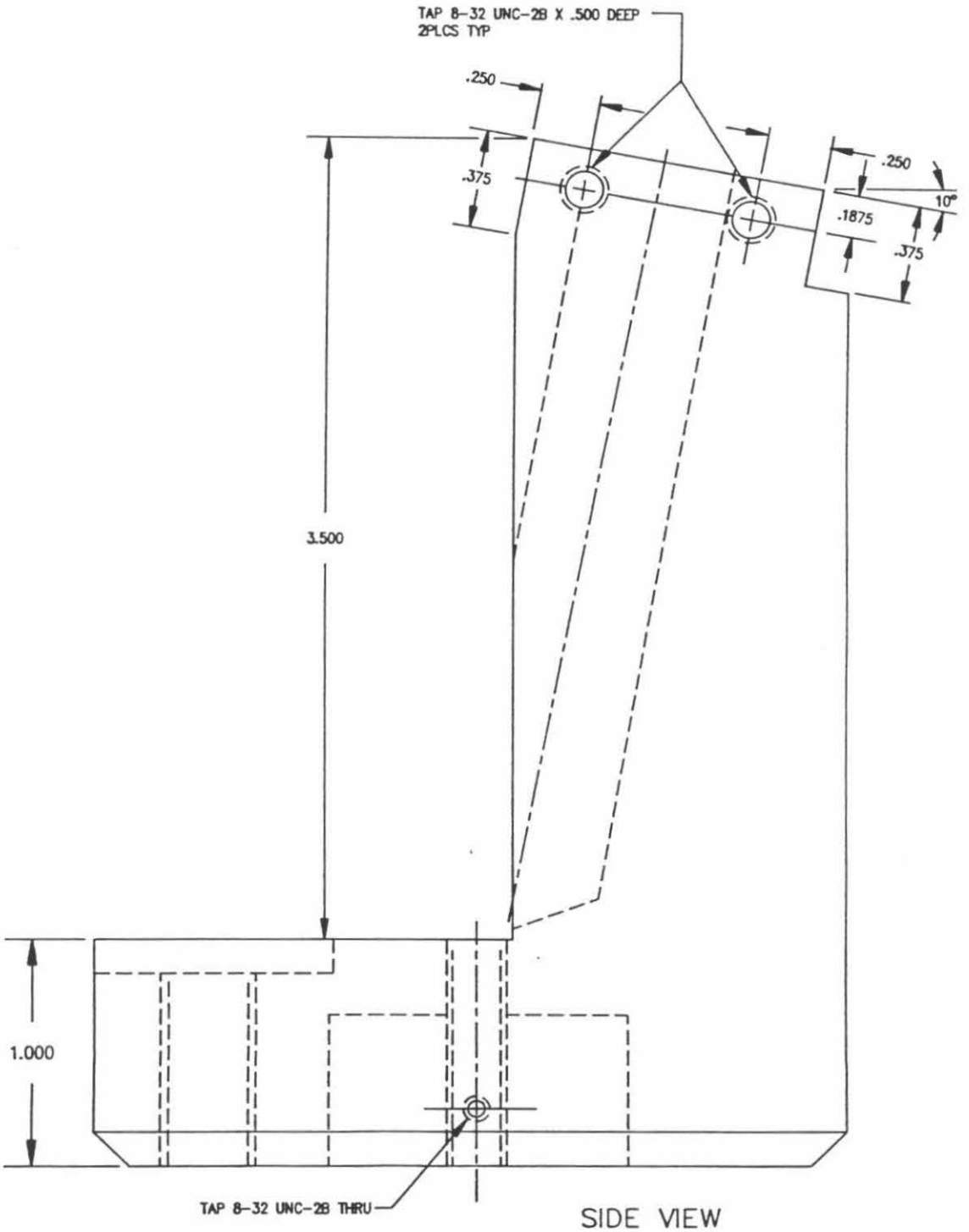
TAP 8-32 UNC-2B X .500 DEEP
2PLCS TYP
.250
.375
.250
10°
.1875
.375
3.500
1.000
TAP 8-32 UNC-2B THRU

SIDE VIEW

In this head design the piezo tube is directly glued to the head. Usually Devcon 2-Ton Epoxy™ is used and, because it takes several hours to cure, some provision must be made to hold the tube in the proper position during this time. For this we use a piece of plastic machined so that it fits over the outside of the piezo and slips into the 1.250" bore in the bottom of the head. Once the piezo has been attached to the head, the magnet can be affixed to the other end.

- Telescope for Single Mode Fiber Input

The single mode optical fiber input telescope and the collimating lens retaining sleeve are shown in Figures 6 & 7. The telescope serves to hold the output end of the single mode fiber, the collimating lens and the focusing lens in a fixed relationship. The telescope is assembled by inserting the collimating lens into the telescope body so that its surface of largest curvature is away from the single mode fiber input. Next, the retaining sleeve is inserted and clamped in place with a set screw. Following this, the single mode fiber is installed, its proper position determined and its position fixed by clamping the fiber optic ferrule with a set screw. The proper position for the fiber end may be found by pointing the telescope at a distant wall and inserting or withdrawing the fiber end until the laser spot on the wall is of minimum diameter. After this is done one should use a piece of paper to investigate the diameter of the output beam. The output beam diameter should not go through a focus in the region between the telescope and the wall, but instead it should be approximately the same diameter at all distances from the end of the telescope. After this has been accomplished, the focusing achromat may be installed with its surface of greatest curvature toward the

Figure 6. Single mode fiber input telescope body.

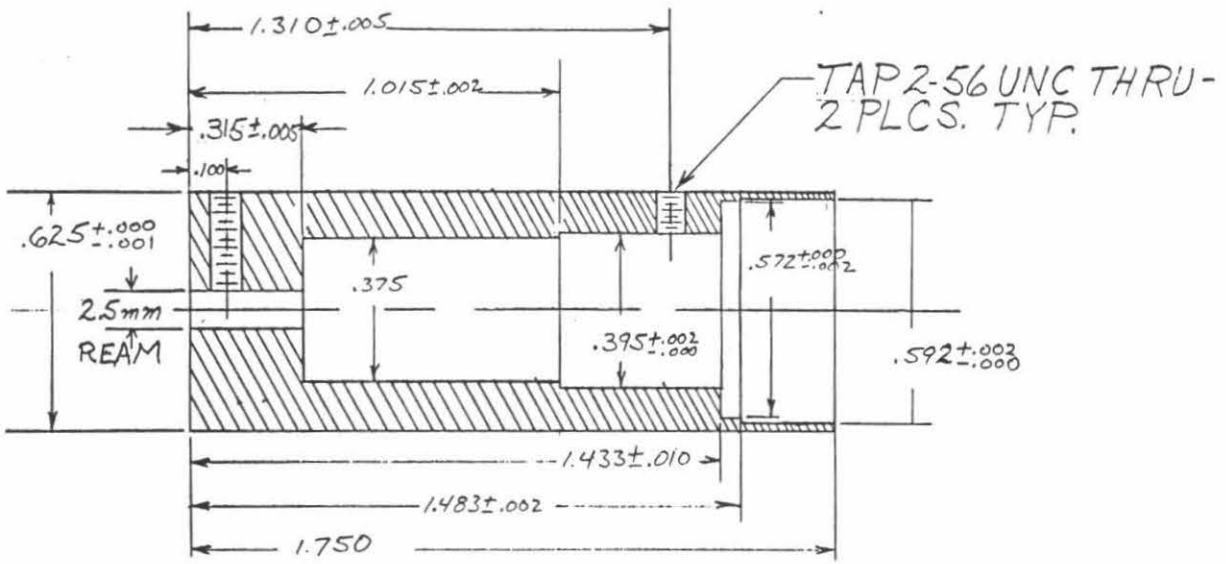

SINGLE MODE FIBER INPUT

TELESCOPE BODY

MATERIAL: 2024 ALUMINUM
FINISH: TYPE II BLACK ANODIZE
TOLERANCE: ±0.005" UNLESS NOTED

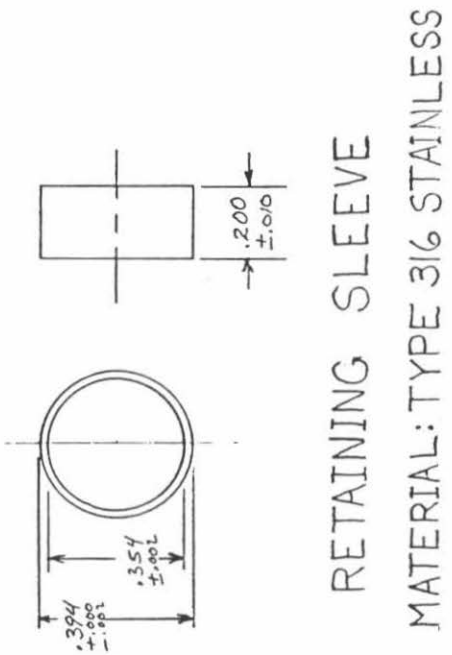

Figure 7. Collimating lens retaining sleeve.

collimating lens and secured in place either by depositing a bead of adhesive (e.g., RTV silicone or epoxy) or placing an O-ring in the end of the telescope. Once the telescope has been assembled, it can be installed in the groove on the head and clamped in place.

- Telescope for Laser Diode Input

The input telescope used in conjunction with a laser diode is shown in Figure 8. The telescope is essentially the same as that used for fiber input except that a larger hole has been bored in the back of the telescope to accommodate the larger diameter of the laser diode assembly. We have been using laser diode assemblies from Melles-Griot which contain the laser diode and a power supply circuit. In order to power the laser diode, +5 Vdc is applied to the connector on the laser diode pen. While this is quite convenient in terms of not having to design circuitry to drive the diode, the package is long and any stresses on the cable to the laser diode pen can cause movement of the telescope. To install the laser diode pen in the telescope one applies heat sink compound to the area around the front of the pen and slips it in place. To hold it fixed a bead of epoxy is placed around the back of the pen where it meets the telescope body. After the epoxy has cured, one is ready to install the focusing lens. As mentioned earlier, because the output of the laser diode pen is collimated, one can use the same type of focusing lens as used with the single mode fiber input. It should be noted that the laser diode pen output does not optimally fill the focusing lens and consequently diffraction limited spot size should not be expected with this scheme as it is presently implemented.

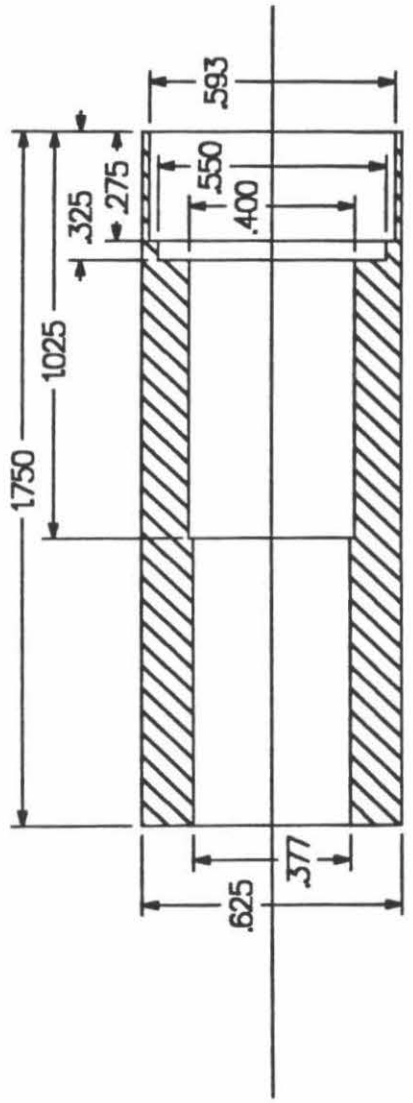

Figure 8. Laser diode input telescope body.

Recently laser diodes which have microlenses mounted directly adjacent to the laser diode have become commercially available. The microlens is designed to eliminate the astigmatism inherent in laser diode architectures and create a "virtual point source." By using laser diodes with microlenses it should be possible to provide an optical input which provides diffraction limited performance with a beam profile similar to that from a single mode fiber while maintaining the low noise, size, cost, efficiency and lifetime advantages of laser diodes.

With the piezo tube and the input telescope in place, one is now prepared to install the bending prism on the top surface of the head. The prism is placed so that the reflection from the first surface lies just inside the exit aperture of the telescope. Positioning it in this location avoids laser intensity instability caused by circulating power fluctuations (as may be caused by returning the beam back down the center of the telescope) while introducing minimal aberration. The other criterion for positioning the prism is that the beam coming out of the prism should pass through the center of the opening of the piezo tube (which should coincide with the hole in the magnet). Often it is helpful to place a piece of translucent tape on the magnet face to visualize the location of the beam in the aperture. Once these criteria are met (and the beam passes through the center of the prism) its position can be fixed with epoxy or optical cement. Having finished this, only the photodiode translator remains to be assembled.

- The Photodiode Translator

The photodiode translator (see Figure 9) is composed of the photodiode mount (Figure 10), five other machined components (Figures 11-15) and some commercially purchased hardware. The idea behind the translator, which was taken from the design of a translator sold by Spindler & Hoyer, Inc., is to use two spring loaded thrust plungers (Figure 11) to force the photodiode mount against the adjustment screws for both dimensions. Because the sides of the photodiode mount are angled in a complementary direction to the thrust plungers, the force transmitted by the plungers has two components, one lateral and one normal. The lateral force components eliminate backlash in the X-Y plane and push the photodiode mount against the adjustment screws, while the normal component forces the photodiode mount down against the bearing surface. This tends to add stability to the translator and decrease drift. After assembly onto the photodiode support post, the X & Y adjustment screw brackets and the X & Y thrust plunger support brackets (Figures 12-15) make up the framework of the translator. The adjustment screw brackets (Figures 12 & 14) have 1/4-80 tapped holes for the ball end adjustment screws, while the X & Y thrust plunger support brackets (Figures 13 & 15) have been machined to accommodate the thrust plungers along with their springs and guidepins.

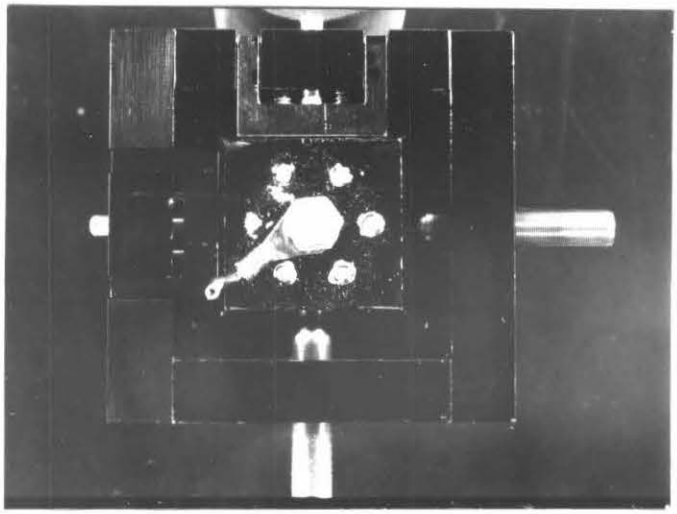

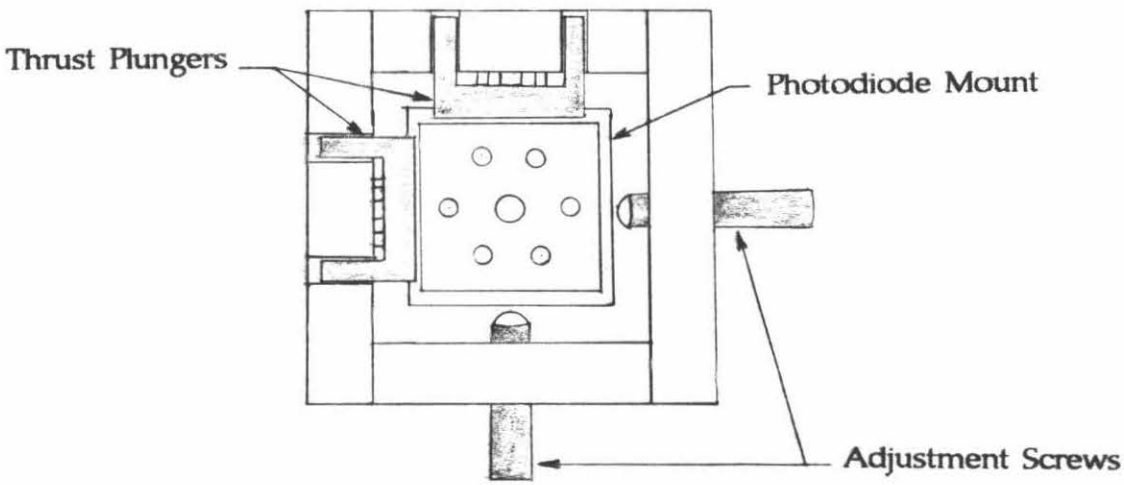

Figure 9. A top view of the assembled photodiode translator. The photodiode pins are visible protruding through the back of the photodiode mount. The two thrust plungers are seen on the top and left sides of the assembly, where they oppose the 1/4-80 adjustment screws.

Figure 10.

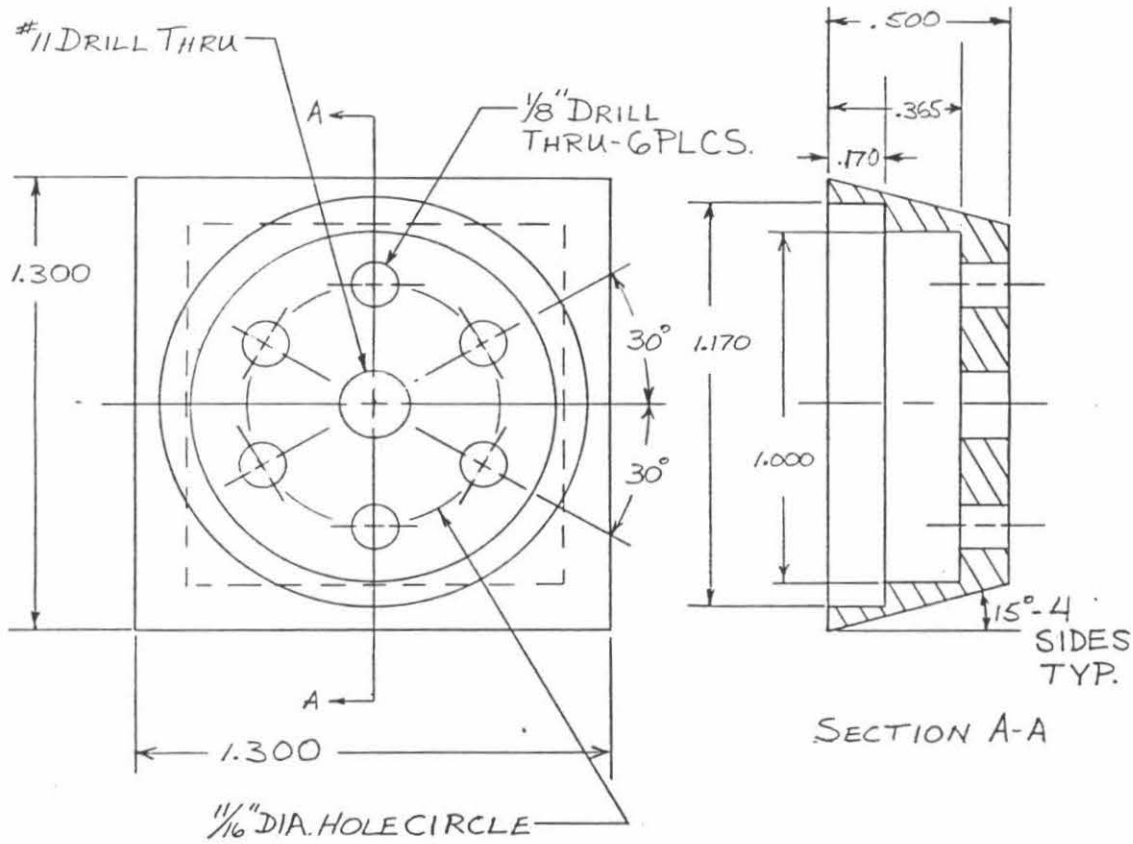

PHOTODIODE MOUNT

MATERIAL: 2024 ALUMINUM
FINISH: TYPE II BLACK ANODIZE
TOLERANCE: .XXX = ±0.002" ∠ ±1°

Figure 11.

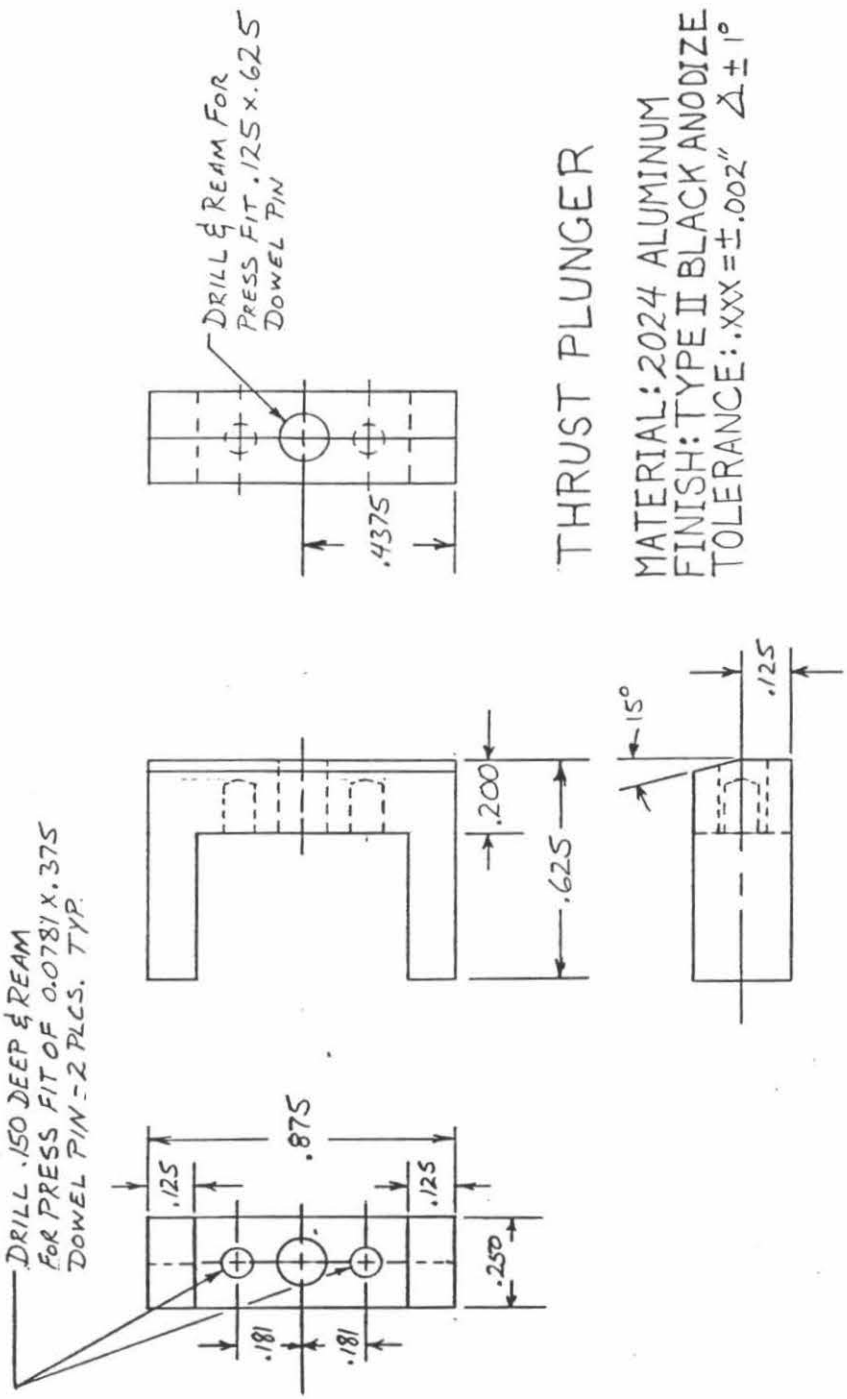
DRILL & REAM FOR
PRESS FIT .125 x .625
DOWEL PIN
.4375
THRUST PLUNGER
MATERIAL: 2024 ALUMINUM
FINISH: TYPE II BLACK ANODIZE
TOLERANCE: .XXX = ±.002" ∠ ± 1°
DRILL .150 DEEP & REAM
FOR PRESS FIT OF 0.0781 X .375
DOWEL PIN - 2 PLCS. TYP.
.125
.875
.125
.250
.181
.181
.200
.625
15°
.125

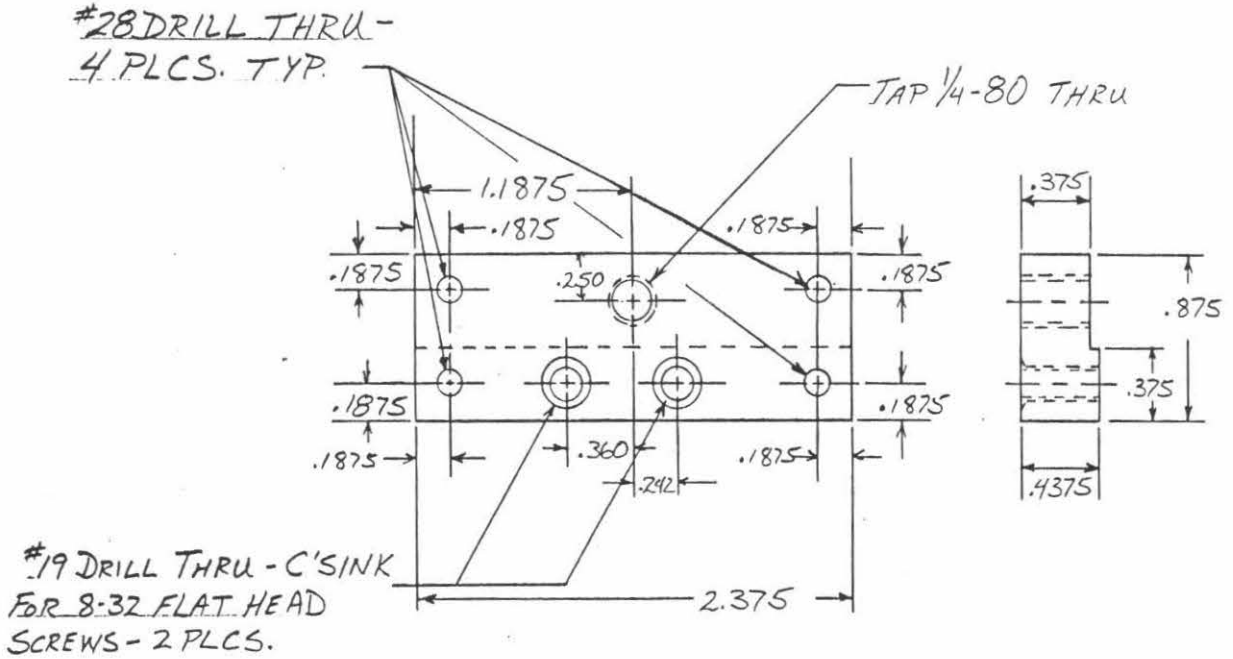

RIGHT SIDE ADJUSTMENT SCREW BRACKET
MATERIAL: 2024 ALUMINUM
FINISH: TYPE II BLACK ANODIZE
TOLERANCE: ±.002"

Figure 12.

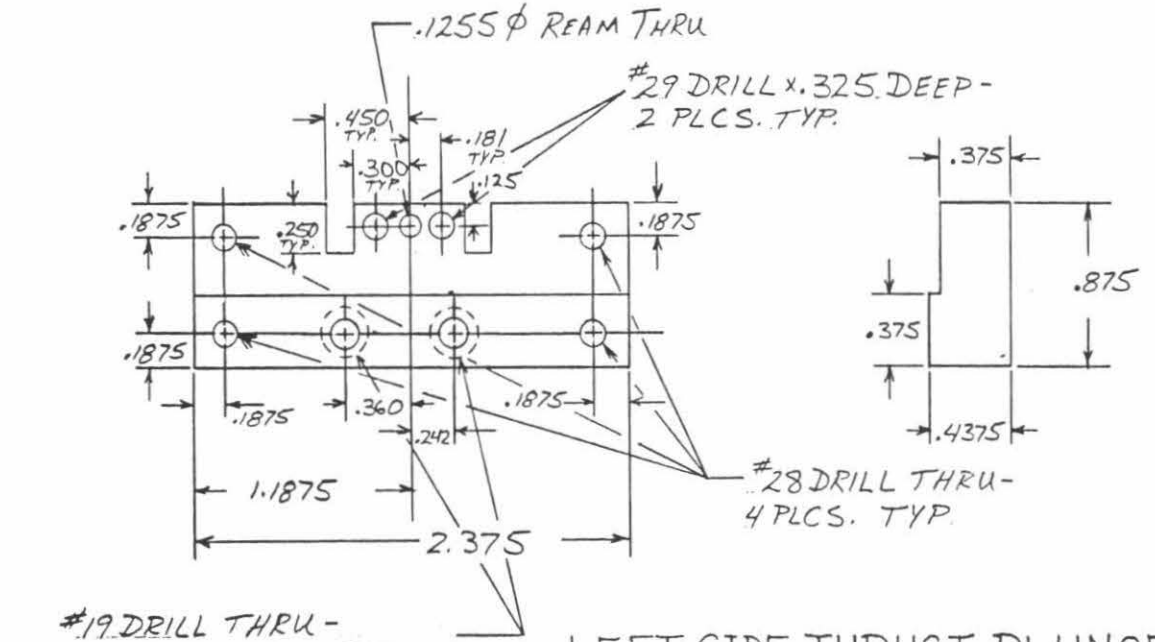

LEFT SIDE THRUST PLUNGER BRACKET
MATERIAL: 2024 ALUMINUM
FINISH: TYPE II BLACK ANODIZE
TOLERANCE: ± .002"

Figure 13.

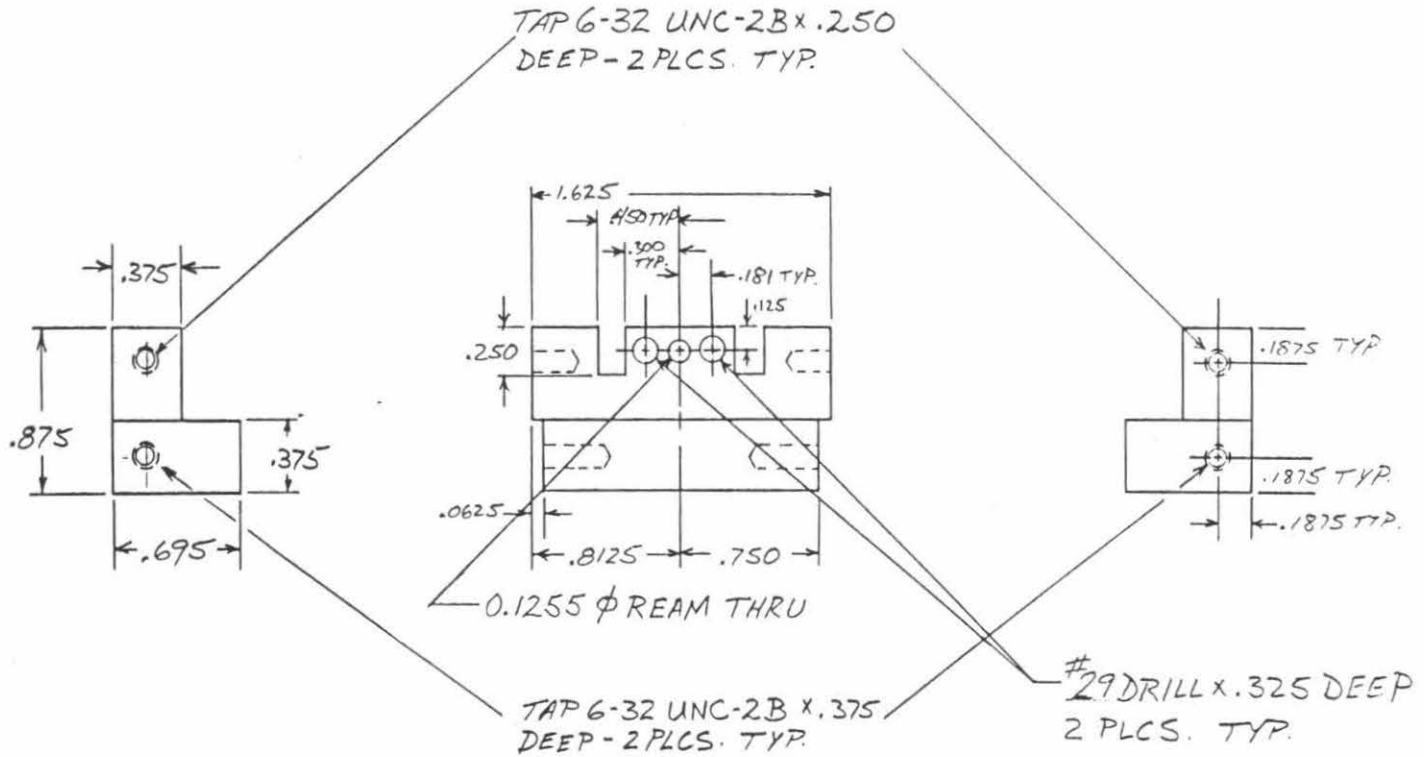

TOPTHRUST PLUNGER BRACKET

MATERIAL: 2024 ALUMINUM
FINISH: TYPE II BLACK ANODIZE
TOLERANCE: .XXX = ±.002"

Figure 14.

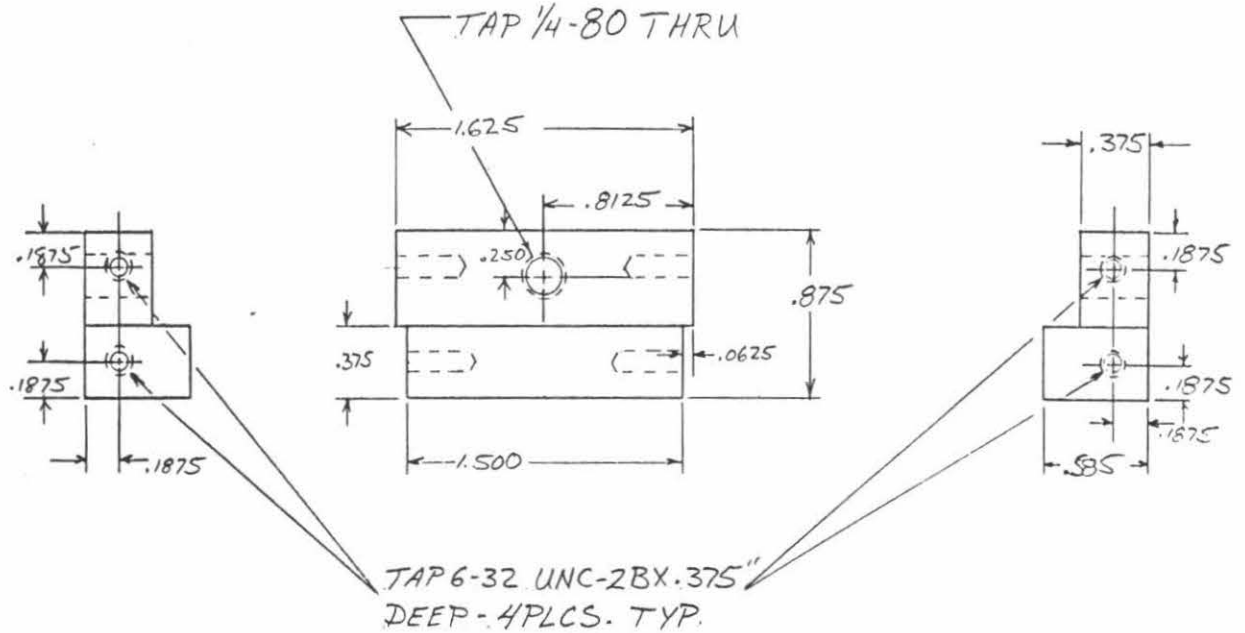

BOTTOM ADJUSTMENT SCREW
BRACKET
MATERIAL: 2024 ALUMINUM
FINISH: TYPE II BLACK ANODIZE
TOLERANCE: ±.002"

Figure 15.

There are two additional parts required to complete the head assembly, the input telescope clamp and the motor counterweight. As mentioned previously, the telescope clamp restrains the telescope from moving once the proper position has been determined. The motor counterweight serves to balance the head such that the approach motor stays in contact with the base. These two components are shown in Figures 16 and 17.

- Parts From Commercial Suppliers

Listed below are the parts required to assemble the head (except the screws) which were purchased from commercial suppliers:

1. .500" diameter x .500" long x .020" thick wall tube with nickel electrodes (quadrant electrodes outside, single electrode inside) made from EBL-2 peizoceramic material from Staveley Sensors Inc., EBL Division, 91 Prestige Park Circle, East Hartford, CT 06108.

2. .500" outside diameter x .0625" thick x .200" inside diameter annular samarium cobalt magnet custom made by Magnet Sales Manufacturing Company, 11248 Playa Court, Culver City, CA 90230.

3. 5mm, 90° Bending prism (RAP-020C with anti-reflection coating on both legs) from CVI Laser Corp., 200 Dorado Place, S.E., P.O. Box 11308, Albuquerque, N.M. 87192-0308.

4. Collimated laser diode "bullet" with power supply (56DLB102/P) from Melles-Griot, 2985 Sterling Court #3, Boulder, Colorado 80301.

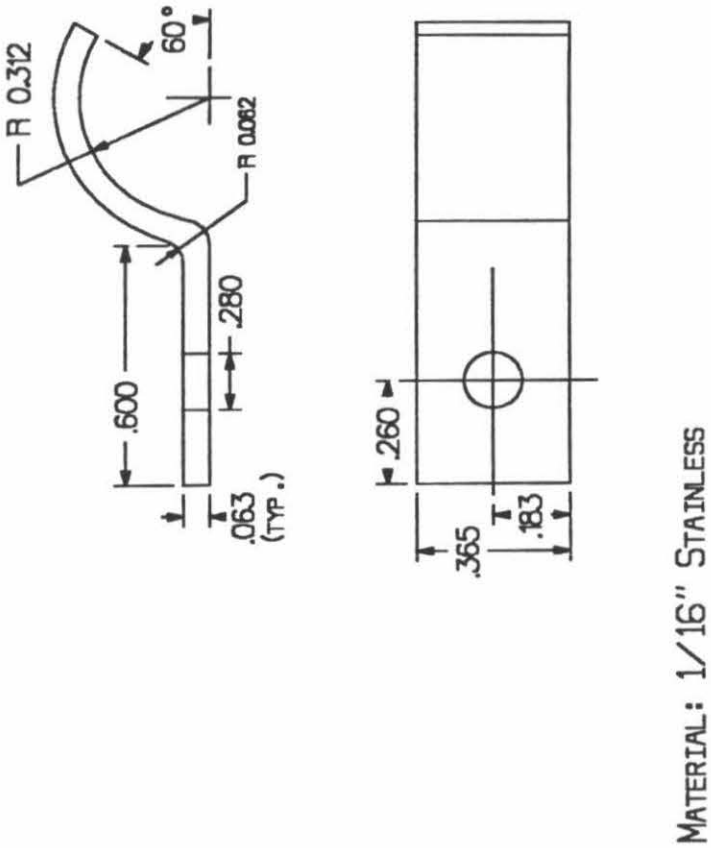

Figure 16. The telescope clamp.

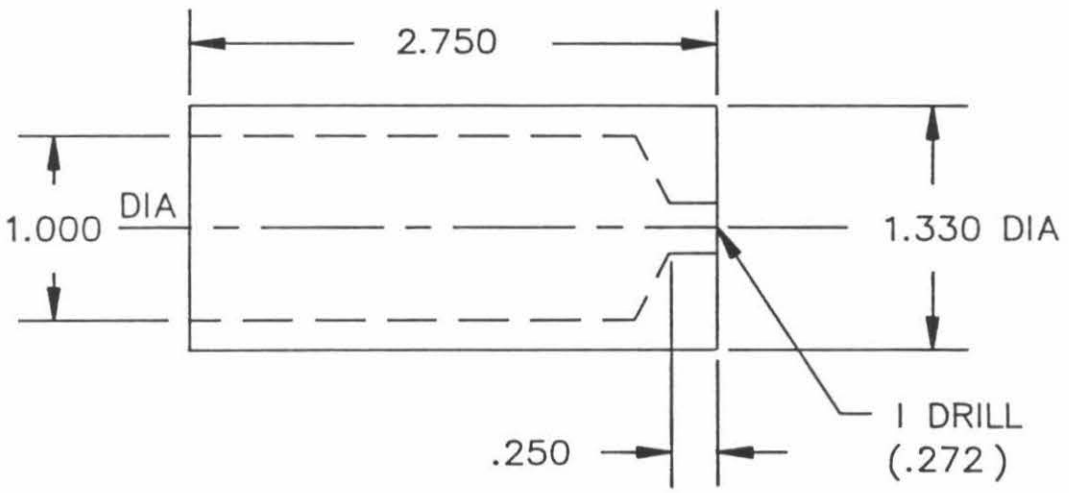

MATERIAL: STEEL(MAGNETIC STAINLESS)
ALL DIMENSIONS IN INCHES, ±.010"

COUNTERWEIGHT,
MOTOR SLEEVE

Figure 17. The motor sleeve counterweight.

5. SGD-444-4 quadrant photodiode

EG&G Canada Limited, 22001 Dunberry Road, Vaudreuil, Quebec J7V8P7, Canada.

6. Mechanical adjustment components:

2 each 1/4-80 x .5" travel fine adjustment screws (AJS-0.5)

2 each 1/4-80 x 2" travel fine adjustment screws (AJS-2)

1 each 1" travel motorized drive (860A-1)

Available from Newport Corporation, P.O. Box 8020, 18235 Mt. Baldy Circle, Fountain Valley, CA 92728-8020.

7. 4 each 1/8" O.D. x 1" free length music wire compression springs (OO-15) from Century Spring Corp., P.O. Box 15287, 222 East 16th Street, Los Angeles, CA. 90015.

Chapter III

A Covalent Attachment Chemistry For Scanned Probe Microscopy*

* Manuscript to be submitted to *Journal of Structural Biology*

A COVALENT ATTACHMENT CHEMISTRY FOR SCANNED PROBE MICROSCOPY

Steven M. Clark, Robert J. Kaiser, Jr.,[†] Leroy E. Hood[†]
and John D. Baldeschwieler[††]

Division of Biology
and
[†]Center for Molecular Biotechnology
and
[††]A. A. Noyes Laboratory of Chemical Physics
California Institute of Technology
Pasadena, CA 91125

Abstract: A covalent immobilization chemistry designed for scanned probe microscopy is presented. The chemistry, which is based on heterobifunctional alkoxysilane compounds, is compatible with various siliceous substrate materials and provides a means to covalently immobilize samples through a variety of reactive moities. Imaging substrate morphology is maintained by using chemical vapor deposition methods to apply the alkoxysilanes.

Introduction

Since its inception in 1985, the atomic force microscope[1] (also known as the scanning force microscope or SFM) has held great promise for providing topographical information on nonconducting samples at sub-nanometer resolution. Early attempts to image relatively inelastic samples such as graphite,[2] crystals of ionic salts,[3] and semiconductors[4] yielded atomic resolution data. This data provided reason to believe that SFM might easily provide high resolution structural information on samples of biological interest. When compared to other techniques which provide structural information, such as X-ray crystallography, multi-dimensional nuclear magnetic resonance experiments and electron microscopy, the simplicity of sample preparation for SFM and the ability to perform high resolution microscopy in physiologically relevant liquid environments added tremendous incentive for developing SFM as a complementary structural assay.

As more compliant samples were examined it became clear that the sub-nanometer resolution hoped for would be difficult to obtain. Among the factors which limit SFM resolution are: i) unavoidable forces involved in tip-sample interaction;[5] ii) tip shape effects;[6] iii) instrument and detection noise;[7] and iv) sample motion, both thermal and tip induced. While advances have been made in several of these areas, the investigation of biomaterials by SFM continues to be hampered by the movement of adsorbed samples relative to the imaging substrates.

Early efforts to image biomolecules relied on the passive adsorbtion of the sample to the imaging substrate. Many of these experiments were done in air

and were prone to sample distortion from drying effects and meniscus forces. To eliminate these surface forces experimenters turned to imaging with the sample and cantilever immersed in liquid environments.[8] While the images obtained using this technique show improved resolution, in many instances much of the adhesion between sample and substrate was lost. The next step in the evolution of immobilization methods for SFM of biomolecules came in the form of substrate treatment to enhance sample-substrate adhesion.[9,10] This is clearly a valuable contribution and images obtained using treated substrates are remarkable,[11] however there are areas which can still be improved. The lack of a covalent linkage between sample and substrate limits the choice of liquid environments which can be used for imaging and the general applicability of substrates treated by these methods for imaging biomolecules other than nucleic acids is not clear.

An ideal chemistry for sample attachment would i) give dense and uniform coverage of the substrate, ii) allow covalent bonding of the sample to the substrate through a short linker segment, iii) be stable against degradation by sample solvents and buffers, iv) provide a variety of functional groups and allow post-deposition derivatization to tailor the linker specificity to particular sample moities, and v) be easy to use and generally compatible with well characterized SPM imaging substrates. The first three points are aimed at maintaining suitably flat and smooth imaging substrates; a consideration peculiar to SPM. The latter two considerations are crucial for utility in imaging biological samples.

When judged by these criteria, members of the family of alkoxysilanes seem particularly promising. Alkoxysilanes can be used to derivatize a variety of silicon containing substrates several of which can be used as SPM

substrates.[12,13] The commercial availability of alkoxysilanes with a diversity of chemical functionalities including the amino, mercapto, quaternary amino and epoxide moities adds to their potential utility.[12,14] The major barrier to the employment of alkoxysilanes is the surface roughness induced by common application techniques, thus necessitating an alternative method for their deposition on SPM substrates.

In this paper we describe the use of chemical vapor deposition techniques to derivatize several different siliceous SPM imaging substrates and show that these substrates meet the criteria set forth above. Additionally, we present an example of the use of the attachment chemistry to obtain SPM images which are difficult or impossible to obtain without covalent sample immobilization.

RESULTS and DISCUSSION

The Character of the Substrate Surface Depends on the Method of Deposition

The selection of an environment for the reaction of alkoxysilane with substrate is crucial to the formation of suitable SPM substrates. For most applications of covalent linker technology high surface loading is of major importance.[15] Often high surface loadings can be achieved by creating a polymeric matrix bonded to the substrate surface with many available attachment sites.[16] In contrast, for SPM, surface morphology is of primary importance because high resolution imaging cannot be performed on rough surfaces. Among the alternative deposition methods are spin coating, reaction in solution, and chemical vapor deposition. In order for the flatness of the substrate to remain uncompromised, monolayer coverage is required; thus spin coating,

which yields thick coatings (≈ 20 nm to 1μm) was rejected without trial. Both solution deposition (SD)[15] and chemical vapor deposition (CVD)[17] methods have been used previously to alter the surfaces of silicon-containing materials. In principle, one should be able to obtain monolayer surface coverage by either method; however, in practice one often finds that surfaces treated by solution deposition can be periodically marred by polymeric species which result from the local condensation of alkoxysilane monomers. A simplified view of this is shown in Figure 1a. By using chemical vapor deposition methods, one can make use of the differential vapor pressure and boiling points of the monomeric alkoxysilanes versus the polymeric species to avoid the deposition of oligomers. This is done by raising the temperature of the alkoxysilane mixture to create an environment in which silane monomer is in the gas phase while dimers and higher order polymers remain predominantly in the liquid or solution phase. Because the substrate surface is exposed only to the vapor phase material, as shown in Figure 1b, it reacts primarily with the monomeric form of the reagent yielding monolayer coverage.

Our attempts to characterize and compare surfaces prepared by solution deposition (SD) with those prepared by chemical vapor deposition (CVD) using scanning electron microscopy (SEM) were inconclusive. Both types of surfaces appeared flat and smooth to better than the resolution limit of the SEM. Next we attempted to prepare Pt-C replicas of the two types of derivatized surfaces for examination by transmission electron microscopy. Our efforts to remove the replicas from the derivatized surfaces were unsuccessful, suggesting that a strong bond had been formed between the replica coating and the surface. We then turned to the SFM as a more sensitive technique for the direct measurement of surface topography.

Figure 1. A comparison of solution deposition and chemical vapor deposition chemistry of bi- and tri-alkoxysilanes. a) solution deposition typically involves four steps: i) hydrolysis; ii) condensation to form polymers joined by siloxane bonds; iii) hydrogen bonding to silanols on the substrate and iv) siloxane bond formation with the substrate. The water required for hydrolysis can be supplied by the solvent, the surface or the atmosphere and occurs spontaneously. Siloxane bond formation with the substrate (step iv) requires heat. b) during chemical vapor deposition the substrate is exposed to predominantly alkoxysilane monomer. Because the monomer is relatively dilute and the system is at an elevated temperature conditions favor the formation of a monolayer of alkoxysilane.

A. SOLUTION DEPOSITION CHEMISTRY

I. Hydrolysis

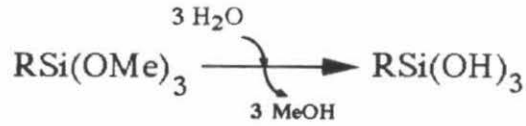

II. Condensation to Form Siloxanes

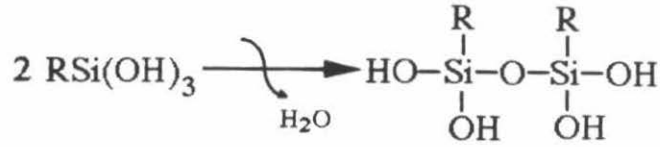

III. Hydrogen Bonding to Substrate Silanols

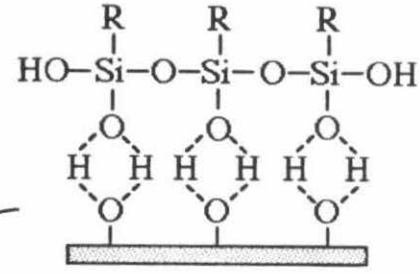

IV. Bond Formation

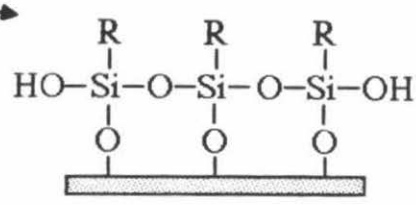

B. VAPOR DEPOSITION CHEMISTRY

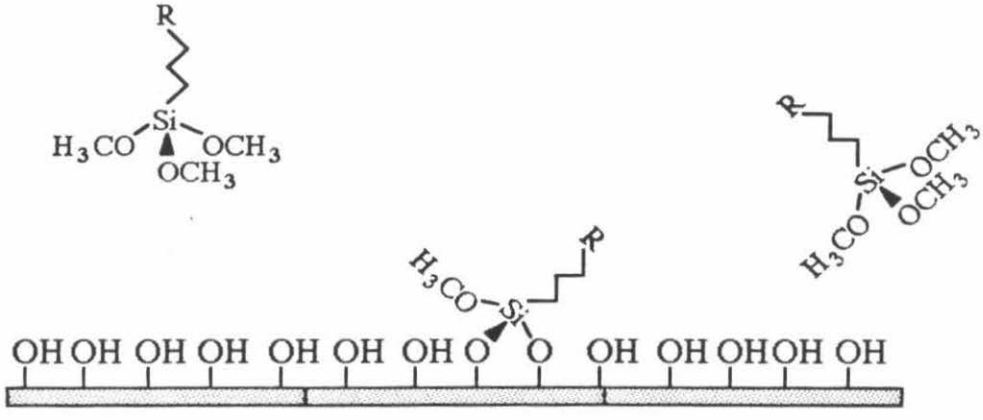

In Figure 2 we present a comparison of surfaces resulting from both SD and CVD processes as assayed by scanning force microscopy (SFM). The sample in Figure 2a was prepared by CVD of 3-aminopropyltriethoxysilane (APTES) onto a freshly cleaved mica surface. In Figures 2b & c we show topographic images of samples prepared by SD of the same alkoxysilane as a 5% solution in toluene and absolute ethanol, respectively. The particles evident on the surface in Figures 2b & c are tentatively identified as polymeric globules formed by the condensation reactions exhibited by alkoxysilanes. Figure 2d shows a topographic image of an unmodified, freshly cleaved mica surface. The conclusion which we draw from the evidence provided by the SFM data is that the surface resulting from the chemical vapor deposition of an alkoxysilane is smoother than that resulting from solution deposition. Because of this we believe CVD to be a superior method for depositing alkoxysilanes for SPM applications.

The two requirements of monolayer coverage are: i) every reaction site on the surface must have only one molecule of the attachment compound bound (no polymeric globules), and ii) every reaction site on the surface must be occupied (no pinholes). To establish surface monolayer coverage by direct analytical methods is complicated because large surface areas must be examined with a molecular size probe which is sensitive to chemical composition. One can, however, make a case for monolayer coverage using indirect evidence. The data discussed above shows no evidence of polymeric globules on short length scales on the CVD prepared surfaces, suggesting that polymeric areas are rare. The second point to be made is that because the surface concentration of alkoxysilane monomer is low during CVD, monomers will tend to react first with surface silanols and not other alkoxysilanes. This would imply that deposition of polymeric alkoxysilanes directly from the vapor phase is unlikely. Another point

Figure 2. Comparison of surface topography resulting from different alkoxysilane methods by scanning force microscopy. Images of ≈ 100 nm x 100 nm areas of mica substrates prepared by each of the substrate preparation methods are shown along with a line cut to assess surface roughness. a) an image of a substrate prepared by CVD of 3-aminopropyl triethoxysilane. b) an image of a substrate prepared by solution deposition of 3-aminopropyl triethoxysilane from anhydrous toluene. c) an image of a substrate prepared by solution deposition of 3-aminopropyl triethoxysilane from absolute ethanol. d) an image of freshly cleaved mica without any surface treatment. Polymeric globules are evident in parts b & c.

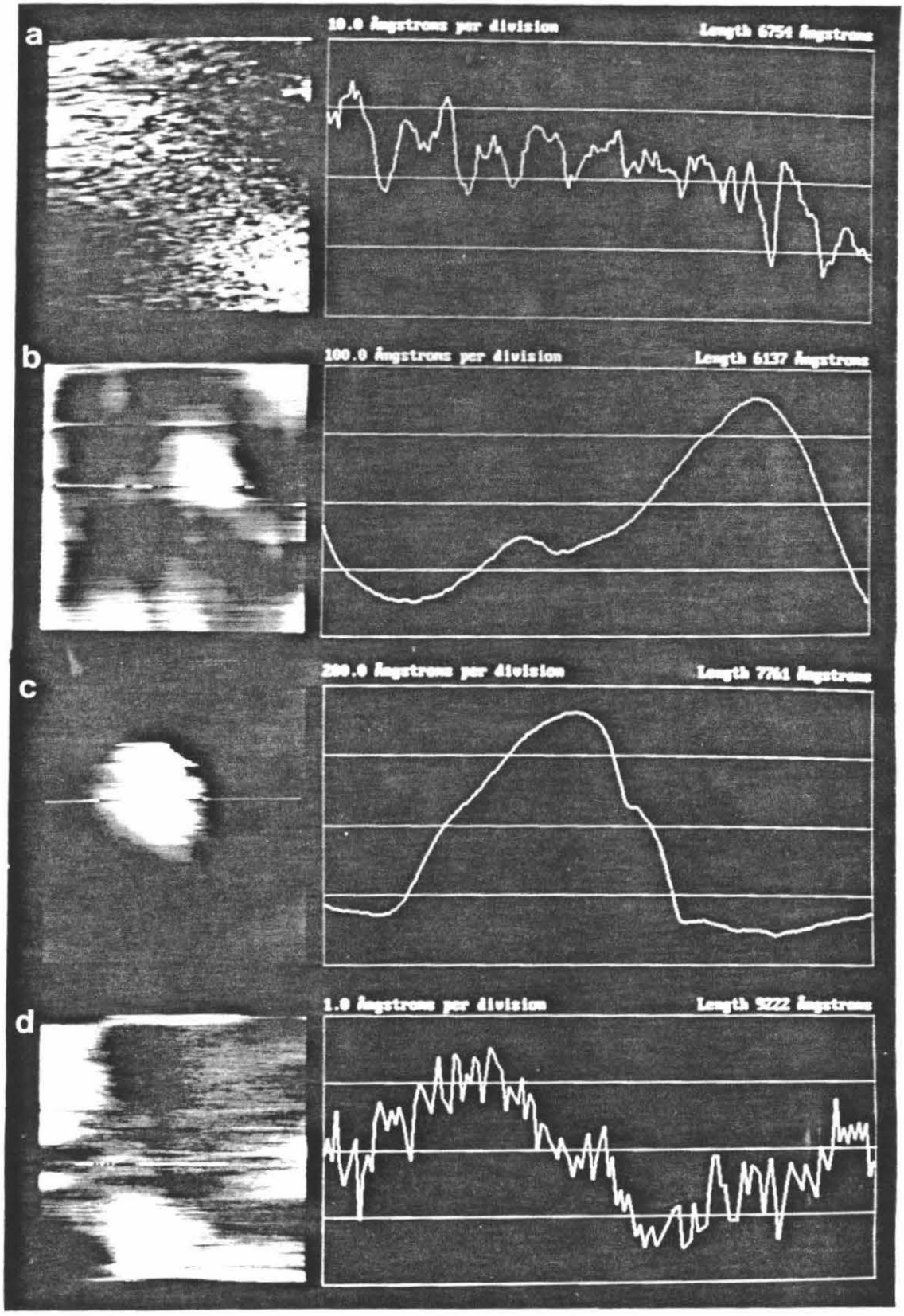
a
10.0 Ångstroms per division
Length 6754 Ångstroms
b
100.0 Ångstroms per division
Length 6137 Ångstroms
c
200.0 Ångstroms per division
Length 7761 Ångstroms
d
1.0 Ångstroms per division
Length 9222 Ångstroms

to be made is that, once a covalent bond has been formed between an alkoxysilane monomer and a surface silanol, that particular reactive site becomes unavailable for further additions of alkoxysilane monomers. This would lead one to believe that, if a surface can be derivatized by CVD of an alkoxysilane, the first criterion for monolayer coverage is probably satisfied. Taken together, these facts imply that the first criterion has been met.

Indirect evidence indicating that there are no pinholes in the surface coverage resulting from the CVD process can be obtained by examining the apparent uniformity of the deposited coating. In this area we have data on two different length scales. On small scales (< 3 μm), we find that derivatized substrates, when imaged by SFM, give larger friction (lateral force) signals than underivatized substrates. We can use the uniformity of friction images acquired by SFM as a measure of the uniformity of the derivatization on a small scale. In the course of imaging with the SFM we have noticed no lack of uniformity in the friction images of derivatized substrates. Another piece of data on this scale comes from the uniformity of immobilized sample distribution. When working with the derivatized substrates we observe a random sample distribution. This implies that all locations on the substrate are equally accessible for sample immobilization and so surface coverage appears to be relatively uniform. On larger scales (>25 μm), one can use the fluorescence uniformity of a derivatized surface which has been reacted with a functional group specific fluorescent probe to judge the chemical uniformity of the surface. With this approach, we found that the fluorescence was uniformly distributed within a factor of 2, thus implying that there are no larger scale regions which remained underivatized. Taken together these data suggest that the second criterion of monolayer coverage has been met in the CVD of alkoxysilanes.

The Sample-Substrate Linkage is Covalent and Stable

For an attachment chemistry to be covalent two bonds must be formed; one between the linker and the substrate and another between the linker and the sample. To establish the formation of both of these bonds we have used the fluorescence based chemical assay which is a sensitive probe of the chemical nature of the modified surface.

In Table 1 we present some of the data gathered to investigate the covalent nature and stability of the attachment chemistry. In this experiment a cleaned glass slide was derivatized by CVD of 3-aminopropyltriethoxysilane (APTES) from anhydrous toluene. After deposition the slide was washed sequentially in toluene, acetone and ethanol and air dried. The slide was then spotted with a serial dilution series of fluorescein-5-isothiocyanate ranging in concentration from 1mM to 10 nM in coupling buffer (1mM $NaHCO_3$ pH 9.0). These probe solutions were incubated with the glass for 10 minutes at which time the excess solution was removed by micropipette. The slide was then washed in coupling buffer, water and air dried. The slides were imaged with the scanning fluorimeter and the spot intensities measured. The data for the 100 nM & 1 µM concentrations of fluorescein-5-isothiocyanate (FITC) are shown in Table 1. The slide was then washed using various conditions to establish the covalent linkage of probe bound to the sample. The final steps of each wash were the same and consisted of a rinse with coupling buffer to insure consistency of pH, followed by air drying. The order of washes was ethanol, chloroform and dimethyl sulfoxide (DMSO), 10 mM $NaHCO_3$ pH 10.5, 1M NaCl, another wash in chloroform and DMSO, 80% acetic acid, 1% sodium dodecylsulfate with light scrubbing using a Kimwipe and a final 10 minute wash in 1% trifluoroacetic acid in acetonitrile. All

washes were for five minutes except as indicated. The sample was reimaged between washes and the intensities measured.

Table 1. Stability of Fluorescence Intensity After Various Washes

Wash Reagents	100 nM FITC	1 µM FITC	Background
Ethanol	449	716	81
Chloroform and Dimethylsulfoxide	366	624	90
10 mM $NaHCO_3$ pH 10.5	346	623	56
1 M NaCl	276	510	45
Chloroform and Dimethylsulfoxide	220	480	42
80% Acetic Acid	194	437	49
1% Sodium Dodecylsulfate	185	422	47
1% TFA in Acetonitrile (10 min.)	135	345	48

In order to thoroughly test the surface linkage and establish that covalent bonds had been formed, the sequential washes explored extremes of pH as well as trying to eliminate probe bound through hydrophobic interaction. We interpret the fact that there was still bound probe following these washes as strong evidence that two covalent bonds were formed, one between the linker and the substrate and another between the amino functionality of the linker and the isothiocyanate functionality of the FITC probe. We also believe that the apparent stability of these bonds through the washes is indicative of good long term stability. Another piece of evidence indicating good surface stability is that,

in routine use of the derivatized surfaces, we have seen no loss of reactivity after storage.

Functional Groups Remain Accessible for Modification After Deposition

One of the crucial requirements for an attachment chemistry to be useful is that the reactive functionalities remain accessible after deposition. This is required both for fixation of samples to the substrate (e.g., by glutaraldehyde crosslinking) as well as direct sample immobilization. Another aspect of the attachment chemistry which increases its utility is the ability to modify the reactive functionality of the linker after deposition to provide altered specificity for groups known to be accessible on a particular sample. The functional groups of the linker must clearly be accessible for this to be possible.

The fluorescent assay data presented throughout the paper demonstrates that the functional groups on the deposited linkers are chemically accessible. We have also tried several examples of specificity tailoring such as the formation of iodoacetates and N-hydroxysuccinimidal esters, etc. and we present one in detail here.

We were interested in derivitizing the amino functionality of 3-aminopropyl triethoxysilane (APTES) to an isothiocyanate (NCS) after deposition to create a surface particularly reactive toward amino groups on samples. One application of such a surface is to target free amino groups which are present on a particular protein of interest (i.e., the epsilon amino groups of exposed lysine sidechains or exposed amino termini) for linkage to a substrate. This derivatization can be accomplished by several routes; two routes are shown in

Figure 3. The first route utilizes the condensation of CS_2 in the presence of a diimide while the second route involves the thiocarbamylation of the amino group with thiophosgene. We chose to use the first route because of its convenience and relative lack of harsh reaction byproducts. The details of how the reaction was performed can be found in the Materials and Methods section.

After the derivatization had been performed, the assay for NCS functionality was done by fluorescent imaging. The data is shown in Table 2. In this case the fluorescent probe was 5-(aminoacetamido) fluorescein, hereafter referred to simply as AAAF, which was spotted onto the substrate in a six order of magnitude serial dilution series (highest concentration 100 µM) in coupling buffer. As an indicator of specificity, fluorescein-5-isothiocyante (FITC) was spotted in the same way. The reaction was sampled at two time points; one hour and 16 hours. After the respective periods had elapsed, excess probe solution was removed and the substrates were washed in coupling buffer and water and allowed to air dry.

Table 2. Isothiocyanate Derivatization of Aminopropyl Glass

Substrate	**Background**	**AAAF**	**FITC**
Glass	670	614	1,008
Aminopropyl Glass	642	658	15,000
Isothiocyanate Glass (1 Hr. Coupling)	738	1,545	2,400
Isothiocyanate Glass (O/N Coupling)	603	9,150	N/D

N/D = Not Determined

Figure 3. Two synthetic routes to the isothiocyanate derivatives of 3-aminopropyl alkoxysilane treated substrates. Scheme I uses the carbodiimide mediated condensation of carbon disulfide to form the desired isothiocyanate. Scheme II involves the thiocarbamylation of the amino group with the acid by product scavenged by triethyl amine, a hindered vapor phase base.

Scheme I.

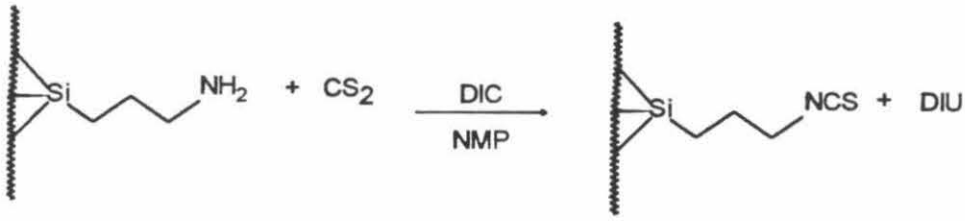

Scheme II.

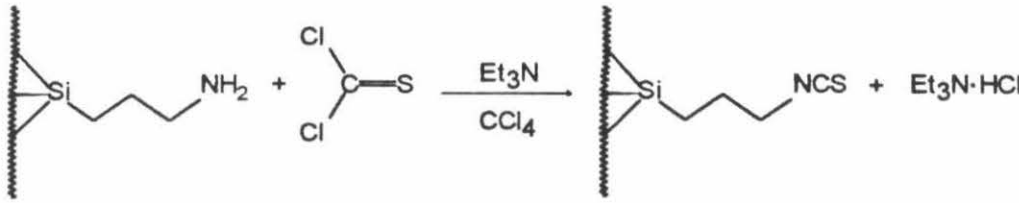

Several points can be made from the data of Table 2. The first is that the amino group of the APTES has been derivatized to become an isothiocyanate. This is indicated both by the increased coupling of AAAF to the NCS functionalized glass with time and the preferential binding of AAAF to NCS glass compared to AAAF binding to aminopropyl glass. The second point to be made is that the reaction time for coupling of AAAF to NCS glass is markedly longer than the reaction time required for the coupling of FITC to aminopropyl glass as would be expected from the relative reactivities of aliphatic versus aromatic isothiocyanates. The last point has to do with the yield of the reaction. From the spot intensities on the NCS glass treated with FITC it is clear that the conversion reaction from amine to isothiocyanate does not occur with quantitative yield and thus even after the conversion of the majority of the surface groups to NCS many amino groups are still available to react with FITC. For most SPM applications the lack of quantitative yield in the amino to NCS conversion does not pose a problem, however if increased yield is desired the second route (Scheme II of Fig. 3) may prove to have higher yield. One of the attractive aspects of this latter route is that it can be done in the gas-phase using carbon tetrachloride as a reflux solvent for the thiophosgene and a highly sterically hindered gas-phase base such as triethylamine as an acid scavenger.

The CVD Process Can Be Used to Deposit a Variety of Alkoxysilanes

In many cases it is useful to have functional groups other than amines on a substrate surface. One way to achieve this is post-deposition derivatization as discussed above; but a more straightforward method is to use an alkoxysilane containing the desired functionality for CVD. Alkoxysilanes are commercially available which contain other interesting functionalities such as terminal

sulfhydryls, epoxides or quarternary amines. We have successfully used CVD methods to deposit 3-mercaptopropyl trimethoxysilane as well as N-trimethoxy silylpropyl-N,N,N-trimethyl ammonium chloride.

The deposition of 3-mercaptopropyl trimethoxysilane (MPTMS) by CVD from anhydrous toluene onto glass was accomplished using the same apparatus and procedure used for APTES. The deposition results were assayed by scanning fluorimetry using 1 mM iodoacetamido fluorescein in a 10 mM $NaHCO_3$ buffer (pH 9.0) which was 10 mM in dithiothreitol (DTT). The probe solution was allowed to stand for ten minutes on the treated substrates after which time the excess was removed by micropipette and the substrate washed in coupling buffer and ethanol. The fluorescence intensities of the spotted areas are shown in Table 3.

Table 3. CVD of 3-Mercaptopropyl Trimethoxysilane (MPTMS)

Substrate	Background	1mM IAAF
Glass	180	635
Mercaptopropyl Glass	93	4200

As can be seen from the data of Table 3, CVD can be easily used to derivatize glass substrates with MPTMS. Potential applications for this type of surface include anchoring samples through the formation of disulfide bonds and so forth. Although we have not attempted CVD of MPTMS onto mica or other substrate materials, as we will show later, there is no reason to believe that this approach would not provide suitable results.

Another useful functionality for immobilizing biomolecules, particularly nucleic acids, is the quarternary amine. Previously quarternary amines have been used for binding both proteins and nucleic acids to a variety of supports.[20] When used to bind nucleic acids, the interaction between the quarternary amine and the nucleic acid phosphate groups is of an ionic character as opposed to the covalent linkages discussed above. We find that we are able to deposit the commercially available compound N-trimethoxysilylpropyl-N,N,N-trimethyl ammonium chloride (alkoxysilylpropyl TMA Cl) by CVD from anhydrous m-xylene. Again, the same apparatus and procedure was used for this compound. To judge the success of the CVD, a carboxyfluorescein-labeled (FAM-NHS, Applied Biosystems) oligonucleotide (23-mer) was used as the probe for scanning fluorimetry. The single stranded DNA containing solution was allowed to stand on the substrates for three minutes, at which time the excess was removed and the substrates washed in running distilled water and allowed to air dry. The substrates were then imaged. The fluorescence data comprises Table 4.

Table 4. CVD of Alkoxysilylpropyl TMA Cl

Substrate	Background	Before Wash	After Wash††
Glass	36	79	45
Blocked Glass†	36	36	36
Aminopropyl Glass	36	2213	437
Quart. Amino Glass	49	6663	2600

† Glass treated with 5% dichlorodimethylsilane in chloroform

†† Wash with 10 mM $NaHCO_3$ pH 9.0

After the initial imaging was done the substrates were washed with 10 mM carbonate buffer (pH 9.0) in order to ascertain the difference in oligonucleotide binding between the aminopropyl glass and quarternary amino propyl glass. As can be seen from the fluorescence data, the aminopropyl glass showed a greatly reduced signal following the wash, but the signal reduction in the quarternary amino propyl glass is not nearly as substantial. This evidence supports the contention that CVD of the alkoxysilylpropyl TMA Cl has been accomplished and that this surface binds oligonucleotides even in aqueous environments.

A Variety of Substrates Can Be Derivatized

The utility of a covalent attachment chemistry for SPM depends not only on the diversity of available linkage moities, but also on its compatibility with well characterized imaging substrates. Among the most popular imaging substrates for scanned probe microscopy are graphite, mica, glass and silicon. Graphite presents a rather chemically inert surface which is not easily amenable to derivatization, but the other materials, along with silica, contain silicon and thus are candidates for alkoxysilane modification. We have already demonstrated the ability to covalently link alkoxysilanes to glass and the derivatization of silicon is well established, so we now focus on the derivatization of silica and mica.

Although silica (fused quartz) is not a common SPM substrate, it has several properties that make it an interesting substrate for derivatization. It is much better chemically defined than glass and mica and it is optically clear over the visible and into the ultra-violet portions of the light spectrum. This optical

transparency makes silica an ideal substrate for fluorescence microscopy, especially for fluorophores which require ultra-violet excitation. Because we are interested eventually in doing experiments involving concurrent epifluorescence and atomic force microscopy, we think the ability to produce optically clear derivatized substrates may prove valuable.

We treated silica substrates as described in the Methods & Materials section. The chemical vapor deposition was done in the same apparatus (shown in Figure 7), but a different sized Teflon rack was made to hold the substrates. Following deposition, the derivatized substrates were treated in the same manner as the derivatized glass substrates. To assay surface derivatization we performed the fluorescence assay on the silica substrates using various concentrations of FITC. The fluorescence intensities comprise the data of Table 5. As can be seen from Table 5, we were able to derivatize silica substrates as effectively as glass substrates.

Table 5. CVD Derivatization of Silica

Substrate	**Background**	**1 µM FITC**
Silica	40	75
Aminopropyl Silica	60	500

For many SPM experiments mica is the substrate of choice, so the ability to derivatize mica is most useful. Although mica is not necessarily transparent, nor is it particularly well defined chemically, the utility of mica as a SPM substrate arises because cleavage of mica results in large areas which are atomically flat. This substrate flatness has proved to be crucial for high resolution SPM. One

should note that, given the crystal structure of mica there is little reason to suspect, *a priori*, that the silicon atoms of the mica should be accessibile to form siloxane bonds in the same manner that the silanols of other substrate materials are. Despite this, we attempted CVD of alkoxysilane onto mica with gratifying results.

The mica was prepared as described in the Materials and Methods section, and the CVD was done in the same apparatus and under the same conditions used for other substrates. After deposition the substrates were rinsed with toluene, acetone, ethanol and water and allowed to air dry. The substrates were either assayed for derivatization using the scanning fluorimeter or were stored in a desiccator at room temperature.

The screen display from a typical scanning fluorescence measurement of derivatized mica is shown in Figure 4. As one can see from the image, areas adjacent to the regions spotted with fluorescent probe can be used as a baseline for background fluorescence. In this experiment FITC was the fluorescent probe and it was applied in two rows as a serial dilution series starting at a concentration of 10 mM on the left with more dilute solutions applied to the right. This particular assay was one of the earlier assays and excess reagent was not carefully removed as was done in later assays; the attempt at merely washing excess fluorophore off the surface can be seen to leave a residue toward the right-hand side of the image. The fluorescence intensity data for the derivatized mica is shown in Table 6.

Figure 4. A typical image taken with the scanning fluorimeter. In this case, a mica substrate which has undergone CVD of 3-aminopropyl triethoxysilane and been probed with fluorescein-5-isothiocyanate is shown. The resolution obtainable with this instrument is ≈ 50 µm, thus the resolution displayed in this image is limited by the display device. Although spatial resolution can be increased further by sampling more frequently and performing a deconvolution of the intensity profile with the excitation and collection optics, such processing was not deemed necessary for this application.

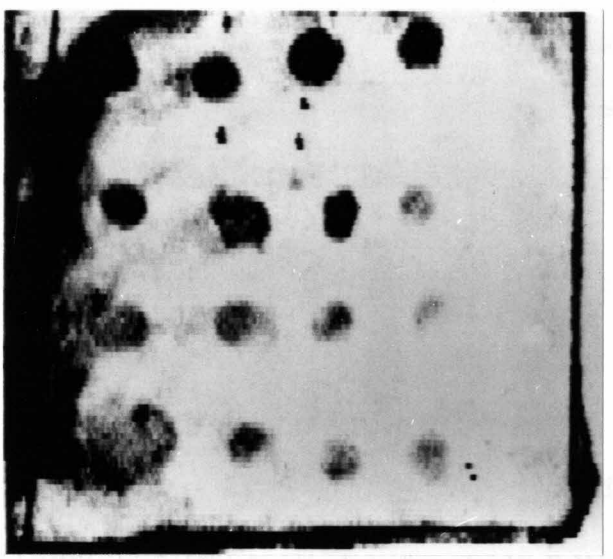

Table 6. CVD Derivatization of Mica

Substrate	Background	1 µM FITC
Mica (Ruby Muscovite)	35	40
Aminopropyl Mica	32	237

When taken together the data of Tables 1,5 & 6 show that a variety of siliceous substrates can be derivatized by chemical vapor deposition. As we will show later, this provides a body of evidence upon which more sophisticated deposition and derivatization schemes can be built.

Immobilization of Biological Samples for SPM

As mentioned in the Introduction, we initially embarked on this work in an effort to gain structural information on biomaterials of a complementary nature to that supplied by more traditional methods such as X-ray crystallography and multi-dimensional NMR. Among the more interesting subjects for study from a biological point of view are nucleic acids and proteins.

Nucleic Acid Immobilization-

Recently DNA has received a great deal of attention from the scanned probe microscopy community. Much of the work in this area has been motivated by the hope that someday scanned probe microscopy might be able to directly provide DNA sequence information.[18] Although this potential is far from being realized, some tentative steps in this direction have been made. For sequence

analysis, the native conformation of DNA during SPM is unimportant as long as i) the sample is stable during image acquisition and ii) adequate resolution to reveal the identity of individual bases of the DNA molecule is achieved. Thus, imaging in organic environments[11] can be tolerated for this sort of application.

For more biologically sophisticated applications such as the direct investigation of protein-DNA interactions or chromatin structure, the imaging environment must more closely approximate the natural environment in which the biological processes occur. Other investigators have recognized the importance of sample immobilization in the reproducible imaging of nucleic acids in biologically relevant buffers. In fact, the use of 3-aminopropyl triethoxysilane treated surfaces for SPM imaging of DNA and RNA has been reported.[19-21] In these studies both solution deposition and chemical vapor deposition have been used and images of nucleic acids have been acquired under water.

Immobilization of Proteins-

Previous attempts to image protein samples by SFM (reviewed in Reference 22) have provided a valuable window on intermolecular processes, however the character of most protein images falls short of realizing the potential sub-nanometer resolution of SFM. Recent efforts to fabricate sharper tips for SFM[23-26] have done much to ameliorate tip radius effects which have limited resolution and sample preparation techniques have been developed which allow imaging in nondestructive environments, but sample motion and solubility still restrict the use of truly physiologically relevant conditions during SFM on many samples.

One way to eliminate sample motion during SFM is to affix the sample to the substrate through one or more covalent bonds via linkers as described in this paper. The attachment of a sample through such a linker should result in decreased motion of the sample relative to the substrate and in an increase in the force required to remove the sample from the substrate. While the attachment of the sample to a substrate will do little to address the issue of intra-molecular motion, our hope was that it would allow the use of more natural conditions during imaging and thereby facilitate the investigation of biological structures in solution.

Several experiments were performed to ascertain if the covalent attachment of samples to imaging substrates yields a significant benefit over other sample preparation methods. There are two conceptually different ways to immobilize protein samples: i) direct formation of a covalent bond between a reactive group inherent in the sample and the reactive group at the distal end of the linker; and ii) the use of a crosslinking agent to act as an intermediary between the sample and the substrate. We have investigated the efficacy of the first type of linkage by immobilizing carboxymethyl modified polystyrene microspheres (data not shown). This was readily accomplished by a standard carbodiimide mediated coupling reaction.

We have established the utility of the second kind of sample attachment, crosslinking, in the course of our work with protein micro-crystals. Figure 5 shows an image of a protein micro-crystal obtained using the attachment

Figure 5. Image of a microcrystal of bovine catalase fixed to a 3-aminopropyl alkoxysilane treated glass substrate obtained under water. In this image the micro-crystal is seen in the lower left as a plate shaped object with sharply defined edges. The surface of the micro-crystal is seen to be textured, and although molecular resolution is not apparent, small defects in the surface are observed. The gradual curve seen crossing the upper portion of the image is believed to be a scratch in the glass substrate. The texture of the substrate is similar to that seen in electron micrographs (data not shown). It is thought to be caused by molecules of catalase present in the micro-crystal suspension which are immobilized in the same manner as the micro-crystals. The image is ≈ 1.0 µm x 1.2 µm and was taken under water using a commercial cantilever with an electron beam deposited tip.[23,24] Image processing consisted of image tilt removal by best fit plane subtraction and displaying the image in light shaded mode, thus brightness is proportional to both height and slope with higher regions being lighter.

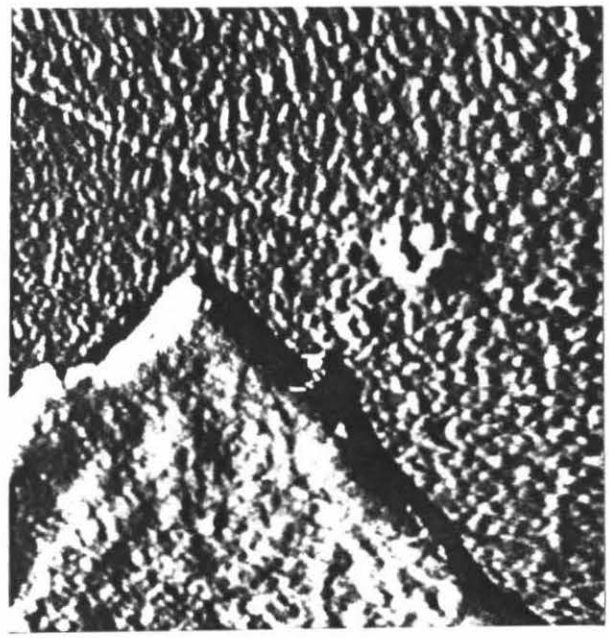

chemistry. In our attempts to obtain high resolution images of protein micro-crystals we found it advantageous to image in an aqueous environment. Our early attempts in this vein were thwarted by sample motion; even though micro-crystals were plainly visible by Nomarski microscopy and could be found on dried samples imaged in air at low magnification, when water was introduced the crystals were easily washed off the substrate. This problem was readily solved by "preactivating" the substrate with a 2% glutaraldehyde solution for 5 minutes, followed by rinsing with water and application of the micro-crystal suspension. The suspension was incubated at 4° C in a humid environment for several hours to allow the crystals to settle onto the surface and react. After incubation, the substrate was rinsed in running distilled water to remove unattached sample and imaged immediately.

As can be seen in Figure 5, not only are the micro-crystals immobilized but individual catalase molecules are also affixed to the substrate. It is perhaps not evident from this image, however, that the micro-crystals were able to be imaged reproducibly and without visible damage. In any case, obtaining images of micro-crystals in an aqueous environment depended crucially on the use of the immobilization chemistry.

MATERIALS AND METHODS

Substrate Preparation-

Glass microscope slides (Corning 2948) and silica substrates (1" square S1-UV grade silica slides, Part Number R310110, Esco Products, Oak Ridge, N. J. 07438 U.S.A.) were cleaned, while held in a chemically inert rack, by immersion in stirred xylenes, washed with acetone and rinsed in running distilled water. Following this treatment the substrates were further washed in stirred detergent (Alconox or Lemon Fresh Joy), rinsed with running distilled water, sonicated in RBS 35 detergent (Pierce Scientific) with ethanol for at least one hour and rinsed again with running distilled water. The glass and silica substrates were then soaked in stirred, hot (70-80 °C) fuming nitric acid for at least one hour and were then rinsed with running distilled water for five minutes and running deionized water for 10 minutes. The substrates were then oven dried at 70 °C for one hour and stored in a desiccator until use. During the final rinse substrates which did not appear highly hydrophilic were reprocessed starting at the nitric acid step. After cleaning, any substrates with visible defects were discarded.

Mica substrates (Grade 5 Ruby Muscovite from New York Mica Corporation) were cut to size from small sheets. The mica was cleaved using Scotch tape while held with a vacuum fixture. The freshly cleaved mica was immediately placed in the deposition apparatus which had been dried and purged with dry argon.

Deposition Methods-

The solution deposition of alkoxysilane was effected from both organic and aqueous solvents. For deposition from organic solvents a 5% (v/v) solution of the alkoxysilane in anhydrous toluene or neat ethanol was used at room temperature. The substrates were immersed in the solution and the reaction was allowed to proceed overnight (> 12 hours). Following the reaction the substrates were removed from the solution and washed extensively with fresh toluene, neat ethanol and finally oven dried. Any substrates with visible defects, such as fogging or streaking, when examined under intense illumination were discarded.

A 5% (v/v) concentration of alkoxysilane was also used for deposition from aqueous solution. Substrates were immersed for 15 minutes at room temperature in freshly prepared alkoxysilane solution and washed extensively with water following the reaction. Again, any substrates which showed visible defects after deposition were not used further.

The chemical vapor deposition of alkoxysilane was performed in the apparatus shown schematically in Figure 6. This apparatus is similar to that of Haller.[17] The prepared substrates are held in a Teflon rack and come into contact only with the refluxing vapors of the alkoxysilane solution. The apparatus was flushed for an hour or more with dry argon before the addition of anhydrous solvent which was brought to a rolling boil and a steady refluxing condition was established. After condensing solvent vapors were seen steadily midway up the condenser for several minutes, sufficient alkoxysilane was added by syringe to make the solution 5% (v/v) alkoxysilane. The solution was refluxed for several hours and was then allowed to cool to room temperature.

Figure 6. The chemical vapor deposition (CVD) apparatus. The apparatus is similar to that used by Haller[17] for CVD of alkoxysilanes onto silicon. The apparatus is designed to hold a substrate rack above a refluxing silane and solvent solution. During deposition, the solvent is heated to a uniform temperature by the oil bath and allowed to reflux. After the solvent has attained a state of steady reflux and the condensing vapors are reaching up one third of the condenser length, the deposition is started by injecting the silane into the apparatus. The deposition is typically allowed to continue for several hours. After this the heater is turned off and the apparatus allowed to cool. Once the apparatus has reached room temperature, the substrates are removed and washed and stored as described in the text.

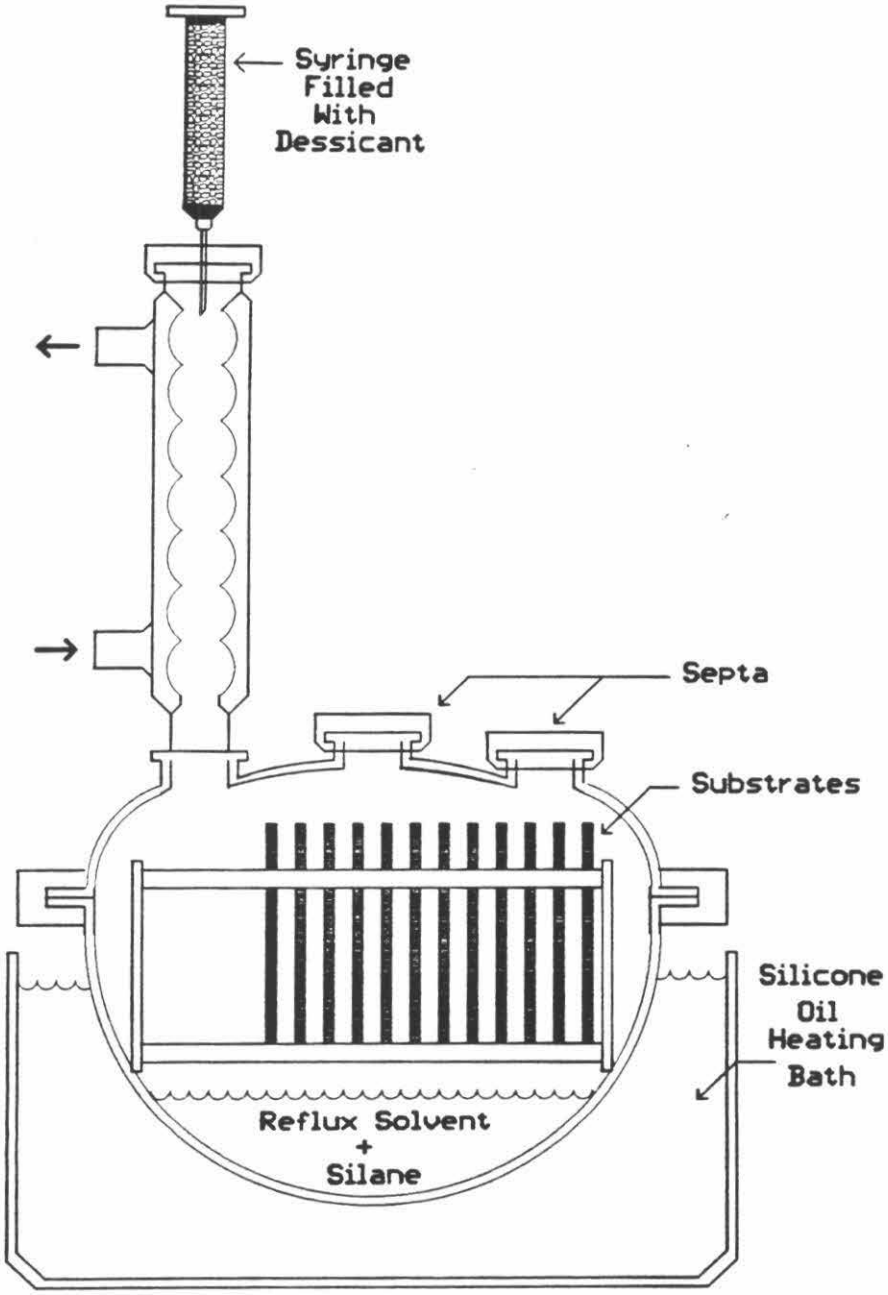
Syringe
Filled
With
Dessicant
Septa
Substrates
Silicone
Oil
Heating
Bath
Reflux Solvent
+
Silane

The substrates were recovered from the apparatus and washed with fresh solvent. Often the substrates underwent additional washes with water and neat ethanol. As before, substrates showing visible damage were discarded.

Post-Deposition Derivatization of 3-Aminopropyl Glass to Isothiocyanate Glass

Derivatization was done at room temperature by immersing the substrates in a solution consisting of 25 ml CS_2 , 25 ml of anhydrous pyridine and 8 ml of diisopropylcarbodiimide (DIC). Diisopropylcarbodiimide was used because of the increased solubility of its urea byproduct as compared to the urea resulting from the use of dicyclohexylcarbodiimide (DCC). The reaction was performed in a dry argon atmosphere. At the end of one hour the substrates were removed from the solution and washed in fresh pyridene, tetrahydrofuran and ethanol followed by air drying.

Assays of Surface Modification-

After deposition of alkoxysilane, substrates were assayed by several methods, including fluorescence imaging and scanned force microscopy.

Fluorescence Imaging

Fluorescence imaging of derivatized substrates was done using a two-dimensional scanning fluorimeter. This instrument is of an original design and is described more fully in Reference 28. The fluorescence excitation is provided by an argon ion laser which supplies ≈ 5 mW (488 nm line) at the sample in a 300 μm

diameter ($1/e^2$) spot. Sample fluorescence emission is measured by a photomultiplier tube (PMT) after the light has passed through an optical bandpass filter. The PMT signal is digitized by a 16-bit analog to digital converter and recorded as a function of position and/or time. The spatial resolution of the instrument is ≈ 50 μm in both the X and Y dimensions. The data display software allows the measurement of signal intensity at individual pixels and average signal intensity over a user defined circular area. These features were used to provide the numerical data presented in this paper.

The fluorescence assay of surfaces was performed by spotting one of the assay reagents shown in Figure 7 on the surface under investigation and allowing some time for the reaction to proceed. Excess reagent was removed by micropipette and the surface was then washed in the reaction buffer frequently followed by more stringent washes. The surface was then air dried and placed on the scanning fluorimeter with other surfaces to be assayed. If samples required storage after they had been treated with fluorescent probes, they were stored in a desiccator at room temperature in the dark to avoid photobleaching. Image data was gathered and spot intensities were measured. By spotting the surfaces to be assayed, the unstained areas can be used to control for background fluorescence. Typically, the fluorescent background was quite small (< 0.2% of full scale fluorescence). In cases where substantial background was observed, the samples were discarded and the experiment repeated.

Scanned force microscopy

Scanned force microscopy was done using a custom built scanned force microscope described in Reference 7 and references therein.

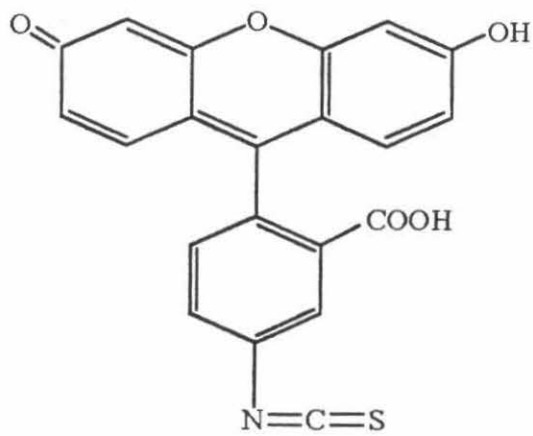

a) Fluorescein-5-isothiocyanate

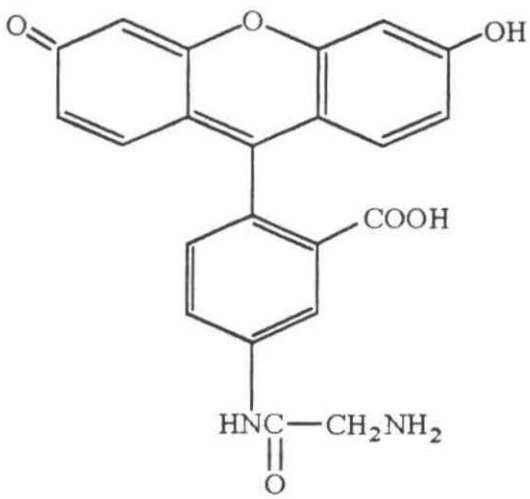

b) 5-(aminoacetamido)fluorescein

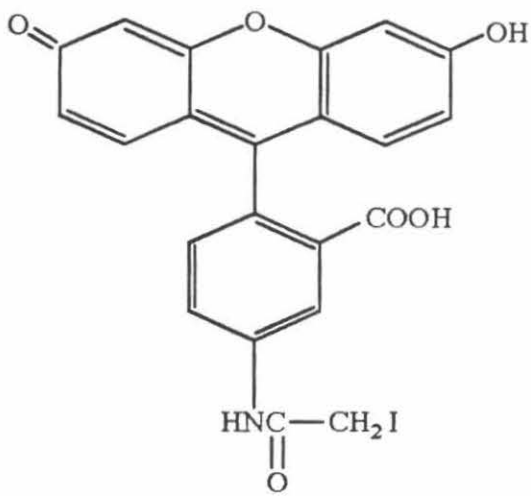

c) 5-iodoacetamidofluorescein

Figure 7. Chemical structures of the small molecule fluorescent probes used to assay for various surface derivatives. a) fluorescein-5-isothiocyanate, b) 5-(aminoacetamido) fluorescein, c) 5 - iodoacetamido fluorescein.

CONCLUSION

In this paper we have shown that the chemical vapor deposition of heterobifunctional alkoxysilanes onto scanned probe microscopy imaging subtrates provides a means by which biologically interesting samples can be immobilized. The data presented suggests that substrates which have been treated by CVD of alkoxysilanes maintain their surface morphology to a reasonable degree and that these surfaces are able to be further derivatized as well as used directly for sample immobilization.

While there are many biological systems which can be investigated without an attachment chemistry, such as molecular motor preparations or living cells, the additional capability offered by chemical immobilization methods is easily recognized. Particularly in applications where sample motion has been problematic, such as imaging nucleic acids or highly soluble proteins, the need for an attachment chemistry has been keen.

It is hoped that the attachment chemistry described here and in References 19-21 fills this need and that it is both simple and effective enough to find wide spread application in scanned probe microscopy of biomaterials.

References:

1. Binnig, G., C. F. Quate and Ch. Gerber. (1986). "Atomic Force Microscope." *Phys. Rev. Lett.* **56**:930-936.
2. Marti, O., B. Drake, S. Gould, P. K. Hansma. (1988). "Atomic resolution atomic force microscopy of graphite and the native oxide on silicon." *J. Vac. Sci.* **A6** (2):283-286.
3. Meyer, G. and N. M. Amer. (1990). "Optical-beam-deflection atomic force microscopy: the NaCl (001) surface." *Appl. Phys. Lett.* **56** (21):2100.
4. Kim, Y., C. M. Lieber. (1991). "Chemically etched silicon surfaces: surfaces viewed at the atomic level by force microscopy." *J. Am. Chem. Soc.* **113** (6):2333.
5. Butt, H.-J. (1991). "Measuring electrostatic, van der Waals and hydration forces in electrolyte solutions with an atomic force microscope." *Biophys. J.* **60** (12):1438.
6. Allen, M. J. et al. (1992). "Tip-radius-induced artifacts in AFM images of protamine-complexed DNA fibers." *Ultramicros.* **42**:1095-1100.
7. Clark, S. M. et al. (1992). "Hardware for digitally controlled scanned probe microscopes." *Rev. Sci. Instrum.*, **in press**.
8. Wiesenhorn, A. L., P. K. Hansma, T. R. Albrecht, C. F. Quate. (1989). "Forces in atomic force microscopy in air and water." *Appl. Phys. L.* **54** (26):2651-53.
9. Vesenka, J., et al. (1992). "Substrate preparation for reliable imaging of DNA-molecules with the scanning force microscope." *Ultramicros.* **42**:1243-49.
10. Bustamante, C., et al. (1992). "Circular DNA-molecules imaged in air by scanning force microscopy". *Biochem.* **31** (1):22-26.

11. Hansma, H. G., et al. (1992). "Reproducible Imaging and Dissection of Plasmid DNA Under Liquid with the Atomic Force Microscope." *Science* **256**:1180-1184.

12. Petrarch Systems Division of Hulls America, Inc., Bartram Road, Bristol, PA 19007, U. S. A.

13. Edwin P. Plueddeman, Silane Coupling Agents (Plenum Press, New York, ed. 2, 1982.

14. PCR, Inc., P. O. Box 1466, Gainesville, Florida 32602, U. S. A.

15. see for example, Methods in Enzymology Volumes 44, 135-137, K. Mosbach, ed. (Academic Press, New York).

16. Janowski, F., et al. (1991). "Aminopropylsilane Treatment for the Surface of Porous Glasses Suitable for Enzyme Immobilisation." *J. Chem Tech Biotechnol.* **51**:263-272.

17. Haller, I. (1978). "Covalently Attached Organic Monolayers on Semiconductor Surfaces." *J. Am Chem Soc.* **100** (26):8050-8055.

18. Hansma, H. G. et al. (1991). "Progress in sequencing deoxyribonucleic-acid with an atomic force microscope." *J. Vac. Sci. Technol.* **B9** (2):1282-1284.

19. Lindsay, S. M. et al. (1992). "Imaging DNA molecules chemically bound to a mica surface." SPIE Proceedings Vol. 1639, Scanning Probe Microscopies, S. Manne, ed. pages 84-90.

20. Lyubchenko, Y. L., B. L. Jacobs, S. M. Lindsay. (1992). "Atomic force microscopy of reovirus dsRNA: a routine technique for length measurements." *Nucleic Acids Res.* **20** (15):3983-86.

21. Lyubchenko, Y. L. et al. (1992). J. Biomol. Struct. Dyn., in press.

22. Engel, A. (1991). "Biological applications of scanning probe microscopy." *Ann. Rev. Biophys. Biophys. Chem* **20**:79-108.

23. Keller, D. J. and C. Chih-Chung. (1992). "Imaging steep, high structures by scanning force microscopy with electron beam depositedtips." *Surface Science* **268**:333-339.

24. Lee, K. L., D. W. Abraham, F. Secord and L. Landstein. (1991). "Submicron Si trench profiling with an electron-beam fabricatedatomic force microscope tip." *J. Vac. Sci. Technol.* **B9** (6):3562-3568.

25. Vasile, M. J. et al. (1991). "Scanning probe tips formed by focused ion beams." *Rev. Sci. Instrum* **62** (9):2167-71.

26. Vasile, M. J. et al. (1991). "Scanning probe tip geometry optimized for metrology by focused ion beam ion milling." *J. Vac. Sci. Technol.* **B9** (6):3569-72.

27. Clark, S. M., J. D. Baldeschwieler and J.-P. Revel. "High resolution imaging of bovine catalase microcrystals using the atomic force microscope." manuscript in preparation.

28. Spence, C. F. et al., "A scanning fluorimeter for biological applications." manuscript in preparation.

Appendix D.

Detailed Protocols for the Preparation of Derivatized Substrates for Scanned Probe Microscopy

I. Introduction

II. Commercial Availability of Alkoxysilanes

III. Apparatus for the Chemical Vapor Deposition of Alkoxysilanes

IV. Substrate Preparation

V. Deposition Protocols

I. Introduction

Alkoxysilanes find broad application in both laboratory and industrial processes. Industrially, alkoxysilanes are often used as coupling reagents to bond organic polymers to inorganic substrates (e.g., the manufacture of fiberglass) or to acts as primers.[1] In these types of processes the alkoxysilane is often used in bulk leading to the inexpensive commercial availability of the reagent.

In research settings, alkoxysilanes have been widely used for the immobilization of biomaterials (e.g., enzymes, antibodies, etc.). Whole volumes have been written about this type of application[2] and an extensive literature is available in research journals. Other common applications include the familiar oligonucleotide synthesis support, nucleoside CPG, which is made by derivatizing CPG with 3-aminopropyl alkoxysilane and subsequently attaching the desired nucleoside.

It is not surprising then, given a method for the application of alkoxysilanes which does not degrade the quality of surfaces, that one is able to use these compounds to covalently tether samples to imaging substrates.

II. Commercial Availability of Alkoxysilanes

Many of the more commonly used alkoxysilanes are available from the standard suppliers of fine chemicals (e.g., Aldrich,[3] Sigma,[4] Fluka,[5] etc.), however there are at least two companies which specialize in silanes. The company with the larger selection of silanes and silicones is the Petrarch Systems

Division of Hulls America, Inc.[6] The other company supplying silanes is PCR, Inc.[7] This company carries a variety of compounds including many fluorinated reagents and miscellaneous silanes. The Table I gives an idea as to which reagents are available from the different suppliers.

Table I. Suppliers of Alkoxysilanes

Compound	Aldrich	Fluka	PCR	Petrarch	Sigma
3-aminopropyl triethoxysilane	Yes	Yes	Yes	Yes	Yes
3-aminopropyl trimethoxysilane	Yes	Yes	Yes	Yes	Yes
3-aminopropyl alkoxysilanes*	No	Yes	Yes	Yes	No
3-mercaptopropyl trimethoxysilane	Yes	Yes	Yes	Yes	Yes
N-trimethoxysilyl-propyl-N,N,N - tri-methyl ammonium chloride	No	No	No	Yes	No
3-glycidoxypropyl alkoxysilanes †	Yes	Yes	Yes	Yes	No

* This category includes the different mono- and di-alkoxysilanes such as dimethyl ethoxysilanes, etc.

† This category includes the different methoxy- and ethoxysilanes.

III. Apparatus for Chemical Vapor Deposition of Alkoxysilanes

We are currently using two different types of apparatus for chemical vapor deposition of alkoxysilanes. The first type, shown in Figure 1, is a simple wide mouth reaction flask for which a Teflon substrate rack has been made.

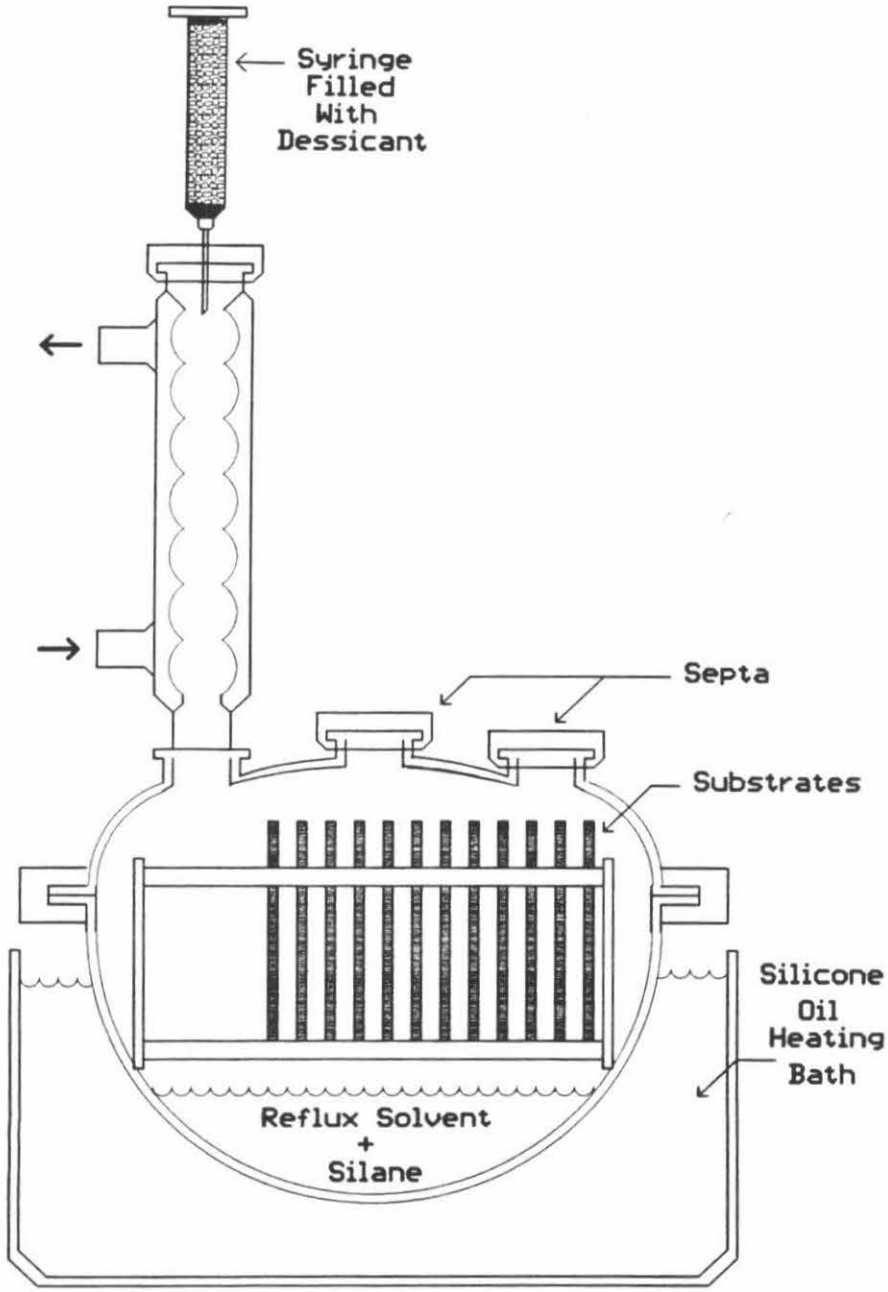

Figure 1. Reaction flask type CVD apparatus.

The rack design depends on the type and size of substrate to be treated and so new racks often have to be made for different substrates. The flask and associated components are available from Kontes Glass [8] and the part numbers are listed in Table II. The other parts required to set up the apparatus can be purchased from standard scientific supply houses; although they are listed, no part numbers are given for these items.

Table II. Parts for Reaction Flask Chemical Vapor Deposition Apparatus†

Description	Part Number
Flask, Cylindrical Reaction 500 ml	612000-0500
Flask Top, Four Neck Reaction	613000-0021
Flask Clamp, Reaction	613750-0000
Thermometer, 10/30 Standard Taper -10 to 250°C	871000-0225
Condenser, Reflux	457000-0225
Silicone Oil	
Dish, Crystallization	
Nichrome Wire Heating Coil	
Variac (Variable Output Autotransformer)	

† Available from Kontes Glass (Ref. 8)

The only additional items required are expendables such as anhydrous solvents and equipment for handling air or moisture sensitive reagents. We find that Aldrich Chemical Company is a good source for many of the anhydrous solvents and that they also carry most of the equipment for performing air sensitive chemistry. If one is unfamiliar with the techniques used for handling

air sensitive reagents, a good tutorial is available from Aldrich (Technical Information Bulletin No. AL-134). Table III lists equipment which may be purchased from Aldrich and is used for handling the reagents needed for a CVD run.

Table III. Equipment for Handling Air Sensitive Reagents†

Description	Part Number
Septa, White Rubber for 24/40 Joints	Z10,145-1
Tape, Teflon Sealing	Z10,438-8
Bottle Caps, Bakelite with Liner	Z10,216-4
Bottle Caps, Bakelite with 3/8" Hole	Z10,807-3
Rubber Liners	Z10,808-1
Syringe, Disposable Polypropylene/Polyethylene 10 ml	Z11,687-4
Needles, 17 Ga. 3 1/2 " Long Stainless Steel	Z10,112-5
Needle, 16 Ga. 24" Long Double Tipped Stainless Steel	Z10,089-7

† Available from Aldrich Chemical Company (Ref. 3)

The last item in Table III is a double ended needle which we cut with a tubing cutter into two needles (one 6" long and the other 18" long). We connect these needles with a 4-5 foot length of .062" I. D. x 1/8" O. D. Tefzel tubing (available from Upchurch Scientific[9]) and use this as a transfer cannula. We went to the trouble to make our own cannula because we found that using the transfer cannula from Aldrich (which has 14 Ga. needles) left large holes in the septa on the solvent bottles resulting in a questionable seal.

We also routinely use anhydrous solvents from Aldrich. Some of the more common solvents are toluene, carbon tetrachloride and N,N-dimethyl formamide. These are all available from Aldrich in packages and grades suitable for use with the air sensitive techniques needed for CVD of alkoxysilanes. Using these chemicals saves one the trouble of having to redistill or dry any of the solvents before use.

The other type of apparatus which we have used for CVD of alkoxysilanes is a large bore Abderhalden drying apparatus. While this apparatus is more expensive than the reaction flask based apparatus, it offers the advantages of being able to do the deposition without mixing the reagent with solvent and minimized splattering of reagent onto the substrates. In Table IV we list the components required for setting up this apparatus and their Aldrich part number.

Table IV. Parts for the Drying Apparatus Based Chemical Vapor Deposition Apparatus †

Description	Part Number
Drying Apparatus, Large Capacity Abderhalden	Z10,318-7
Boiling Flask, Round Bottom 24/40 Joint	Z14,020-1
Condenser, Allihn (300 mm jacket length) 24/40 Joint	Z13,868-1
Heating Mantle (for 250 ml capacity flask)	Z16,587-5
Voltage Controller for Heating Mantle	Z16,592-1

† Aldrich Chemical Company (Ref. 3.) catalog numbers given.

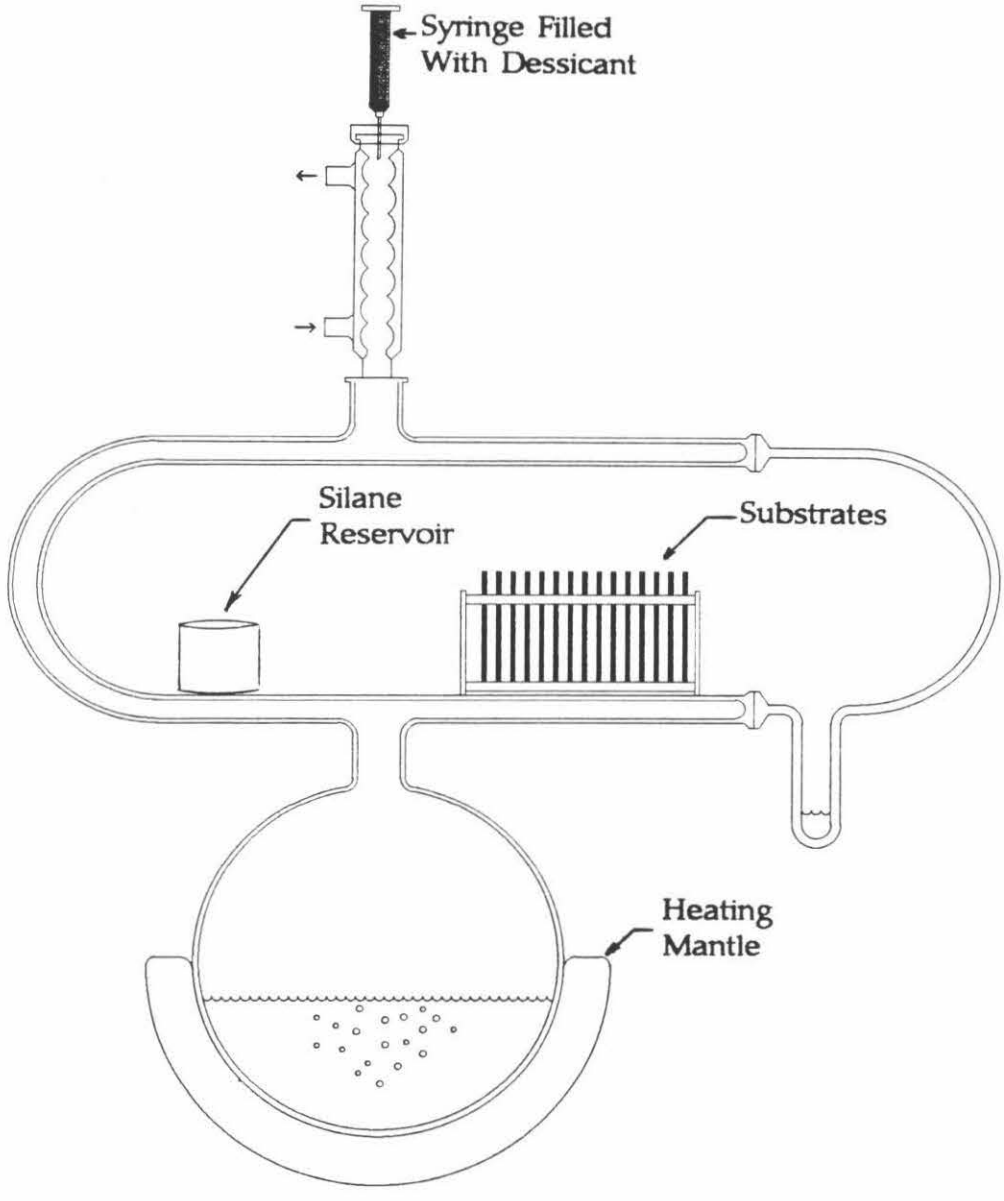

Figure 2. Use of an Abderhalden drying apparatus for CVD.

In the second type of apparatus, shown in Figure 2, the refluxing solvent serves to create a uniform high temperature environment to vaporize the deposition reagent. The deposition reagent is held in a small inert container on a platform in the bore of the drying apparatus. The substrates are also placed in the bore of the apparatus away from the silane reservoir and are held by a rack. The deposition may either be done in an inert, dry atmosphere or a vacuum may be applied. Because the solvent does not come in contact with the reagent, there is no need to use anhydrous solvents.

IV. Preparation of Substrates for Chemical Vapor Deposition

There are predominately two classes of substrate materials that we have used for scanned probe microscopy: i) mica; and ii) silicon based materials such as silicon wafers, fused silica and glass. The preparation steps for each of these classes is quite different.

In the case of mica (ruby Muscovite Grade 5 or better), preparation consists of cutting it to the proper size and cleaving it to expose a fresh surface. Once this is done the mica is placed in the inert atmosphere of the CVD apparatus and the CVD process is begun. A more detailed protocol is given below-

1. Cut properly sized and shaped pieces from the mica sheets.
   We often use scissors to cut square or rectangular pieces, but circular pieces are cut using a punch and die. The object is to avoid separation of the mica layers that can occur when using razor blades etc.

2. Check to be sure that the pieces fit in the rack and that the full rack fits in the CVD apparatus.
3. Hold the mica with a vacuum chuck and cleave it using Scotch tape. We have found that a simple vacuum chuck can be made by using an aspirator with a side arm flask as a trap. The aspirator inlet is connected to the side arm of the flask with thick wall Tygon tubing. The distal end of the hose coming from the top of the flask is used as the chuck. The chuck itself consists of a cut off blue tip pipette inserted into the end of the hose and the rolled end of a cut off rubber pipette bulb is fitted over the wide end of the blue pipette tip. This provides a compliant annulus which forms the vacuum seal. After a seal has formed and the mica is being held firmly in place by the vacuum, it can be cleaved by applying a piece of Scotch tape to the surface and peeling it back off. One can check for uniformity of cleavage by inspecting the tape back following removal. A uniform cleave will result in the back of the tape being shiny from the attached mica. If the cleave is not uniform the process should be repeated.
4. Place the mica pieces in the rack noting which surfaces are the freshly cleaved (and therefore useful) ones.
5. Start the CVD process.

Preparation of the second class of substrates is more laborious than preparing mica. The process involves a sequence of treatments designed to remove particular types of contaminants; first greasy substances are removed, followed by removal of lighter contaminants and residual solvent by detergent. This is followed by a hot acid soak to finish removing organic contaminants and leave the substrate surface hydrophilic. The detailed protocol is-

1. Cut the substrates to size as required and be sure they fit in the rack.
2. Immerse the substrates in stirred xylenes for 10-30 minutes.
3. Wash with acetone and rinse with running distilled water for 5 minutes.
4. Wash in stirred detergent solution (Lemon Fresh Joy or Alkonox) for 15-30 minutes. Rinse repeatedly with distilled water until no suds appear then rinse with running distilled water for 5 minutes.
5. Sonicate in RBS 35 detergent (Pierce Scientific) with 10% ethanol for at least one hour. Rinse again with running distilled water for 5 minutes.
6. Soak in hot (80-90°C), stirred concentrated nitric acid for at least one hour. Allow to cool and drain acid. Rinse with running distilled water for 5 minutes followed by a 10 minute rinse with running distilled, deionized water (> 18 Mohm cm).
7. Allow substrates to air dry and then oven dry (>70°C) or dry with a heat gun.
8. If necessary, store in a clean desiccator until ready for CVD.

A few comments should be made about this protocol. The first point is that this protocol has not been extensively refined either for ease of preparation or time savings; there are bound to be steps that can be eliminated or things that can be added for special circumstances. Another point worth comment is that, in our laboratory, substrates are most often prepared as required and so studies of long term storage of cleaned or derivatized substrates have not been done. The final point concerns the evaluation of the cleanliness of the substrates. Clean substrates should be highly hydrophilic and this can easily be judged in the final rinse step. The rinse water should not bead or readily run off clean substrates; instead water should spread evenly across the substrate.

The preparation of single crystal silicon for CVD is not difficult, but typically involves the use of wet etching or heating in a vacuum to produce an oxide free surface upon which an oxide layer of known thickness is grown. While the detailed description of this process is beyond the scope of this discussion, we would refer the interested reader to References 10-14. After the growth of a thin oxide layer, the substrate should be used immediately for CVD. If this is not done the oxide layer thickness will continue to increase thus precluding the substrate's use for scanning tunneling microscopy.

V. Deposition Protocols

In this section we present two protocols for doing CVD; one for each type of apparatus. The first protocol is more complex and is for use with the reaction flask type of apparatus, while the second protocol, for use with the Abderhalden drying apparatus is simpler. The main point of either protocol is to create a dry, inert environment in which the alkoxysilane monomer can be put into the vapor phase and allowed to react with the prepared substrate surface. To achieve this goal the reaction vessel must be dry and residual gasses in the deposition chamber must be inert and dry.

A point needs to be made concerning the selection of solvent to use for the CVD process. It is desireable that the solvent be inert to reaction with the alkoxysilane and that it have a boiling point close to, but slightly greater than, the boiling point of the alkoxysilane monomer. Other than these considerations, any solvent which is available in the proper grade and package will do.

Protocol for CVD of Alkoxysilanes Using the Reaction Flask Apparatus

1. Check to be sure there are enough solvents and reagents on hand. If redistilled alkoxysilane is to be used, be sure that this is available.

2. Check the apparatus for potential problems. Troubles such as no running water for the condenser or water leaks at condenser hose barbs can be dangerous when complicated by a hot oil bath. Also check to be sure that the heating set-up is working (i.e., the paper clip or stir bar used to stir the oil bath moves etc.) and that no exposed electrical leads will come into contact with clamps, etc.

3. Arrange the substrates in the rack. If there is room, leave a little extra space at one end of the rack and place that end nearest the joint with the condenser. This will help cut down on the splattering on the substrates.

4. Clean and dry a piece of glass tubing (e.g., a Pasteur pipette) and place it between the leaves of a clean paper towel and smash it. Retrieve the shards and place them in the bottom of the flask for use as boiling chips.

5. Place the rack in the flask and adjust its position so that condensate will not drip directly onto the substrates.

6. Apply a thin bead of silicone grease around the periphery of the ground glass flange between the top and bottom of the apparatus. We use a 5 ml syringe filled with silicone grease for this. It is important to minimize the amount of solvent that comes in contact with the silicone grease because it is soluble in most of the solvents used for the CVD and will run into the

reaction vessel and contaminate the reaction. (We have also tried a Teflon gasket to seal the chamber, but found that the compressive force generated by the flask clamp was insufficient to form a good seal.)

7. Wrap the ground glass joint of the condenser with Teflon tape and insert the condenser into one of the side joints in the flask top.

8. Wrap the ground glass joint of the thermometer with Teflon tape and insert it into the thermometer port in the flask top.

9. Seal the top of the condenser and the two unoccupied ports on the flask top with rubber septa.

10. Remove the plunger from a 10 ml disposable syringe and place a small plug of glass wool in the bottom of the syringe barrel. Fill the syringe to about 1 cm from the top with desiccant (e.g., indicating Dri-Rite). Use another small plug of glass wool to seal the top so that the desiccant does not fall out. Attach a 16 Ga. x 1.5" disposable needle to the syringe and insert the needle through the septum at the top of the condenser. The idea here is to make a drying trap which will help prevent the CVD vessel from becoming pressurized.

11. Make another drying trap and put it in line with the argon purge. Again, it needs to have a needle on the end so it can be inserted into one of the septa in the unoccupied ports. We have found an easy way to make this is to use a syringe as before with a tubing connector forced into the syringe barrel. The tubing connector has a hose barb on one end and mates with

another hose connector on the other. Instead on the mating connector, this end is forced into the barrel of the syringe. One should test this at pressure before using it.

12. Start purging the apparatus with dry argon and begin heating. It might be a good idea to turn on the cooling water to the condenser at this point, although occasionally we wait until the reflux is established before starting the water.

13. After ≈ 30-45 minutes withdraw the purge and transfer the solvent into the apparatus using the transfer cannula. The cannula should be purged with argon before use. The volume of solvent typically used in our apparatus is ≈ 100 ml which brings the surface of the solvent to about 1.5 cm from the bottom of the substrates. Allow the solvent to come to full reflux (the vapors should reach up about 1/3 of the condenser height). We usually cover the flask top with aluminum foil to help the uniformity of heating.

14. After a stable reflux has been established for about half an hour, it is time to add the alkoxysilane. This is done using a polypropylene/polyethylene syringe and a stainless steel needle. Take up enough of the desired silane in the syringe to make the solution 1-5% silane after it has been added. Add the silane through the unoccupied port in the flask top that is furthest from the substrates. Be careful not to squirt the silane directly onto the substrates. If a smoky vapor appears in the condenser as the silane is added, the apparatus is not entirely dry. The smoky vapor is some of the silane undergoing condensation with residual water to become

siloxanes. This does not mean that the run is worthless, it just indicates that there is still some water in the reaction vessel.

15. Maintain the refluxing for at least another 2 hours after adding the silane.

16. Turn off the heater and allow the apparatus to cool.

17. After the apparatus has cooled, disassemble the apparatus and recover the substrates. We often wash the substrates with the reflux solvent, followed by acetone and ethanol. After this the substrates are air dried and stored in a clean environment until needed.

One of the easiest ways to tell if the CVD has occurred is to spot a corner of the treated substrate with water. Before CVD the substrates should have been very hydrophilic and after successful CVD they tend to be hydrophobic, so the water should form a distinct droplet as opposed to wetting the surface.

The protocol for CVD of alkoxysilane in the Abderhalden apparatus is much simpler and is as follows-

1. Check the apparatus to be sure there are no cracks or defects.

2. Dry the apparatus. This can be done either by oven drying or more conveniently by heating the apparatus to 150°C while pulling a vacuum (baking out the apparatus).

3. Back fill the reaction chamber with dry argon.

4. Place an aliquot of the desired silane in a small inert open top vessel and place the vessel on an appropriate support located as far in the bore of the apparatus as practical.

5. Load the substrates in their rack into the bore of the apparatus and close replace the desiccant chamber.

6. Pull a vacuum in the chamber and back fill with dry argon as required.

7. Begin heating and wait until the aliquot of alkoxysilane transfers to the desiccant chamber.

8. Allow the apparatus to cool and disassemble to recover substrates.

9. Wash as desired and store in a clean environment until needed.

References

1. Edwin P. Pluedderman, Silane Coupling Agents (Plenum Press, New York, ed. 2, 1982).
2. see for example, Methods in Enzymology Volumes 44, 135-137, K. Mosbach, ed. (Academic Press, New York).
3. Aldrich Chemical Company, 1001 West Saint Paul Avenue, Milwaukee, WI 53233, U.S.A.
4. Sigma Chemical Company, P. O. Box 14508, St. Louis, MO 63178 U.S.A.
5. Fluka Chemie AG, Industriestrasse 25, CH-9470 Buchs/Switzerland
6. Petrarch Systems Division of Hulls America, Inc., Bartram Road, Bristol, PA 19007, U.S.A.
7. PCR, Inc., P.O. Box 1466, Gainesville, Florida 32602, U.S.A.
8. Kontes Inc., 1020 Spruce Street, Vineland, N.J. 08360 U.S.A.
9. Upchurch Scientific, 619 West Oak Street, P.O. Box 1529, Oak Harbor, WA 98277 U.S.A.
10. S. Wolf and R. N. Tauber, Silicon Processing for the VLSI Era Volume 1-Process Technology. Chapter 7: "Thermal Oxidation of Single Crystal Silicon" and References Therein (Lattice Press, Sunset Beach, CA, 1986).
11. E. A. Taft, *J. Electrochem. Soc.* **135**, 1022 (1987).
12. P. J. Grunthaner, *et al*, *Thin Solid Films*, **183**, 197 (1989).
13. D. J. Eaglesham, G. S. Higashi and M. Cerullo, *Appl. Phys. Lett.*, **59**, 685 (1991).
14. G. S. Higashi, R. S. Becker, Y. J. Chabal and A. J. Becker, *Appl. Phys. Lett.*, **58**, 1656 (1991).

Chapter IV

High Resolution Imaging of Bovine Catalase Microcrystals Using The Atomic Force Microscope

* Manuscript to be submitted to *Science*

High Resolution Imaging of Bovine Catalase Microcrystals Using The Atomic Force Microscope

Steven M. Clark, John D. Baldeschwieler† and Jean-Paul Revel

Division of Biology

and

†Division of Chemistry and Chemical Engineering

California Institute of Technology

Pasadena, CA 91125

Abstract

High resolution images of bovine liver catalase micro-crystals obtained by atomic force microscopy in an aqueous environment are presented. These images are directly comparable to images obtained by transmission electron microscopy and show similar features at slightly better resolution. This work demonstrates the ability of the atomic force microscope to provide high resolution structural data on protein micro-crystals.

Since its invention in 1985,[1] atomic force microscopy has held the promise of providing high resolution images of biological materials in physiologically relevant environments. While the atomic force microscope (AFM) has proved to be a tool of unprecedented sensitivity, which can provide atomic resolution images of inelastic samples[2] and is capable of detecting what may be individual hydrogen bonds,[3] the goal of sub-nanometer resolution imaging of biological samples has remained elusive. Here we report a significant step toward reaching this goal for protein micro-crystals.

To explore the ability of the AFM to image proteins at high resolution, beef liver catalase micro-crystals were chosen as a sample since they have been studied by a variety of techniques[4-12] and contain recognizable features of a size that should be resolvable by AFM. Catalase crystals have been reported in at least three forms;[13] needles, prisms and plates. The latter form, obtained by crystallization from low ionic strength solution near the isoelectric point, have the space group $P2_12_12_1$ and are typically several tenths of microns in lateral extent, but only fifty to one hundred nanometers thick.[14] This morphology makes them well suited for imaging by AFM. The crystal structure of beef liver catalase (EC 1.11.1.6), solved by Murthy *et al*,[12] showed the enzyme to be tetrameric with 222 symmetry. Each of the four polypeptide chains contains a high-spin Fe(III) protoporphyrin IX. Figure 1 shows two views of the catalase tetramer.

Initial efforts to prepare catalase micro-crystals[15] for microscopy involved simply allowing drops of an aqueous suspension containing micro-crystals to air dry on cleaned glass slides. Samples prepared by this method could be used for preparation of replicas for electron microscopy and atomic force microscopy in

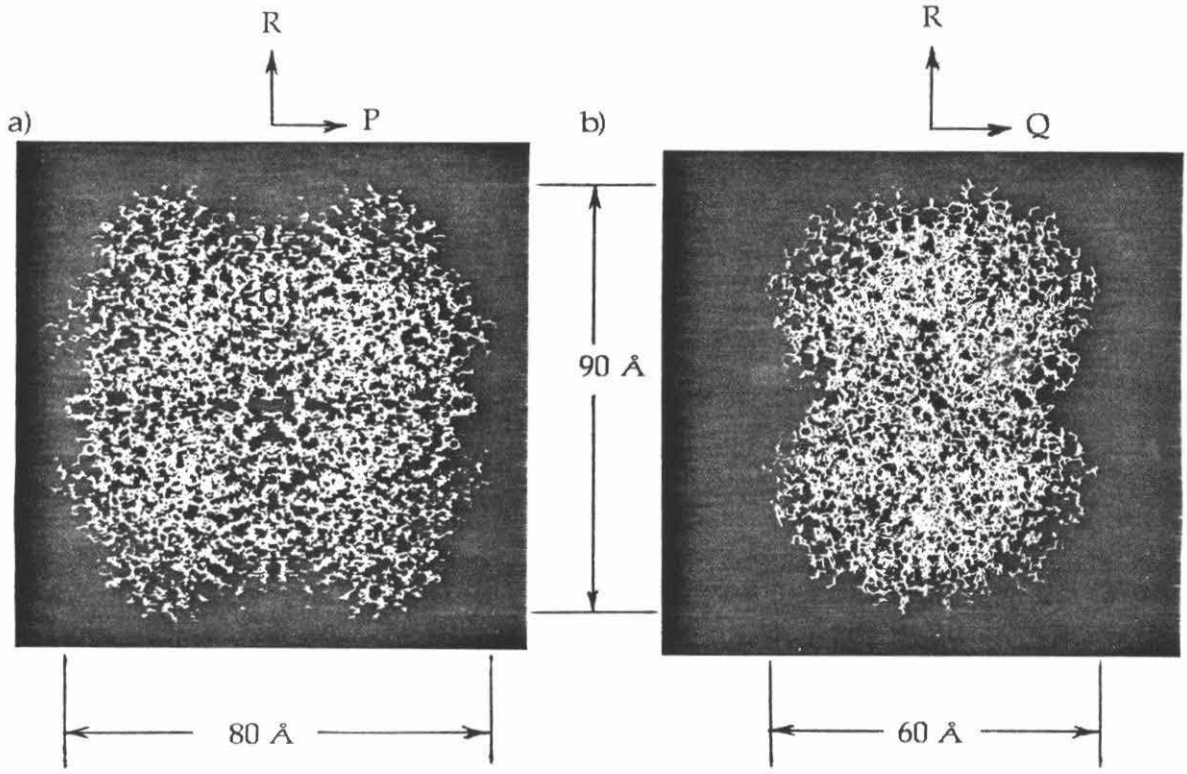

Figure 1. Two views of the catalase tetramer. a) a view of the molecule projected onto the P-R plane. In this view the tetrameric nature of the molecule is evident. b) a view of the molecule projected onto the Q-R plane. In this view the molecule has a "dumbell" shape.

air. However, when AFM was attempted in an aqueous environment no microcrystals were observed. Closer examination of samples exposed to water showed that the micro-crystals had detached from the glass surface and were instead in suspension. To prevent this, micro-crystal samples were applied to glass slides which had been derivatized by chemical vapor deposition of 3-aminopropyl triethoxysilane.[16] This process yields a surface with free amino groups which can be pre-activated with glutaraldehyde and then washed. Application of catalase micro-crystals to surfaces prepared in this way resulted in their immobilization.

Images of microcrystals were obtained in a water imaging environment using a commercial cantilever,[17] selected by examination in a TEM, with a custom built AFM which has been described elsewhere.[18] The forces applied by the cantilever, as calculated from the manufacturer's spring constant data, were in the nanonewton range. In low magnification images micro-crystals could be observed (Fig. 2a). The plate morphology of the micro-crystal is evident and step edges at the end of molecular layers are easily visible. Even at low magnification the crystal surface is not smooth and there are areas of differing sizes in which lattice sites are unoccupied. With the AFM, direct relative height measurements are possible. We measured the thickness of the crystal in Fig. 2a to be $\approx$ 600 Å, confirming that it was at most six molecular layers thick. After imaging regions like the upper left hand portion of the crystal (outlined) at high magnification we returned to the original scan size and checked for AFM induced distortion of the crystal; the sample appeared unaltered.

At higher magnification (Fig. 2b), images of the catalase micro-crystal surface reveal a crystalline array composed of features resembling individual

Figure 2. AFM images of beef liver catalase microcrystals. a) a low magnification image of a catalase micro-crystal. The boxed region indicates roughly the area imaged in b). By comparison with TEM images (not shown) it becomes clear that the concavities seen at the surface of the crystal and the edges represent individual molecular planes. b) a higher magnification image of the boxed area on the terrace of the crystal of a). In this image the tetrameric structure of the catalase molecules can be seen. We attribute the fact that the lattice lines in this image are curved to piezoceramic actuator nonlinearities (a well known phenomenon in scanned probe microscopy).

a)

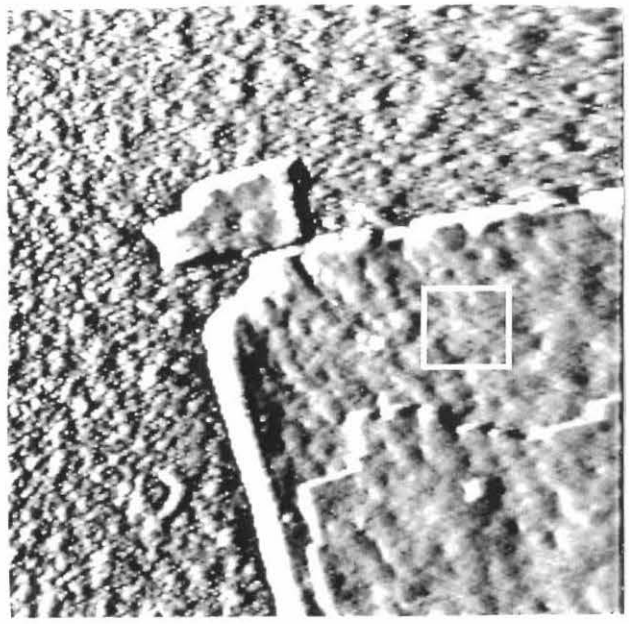

b)

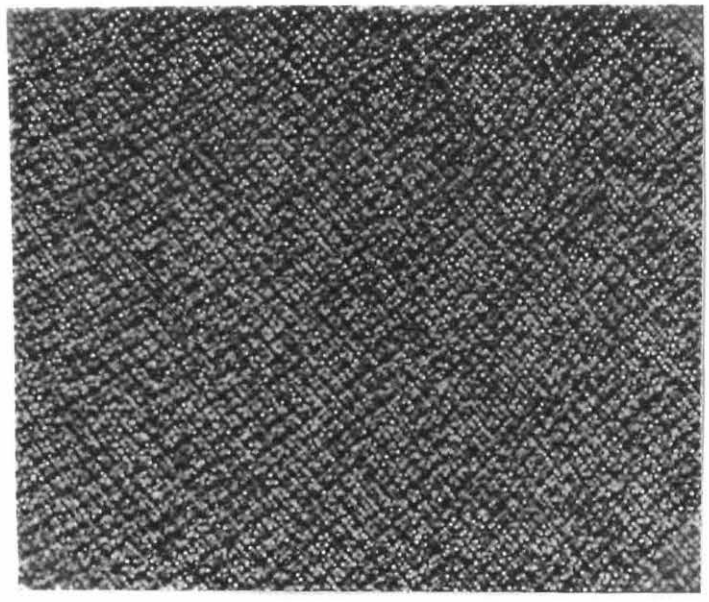

catalase tetramers in both size and morphology. The lattice is composed of features which alternate in their apparent depth; our interpretation is that the darker regions demarcate the boundary between adjacent tetramers. The small, roughly circular, dark regions located in the center of the tetralobate features are believed to indicate a centrally located depression between catalase tetramers. By using published values for the cell constants and measuring directly from the image, the resolution is better than 2 nm. We attribute the long range disorder in the image (the array does not follow a straight line) to piezoceramic transducer nonlinearity.[19] This type of distortion is not observed in TEM images of replicas taken from the micro-crystals. We believe this to be the first report of a high resolution image of the surface of a protein micro-crystal obtained by AFM.

It is often useful to compute the 2-dimensional Fourier transform to ascertain the symmetry properties, lattice constants and resolution of periodic images. In Fig. 3 we show a gray-scale representation of the 2-dimensional power spectrum derived from Fig. 2b.[20] This representation of the image emphasizes the presence of periodic features which appear as peaks in the spectrum. In the case of Fig. 3, the presence of peaks representing periodic features are visible out to the edges of the spectrum. These peaks correspond to image detail on the scale of a few pixels. We anticipate that further image processing[21,22] of the data of Fig. 2b might yield higher resolution on the nature of substructure of the catalase tetramers, however this relies on the increase in signal to noise ratio obtained by averaging the individual tetramers and thus does not represent an actual increase in the point to point resolution performance of the AFM.

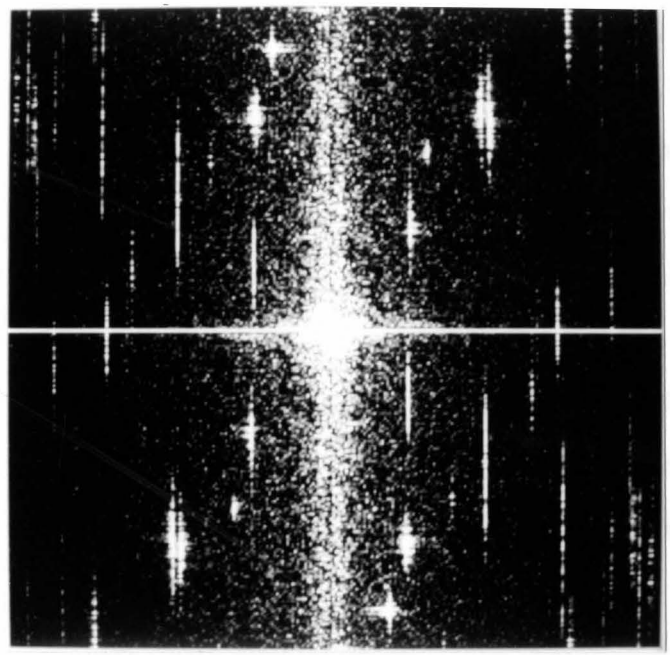

Figure 3. A gray scale representation of the 2-dimensional power spectrum of a portion of the image shown in Fig. 2b. In this representation the two axes are the axes of 2-dimensional reciprocal space and have units of nm^{-1}. Peak height is inversely proportional to gray scale, i.e., higher peaks are lighter.

We have also prepared surface replicas for TEM of the same catalase samples which were used for AFM. To do this, catalase micro-crystals were air dried on glass or mica and Pt-C coated in a Balzers freeze etch evaporator operated at room temperature. The replicas were floated off on water and mounted on EM grids for examination in a Phillips 420 EM. At low magnification features with a plate morphology similar to the micro-crystals seen in the light microscope and by AFM are found. It is not uncommon to find micro-crystals appearing to lay on top of one another. In a number of these cases the upper crystal appears to be split along a crystal plane. This apparent cracking of the crystals suggests that they are thin; counting molecular steps at the crystal edges gives an indication that they may be only five to ten molecular layers thick. We also note that the lateral dimensions of the crystals agree with the observations of earlier workers.

In the higher magnification TEM image (Fig. 4) an ordered crystalline array of objects corresponding to the size of individual catalase tetramers can be resolved and in some areas a tetralobate sub-structure similar to that visualized by AFM can also be seen. We presume that, as suggested by previous investigators, these structures represent catalase tetramers. Besides obvious crystals, there also were small (≈ 10 nm) structures present both on the substrate and on the crystals. We suppose that these structures represent individual catalase tetramers or multiples which have not been incorporated into a crystal.

Most studies of catalase have been done on whole crystals by transmission electron microscopy using various staining and sectioning techniques [10] or by X-ray and electron diffraction to visualize molecular orientation in the body of catalase micro-crystals. These techniques are oriented toward providing

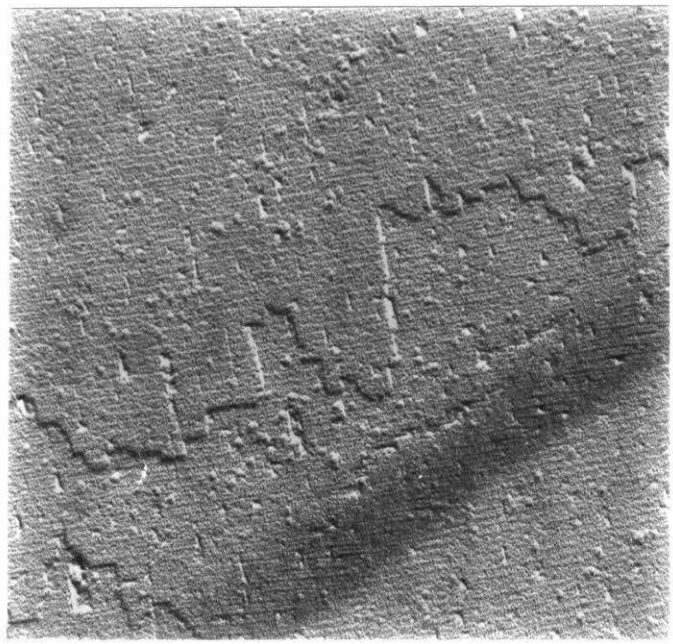

Figure 4. A transmission electron micrograph of a Pt-C replica of a catalase micro-crystal sample.

information on three-dimensional structure and give a general picture of the crystal packing, however they seem to differ in detail and, in at least one case, different molecular arrangements were noted. [9] Additionally, these techniques give relatively little information about the detailed structure of the surface of the micro-crystals, which is directly visualized by the AFM. Catalase crystal surfaces were first investigated with the transmission electron microscope by C. E. Hall[4] as early as 1950 and more recent studies by Furuno et al.[11] using high resolution SEM have also examined the surface structure of the crystals.

While the AFM is primarily a surface technique, some idea of molecular orientation can be obtained by measuring the thickness of step edges found in images of the catalase micro-crystals. When this measurement was performed it was found that step height was typically ≈ 10 nm, hinting that the orientation of the tetramers in the micro-crystals may be such that they are stacked like wafers in a box with the P and Q axes lying in the plane of the crystals. This would mean that the surface features visualized by the AFM are composed of the molecular corrugations along the R axis. Thus, the apparent tetralobate structure could be attributted to the arrangement of the tetramers in the crystal lattice. Further examination of electron micrographs provides evidence to support this model of molecular orientation (data not shown).

The data presented in this paper establishes the feasibility of using the AFM to image the surfaces of protein crystals at molecular resolution in a solvent environment. This capability could be important in the examination of micro-crystals and samples which do not exhibit X-ray diffraction to high resolution. However, perhaps the most intriguing extension of this ability is to investigate the growth of protein crystals in real time. Presently, studies of protein crystal

growth have been limited to a static representation of an inherently dynamic process.[23] The ability to directly visualize the process of protein crystal growth could lead to a better understanding of the factors which control crystal size and morphology.

High resolution imaging of biological samples has been a long standing goal in microscopy. Recent success in using the AFM to image samples such as DNA[24] and gap junctions[25] and other samples, in conjunction with the data presented here, indicates substantial progress toward achieving this goal. The resolution of biological images obtained by AFM still needs to be increased if the promise of "atomic" resolution is to be fulfilled. Presently, however, images with resolution which rivals or surpasses that available using other methods are easily obtained in physiologically relevant environments giving biologists a chance to directly investigate phenomenon with the AFM which would otherwise be inaccessible.

References and Notes

1. G. Binnig, C. F. Quate, Ch. Gerber, *Phys. Rev. Lett.* **56**, 930 (1986).
2. E. Meyer, H. Heinzelmann, H. Rudin, H. J. Guntherodt, *Z. Phys. B* **79**(1), 3 (1990).
3. J. H. Hoh, J. P. Cleveland, C. B. Prater, J.-P. Revel, P. K. Hansma, *J. Am. Chem. Soc.* **114**, 4917 (1992).
4. C. E. Hall, *J. Biol. Chem.* **185**, 749 (1950).
5. A. G. Malmon, *Biochim. Biophys. Acta* **26**, 233 (1957).
6. V. R. Matricardi, R. C. Moretz, D. F. Parsons, Science 177, 268 (1972).
7. D. L. Dorset and D. F. Parsons, *Acta Cryst.* A**31**, 210 (1975).
8. P. N. T. Unwin and R. Henderson, *J. Mol. Biol.* **94**, 425 (1975).
9. P. N. T. Unwin, *J. Mol. Biol.* **98**, 235 (1975).
10. C. W. Akey and S. J. Edelstein, *J. Mol. Biol.* **163**, 575 (1983).
11. T. Furuno, K. M. Ulmer, H. Sasabe, *Microscopy Res. and Technique* **21**, 32 (1992).
12. M. R. N. Murthy, T. J. Reid III, A. Sicignano, N. Tanaka, M. G. Rossmann, *J. Mol. Biol.* **152**, 465 (1981).
13. J. B. Sumner and A. L. Dounce, *Methods Enzymol.* **2**, 775 (1955).
14. It should be noted the the X-ray crystal structure was solved using trigonal crystals (space group $P3_221$) and the orthorhombic crystals (plate morphology) have a different space group ($P2_12_12_1$), thus it is impossible to generate a model of molecular orientation and lattice structure for the orthorhombic crystals using the available X-ray diffraction data.
15. Several milliliters of bovine liver catalase suspension (Calbiochem) were dissolved by dialysis against 100 volumes of 20 mM KH_2PO_4 / Na_2HPO_4 buffer (pH 7.4). The solution was then centrifuged at X 10,000 g for 5

minutes to remove undissolved material. The supernatant was harvested and adjusted to pH 5.3 with saturated KH_2PO_4. The solution was allowed to stand at 4 °C for several days at which time crystals were evident as schlieren when the solution was shaken. Crystals were harvested by centrifugation and washed with water repeatedly before use.

16. S. M. Clark, unpublished material.

17. Park Scientific Instruments, Inc., 1171 Borregas Avenue, Sunnyvale, CA 94089.

18. S. M. Clark, D. R. Baselt, C. F. Spence, M. G. Youngquist, J. D. Baldeschwieler, *Rev. Sci. Instrum, in press*; S. M. Clark and J. D. Baldeschwieler, unpublished material.

19. We have also noticed that the magnification may not be a linear function of the voltage applied to the piezoceramic; that is to say that calibrating the piezo response at two scan ranges does not allow one to measure intermediate distances with certainty. In general, piezo response is not only a function of the scanning voltages, but also depends on the mean value of the voltage and previous history.

20. The two-dimensional power spectrum was generated by the KHOROS software package. The image has been scaled such that the central (or "D.C." peak) does not obscure the other peaks in the spectrum.

21. W. O. Saxton and W. Baumeister, *J. Microscopy*, **127**, 127 (1982).

22. R. A. Crowther and L. A. Amos, *J. Mol. Biol.* **60**, 123 (1971).

23. See, for example, Durbin, S. D. and G. Feher, *J. Mol. Biol.* **212**, 763 (1990).

24. H. G. Hansma *et al*, *Science* **256**, 1180 (1992).

25. J. H. Hoh, R. Lal, S. A. John, J.-P. Revel, M. F. Arnsdorf, *Science* **253**, 405 (1991).

26. The authors wish to thank Michael Stowell for assistance with the molecular graphics of Fig. 1 and Wei Wu for assistance with the preparation of the 2-dimensional power spectrum of Fig. 3.

Future Directions for Scanned Probe Microscopy in Biology

Scanning Force Microscopy

Present Technological Limitations

Perhaps the predominating factor presently limiting resolution in scanning force microscopy (SFM) is tip-sample interaction. The emphasis of most of the work done to address tip-sample interaction has been on the development of methods for making sharper tips. While tip sharpness has been shown to be an important factor in obtaining high quality images, it almost certainly is not the only factor. Among the other variables which influence tip-sample interaction are tip surface chemistry, tip conductivity, etc.

Further development of tips will continue to be a key area of research for those interested in obtaining higher resolution images. It is likely that there will be additional effort placed on the reproducible fabrication of sharp tips using both more sophisticated micromachining techniques [1] and the electron beam deposition and ion milling approach. [2-5] Besides the more traditional approaches, carbon nanotubes [6] and other elongated structures may find novel application as SFM tips. One should also expect that there will be more advanced attempts to directly measure tip shape in the SFM and use this information to deconvolve the tip shape from the sample topography information. [7]

Perhaps, as more information concerning tip-sample interaction becomes available, it will be possible to use synthetic structures such as buckminsterfullerenes and chemically synthesized protein or nucleic acid

fragments to provide tip-sample interactions which are better defined. Some have even proposed that tips tailored to catalyze specific chemical reactions might be used to modify a surface on a very local scale.[8,9] However, without laying solid scientific groundwork on tip-sample interaction, these ideas will remain in the realm of science fiction.

Another area which requires further development is SFM sample preparation. Until now, only very rudimentary sample preparation techniques have been used for SFM. These have often consisted of drying a sample on an imaging substrate and imaging in air. For most samples this sort of treatment will not suffice and many of the lessons learned from electron microscopy should be applied to SFM. Perhaps one should consider the resolution of an image and the presence of artifacts as a figure of merit not only for the SFM but also for the sample preparation technique. Once the issues surrounding tip-sample interaction have been resolved, it should prove feasible to routinely obtain images having resolution in the 3 to 10 Å range. If this proves difficult, sample elasticity or intramolecular motion will need to be examined.

At the other end of the resolution spectrum lies the challenge of live sample preparation for SFM. The SFM can provide cell biologists and biophysicists with a powerful tool to probe processes and structural changes within cells and tissues. The biggest hurdle to realizing the potential of SFM in this area is the ability to integrate SFM with other cellular and neurobiological techniques such as confocal microscopy, microinjection, flash photolysis of caged analogs, etc. To accomplish this requires not only an effort in instrumentation, but also the modification or development of methods to

handle living tissues on the microscope stage. Already there are reports of concurrent epifluorescence and scanning force microscopy, [10] and we anticipate that other combinations will be developed and that their application to biology will be extraordinarily fruitful.

The final area requiring development that we will touch on here is the area of contrast enhancement. For light microscopy this is the area in which the most effort has been placed and the largest gains have been made. What is needed for SFM are the analogs of fluorescent antibodies and specific stains and dyes that are such powerful tools in light microscopy. One could envision a couple of different approaches to developing these markers. For high resolution imaging, it seems unlikely that new contrast enhancing agents which are roughly the size of a few atoms will be readily found. Perhaps the most fruitful approach to this problem will be to investigate ways to induce local charge at specific sites in samples and to then rely on charge sensitive styli to provide improved contrast. Another variation of this approach is to attempt to use chemically sensitive styli in conjunction with optical pumping to interrogate the composition of the sample. There are other methods which come readily to mind, but the point here is to emphasize that, given some effort, it is entirely possible that SFM can be made sensitive to many of the forces which play crucial roles in molecular interaction.

On a different scale, "stains" for scanning force microscopy of cellular components and tissues need to be developed. Scanning force microscopes can be easily used in modes which make use of contrast mechanisms such as elasticity and lateral force. These modes may actually provide more valuable

biological information than do topographic imaging modes. With the use of these alternative modes it may be possible to "stain" cellular components and organelles by applying reagents that selectively alter the compliance or elasticity of particular structures. A crude, but familiar, example illustrating this type of staining is the decrease in flexibility exhibited by DNA molecules following the intercalation of the rather nonspecific dye ethidium bromide.

Promising Areas in Scanning Force Microscopy of Biological Specimens

It would be remiss not to point out some of the areas of biology in which SFM can make immediate contributions. The first area of application, that of ultrastructural studies, is the most obvious. In many ways this area is quite challenging because to effectively study biological ultrastructure specimen preparation and comparative microscopy will be crucial. The targets most amenable for study will be samples which exhibit surface features of biological interest and are easily prepared such that they form layered structures. Some of the more obvious candidates meeting these requirements are protein micro-crystals, membrane structures (such as ion channels, pores, etc.) and cytoskeletal components. A comment should also be made on the types of structures which would probably be difficult to image well at high resolution. This category includes structures with substantial extent in the Z direction and structures which are prone to move as the tip scans over them (such as structures embedded in intact cell membranes).

SFM should also be a powerful adjunct to optical microscopy in the study of cellular structures at lower resolution. This type of work would

probably best be accomplished with an instrument capable of concurrent optical (epifluorescence or confocal) and scanning force microscopy. Such an instrument would allow the location of structures by optical microscopy at low resolution and subsequent investigation of the same structure by SFM, thus avoiding most of the problems of interpretation encountered when a sample is moved from a light microscope to a SFM.

The last area we will highlight is that of "real-time" measurements and the production of movies by SFM. Because SFM can scan a sample in less than a second, it is conceivable that, as instruments mature, it will be possible to assemble scan frames and record microscopic motions in "real-time." Perhaps the more exciting potential of SFM lies in its ability to measure piconewton forces directly. Once reliable methods are established for calibrating individual cantilevers, it should be possible to use the cantilever to monitor forces generated by molecular motors. By combining cantilever force measurement with the ability to release controlled quantities of caged analogs such as caged ATP, it should be possible to probe the intricacies of individual molecular motors more accurately than ever before.

Scanned Probe Microscopy for Biology

As mentioned in the introduction to this thesis, two other scanned probe microscopes hold special promise for the biologist. These are scanning ion conductance microscopy[11] and near-field scanning optical microscopy. [12] It is hoped that these instruments will be developed at a rapid pace and become available in a robust form for biologists to work with.

Some Perspective

As pointed out previously, microscopy has been evolving since ancient times. Curious minds have always sought to visualize finer and finer detail hoping that the details would suggest a pattern obeyed by the whole, thus providing a unifying framework which advances understanding. For the last four hundred years scientists from various fields have advanced and honed light microscopy to its present state. In the last sixty years electron microscopy and X-ray diffraction have emerged as the workhorses for high resolution studies in biology; while in the last fifteen years applications of NMR techniques to structural problems in biology has blossomed.

When compared to these venerable fields, scanned probe microscopy is still in its infancy, and while this should not be used to excuse substandard science, it should serve to encourage those who would use the scanning probe microscope as a tool for investigating the natural world, particularly its biological aspects. Like any tool SPM has its limitations, artifacts and inappropriate uses, but it also has great advantages when used judiciously. Also, as with any developing technique, SPM requires patience, dedication and creativity for success. But the most important point is that, after seven years of scanning force microscopy, it is still an exciting field with room for improvement and innovation and for biology, the best is yet to come.

References:

1. Ravi, T. S. *et al.* (1990). "Fabrication of atomically sharp tungsten tips." *Appl. Phys. Lett.* **57** (14):1413-1415.
2. Keller, D. J. and C. Chih-Chung. (1992). "Imaging steep, high structures by scanning force microscopy with electron beam depositedtips." *Surface Science* **268**:333-339.
3. Lee, K. L, D. W. Abraham, F. Secord and L. Landstein. (1991). "Submicron Si trench profiling with an electron-beam fabricatedatomic force microscope tip." *J. Vac. Sci. Technol.* **B9** (6):3562-3568.
4. Vasile, M. J. *et al.* (1991). "Scanning probe tips formed by focused ion beams." *Rev. Sci. Instrum.* **62** (9):2167-71.
5. Vasile, M. J. *et al.* (1991). "Scanning probe tip geometry optimized for metrology by focused ion beam ion milling." *J. Vac. Sci. Technol.* **B9** (6):3569-72.
6. Ebbesen, T. W. and P. M. Ajayan. (1992). "Large-scale synthesis of carbon nanotubes." *Nature* **358**:220-222.
7. Griffith, J. E. *et al.* (1991). "Characterization of scanning probe microscope tips for linewidth measurement." *J. Vac. Sci. Technol.* **B9** (6):3586-3589.
8. Drexler, K. E. and J. S. Foster. (1990). "Synthetic Tips." *Nature* **343**:600.
9. Drexler, K. E. (1991). "Molecular tip arrays for molecular imaging and nanofabrication." *J. Vac. Sci. Technol.* **B9** (2):1394-1397.
10. Putman, C. A. J. *et al.* (1992). "Atomic force microscope with integrated optical microscope for biological applications." *Rev. Sci. Instrum.* **63** (3):1914-17.

11. Prater, C. B., P. K. Hansma, M. Tortonese, C. F. Quate. (1991). "Improved scanning ion-conductance microscope using microfabricated probes." *Rev. Sci. Instrum.* **62** (11):2634-2638.

12. Betzig, E. and J. K. Trautman. (1992). "Near-Field Optics: Microscopy, Spectroscopy and Surface Modification Beyond the Diffraction Limit." *Science* **257**:189-195.